



HAL
open science

Cavity-enhanced Photon-Photon Interactions With Bright Quantum Dot Sources

Valérian Giesz

► **To cite this version:**

Valérian Giesz. Cavity-enhanced Photon-Photon Interactions With Bright Quantum Dot Sources. Quantum Physics [quant-ph]. Université Paris Saclay (COMUE), 2015. English. NNT: 2015SACLS188 . tel-01272948

HAL Id: tel-01272948

<https://theses.hal.science/tel-01272948>

Submitted on 11 Feb 2016

HAL is a multi-disciplinary open access archive for the deposit and dissemination of scientific research documents, whether they are published or not. The documents may come from teaching and research institutions in France or abroad, or from public or private research centers.

L'archive ouverte pluridisciplinaire **HAL**, est destinée au dépôt et à la diffusion de documents scientifiques de niveau recherche, publiés ou non, émanant des établissements d'enseignement et de recherche français ou étrangers, des laboratoires publics ou privés.

NNT : 2015SACLS188

THÈSE DE DOCTORAT
DE L'UNIVERSITÉ PARIS-SACLAY
préparée à l'Université Paris Sud

DISCIPLINE : Nanophysique

École Doctorale Onde et Matière (EDOM) n° 572

par

M. Valérian Giesz

Cavity-Enhanced Photon-Photon Interactions
Using Bright Quantum Dot Sources

préparée au :

Laboratoire de Photonique et Nanostructures (LPN) - CNRS

**Thèse soutenue publiquement
à Marcoussis le 14 décembre 2015**

Composition du jury:

Pr. Philippe Grangier	Institut d'Optique	Président
Pr. Valia Voliotis	UPMC	Rapporteur
Pr. Glenn S. Solomon	NIST - Univ. of Maryland	Rapporteur
Pr. Khaled Karrai	Attocube Systems	Examineur
Pr. Jean-Michel Raimond	LKB - Collège de France	Examineur
Pr. Pascale Senellart	LPN	Directrice de thèse



*Lorsqu'ils chassaient le bison, nos ancêtres y allaient en groupe.
C'est ensemble qu'ils pouvaient encadrer l'animal et
ensemble qu'ils joignaient leurs efforts pour le capturer.
Celui qui avait porté le coup final n'était pas le plus méritant.*

ALBERT JACQUARD (1925-2013)

Remerciements

Comme illustré par Albert Jacquard avec sa chasse en troupe, ce travail n'aurait pas été le même s'il n'avait pas impliqué de nombreuses personnes. Pendant ces trois années, j'ai eu la chance de rencontrer et de côtoyer de nombreuses personnes. J'aimerais, ici, adresser quelques mots de remerciement à celles qui ont influé de près ou de loin à ce travail.

J'adresse mes premiers remerciements aux membres du jury à qui j'ai pu présenter mes travaux avec beaucoup de plaisir. Je remercie Jean-Michel Raimond et Khaled Karrai d'avoir accepté de prendre le temps de lire mon manuscrit et de venir examiner ce travail avec un regard expert. Je remercie également Philippe Grangier d'avoir présidé ce jury et d'avoir animé une séance de discussion très enrichissante. J'adresse des remerciements tout particuliers à Glenn Solomon et à Valia Voliotis pour avoir accepté d'être rapporteurs et d'avoir lu attentivement mon travail.

L'intégralité de ma thèse s'est effectuée dans ce cadre idyllique qu'est le LPN, j'en remercie sincèrement Dominique Mailly. Je remercie chaque membre du laboratoire, pour cette atmosphère de travail et d'entraide que chacun peut sentir au quotidien. J'adresse une pensée particulière à Stéphane Guilet et aux sportifs du midi, vous m'avez tiré en dehors de ma salle de manip pour partager une bonne dose d'oxygène et de sueur.

Je n'aurais jamais pu réaliser cette thèse sans la confiance de ma directrice de thèse Pascale Senellart. Je suis infiniment reconnaissant pour la confiance qu'elle a placée en moi en m'acceptant dans son équipe et pour l'encadrement exceptionnel qu'elle a apporté pendant ces trois ans. Si cette thèse avait été un combat de boxe, j'ai eu la chance de l'avoir dans mon coin, pour m'accompagner et me guider afin que j'évite les mauvais coups. Je la remercie infiniment pour son enthousiasme et son énergie quotidiens, pour savoir manier qualités scientifiques et qualités humaines à la perfection. Grâce à elle, je suis toujours allé au labo avec une énorme motivation. Les discussions scientifiques qu'elle animait et les connaissances qu'elle a transmises ont été d'une valeur inestimable

et m'ont donné les outils pour passer ma thèse de doctorat. Mille mercis.

A mon arrivée, j'ai eu la chance d'être initié aux expériences par Olivier Gazzano, Simone Luca Portalupi et par Anna Nowak. Je remercie Anna Nowak pour sa gentillesse et la précision avec laquelle elle m'a montré les techniques dans la salle blanche. Un énorme merci à Olivier Gazzano qui a été très patient avec moi pour me communiquer tout ce qu'il savait malgré la pression de fin de thèse qu'il devait subir, merci pour ce regard de grand frère. Je remercie beaucoup Simone Luca Portalupi pour avoir partagé mes deux premières années de thèse. Il m'a initié aux techniques de fabrication, de caractérisation optique mais aussi à l'italien. Simone a été un compagnon de labo extraordinaire et un formidable partenaire dans l'élaboration de notre premier réseau quantique.

Merci à Loic Lanco pour son enthousiasme, ses idées et ses conseils. En plus de grandes compétences scientifiques, Loic sait toujours garder son optimisme et son sourire dans toutes les situations. Sa bonne humeur permanente a été une grande leçon pour moi. Merci encore.

Je remercie Justin Demory pour avoir partagé ces trois années de thèse avec moi. Justin a été un frère de thèse, avons commencé et fini en même temps, nous sommes serré les coudes pour affronter les difficultés de la thèse.

Je remercie Daniel Kimura pour avoir apporté son sourire, son énergie et de m'avoir fait profiter de ses très grandes qualités à la fois scientifiques et humaines. Le CNRS et le labo ont vraiment de la chance de l'avoir recruté, car Daniel fait partie du cercle de ceux qui apportent beaucoup à leur environnement. Merci infiniment pour sa disponibilité et son aide.

Niccolo Somaschi a rejoint l'équipe pendant ma deuxième année de thèse. J'ai eu la chance de faire ma dernière année à ses côtés. Alors que je subissais la pression de la dernière année, Niccolo m'a communiqué son calme. La maîtrise avec laquelle il a travaillé m'a permis d'affronter la fin de ma thèse avec confiance. Grâce à sa très grande précision expérimentale, j'ai pu travailler sur de superbes échantillons avec lui. Merci beaucoup Niccolo. Je suis absolument ravi et confiant à l'idée de commencer de nouveaux projets avec lui.

Je remercie Lorenzo pour sa rigueur et sa précision à plusieurs chiffres après la virgule. Il a su soulever des points où je n'étais pas aussi rigoureux que lui, il m'a aidé à y voir plus clair à propos des questions que je n'avais pas élucidé tout seul. Un grand merci

pour son aide et sa gentillesse. Je sais que les expériences seront en de bonnes mains avec lui.

Je remercie Carlos Anton pour sa joie de vivre et ses compétences scientifiques. Carlos apporte une grande énergie dans tous les projets où il s'implique, c'est inestimable.

Un grand merci à Alexia Auffèves et son équipe à l'Institut Néel : Gaston Hornecker, Thomas Grange et Bogdan Reznichenko. Grâce à nos discussions et nos nombreuses sessions Skype, j'ai compris énormément de mécanismes jusqu'à alors très flous. Leurs calculs nous ont permis d'y voir clair là où nous étions complètement perdus.

Merci à Andrew White et à son équipe de l'université de Queensland en Australie avec Marcelo de Almeida et Juan Loredó. Leur expérience en optique quantique a été d'une aide très précieuse.

Merci aux membres de l'équipe NAPHEL du LCF, je pense que je n'aurais pas pu réaliser cette thèse dans le groupe de Pascale sans le soutien de François Marquier et de Jean-Jacques Greffet. Nos rencontres, dans un cadre scientifique ou non, sont toujours un moment agréable. J'espère qu'elles seront encore nombreuses.

Merci à Fabrice Lamberti dont l'humour quelque peu décalé a été une réelle bouffée d'oxygène. Je suis sûr que son investissement avec Daniel sera l'impulsion de départ à de nouvelles expériences chez les GOSS.

Je remercie sincèrement Olivier Krebs. La porte de son bureau a toujours été ouverte et il a toujours accepté de m'aider. Merci pour ses conseils et son aide.

Plus globalement, je remercie Paul Voisin dont les qualités scientifiques et humaines maintiennent le groupe GOSS à un niveau d'excellence et d'entente exceptionnel.

Merci à Jacqueline Bloch et à Alberto Amo, leur porte a toujours été ouverte pour moi, que ce soit pour m'aider à résoudre un problème scientifique ou simplement pour l'une des discussions que j'ai adorées avoir avec eux. Merci pour leurs conseils, leurs remarques et leur écoute.

Je remercie Aristide Lemaître et Carme Gomez pour avoir assuré la croissance des échantillons de ma thèse et également pour avoir initié aux techniques de croissance

le néophyte que je suis.

Je remercie Dimitrii Tanese, Vera Giulia Sala, Félix Marsault, Florent Baboux, Marijana Milicevic, Valentin Goblot et Christian Kessler pour avoir été de formidables voisins de bureau. Merci d'avoir été patient, pour la belle ambiance de travail et de détente selon les heures.

Merci beaucoup à Guillaume Coppola, Paul Hilaire, Said Rodriguez, Peristera Andreakou, Hai Son Nguyen, Thibaut Jacqmin, Chris Sturm pour avoir partagé de nombreuses discussions scientifiques ou non.

Je remercie également l'équipe administrative du LPN au grand complet. Elle a toujours fait en sorte que les problèmes administratifs nous touchent peu et a toujours été très arrangeante et réactive. C'est un gain de temps considérable pour une thèse qui sera toujours trop courte.

J'aimerais également remercier l'équipe de l'institut Villebon-Charpak que j'ai rencontrée dans le cadre de mon monitorat à l'université Paris-Sud. Je remercie Fabienne Bernard, Tatiana Séverin-Fabiani, Jeanne Parmentier, Sébastien de Rossi, Martine Thomas, Cécile Narce, Isabelle Demeure et Bénédicte Humbert avec qui j'ai eu la chance de travailler pendant deux ans. Le projet de l'institut Villebon-Charpak est, je l'espère, un projet d'avenir qui facilitera l'accès aux études supérieures à tous les profils, qui est une problématique qui m'est chère.

Merci également à Zoé Chanau et à Thibault Gosselin, étudiants de l'institut Villebon-Charpak qui ont accepté de venir travailler avec moi au cours d'un stage. Leur bonne humeur, leur curiosité et leur motivation ont fait que ce stage a été un réel plaisir. En leur souhaitant beaucoup de réussite pour l'avenir.

Je remercie également Augustin d'Humières, mon professeur de grec ancien au lycée, avec qui j'ai collaboré au sein de l'association Mêtis. J'ai accepté la présidence de l'association pendant ma thèse, et Augustin a été un partenaire indispensable dans le bon fonctionnement quotidien de l'association. Grâce à sa présence, j'ai pu conduire mes travaux de thèse relativement paisiblement.

Enfin, j'adresse mes plus tendres remerciements à mes proches. Je remercie mes familles de tous horizons, avec mes excuses les plus sincères pour les réunions familiales où j'étais absent. Le soutien familial dont je profite est un atout qui m'a beaucoup aidé pour en

arriver là. Encore merci.

Je remercie également l'ensemble de mes amis, de tous horizons. Merci à mes amis briards, cette éternelle bande de vieux kepons. J'ai une pensée spéciale à mes amis de coloc. Pendant ces trois ans de thèse, nous en avons profité pour partager beaucoup. J'espère que ça continuera.

J'adresse un remerciement particulier à Marie-Christine. Merci pour son soutien pas toujours réciproque (et j'en suis sincèrement navré). Merci pour son amitié qui m'est très chère. En lui souhaitant beaucoup de réussite.

Merci à tous.

Valérian

Contents

Remerciements	v
Contents	x
Résumé	xv
1 Introduction	1
2 Fundamentals of QD Based Single Photon Sources	7
2.1 Structure of Self-Assembled Quantum Dots	8
2.1.1 Self-Assembled Quantum Dots in Semiconductor	8
2.1.2 Energy levels of carriers in a Quantum dot	9
2.1.3 Coulomb Interactions in a QD and Exciton Fine Structure Splitting	11
2.1.4 Occupancy States of a Quantum dot	14
2.1.5 Spontaneous Emission by recombination of charges	17
2.1.6 Single QD Spectroscopy	18
2.1.6.1 Optical excitation	18
2.1.6.2 Power measurements	19
2.1.7 Single photon emission from a QD	23
2.1.8 Coupling to phonons	23
2.2 Characterization of a QD as a Quantum Light Source	24
2.2.1 Introduction to light sources statistics	24
2.2.1.1 Second order correlation function	24
2.2.1.2 Bunched sources: example of thermal sources	26
2.2.1.3 Poissonian Sources	26
2.2.1.4 Anti-bunched Sources (example of the Fock states)	27
2.2.1.5 The Hanbury-Brown and Twiss setup	28
2.2.2 Emission of indistinguishable photons from a QD	29
2.2.2.1 Introduction: The HOM experiment	29
2.2.2.2 Overlap of photon wavepackets emitted by one QD	30
2.2.2.3 State-of-the-art	30
2.3 Cavity Quantum ElectroDynamics (CQED)	32
2.3.1 Theory of coupled emitter-cavity systems	32
2.3.1.1 The Jaynes-Cummings model	32
2.3.1.2 Spontaneous emission in a cavity	33
2.3.1.3 The lossy cavity: the Purcell effect	34
2.3.2 Semiconductor Structures Confining Light	37
2.3.2.1 Cavities	38

2.3.2.2	Semiconductor waveguides	39
2.4	Techniques of cavity-QD coupling	41
2.4.1	Deterministic techniques of coupling of a QD in a cavity	41
2.4.2	Coupling a single QD in a cavity using the <i>in situ</i> lithography	42
2.5	Brightness of a single-photon source	46
2.5.1	Definition of the brightness	47
2.5.1.1	Brightness of a parametric down conversion source	47
2.5.1.2	Brightness of a single QD in a bulk	49
2.5.1.3	Brightness of a single QD in a micropillar	50
2.5.2	Recent progresses in the extraction of photons emitted by a QD	51
3	Purity And Indistinguishability of Devices Based on Adiabatic Cavities	53
3.1	Latest Results in 2012 : Bright Indistinguishable Photons from a Micropillar	54
3.2	Fabrication of Devices Operating in the High Purcell Regime	57
3.2.1	Adiabatic Cavity Design	58
3.2.2	Design and Characterization of the Planar Structure	59
3.2.3	Fabrication of QD-Adiabatic Pillar Devices	61
3.3	Experimental Characterization of a QD Coupled to an Adiabatic Pillar Cavity	62
3.3.1	Microphotoluminescence Setup and Thermal Control of the Spectral Detuning δ_{X-CM}	62
3.3.2	Influence of Temperature on PL Spectra	64
3.3.3	Evolution of the Decay Times With the Spectral Detuning	65
3.3.4	Brightness of a High Purcell Device	68
3.4	Purity of a Single-Photon Source	70
3.4.1	Temperature Tuning of the Purcell Effect	70
3.4.2	Single-photon Purity as a function of Purcell Effect	72
3.4.3	Recapture Processes Induced by Non Resonant Excitation	74
3.5	Characterization of the Photon Indistinguishability	78
3.5.1	Description of the HOM-Interferometer	78
3.5.2	Measurement and Extraction of the Mean Photon Overlap	82
3.5.3	Influence of Excitation Conditions on the Mean Wave Packet Overlap	85
3.5.4	Memory Effects and Influence of Electronic Charges	89
3.5.4.1	Blinking Effect	90
3.5.4.2	Long-term Antibunching	92
3.6	Conclusion	92
4	Indistinguishability of Electrically Controlled Sources	95
4.1	Fabrication of Electrically Controlled Devices	95
4.1.1	State-of-the-art	96
4.1.2	First Deterministic Fabrication of a Bright Tunable QD Based Source	98
4.1.3	Optimized Sample for the Control of Charges	102
4.1.4	Voltage Tunable PL	103
4.2	Full characterization of the Pillar 13A	105
4.2.1	Setup Transmission	105

4.2.2	Single-Photon Purity and Measured Brightness	105
4.2.3	Indistinguishability of Successively Emitted Photons	108
4.3	Results on Another Device: 15B	110
4.3.1	Excitation-Jitter-limited Indistinguishability	111
4.4	Conclusion	112
5	High Indistinguishability and High Brightness from Resonant Fluorescence Spectroscopy	115
5.1	Introduction	115
5.2	Setup Used for the Resonant Excitation	117
5.2.1	Reflectivity Measurements	122
5.3	Emission Mechanisms in Crossed Polarization	124
5.3.1	Qualitative Discussion	124
5.3.2	Theoretical Model of the Emission in Crossed Polarization	125
5.4	Coherent Control With Few Photon Pulses	128
5.4.1	Observation of Rabi oscillations under a pulsed excitation	128
5.4.2	Connecting Flying Qubit with Quantum Nodes	130
5.4.3	Coherent Control With Few Photon Pulses	130
5.5	Characterization of the Device 18B under Resonant Excitation	133
5.5.1	Single Photons Emission under Resonant Excitation	133
5.5.2	Two-photon Interference with Near-Unity Photon Indistinguishability	134
5.5.3	Brightness	138
5.6	Comparison With State-Of-The-Art and Conclusion	139
6	Cavity Enhanced Two-Photon Interferences Using Remote Sources	141
6.1	Introduction	141
6.2	Photons Emitted With a Common Excitation	145
6.2.1	Synchronisation of Emission from Remote Sources	147
6.2.2	Single-Photon Properties Using a Common Excitation	148
6.2.3	Indistinguishability between Photons Successively Emitted from the same Source	149
6.3	Measurement of the Two-Sources Interference	151
6.3.1	Simultaneous Emission of Remote Sources for the Interference	151
6.3.2	Spectral Tuning using the Temperature	151
6.3.3	Measurement of the Correlations	152
6.3.4	Measured Photon Overlap	153
6.4	Cavity Enhanced Interference	154
6.4.1	Theoretical Model - Overlap of Distinct Photons	154
6.4.2	Comparison with the Measured Photon Overlap	156
6.4.3	Conclusion	159
7	Conclusion and Perspectives	161
7.1	Strategies to Improve the Sources	162
7.2	Toward Ultrabright and Highly Indistinguishable Sources of Entangled Photon Pairs	163
7.3	Generation of a High Photonic NOON States using QDs	164
7.4	Boson Sampling Experiments with QD sources	167

7.5 A Step Closer to the Quantum Repeater and the Single-Photon Router ?	171
--	-----

List of Publications	173
-----------------------------	------------

A Phonon influence on the emission of a QD coupled to a cavity	175
---	------------

A.1 Spontaneous emission of a quantum dot in a cavity assisted by phonons bath	175
---	-----

A.2 Photon statistics	178
---------------------------------	-----

A.3 Phonon assisted bright single-photon source	179
---	-----

Bibliography	181
---------------------	------------

Résumé

Les recherches dans le domaine de l'information quantique ont mené à de réelles avancées dans le stockage, le traitement et la transmission de l'information quantique sous forme de bits quantiques (appelés qubits). Ces recherches portent sur divers systèmes tels que les qubits supraconducteurs, des défauts dans du diamant, des atomes, des ions et des molécules isolés ou des boîtes quantiques (BQs) semiconductrices. Ces systèmes forment alors des nœuds statiques dans un réseau d'information où le photon unique est le meilleur messenger pour transporter des qubits d'un nœud à l'autre. Ces recherches ont mené à de nouvelles techniques rendant la manipulation et la détection de photons uniques de plus en plus simples et efficaces.

Dans ce contexte, le développement d'une source idéale de photons uniques est une clé de voûte dans le développement de nouvelles technologies. La source idéale doit émettre des photons uniques sur demande avec une très grande efficacité et ne doit pas émettre plusieurs photons simultanément. La brillance d'une source est une caractéristique importante et est définie comme la probabilité qu'un photon demandé soit bel et bien collecté. Une autre propriété est cruciale pour certaines applications, les photons doivent être indiscernables. Les photons émis doivent tous présenter les mêmes propriétés (énergie, modes spatial et temporel, polarisation). Leur degré d'indiscernabilité est mesuré en envoyant deux photons sur chaque entrée d'un séparateur de faisceaux. Si les deux photons sont indiscernables, ils interfèrent constructivement et ressortent obligatoirement ensemble.

La majorité des avancées dans le domaine de l'information quantique ont été réalisées en utilisant des lasers atténués ou des sources à conversion paramétrique. Dans les deux cas, la brillance est fortement limitée à cause de la statistique poissonnienne des sources. La manipulation d'émetteurs uniques (atomes, BQs,...) offre donc une alternative viable aux sources poissonniennes car ils sont capables d'émettre un photon à la fois. Parmi les diverses solutions disponibles, les BQs semiconductrices offrent d'excellents résultats en terme de brillance, de pureté des photons uniques et d'indiscernabilité des photons. En tant que petit groupe d'atomes semiconducteurs de faible énergie de gap

dans une matrice semiconductrice, une BQ est capable de confiner un petit nombre de charges électroniques. Grâce au confinement spatial, ces charges se relaxent une à une en émettant des photons à des énergies discrètes à l'image des électrons orbitant autour du noyau d'un atome. La difficulté est alors de collecter ces photons émis dans toutes les directions de l'espace dans un milieu d'indice optique élevé. Le taux de collection avec des BQs dans un semiconducteur est de l'ordre de deux ou trois photons sur cent. Depuis 2010, des brillances de l'ordre de 80% ont été atteintes dans différents groupes grâce à diverses techniques. L'une d'entre elles consiste à contrôler l'émission spontanée d'une BQ en la couplant dans une cavité optique. Le taux d'émission spontanée de la BQ dans le mode de la cavité est alors multiplié par un nombre appelé le facteur de Purcell.

Cette thèse a été réalisée au sein du groupe du Dr. Pascale Senellart au Laboratoire de Photonique et Nanostructures (LPN) du CNRS. Depuis une dizaine d'années, Pascale Senellart a développé une expertise dans la fabrication de sources brillantes de photons uniques en couplant de manière déterministe et contrôlée une BQ unique dans un micropilier et en contrôlant l'émission spontanée de la BQ dans le mode optique du pilier. En 2013, la fabrication de sources brillantes de photons uniques et indiscernables a été démontrée par l'équipe.

Le but de cette thèse a donc été d'améliorer les performances des sources fabriquées au LPN en utilisant diverses techniques. Dans un premier temps, une nouvelle architecture de cavité a été utilisée pour augmenter le facteur de Purcell. Nous avons démontré alors la fabrication d'une source très brillante de photons uniques en accélérant fortement l'émission spontanée de la BQ dans le mode de la cavité avec un facteur de Purcell supérieur à 10 (chapitre 3). Cependant, nous démontrons également que l'indiscernabilité des photons est globalement dégradée à cause d'instabilités électroniques liées à la proximité des BQs avec les miroirs de la cavité, spécifique à cette nouvelle architecture. Dans un second temps, nous avons travaillé sur le développement de sources brillantes contactées électriquement pour (i) contrôler l'énergie d'émission des BQs par effet Starck et (ii) stabiliser l'environnement électronique des BQs. Grâce à une autre architecture de cavité innovante, nous avons combiné le couplage en cavité de BQs avec un contrôle électrique externe (chapitre 4). Grâce au contrôle électrique, l'indiscernabilité a été améliorée et n'est plus limitée par les fluctuations électroniques environnantes des BQs mais par la relaxation des charges confinées avant la recombinaison radiative. L'indiscernabilité parfaite est alors obtenue en excitant la BQ avec un laser résonant avec sa transition radiative (chapitre 5). Nous montrons également le contrôle cohérent de l'état quantique de la BQ en envoyant seulement quelques photons par impulsion

laser sur l'échantillon. Cette performance est notamment liée à l'excellent couplage entre le mode de la cavité utilisée et le mode fondamental d'une fibre optique et ouvre de nombreuses perspectives pour la réalisation de mémoires quantiques de qubits uniques.

Enfin, la dernière partie de ce manuscrit (chapitre 6) décrit une expérience impliquant plusieurs sources brillantes connectées optiquement. Les interactions entre photons émis par deux sources ont été étudiées qualitativement et quantitativement. Nous avons étudié l'intérêt de modifier l'émission spontanée d'une des sources dans le cas où le contraste d'interférences serait dégradé.

En somme, ce manuscrit résume les optimisations utilisant les techniques développées dans le groupe de Pascale Senellart au LPN. Les performances des sources brillantes de photons uniques et indiscernables ont été largement optimisées jusqu'à obtenir des photons parfaitement indiscernables avec une très grande brillance. De telles sources ouvrent de nombreuses perspectives dans divers domaines : communications quantiques, émulations quantiques, métrologie ou encore de nouvelles techniques en imagerie.

Chapter 1

Introduction

The latest developments in quantum technologies have shown impressive progress in the storage, process and transmission of quantum information using quantum bits (qubits). Many systems have been explored, such as: photons [1, 2], ions [3, 4], superconducting qubits [5], defects in diamond (NV centers) [6], atoms [7] and semiconductor quantum dots (QDs) [8] obtaining spectacular progress in every research area. Currently, the continuously increasing number of entangled qubits with ions [9] and superconducting qubits [10] (up to 14 qubits and to 9 qubits, respectively), make them the best systems for local information processing. Yet, to connect two of such local nodes, photons appear as the most natural channel [11, 12].

Indeed, the speed of the information transmission and the low-noise properties of photons constitute extremely attractive characteristics for quantum information communications. Encoding information on a single photon is relatively easy. Moreover, they can interact with a large variety of quantum nodes: atoms [13, 14], ions [15], NV centers [16, 17] and quantum dots [18–20]. Finally, at the single photon level, the communication is secured since the measurement of the information contained in a photon by an eavesdropper affects the information itself, which triggers an alert.

In this context, the ideal photon source is an **on-demand deterministic single-photon source**. A “single photon” source emits photons one by one, and never two photons simultaneously. This single photon emission should be provided “on-demand” and never at a random time. This excludes the continuous wave operation regime. The source should produce pulses of single photons at a well-defined frequency; the higher the frequency, the higher the communication transfer rate. Finally, this emission process should be deterministic: each pulse should contain a single photon with a probability of one. This crucial characteristic is quantified by the source **brightness**: the probability that one collected pulse actually contains one photon. Of course, such properties are very difficult to gather, optical losses inevitably degrade the deterministic nature of the source even if this one is ideal.

An additional and very important requirement for quantum information processing applications and long distance communications is to implement and control the two-photon interactions. In the current photonic technologies, this interaction is based on the photons indistinguishability. When two identical photons meet on a beamsplitter, they interfere exiting together through the same output port, with a zero probability of leaving the beamsplitter separately. This quantum phenomenon allows implementing two photon optical gates for quantum processing of information or Bell state measurements in quantum relays for instance.

Today, most commonly used sources in optical quantum technologies are attenuated lasers or sources based on spontaneous parametric-down conversion (SPDC) [12]. Attenuated lasers are used in commercial quantum cryptography systems: by strongly attenuating the light, one can reach a regime where the probability to obtain two photons is very low. However, this is of course at the expense of having a very low probability to obtain one photon. The brightness is thus limited to few percent in practice. Such solution imposes a strong limitation in the quantum information transfer rate.

Alternatively, SPDC sources are used to obtain heralded single photon sources. An intense beam sent to a nonlinear crystal is converted into two down-converted beams. Because these photons are created in pairs, the detection of one photon in one beam can be used to herald the presence of another one in the other beam. The heralding process leads to a sub-poissonian statistic for the heralded signal. Heralded SPDC sources offer the advantage of relatively easy room temperature operation and very high degrees of indistinguishability. They have been extensively used in the last two decades, with beautiful demonstrations like the implementation of an optical quantum CNOT gate [21], the measurement of a phase below the classical limit [22, 23], the quantum teleportation [24], the implementation of optical quantum computing [25] or even the quantum simulation of chemical [26] and physical processes [27, 28]. Yet, because the conversion process is super-poissonian, the single photon purity of a heralded source rapidly degrades with the source brightness. Experiments involving the measurement of coincident event among three or four photons require acquisition times of tens or hundreds to hours.

In parallel, strong efforts have been made by the solid-state community to develop alternative single photon sources based on single quantum emitters. So far the best results in terms of single photon generation, brightness and photon indistinguishability have been obtained using semiconductor quantum dots. Semiconductor quantum dots are nanometric insertions of a small bandgap material in a larger bandgap matrix. The strong confinement of charges in quantum dots makes the electronic occupancy states discrete, very similarly to the electronic states in a single atom. QDs have been shown to emit single photons in 2000 by the group of Pr. Imamoglu [29]. Since then, many

progress have been obtained to fabricate devices that would perform as ideal single photon sources [30–32].

In a bulk material, single photons are emitted from a QD quasi-isotropically in high refractive index material, limiting the collection efficiency to a few percent. Strategies have been efficiently developed to overcome this limitation. Controlling the QD emission in photonic structures like microcavities [30, 31, 33–35] or single mode optical waveguides [32], single photon sources with brightness close to 80% have been demonstrated in 2010–2013 [31, 32]. Embedded in a GaAs matrix, confined charges are prone to dephasing mechanisms induced by the electronic fluctuating environment or by the lattice vibrations. Coupling QDs to optical cavities to shorten their emission lifetime, the generation of indistinguishable photons has been demonstrated in 2002 by Santori and coworkers [36]. Since then, many groups have studied the photon indistinguishability using different excitation schemes [31, 37–44] and obtaining remarkable results in the last few years.

This thesis has been done in the group of Pr. Pascale Senellart at the Laboratoire de Photonique et Nanostructures (LPN). The group has developed a long expertise in QD-based photonic devices, based on cavity quantum electrodynamics (CQED). A great challenge to study CQED with QDs is that QDs are randomly distributed both spatially and spectrally. The LPN team developed in 2008 a technique that allows a full control of the coupling between a single QD and a micro-cavity [45]. This technique, called *in situ* lithography technique, allowed the group to demonstrate on demand control of spontaneous emission of a QD both in the weak and strong coupling regime. Using this technique, the group demonstrated the fabrication of an ultrabright source of polarization-entangled photon pairs in 2010 [46]. In 2013, Gazzano et al. fabricated a bright sources of indistinguishable single photons [31] and used it to implement a two-photon quantum logic CNOT gate [47].

When I started my PhD, in a first place our objective was to further improve the properties of the sources by increasing the Purcell factor using new optical cavity structures. A larger acceleration of spontaneous emission should improve both the source brightness and indistinguishability. I demonstrated the fabrication of bright single photon sources in a regime of high Purcell factor and studied the properties of these new structures. After studying in depth the conditions to obtain single and indistinguishable photons, we used two of these sources to demonstrate an elementary photonic network based on the quantum interference using two remote sources.

However, these new structures showed limitations in terms of performance reproducibility due to an important charge noise. In the second part of my PhD, I studied a new generation of samples with an electrical control of electronic states in the QD. We first

demonstrated the fabrication of ultrabright tunable single photon sources in a reproducible way. Then, the resonant fluorescence spectroscopy was implemented on one of these devices, this allowed us to obtain for the first time single photon emission with very high indistinguishability values and high brightness. This was obtained through a coherent control of the QD state under a very weak pulsed excitation containing only few photons.

This manuscript reports on these various results, not following chronological order, but focusing first on the properties of single sources, before presenting the work realized with remote sources. The outline is the following:

- In **chapter 2**, we give the basics on the optical properties of InAs QDs. Energy levels of carriers in QDs, the effects of coupling to phonons and the light matter interaction are described as well as the corresponding experimental setups. The basics of light-matter coupling for a two-level system in a cavity are presented and the applications for the fabrication of bright single photon sources are discussed. Finally, we describe how a single QD is coupled to a micropillar using the *in situ* lithography technique, used for the fabrication of all devices used in this work.
- **Chapter 3** shows the development and the use of an alternative design of cavity structure to obtain a better light confinement in the optical cavity and an enhancement of the Purcell effect. QDs deterministically coupled to **adiabatic** micropillars cavities are studied in detail. We study the experimental conditions required to obtain a high single photon purity and indistinguishability. State-of-the-art in single photon emission is demonstrated in terms of brightness and indistinguishability. Signatures of strong charge noise is evidenced, which limits the reproducibility of the performance with such cavities.
- In **chapter 4**, we describe the next generation of sources, with electrical control of the QD electronic states, developed in the group including an electrical control of the devices. The single photon purity and indistinguishability are measured on two devices under a quasi resonant excitation. The emission of highly indistinguishable photons, when the source is at its maximum emission rate, is demonstrated in a reproducible way.
- In **chapter 5**, the electrically tunable sources are studied under strictly resonant excitation. Under pulsed excitation, Rabi oscillations are observed as a function of excitation power. It is experimentally demonstrated that the photons emitted by the QD are perfectly indistinguishable under these excitation conditions.
- In **chapter 6**, using devices presented in chapter **3**, we report on the interferences between single photons emitted by remote sources. We demonstrate that

controlling the lifetime of one source is a powerful tool to improve the two-photon interference process between remote devices.

- Finally, perspectives to this PhD work are sketched in **chapter 7**.

Chapter 2

Fundamentals of QD Based Single Photon Sources

An ideal source of single photons emits light pulses that deterministically contains only one photon. This criterion is important for the security and the reliability of the quantum communication as well as for the fidelity of quantum information processing protocols. For most applications in quantum information processing, the photons are also required to be indistinguishable. With identical properties (energy, polarization, spatial and temporal profiles), indistinguishable photons can interfere with each other due to their boson nature. With the goal of building more complex systems for the quantum information processing, huge efforts are made to develop bright sources of single photons.

The source brightness is related to the probability that the source effectively provides a single photon when needed. The brightness, as well as the emission rate (defined as the time between two emissions) directly influences the communication rate as well as the acquisition time in quantum optics experiments. Currently, most of the experiments are done with attenuated lasers or heralded single photon sources based on parametric-down conversion (SPDC). Yet, to limit the multiple photons contribution, PDC sources are strongly attenuated, leading to an extremely low mean number of photons (below 0.01 photon per pulse). As a consequence, the development of a bright, reliable and scalable single-photon source has become a crucial milestone in the global roadmap of quantum optics. To increase the single-photon rate with PDC sources, it is possible to multiplex several sources [48]. Using this technique, about 17 PDC sources are required to achieve a single-photon probability higher than 0.99 (without taking into account any optical losses) [49]. An alternative is to develop ideal single-photon sources based on single quantum emitters.

Different types of two-level systems are studied to that end: trapped ions [50], trapped atoms [51, 52], single molecules [53], NV centers in diamond [16, 17] or semiconductor

quantum dots [54]. Since semiconductor quantum dots (QDs) can be integrated in photonic devices, they appear as a scalable solution. In this PhD, we focus our attention on semiconductor quantum dots only. After describing the energy levels of charges in a QD, we describe the spontaneous emission of photons that results from the recombination of carriers. The single-photon purity, quantified by the autocorrelation function $g^{(2)}(\tau)$, is then briefly discussed. After a short introduction about two-photon interferences, we discuss the state of the art in terms of QD based indistinguishable photon sources.

In a second part, we discuss the coupling between a QD and a cavity mode used to implement a modification of the spontaneous emission and obtain bright sources. It is particularly important to note that the cavity-QD coupling requires an excellent matching between the position of the QD and the maximum of the field in the optical cavity as well as the spectral matching between the QD and the cavity resonances. The technique of *in situ* lithography used to fabricate the spectrally and spatially matched devices studied in this work is described.

Finally the brightness of sources is defined and discussed. We compare the brightness of different sources such as QDs in bulk material, QDs in a cavity, and parametric down conversion sources, the latter being the most commonly used sources used in current quantum optics experiments.

2.1 Structure of Self-Assembled Quantum Dots

2.1.1 Self-Assembled Quantum Dots in Semiconductor

A InAs/GaAs quantum dot (QD) is a small cluster of InAs atoms in a GaAs lattice. Since InAs bandgap is lower in energy as GaAs bandgap, it forms a local potential well for the carriers in all the directions of space.

The samples studied during this PhD were grown at the laboratoire de Photonique et de Nanostructures by the group of Aristide Lemaître. The formation of InAs quantum dots occurs during the Stranski-Krastanov growth (theoretically predicted in 1938) [55, 56] in a MBE (Molecular Beam Epitaxy) system. Due to the lattice mismatch between GaAs and InAs (the latter having a lattice constant 7% larger), the InAs layer suffers strong mechanical strain. When the thickness of InAs reaches a critical point (1.7 monolayer), it becomes energetically favorable for the material to change its atomic configuration, inducing the apparition of small InAs clusters made of few thousands of atoms. The surface density of dots can vary with the growing conditions (like temperature of the substrate, the amount or the indium flow [57]). The typical densities of InAs dots can

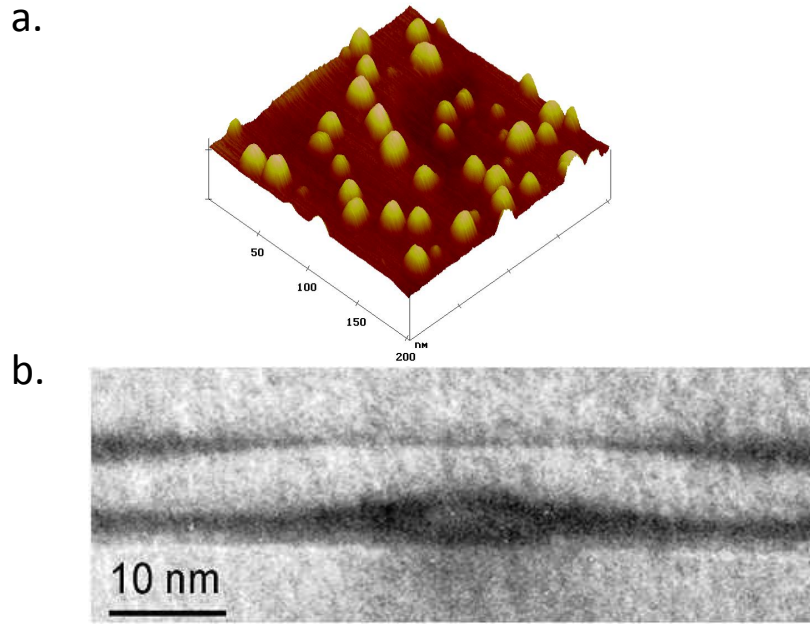


FIGURE 2.1: **a.** Atomic Force Microscope (AFM) image of InAs quantum dots **b.** Transmission electron microscopy image of a quantum dot. Image from Gilles Patriarche

vary from $10 \mu\text{m}^{-2}$ to $500 \mu\text{m}^{-2}$. The typical shape basically consists of flat lenses laying on a 2D InAs layer. The lateral size is typically around 10-20 nm with a height of 3 nm, as shown in fig.2.1a. and 2.1b.. Figure 2.1a. shows also the randomness of the QDs position as well as the size dispersion. This random distribution and shape diversity make the coupling of a single QD with a cavity a very challenging task as it will be shown in the following sections.

The InAs quantum well forming the common base of the QDs is called the **wetting layer**. In the wetting layer, the confinement of charges is only in the growth direction (1D), the fundamental energy level is higher (1.442 eV, corresponding to a emission wavelength of 860 nm) than in the QD (1.319 eV or 940 nm). Several works have addressed the study of QD ensembles [58]. The optical emission from single InAs quantum dots was studied for the first time by Marzin and coworkers in 1994 [59].

2.1.2 Energy levels of carriers in a Quantum dot

Highly sophisticated models have been developed to describe the energy levels of carriers in QDs accounting for the various shapes of the potential, taking into account realistic shapes or the effects of strain [60, 61]. However, many important features can be derived from a basic model as discussed below.

Consider a single electron in the conduction band of a semiconductor. For the sake of clarity, we will ignore the spin in this theoretical description. The electron wavefunction can be written as

$$\psi_e(\mathbf{r}) = e^{i\mathbf{k}\cdot\mathbf{r}}u_{\mathbf{k}}(\mathbf{r}) \quad (2.1)$$

where $u_{\mathbf{k}}(\mathbf{r})$ is the Bloch wave function. $\psi_e(\mathbf{r})$ describes the electron delocalized in the whole crystal. Using the effective mass approximation (or the approximation of the envelope wave function) [62], one can describe the electron wavefunction in a heterostructure as:

$$\psi_e(\mathbf{r}) = f(\mathbf{r})u_{\mathbf{k}}(\mathbf{r}) \quad (2.2)$$

where $f(\mathbf{r})$ is the envelope function. This function is determined by the Schrodinger equation:

$$\left(\frac{-\hbar^2}{2m^*(\mathbf{r})}\nabla^2 + V(\mathbf{r}) \right) f(\mathbf{r}) = Ef(\mathbf{r}) \quad (2.3)$$

where $m^*(\mathbf{r})$ is the effective mass of the electron in the quantum dot.

We use a highly simplified model describing the trap by a square well in the three directions:

$$V(\mathbf{r}) = \begin{cases} 0 & \text{if } 0 < x < L_x, 0 < y < L_y, 0 < z < h \\ +V_0 & \text{otherwise} \end{cases} \quad (2.4)$$

The solutions with a wavevector k are given by the following relations [63]:

$$\begin{cases} |\cos(\frac{kL}{2})| = \frac{k}{k_0} \\ \tan(\frac{kL}{2}) > 0 \end{cases} \quad \text{or} \quad \begin{cases} |\sin(\frac{kL}{2})| = \frac{k}{k_0} \\ \tan(\frac{kL}{2}) < 0 \end{cases} \quad (2.5)$$

where $k_0 = \sqrt{\frac{2m^*V_0}{\hbar^2}}$. In the case of an electron, $k_0 \approx 10^9\text{m}^{-1}$. So $h \approx 3 - 5\text{nm}$ leads to the confinement of only one electronic state in the z -direction. In the x and y directions where $\frac{\pi}{L} \approx 5.10^8\text{m}^{-1}$, the ratio $\frac{k_0L}{\pi}$ leads to the existence of at least two confined states. In this simplified picture, the energy levels of the carriers can be roughly estimated in the case of an infinite well ($V_0 \rightarrow +\infty$):

$$E = \frac{\hbar^2}{2m^*}(k_x^2 + k_y^2 + k_z^2) + E_{gap} = \frac{\hbar^2}{2m^*} \left(\frac{n_x^2\pi^2}{L_x^2} + \frac{n_y^2\pi^2}{L_y^2} + \frac{n_z^2\pi^2}{L_z^2} \right) + E_{gap} \quad \text{with } L_x, L_y \gg L_z \quad (2.6)$$

where $n_x, n_y \geq 0$ are integers. The energy gap between the lowest energy state ($n_x, n_y, n_z = 1$) and one excited state is of the order of:

$$\Delta E_{s,p} = \frac{3\hbar^2}{2m^*} \left(\frac{\pi}{L_x} \right)^2 \approx 166 \text{ meV for the electron for } L_x = 10 \text{ nm} \quad (2.7)$$

$$\Delta E_{s,p} = \frac{3\hbar^2}{2m^*} \left(\frac{\pi}{L_x} \right)^2 \approx 22 \text{ meV for the heavy holes for } L_x = 10 \text{ nm} \quad (2.8)$$

This extremely simplified model gives the right order of magnitude for the energy separation of the electron and hole levels in a QD.

Origin of the spectral variety of discrete states in InAs QDs

As shown by fig.2.1 **a.**, self assembled InAs quantum dots exhibit different sizes and shapes.

From eq.2.6, we estimate that the relative fluctuation of energy related to a fluctuation in height is:

$$\frac{\Delta E_z}{E_z} = 2 \frac{\Delta L_z}{L_z} \quad (2.9)$$

Considering realistic values for $E_z \sim 400 \text{ meV}$, if L_z varies by 1 atom ($\sim 10\%$), then $\Delta E_z = 80 \text{ meV}$.

This simple estimation shows why QDs present large inhomogeneous distribution of their spectral properties. It also shows that these strong fluctuations are not likely to be controlled even with a highly optimized growth process.

2.1.3 Coulomb Interactions in a QD and Exciton Fine Structure Splitting

Two carriers (electrons or holes) can be trapped simultaneously in a QD. The spatial confinement makes their wavefunction (ϕ and ψ) overlap and Coulombian interaction is an important term in the total energy [64]. Two terms must be considered, the direct term:

$$J = \frac{e^2}{\epsilon} \iint \frac{|\phi(\vec{r}_1, \sigma_1)|^2 |\psi(\vec{r}_2, \sigma_2)|^2}{|\vec{r}_1 - \vec{r}_2|} d\vec{r}_1 d\vec{r}_2 \quad (2.10)$$

and the exchange interaction term:

$$K = \frac{e^2}{\epsilon} \iint \frac{\phi^*(\vec{r}_1, \sigma_1) \psi^*(\vec{r}_2, \sigma_2) \phi(\vec{r}_1, \sigma_1) \psi(\vec{r}_2, \sigma_2)}{|\vec{r}_1 - \vec{r}_2|} d\vec{r}_1 d\vec{r}_2 \quad (2.11)$$

The first Coulomb term leads to a shift of the confined levels of about 20meV for the *s-shell* transition [65]. The calculation of the exchange interaction is more complicated. If we consider only the heavy holes due to their high energy separation with the light holes, the z-component of the spins of heavy-holes and electron gives rise to four possible

spin states:

$$|+1\rangle \equiv |\uparrow, \downarrow\rangle = |3/2, -1/2\rangle \quad (2.12)$$

$$|-1\rangle \equiv |\downarrow, \uparrow\rangle = |-3/2, +1/2\rangle \quad (2.13)$$

$$|+2\rangle \equiv |\uparrow, \uparrow\rangle = |3/2, +1/2\rangle \quad (2.14)$$

$$|-2\rangle \equiv |\downarrow, \downarrow\rangle = |-3/2, -1/2\rangle \quad (2.15)$$

where the bright exciton states are denoted $|\pm 1\rangle$, defined by the optical selection rules. The $|\pm 2\rangle$ exciton states are called dark excitons.

In this basis, the exchange interaction Hamiltonian of an exciton composed by a hole (with a spin J_h) and by an electron (with a spin S_e) reads:

$$H_{\text{exc}} = - \sum_{i=x,y,z} (a_i J_{h,i} S_{e,i} + b_i J_{h,i} S_{e,i}) \quad (2.16)$$

In the exciton spin basis $|+2\rangle, |-2\rangle, |+1\rangle, |-1\rangle$, H_{exc} can be written as:

$$H_{\text{exc}} = \frac{1}{2} \begin{pmatrix} \delta_0 & \delta_2 & 0 & 0 \\ \delta_2 & \delta_0 & 0 & 0 \\ 0 & 0 & -\delta_0 & \delta_1 \\ 0 & 0 & \delta_1 & -\delta_0 \end{pmatrix} \quad (2.17)$$

with $\delta_0 = 3/2(a_z + 9/4b_z)$, $\delta_1 = -3/4(b_x + b_y)$ et $\delta_2 = -3/4(b_x - b_y)$.

Figure 2.2 shows a schematic of the resulting energy levels according. Some typical values are presented below:

δ_0	δ_1	δ_2
$\sim 400\mu\text{eV}$	$\sim 10 - 100\mu\text{eV}$	$\sim 50\mu\text{eV}$

The QD shape often presents an in-plane (along x and y) structural asymmetry. When the rotational symmetry is broken ($b_x \neq b_y$), an exciton shows a fine structure splitting (FSS). The energy splitting between the two states $|\pm 1\rangle$ is typically several tens of μeV [66].

This exchange interaction can be experimentally observed in a photoluminescence (PL) experiment. Figure 2.3 shows typical emission spectra evidencing the splitting of the exciton line, measured by rotating a half-wave plate placed before a polarization analyser. The splitting here is around $20\mu\text{eV}$. The points on fig.2.3b. shows the spectral shift of the line as a function of the polarization axis evidencing the QD asymmetric axes.

The fine structure splitting (FSS) of excitons in semiconductor structures has been theoretically studied in many works [67, 68]. In the work by Takagahara [68] a simple

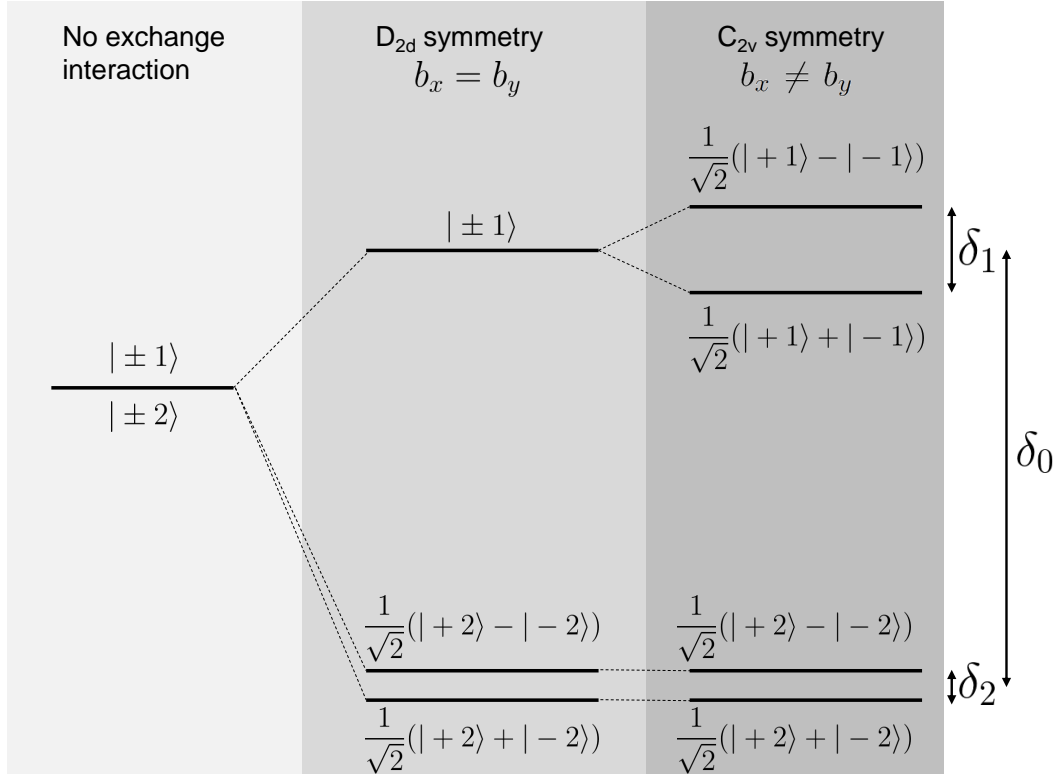


FIGURE 2.2: Schematics of the QD energy levels considering various symmetries.

estimation of the splitting of bright excitons is derived:

$$\delta_1 = \frac{1}{16}(1.559\eta) \left(\frac{\mu_x^2}{\epsilon L^3} \right) \quad (2.18)$$

where μ_x is the dipole amplitude, L is the characteristic size of the quantum dot and η the degree of asymmetry in the QD.

It is interesting to compare this estimation to the radiative decay rate:

$$\frac{\delta_1}{\hbar\Gamma} = \eta \frac{1.559 \times 3}{16 \times 8\pi^2} \left(\frac{\lambda_0}{nL} \right)^3 \approx 66\eta \text{ with } \lambda_0 = 940\text{nm and } L = 10\text{nm} \quad (2.19)$$

We see that even an asymmetry of the order of one atomic monolayer ($\eta \sim 1\%$) gives rise to a FSS of the order of the radiative linewidth of the state. The ratio in eq.2.19 is an important parameter that determines the possibility for the QD to emit entangled photon pairs starting from two excitons in a QD [69].

Different techniques have been developed in order to minimize the FSS. A rapid thermal annealing of the sample has been shown to reduce the exciton confinement, and thus increasing the number of QDs with a small FSS [70–72]. Applying an external strength

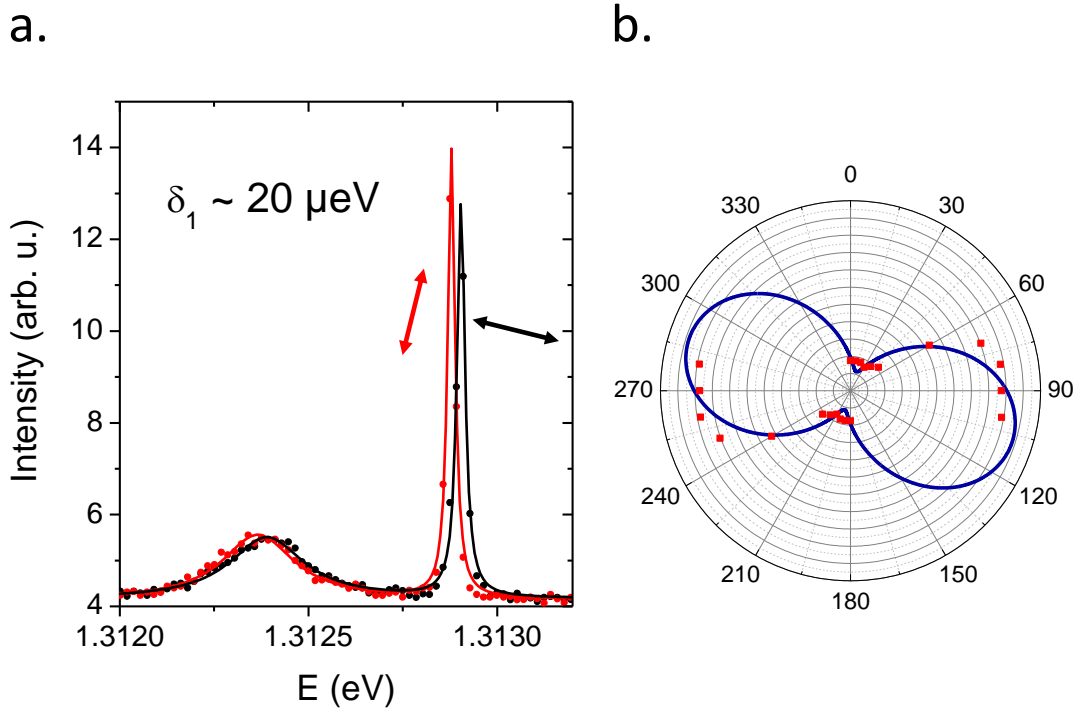


FIGURE 2.3: **a.** PL spectra of a QD under identical excitation conditions measured along two orthogonal polarizations (shown by the arrows). **b.** Points: evolution of the exciton (X) emission line energy as a function of the polarization axis. Line is a fit with an imposed period equal to 90° .

on the sample using a piezo actuator [73] leads to a control of the FSS as well as applying an external electric field [74, 75] or in-plane magnetic field (B perpendicular to the growth axis) [76, 77].

Another approach to decrease the ratio of the FSS over the radiative decay (eq.2.19) is to increase the radiative decay rate Γ . This is done by modifying the electromagnetic environment in which the QD emits. The emission of polarization-entangled photon pairs was demonstrated by Dousse et al. [46] in the group by deterministically coupling a QD to a cavity mode.

2.1.4 Occupancy States of a Quantum dot

Depending on the energy of the excitation, carriers can be generated in the GaAs, in the InAs wetting layer (WL) or even directly in resonance with an energy level of the QD as illustrated in fig.2.4. When created non resonantly, the carriers relax to lower energy levels with a typical relaxation time of 30-50 ps [78]. When a quantum dot is

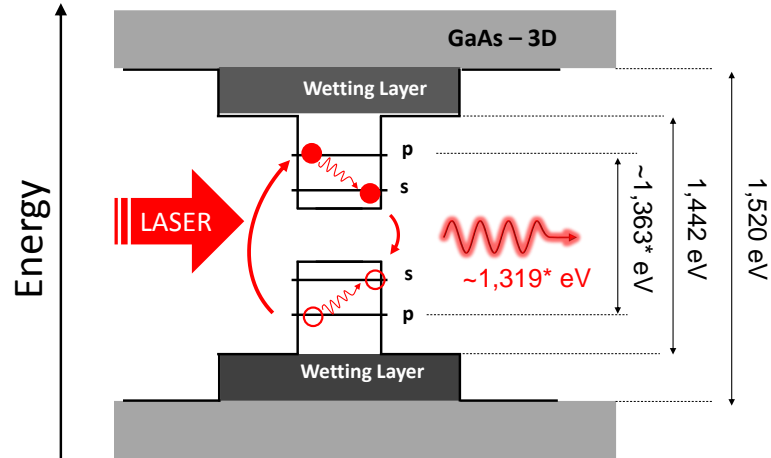


FIGURE 2.4: Schematics of the energy-level diagram of a QD. Quasi-resonant excitation, where charges are created in the p-shell. After the excitation, charges relax to *s-shell* before recombining and emitting one photon. Energies marked by a star can change from one sample to another, depending on the growing conditions.

occupied by one electron-hole pair, the occupancy state is called **exciton** (denoted X). Note that contrary to excitons in systems with less confinement, the exciton is formed by the coulombian interaction between the electron and the hole. Here, the exciton in a InAs QD is mainly formed by the 3D confining potential. As a result, it would be more correct to call an exciton an electron hole pair. A negatively or positively charged exciton is named **trion** (denoted X^+ or X^-) [79]. The case where the dot is occupied by two excitons is called **biexciton** (XX). For all these states, electron/hole pairs can recombine optically, by emitting a photon at a narrow energy band. A biexciton decay to an exciton state by emitting a photon at the wavelength λ_{XX} . The recombination of the second exciton leads to emission at a wavelength λ_X . A negative (positive) trion decays to a single electron (hole) state. This mechanism of successive carriers relaxation is referred to as the radiative cascade, depicted in fig.2.5. The recombination from a given occupancy state can be associated to a given wavelength λ_X , λ_{XX} , λ_{X^+} or λ_{X^-} . Because of the Coulomb interaction, these wavelengths are usually different [80, 81]. Figure 2.6 shows a typical PL spectrum of a QD studied during this thesis. We can identify the exciton (X) emission line around 930.5nm close to a trion (charged exciton CX) emission line. At higher energy, the biexciton (XX) emission line appears following a quadratic dependence with the excitation power.

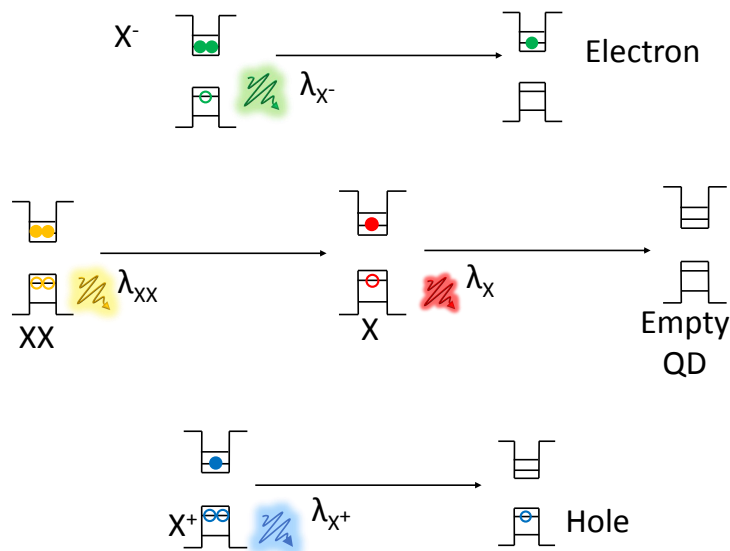


FIGURE 2.5: Schematics representing the occupancy states of a quantum dot. The full (empty) circles indicate the electron (hole) configuration in the conduction (valence) band of the QD. The exciton is denoted X (top-right), the negatively charged trion is denoted X^- (top-left), the positively charged trion (X^+) (bottom-right) and the biexciton (XX) (bottom-left). We can numerate about seven occupancy states by only four of them will recombine radiatively by emitting a photon at a narrow wavelength.

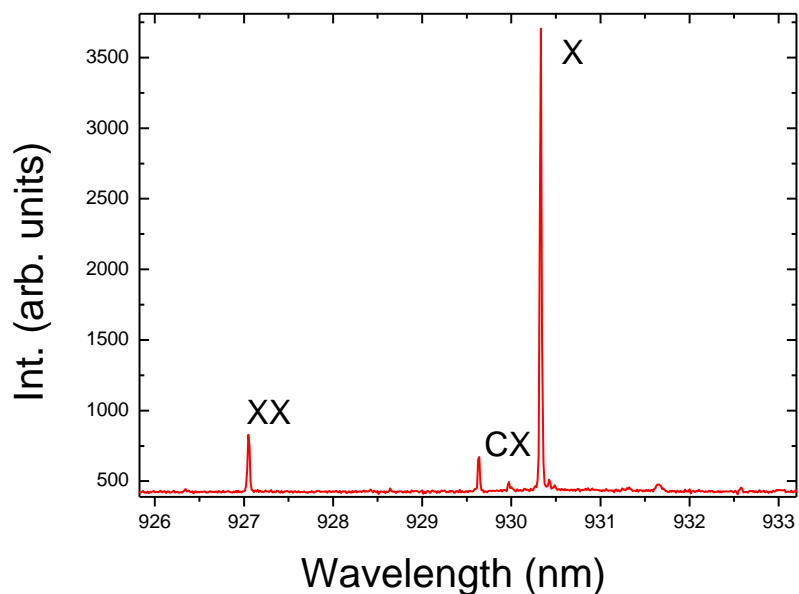


FIGURE 2.6: Photoluminescent spectrum from a single InAs QD in a planar cavity under non resonant excitation.

2.1.5 Spontaneous Emission by recombination of charges

The conduction-band electron of the exciton returns to the valence band radiatively by emitting a photon. This transition is mostly optically active for the $|\pm 1\rangle$ bright exciton state. Quantum efficiencies, defined as the radiative contribution in a GaAs bulk normalized by the total decay, between 0.8 and 1 have been measured in InAs QD [82]. In the rest of this work, we will only consider the case where an electron/hole pair recombine emitting a photon and we neglect any nonradiative mechanisms. The following Hamiltonian describes the interactions between a quantum dot and the modes of the electromagnetic field:

$$H = \sum_i E_i |i\rangle\langle i| + \sum_{\mathbf{k}, \epsilon} \hbar \omega_{\mathbf{k}} a_{\mathbf{k}, \epsilon}^\dagger a_{\mathbf{k}, \epsilon} + \hbar \sum_{\mathbf{k}, \epsilon} \sum_{i, j} g_{i, j, \mathbf{k}, \epsilon} [a_{\mathbf{k}, \epsilon} + a_{\mathbf{k}, \epsilon}^\dagger] |j\rangle\langle i| \quad (2.20)$$

where $|i\rangle$ are the QD states with corresponding energies E_i , $a_{\mathbf{k}, \epsilon}$ are the photon annihilation operators for the wavevector \mathbf{k} along the polarization ϵ and $g_{i, j, \mathbf{k}, \epsilon}$ are the coupling coefficients between the atom and the electromagnetic modes:

$$g_{i, j, \mathbf{k}, \epsilon} = \left(\frac{\omega_{\mathbf{k}}}{2\epsilon_0 \hbar V} \right)^{1/2} \boldsymbol{\epsilon} \cdot \boldsymbol{\mu}_{i, j} \quad (2.21)$$

where $\boldsymbol{\mu}_{i, j} = e\langle i | \mathbf{r} | j \rangle$ are the atomic transition dipole moments and V is the quantization volume of the electromagnetic field.

We denote the initial state where an exciton occupies the QD $|X\rangle$ and the final empty-QD state $|0\rangle$, the dipole moment of the excitonic transition is:

$$\boldsymbol{\mu}_X = e \int d^3 \mathbf{r} \psi_e^*(\mathbf{r}) \mathbf{r} \psi_h(\mathbf{r}) \quad (2.22)$$

where $\psi_e(\mathbf{r})$ and $\psi_h(\mathbf{r})$ describe the wavefunctions for the electron and the hole in the QD. This equation is only valid in the case of bright excitons, where the spin of the sum of the electron spin projected along z ($\sigma_z = \pm 1/2$) and the total hole angular momentum along z ($m_z = \pm 3/2$) is equal to ± 1 .

The Hamiltonian presented in the eq.2.20 can be simplified by considering only the states $|X\rangle$ and $|0\rangle$ in the *rotating-wave approximation* (RWA):

$$H = \hbar \omega_X |X\rangle\langle X| + \sum_{\mathbf{k}, \epsilon} \hbar \omega_{\mathbf{k}} a_{\mathbf{k}, \epsilon}^\dagger a_{\mathbf{k}, \epsilon} + \hbar \sum_{\mathbf{k}, \epsilon} \left[g_{\mathbf{k}, \epsilon}^* |X\rangle\langle 0| a_{\mathbf{k}, \epsilon} + g_{\mathbf{k}, \epsilon} a_{\mathbf{k}, \epsilon}^\dagger |0\rangle\langle X| \right] \quad (2.23)$$

where ω_X is the frequency of the optical transition from the exciton state.

Considering vacuum of the electromagnetic field modes at time $t = 0$ and one exciton is in the QD, the initial state ($|X\rangle|0\rangle$) evolved toward:

$$|\psi(t)\rangle = A(t)e^{-i\omega_X t}|X\rangle|0\rangle + \sum_{\mathbf{k},\epsilon} B_{\mathbf{k},\epsilon}(t)e^{-i\omega_{\mathbf{k}} t}|g\rangle a_{\mathbf{k},\epsilon}^\dagger|0\rangle \quad (2.24)$$

where $\omega_{\mathbf{k}}$ is the frequency of the mode \mathbf{k} . Using the Wigner approximation that holds if the transition linewidth is very small compared to $\omega_{\mathbf{k}}$, then:

$$A(t > 0) = e^{-\Gamma t/2} \quad (2.25)$$

$$B_{\mathbf{k},\epsilon}(t > 0) = g_{\mathbf{k},\epsilon} \frac{1 - e^{-i(\omega_X - \omega_{\mathbf{k}})t - \Gamma t/2}}{(\omega_{\mathbf{k}} - \omega_X) + i\Gamma/2} \quad (2.26)$$

where

$$\Gamma = \frac{n\omega_X^3 |\mu_X|^2}{3\pi\epsilon_0 \hbar c^3} \quad (2.27)$$

is the decay rate of the exciton transition in bulk and n the index of refraction of the QD matrix. The spontaneous emission rate Γ depends on the dipole moment μ_X that depends on the overlap between the electron and hole envelope functions. It also depends only on the refractive index of the environment. When placing the QD in a cavity, this emission rate can be strongly modified.

2.1.6 Single QD Spectroscopy

Here, we describe some basic spectroscopic properties with single QDs: excitation schemes, power dependence of the QD photoluminescence (PL) under a continuous and a pulsed excitation.

2.1.6.1 Optical excitation

In this work, the photoluminescence (PL) of QDs is measured by optically creating charges around or directly in the QD. Several excitation schemes are used, as illustrated in fig.2.7:

- **a.** The **non-resonant** (above-band) excitation consists in the creation of electron-hole pairs in the continuum associated to the GaAs bulk ($>1.51\text{eV}$ at 4K) or in the continuum of the InAs wetting layer (1.45 eV). Single carriers, electron holes, or excitons then scatter in the QD and relax to the lower-energy levels.
- **b.** To minimize the delay induced by the capture of charges in the QD, electron-hole pairs can also be directly created in a discrete resonance inside the QD: this is called a **quasi-resonant excitation**. In 2002, A. Vasanelli et al. showed the

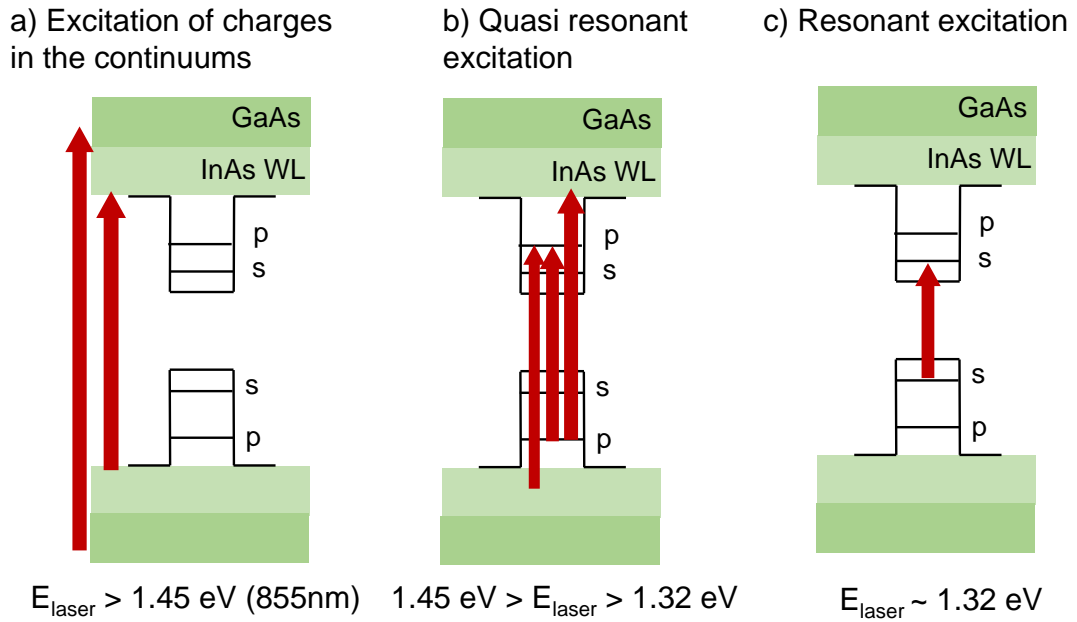


FIGURE 2.7: Schematics of the three optical excitation schemes : **a)** the non-resonant excitation, **b)** quasi-resonant excitation and **c)** resonant excitation

excitation of *mixed states*: one of the charges is in the continuum of states while the other occupies a confined state [83]. A larger laser power is required than in non resonant excitation since the absorption cross-section of a single QD is very small.

- **c.** The **resonant excitation** consists in the optical creation of pairs directly into the considered exciton state.

2.1.6.2 Power measurements

Under a weak optical excitation, a single line corresponding to the exciton (X) transition is observed in the PL spectrum of a single QD. As illustrated in fig.2.8, the exciton (X) emission line intensity increases linearly when the excitation power is increased, while a second line corresponding to the biexciton (XX) grows quadratically. Santori et al. [54] first demonstrated this behaviour. During his thesis, E. Moreau developed a rate equation model which explains the power dependence of the exciton and biexciton lines [84].

In this model, electrons and holes are trapped by pairs only. The capture process is assumed to be random and independent of the number of pairs in the QD. The probability $P(n)$ of having n pairs in the QD is ruled by the following rate equations:

$$\begin{aligned} \text{if } n=0, \quad \frac{dP(n)}{dt} &= \frac{P(n+1)}{\tau_{(n+1)}} - \frac{P(n)}{\tau_{cap}} \\ \text{if } n > 0, \quad \frac{dP(n)}{dt} &= \frac{P(n+1)}{\tau_{(n+1)}} + \frac{P(n-1)}{\tau_{cap}} - P(n) \left(\frac{1}{\tau_{cap}} + \frac{1}{\tau_n} \right) \end{aligned} \quad (2.28)$$

where τ_{cap} is the capture time of pairs in the QD and τ_n the recombination time of the n -pairs occupancy state. If one considers that the recombination time is independent of the state of the QD ($\tau_n = n\tau_{rad}$), the equations read:

$$\begin{aligned} \frac{dP(0)}{dt} &= \frac{P(1)}{\tau_{(1)}} - \frac{P(0)}{\tau_{cap}} \\ \text{if } n > 0, \quad \frac{dP(n)}{dt} &= (n+1) \frac{P(n+1)}{\tau_{rad}} + \frac{P(n-1)}{\tau_{cap}} - P(n) \left(\frac{1}{\tau_{cap}} + \frac{n}{\tau_{rad}} \right) \end{aligned} \quad (2.29)$$

$$(2.30)$$

In what follows, we can analyse the behaviour of $P(n)$ for two different excitation regimes.

Continuous Wave excitation:

For the steady state corresponding to a continuous-wave (CW) measurement, the probability $P(n)$ is found to follow a Poissonian statistics:

$$P(n) = \frac{e^{-\frac{\tau_{rad}}{\tau_{cap}}}}{n!} \left(\frac{\tau_{rad}}{\tau_{cap}} \right)^n \quad (2.31)$$

Since the intensity of PL lines is proportional to the probability that the QD is occupied by the corresponding occupancy state and the state emission rate. We find that:

$$\begin{aligned} I_X &= A \frac{P(1)}{\tau_{rad}} = A \frac{P}{B} e^{-\frac{P\tau_{rad}}{B}} \\ I_{XX} &= A \frac{P(2)}{\tau_{rad}/2} = A \frac{\tau_{rad} P^2}{B^2} e^{-\frac{P\tau_{rad}}{B}} \end{aligned} \quad (2.32)$$

where A and B are constants. We defined the rate of injection $P = B\tau_{cap}^{-1}$ as a variable such as:

$$\begin{aligned} I_X(P) &= I_{sat} \frac{P}{P_{sat}} e^{-\frac{P}{P_{sat}}} \\ I_{XX}(P) &= I_{sat} \frac{P^2}{P_{sat}^2} e^{-\frac{P}{P_{sat}}} \end{aligned} \quad (2.33)$$

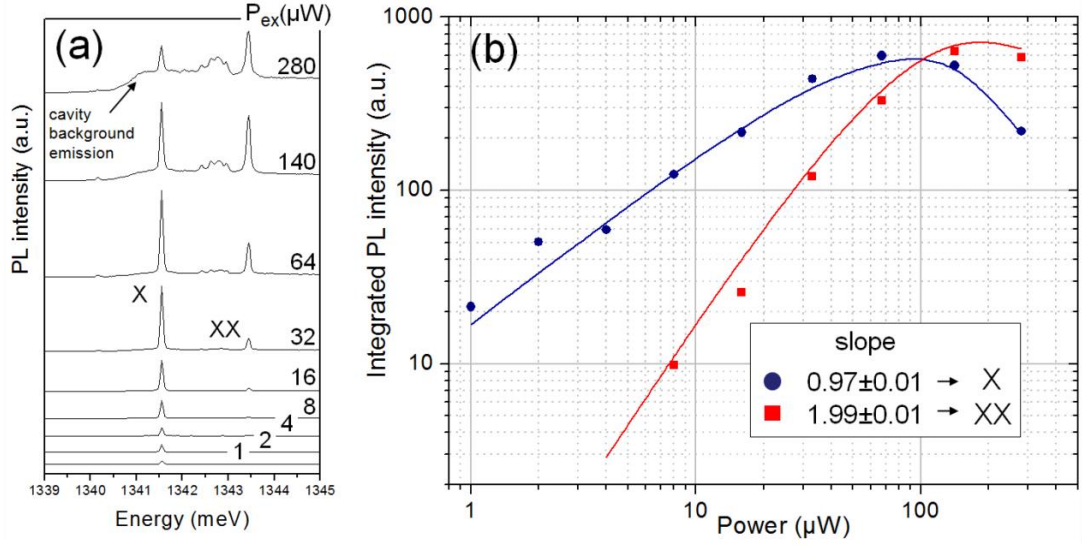


FIGURE 2.8: Figures reproduced from [85]. **a.** Spectra of a single QD's PL as a function of excitation power. The spectra have been vertically shifted for clarity. **b.** Integrated PL intensity of the exciton X and biexciton XX lines as a function of excitation power for continuous wave excitation. Points are measurements from **a.** and solid lines are fit from the theoretical model.

The exciton line intensity exhibits a linear dependence at low excitation power while the biexciton line exhibits a quadratic dependence. Both lines saturate at higher excitation power then decrease. Figure 2.8 **b.** shows the power dependence of the exciton line X (blue disks) and of the biexciton line XX (red squares) as a function of excitation power and fit using equations 2.33.

Under a pulsed excitation:

Considering a pulsed excitation, the emission of a photon at the X energy is given by the probability that the QD contains at least 1 electron-hole pair. The probability that k pairs occupy the QD after the pulsed excitation is given by a poissonian distribution:

$$P(k) = \frac{n^k}{k!} e^{-n} = \frac{1}{k!} \left(\frac{P}{P_{\text{sat}}} \right)^k e^{-P/P_{\text{sat}}} \quad (2.34)$$

where n is the mean number of captured pairs in the QD. It evolves linearly with the excitation power P . As previously, the saturation power is denoted P_{sat} . Due to the

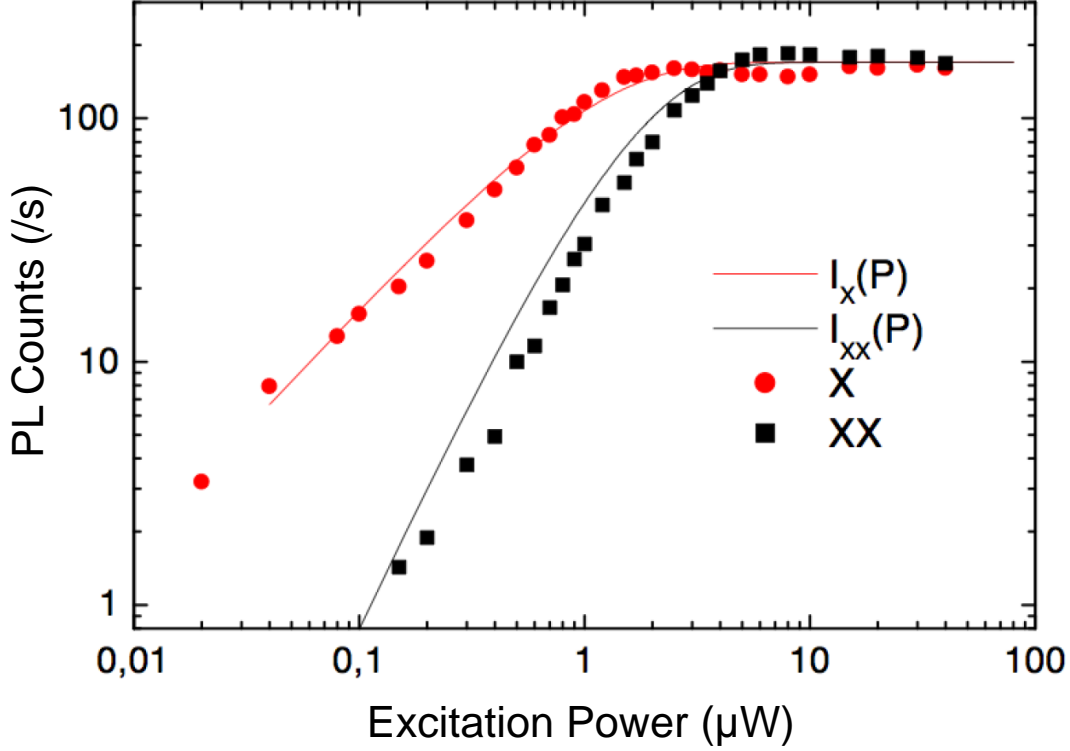


FIGURE 2.9: Figure reproduced from [84]. Evolution of the exciton (X) emission line intensity in red, and of the biexciton (XX) emission line intensity in black as a function of the power for a pulsed excitation.

radiative cascade, the exciton (X) emission intensity is proportional to the probability that the QD captured *at least* one electron-hole pair:

$$I_X(P) = I_{\text{sat}}(1 - P(0)) = I_0 \left(1 - e^{-P/P_{\text{sat}}}\right) \quad (2.35)$$

where I_{sat} is the intensity at saturation.

Similarly, the biexciton emission line intensity I_{XX} is given by the probability that the QD captured at least two electron-hole pairs:

$$I_{\text{XX}}(P) = I_{\text{sat}}(1 - P(0) - P(1)) = I_0 \left(1 - e^{-P/P_{\text{sat}}} - \frac{P}{P_{\text{sat}}} e^{-P/P_{\text{sat}}}\right) \quad (2.36)$$

The red points (black squares) on fig.2.9 show the measured evolution (from [84]) of the exciton (biexciton) emission line intensity as a function of the excitation power. Solid lines show the theoretical evolution from the equations 2.35 and 2.36. Compared to the continuous wave excitation, the intensities of both lines are not reduced at high excitation power but saturate.

In this thesis, we are interested in on-demand single photons so most of the results that are shown are obtained with a pulsed excitation.

2.1.7 Single photon emission from a QD

The single-photon character of the emission from a single QD has first been demonstrated in 2000 simultaneously in the groups of Pr. Imamoglu and Pr. Yamamoto [29, 54]. Under pulsed laser excitation, a single QD generates a train of single-photon pulses at different energies, each corresponding to a charge configuration (see fig.2.6). Due to the anharmonicity of the transitions of multiple charges, a single QD is an ideal single-photon source provided that only one transition is detected. Indeed, the presence of the radiative cascade is highlighted by measuring the correlations between the photons emitted at different energies [86]. Correlating the photons associated to different transitions from the cascade leads to the measurement of bunching or antibunching features.

2.1.8 Coupling to phonons

Due to the presence of discrete energy levels, quantum dots are often compared to single isolated atoms. This comparison is not completely accurate, since a semiconductor QD is still an aggregate of atoms in a semiconductor lattice that can vibrate. These lattice vibrations, or phonons, are a source of dephasing of the photon emission, and give rise to the spectral broadening of the emission line. Moreover, the emission of a photon can also be associated with the absorption or the emission of zero, one or few phonons. L. Besombes and his colleagues showed the effect of temperature on the photon spectra of a CdTe QD [87]. In the absence of phonons, the profile of the spontaneous emission from a QD transition is expected to be a lorentzian (as shown in the previous section 2.1.5). When the temperature is increased the line shape is modified by the *exciton-acoustic-phonon* coupling as shown by fig.2.10 with the broadening of the main emission line (zero phonon line) and the appearance of phonon sidebands. These observations have also been reported with single InAs and GaAs QDs [88, 89]. The bulk phonon bath is a quasicontinuum of phonon states coupled to the QD emission. Because of this coupling, the full spectrum of the emission line from a QD is made of a Lorentzian emission line (called the *Zero-Phonon Line*) and two *phonon side bands*. During the recombination of the exciton, the lattice interacts with the exciton leading the absorption or the emission of a phonon of low energy. As a consequence, the photon energy is shifted in the higher or lower energies compared to the transition energy. It is shown that the fraction of emission within the Zero-Phonon Line (ZPL), defined as the emission at the energy of the QD transition, decrease with the increase of temperature. At high temperature ($T > 50\text{K}$), the PL spectrum is dominated by the phonon sidebands, as shown by fig.2.10. Figure 2.11 from [8] shows examples of calculated spectra of spontaneous emission for

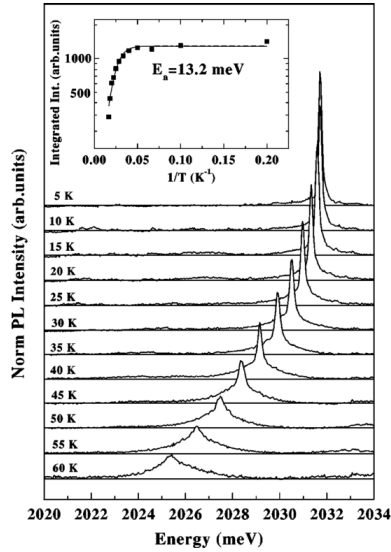


FIGURE 2.10: Figure reproduced from [87]. PL spectra of a single QD at different temperatures. With increasing temperature, side-bands appear progressively around the central zero-phonon line. The inset shows the evolution of the integrated intensity with temperature.

a single QD in bulk at various temperatures. At temperatures lower than 10K, the phonon sidebands are clearly asymmetric due to the low phonon population. Under this condition, the emission of a phonon is more efficient than the absorption of a phonon. When the temperature increases, the phonon sidebands becomes more intense, more symmetric and broader.

The coupling of the QD to the phonon bath is detrimental to the indistinguishability of the emitted photons [89, 90]. As a consequence, most of the studies with InAs QDs are done at 4K and filtering out the phonon sidebands, to achieve good coherence properties as required in quantum-optics experiments.

2.2 Characterization of a QD as a Quantum Light Source

In this section, we discuss the tools used to characterize the quantum properties of the QD emission. We recall the definition of the second-order correlation function and the principle of the two-photon interference. We also give a short overview of previous works.

2.2.1 Introduction to light sources statistics

2.2.1.1 Second order correlation function

The second-order correlation function is used to study photon statistic of a source [91]. We call the autocorrelation function in continuous wave $g_{cw}^{(2)}$ as opposed to the pulsed

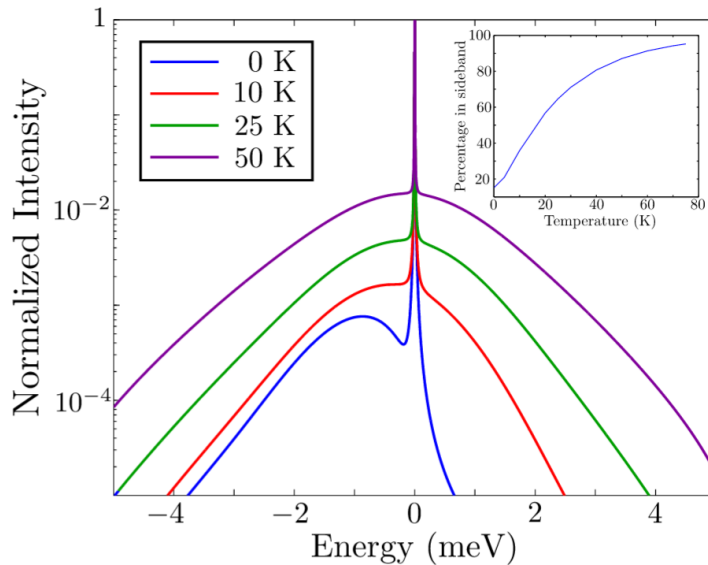


FIGURE 2.11: Figure reproduced from [8]. Calculated normalized emission spectrum for a QD coupled to a phonon reservoir at different temperatures (logarithmic scale). Each spectrum is normalized to unity. The inset shows the fraction of the intensity in the sidebands as a function of temperature.

regime where we use $g^{(2)}$. The photon correlation function $g_{cw}^{(2)}(t_1, t_2)$ is actually the probability that the light source emits one photon at time t_2 given that it already emitted a photon at time t_1 . If one consider the position of distinct detectors \mathbf{r}_1 and \mathbf{r}_2 , the autocorrelation function is:

$$g_{cw}^{(2)}(\mathbf{r}_1, t_1, \mathbf{r}_2, t_2) = \frac{\langle I(\mathbf{r}_1, t_1)I(\mathbf{r}_2, t_2) \rangle}{\langle I(\mathbf{r}_1, t_1) \rangle \langle I(\mathbf{r}_2, t_2) \rangle} \quad (2.37)$$

In a stationary regime, the relevant parameter is the delay $\tau = t_2 - t_1$. In the following, we neglect the spatial dependence assuming a fixed position for the detectors. The equation 2.37 simplifies:

$$g_{cw}^{(2)}(\tau) = \frac{\langle I_2(\tau)I_1(0) \rangle}{\langle I_2(0)I_1(0) \rangle} \quad (2.38)$$

where $I_1(t)$ ($I_2(t)$) is the number of detected photons at time t on the detector 1 (2).

Pulsed regime

In this work, the photon correlations are always done in the pulsed regime i.e., the sample is excited by short laser pulses. Due to the periodicity of the pulses, the photon correlation function is a series of peaks. The temporal distance between each peak is the repetition rate of the laser T ($\sim 12.2\text{ns}$). The relative areas of the peaks reveal some of the characteristics of the source. In the absence of memory effects, the single photon

purity is given by the area of the peak at zero delay normalized to the peaks at 12.2ns:

$$g^{(2)}(0) = \frac{n_2[0]n_1[0]}{n_2[T]n_1[0]} \quad (2.39)$$

The side peaks correspond to the case when two photons from different pulses are detected on both detectors.

By measuring $g^{(2)}$, the statistics of a light source is revealed: Poissonian, superpoissonian or subpoissonian. In the following, we shortly review the main characteristics of these sources.

2.2.1.2 Bunched sources: example of thermal sources

Thermal sources are ruled by the blackbody laws and by the Maxwell-Boltzmann distribution. The emitted field is a superposition of many incoherent waves, with the same time-dependence but with random phase and delay. In this case, the autocorrelation function is [92, 93]

$$\begin{aligned} g^{(2)}(\tau) &= 1 + [g^{(1)}(\tau)]^2 \\ g^{(2)}(0) &= 2 > 1 \end{aligned} \quad (2.40)$$

The source is said to be bunched. In other words, when one photon is detected on one detector, the probability that a second photon is detected simultaneously on the second detector is increased, compared to the long delay case. As a consequence, the total field strongly fluctuates in time around zero. For a mean number of photon $\langle n \rangle$ in the mode, the photon distribution follows the Bose-Einstein distribution of black-body radiation:

$$p(m) = \frac{\langle n \rangle^m}{(1 + \langle n \rangle)^{m+1}} \quad (2.41)$$

Figure 2.12 shows the photon distribution for a thermal source ($\langle n \rangle = 1$) as well as the theoretical autocorrelation function in continuous wave.

In practice, the bunching of a thermal source can be measured on a delay $\tau \approx \Delta\omega^{-1}$ where $\Delta\omega$ is the source bandwidth. Since thermal sources have globally a large bandwidth, the detectors must have an excellent time resolution unless the source is filtered using a narrowband filter.

2.2.1.3 Poissonian Sources

A source is qualified as Poissonian (or Poisson-like) when $g^{(2)}(0) = 1$. Such source follows a Poisson distribution. By definition, a Fock state is a state with a well-defined number of photons (or particles more generally) and is noted $|i\rangle$. The coherent state $|\alpha\rangle$

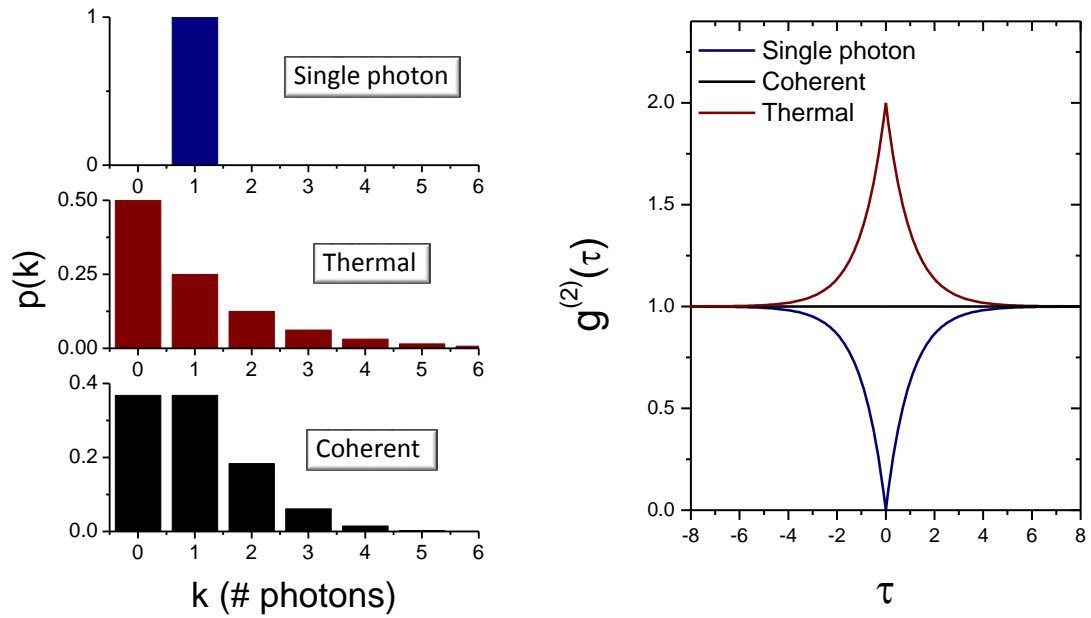


FIGURE 2.12: **a.** Photon distribution for different types of light sources. **b.** Theoretical autocorrelation function for a thermal light, a coherent light and a single-photon source.

can be written in the Fock-states basis as:

$$|\alpha\rangle = e^{-\langle n \rangle / 2} \sum_i \frac{\alpha^i}{\sqrt{i!}} |i\rangle \quad (2.42)$$

where $\langle n \rangle = |\alpha|^2$ is the mean number of photons. So the probability to detect k photons is given by

$$p(k) = \frac{\langle n \rangle^k}{k!} e^{-\langle n \rangle} \quad (2.43)$$

Figure 2.12 shows the photon distribution for a mean photon number $\langle n \rangle = 1$. The statistics of a coherent light is very different from the thermal light statistics. Because $g^{(2)}(0) = 1$, the detection of photons on one detector does not add any knowledge to the other detector. This also means that the variance of the light intensity is null. The associated physical picture is that of independent particles.

2.2.1.4 Anti-bunched Sources (example of the Fock states)

A light source is said subpoissonian if $g^{(2)}(0) < 1$. The detection of one photons decreases the probability that another photon will be detected on the second detector. This property is observed with "non-classical" sources [94]. From the Cauchy-Schwarz inequality, the classical theory predicts that the maximum of the function $g^{(2)}(\tau)$ is reached at $\tau = 0$. Yet, in the case of a anti-bunched source, $g^{(2)}(0) < g^{(2)}(\infty)$ hence its "non-classical" behaviour.

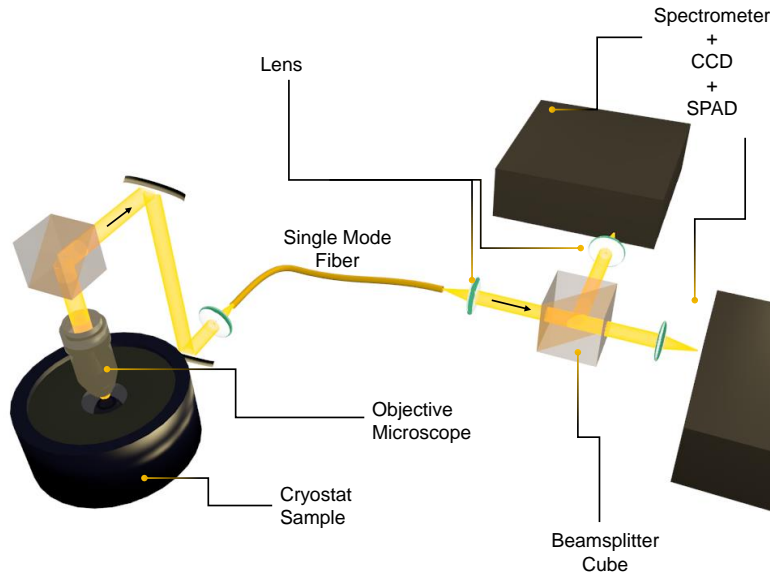


FIGURE 2.13: Schematics of the Hanbury-Brown Twiss (HBT) setup to measure the second-order autocorrelation of one light source.

For a Fock state of light $|n\rangle$, the autocorrelation function reads:

$$g^{(2)}(0) = \frac{\langle n | \hat{a}^\dagger \hat{a}^\dagger \hat{a} \hat{a} | n \rangle}{\langle n | \hat{a}^\dagger \hat{a} \rangle \langle \hat{a}^\dagger \hat{a} | n \rangle} = \frac{n(n-1)}{n^2} = 1 - \frac{1}{n} \quad (2.44)$$

A single-photon source is characterized by a $g^{(2)}(0) = 0$ as depicted by fig.2.12, implying that if a photon is measured on the detector 1, none can be detected on the second detector at the same time.

2.2.1.5 The Hanbury-Brown and Twiss setup

The experiment used to measure the second order correlation function has been developed in 1956. To measure the apparent angular size of the bright star Sirius, the two researchers Robert Hanbury Brown and Richard Q. Twiss developed an interferometer (HBT interferometer) where the light is split and sent to two detectors connected to a correlator [95]. The HBT experiment has been used in quantum optics pioneering experiments [92, 94, 96, 97]. Nowadays, it is routinely used to demonstrate the single-photon emission from a QD.

The HBT setup that we have used is depicted in fig.2.13. The PL from the sample is collected through a microscope objective and split by a 50:50 beam splitter. The PL is filtered by two spectrometers before it is sent to Single-Photon Avalanche Diodes (SPADs). For an autocorrelation measurement (for the single-photon purity), both spectrometers are set to the same energy.

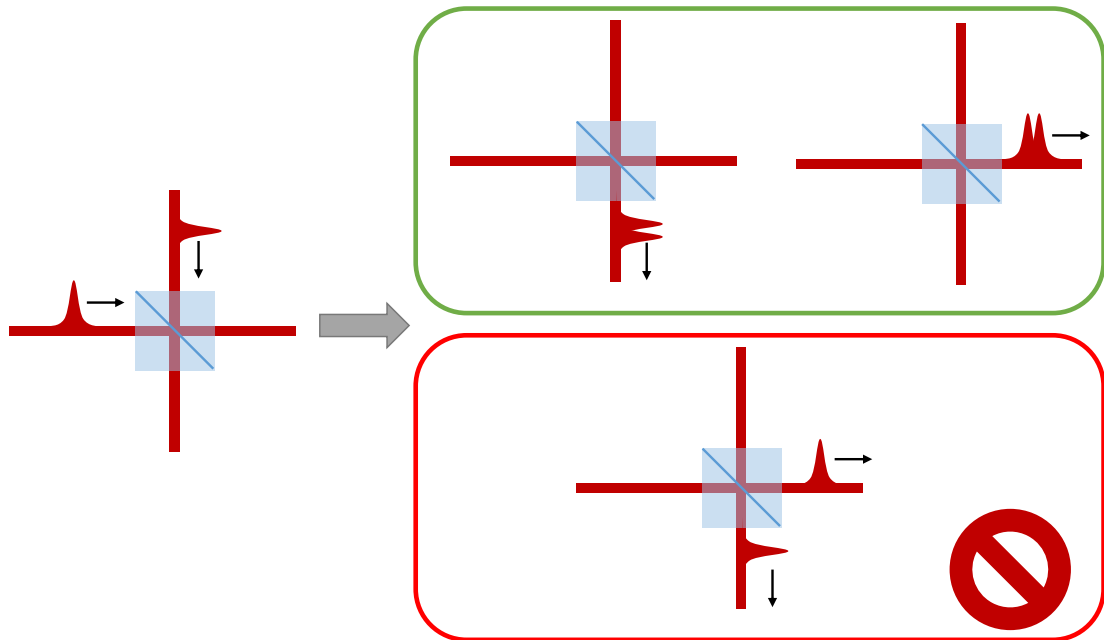


FIGURE 2.14: Schematic of the two-photon interference. Two indistinguishable photons meet on a balanced (50:50) beamsplitter. If they arrive simultaneously and are fully indistinguishable, the probability that they are released in opposite directions vanishes.

Finally the SPADs signals are correlated to an external correlator which constructs the histogram of coincidences.

2.2.2 Emission of indistinguishable photons from a QD

Most applications in quantum information require that the single photons be coherent and identical. When two identical photons are sent to the two inputs of a balanced beamsplitter, the probability that they are exit through different outputs vanished as illustrated by fig.2.14.

2.2.2.1 Introduction: The HOM experiment

In 1987, Hong, Ou and Mandel published the result of such an experiment where the probability to detect photons at the output of a 50:50 beamsplitter was measured as a function of the delay between two indistinguishable photons [98]. When the photons arrive simultaneously on the beamsplitter, they observed an important decrease of the

coincidence detection of photons at the outputs of the beamsplitter. The measured output state is:

$$|\phi_{HOM}\rangle = (R - T)|1, 1\rangle + i\sqrt{2RT}|2, 0\rangle + i\sqrt{2RT}|0, 2\rangle \quad (2.45)$$

where the state $|i, j\rangle$ corresponds to i (respectively j) photons on the first (second) output port of the BS (reflection and transmission coefficients are denoted R and T respectively). If $R = T$, the photons interfere destructively and it is impossible to measure photons on both detectors simultaneously.

2.2.2.2 Overlap of photon wavepackets emitted by one QD

Due to the interactions with its environment, a QD is prone to statistical fluctuations as well as dephasing processes. Many works have addressed the issue of spectral fluctuations in QD emission linewidths [87, 90, 99–102]. To be fully indistinguishable, the QD emission linewidth must be Fourier-transform limited. In most of cases, it is not the case due to the influence of the environment [103–105]. The mean photon overlap M characterizing the photon indistinguishability is given by:

$$M = \frac{\gamma}{\gamma + \gamma^*} = \frac{T_2}{2T_1} = \frac{T_2^*}{T_2^* + 2T_1} \quad (2.46)$$

where, $T_1 = \gamma^{-1}$ is the decay time, $T_2^* = 2\gamma^{*-1}$ is the pure dephasing time and $T_2 = 2(\gamma + \gamma^*)^{-1} = \left(\frac{1}{2T_1} + \frac{1}{T_2^*}\right)^{-1}$ is the coherence time of the photons. There are two methods to optimize the photon overlap:

- Increasing the pure dephasing time T_2^* , by minimizing the influence of the environment surrounding the QD. Among the detrimental effects, the charge noise or the phonon coupling are the main sources of decoherence.
- Decreasing the radiative decay time T_1 : by accelerating the spontaneous emission from the QD, the latter is less prone to feel the environment effects if the spontaneous emission is faster than the sources of pure dephasing.

2.2.2.3 State-of-the-art

The first two-photon interference with successively emitted photons by one QD was demonstrated by C. Santori et al. in 2002 [36]. Under a quasi-resonant excitation, they demonstrated a mean overlap of single photons between 0.72 and 0.81, as shown by fig.2.15 a.. Later the emission of indistinguishable photons has been confirmed by S. Laurent with a single QD in a photonic crystal [37] in the group of Pr. I. Robert at

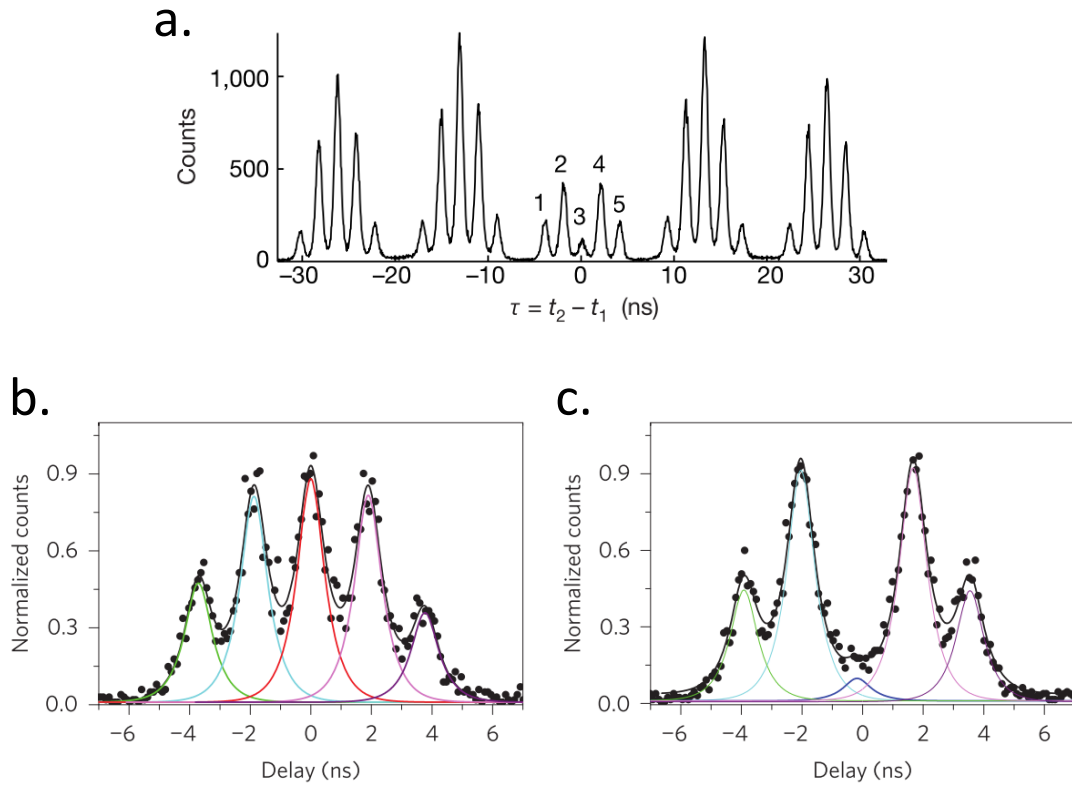


FIGURE 2.15: Figure reproduced from [36] and [40]. Correlation histogram measured by sending pairs of single photons in an interferometer. One photon of the pair is delayed by 2ns from the other photon. This delay corresponds to the difference of lengths between the two arms of the interferometer such as both photons of the pair will meet on a 50:50 beamsplitter. (b),(c) Same measurement under resonant excitation. By playing with the polarization on one of the interferometer's arm, the photons can be distinguishable (b) or indistinguishable (c).

the LPN. The influence of the Purcell effect and of temperature on the photon indistinguishability was also demonstrated by Varoutsis et al. [106]. When the temperature increases, decoherence terms increases. Photon indistinguishability was restored by accelerating the emission of the QD by Purcell effect.

In 2008, Bennett et al. fabricated a diode containing InAs QDs that emits single and indistinguishable photons with a visibility of 0.64 [38]. In 2009, the emission of indistinguishable photons by exciting resonantly a QD in CW was demonstrated by S. Ates and his coworkers. They demonstrated a photon overlap around 0.90 by exciting one QD in one micropillar from the side [39]. More recently, the group of Jian-Wei Pan showed a near-unity photon indistinguishability by exciting a single QD also at resonance but with a pulsed excitation [40, 107]. Figures 2.15 b. and c. show the contrast they measured for distinguishable photons (b.) or indistinguishable photons (with a visibility higher than 0.96).

2.3 Cavity Quantum ElectroDynamics (CQED)

In an abstract published in June 1946 [108], Purcell describes an effect where the spontaneous probability for nuclear magnetic moment transitions changes as a function of the emitter's environment. The system that Purcell studied was a nuclear-magnetic medium in which small metallic particles are mixed. He observed that, coupled to an electrical resonator (i.e. small metallic particles), the spontaneous emission rate was increased by a factor $F_P = 3Q\lambda^3/4\pi^2V$, where V is the volume of the mode of the resonator, Q is the quality factor associated to the resonance at the wavelength λ . F_P is called the Purcell factor. In 1970, Drexhage showed theoretically and experimentally the influence of the electromagnetic environment on the radiative decay of europium ions [109]. He observed a phenomenon of amplification or *quenching* according to the space between the ion and a dielectric surface. In the 80's, the enhancement of spontaneous emission with single atoms coupled to a cavity was observed in the group of Pr. Serge Haroche [110].

In 1998, the enhancement of spontaneous emission from an ensemble of quantum dots was demonstrated in a micropillar cavity [33, 111]. In 2005, the control of spontaneous emission of a single InAs QD in a 2D photonic crystal was demonstrated [112].

2.3.1 Theory of coupled emitter-cavity systems

In this part, we rapidly describe the basics of the theory of emission of an atom-like emitter in a cavity [113, 114].

2.3.1.1 The Jaynes-Cummings model

The Jaynes-Cummings model is a simplified model of the light-matter interaction that considers only an emitter in a cavity without any losses [115]. The emitter is a two-level system that interacts with one single mode of the electromagnetic field determined by the cavity. The emitter-radiation system corresponding Hamiltonian is given by:

$$H = H_{QD} + H_{CM} + H_I \quad (2.47)$$

where $H_{QD} = \hbar\omega_X|X\rangle\langle X|$ designates the exciton transition energy and $H_{CM} = \hbar\omega a^\dagger a$ corresponds to the energy of photons in the cavity mode. In the following, we denote the difference between the cavity mode energy and the exciton energy $\delta = \omega - \omega_X$. The interaction term is given by:

$$H_I = \frac{\hbar\Omega_1^{(1)}}{2} (|g\rangle\langle X| + |X\rangle\langle g|) (a^\dagger + a) \quad (2.48)$$

where the single photon Rabi frequency is:

$$\Omega_1^{(1)} = -\frac{-2q}{m} \frac{\langle g|\boldsymbol{\mu}\cdot\boldsymbol{\epsilon}|X\rangle}{\sqrt{2\hbar\epsilon_0\omega V_{\text{eff}}}} \quad (2.49)$$

As previously, the term $\boldsymbol{\mu}\cdot\boldsymbol{\epsilon}$ corresponds to the overlap between the emitter dipole and the electric field but V_{eff} is now the effective volume of the cavity mode.

The term H_I makes the link between the state of the excited emitter in a cavity containing n photons ($|X, n\rangle$) with the state corresponding to the emitter at its fundamental state in a cavity containing $n + 1$ photons ($|g, n + 1\rangle$):

$$\langle X, n|H_I|g, n + 1\rangle = \sqrt{n + 1}\hbar\Omega_1^{(1)}/2 \quad (2.50)$$

If we simplify the equation 2.50 by restricting to the case where there is only zero or one photon ($n = 0$) in the system, the total Hamiltonian takes the form:

$$H = \hbar \begin{bmatrix} \omega & \Omega_1^{(1)}/2 \\ \Omega_1^{(1)}/2 & \omega - \delta \end{bmatrix} \quad (2.51)$$

After the diagonalization of this matrix, the energy eigenvalues are

$$E_{\pm} = \hbar \left(\omega - \frac{\delta}{2} \pm \frac{1}{2} \sqrt{(\Omega_1^{(1)})^2 + \delta^2} \right) \quad (2.52)$$

with

$$\Delta E = E_+ - E_- = \hbar \sqrt{(\Omega_1^{(1)})^2 + \delta^2} \quad (2.53)$$

corresponding to the eigenvectors

$$|\psi_+\rangle = \cos\theta|g, 1\rangle + \sin\theta|X, 0\rangle \quad (2.54)$$

$$|\psi_-\rangle = -\sin\theta|g, 1\rangle + \cos\theta|X, 0\rangle \quad (2.55)$$

with $\tan\theta = \frac{\Omega_1^{(1)}}{\delta}$.

When the emitter is at resonance with the cavity mode ($\delta = 0$), dressed states appear and the eigenstates are

$$|\psi_{\pm}\rangle = \frac{1}{\sqrt{2}} (|X, 0\rangle \pm |g, 1\rangle) \quad (2.56)$$

These states cannot be factorized and can be considered as entangled states.

2.3.1.2 Spontaneous emission in a cavity

Here, we consider the case where the QD is in the excitonic state at $t = 0$. The exciton resonance is assumed to be resonant with the cavity mode ($\delta = 0$) which is empty. The initial state is written $|\psi(t = 0)\rangle = |X, 0\rangle$, which is not an eigenstate of the Hamiltonian

given by the eq.2.51. By expanding this initial state to the eigenstates $|\psi_{\pm 1}\rangle$:

$$|\psi(t=0)\rangle = \frac{1}{\sqrt{2}} (|\psi_{+1}\rangle + |\psi_{-1}\rangle) \quad (2.57)$$

then the system evolves in:

$$\begin{aligned} |\psi(t)\rangle &= \frac{1}{\sqrt{2}} \left(|\psi_{+1}\rangle e^{-iE_+t/\hbar} + |\psi_{-1}\rangle e^{-iE_-t/\hbar} \right) \\ &= e^{-i\omega t} \left(-i|g, 1\rangle \sin\left(\frac{\Omega_1^{(1)}}{2}t\right) + |X, 0\rangle \cos\left(\frac{\Omega_1^{(1)}}{2}t\right) \right) \end{aligned} \quad (2.58)$$

and the probability that the QD is at the excitonic state is

$$P_X(t) = |\langle X, 0|\psi(t)\rangle|^2 = \cos^2\left(\frac{\Omega_1^{(1)}}{2}t\right) \quad (2.59)$$

The system oscillates with coherent exchange of energy between the QD and the cavity. Such situation is called *vacuum Rabi oscillations*. This situation is highly idealized. This is possible because we have neglected the escape of the photon out of the cavity. In reality, the photon is stored in the cavity during a finite lifetime and the QD can emit photons in other modes of the electromagnetic field.

2.3.1.3 The lossy cavity: the Purcell effect

In a real cavity, photons are stored for only a finite time T . The decay rate κ describes the exponential decrease of the electromagnetic energy in the cavity and corresponds to a quality-factor $Q = \omega_m/\kappa$ (where $\hbar\kappa$ is the mode linewidth).

Under the assumption of a low-number of photons, the system is considered to evolve in the subspace spanned by the vectors $|X, 0\rangle, |g, 1\rangle, |g, 0\rangle$ noted $|1\rangle, |2\rangle$ and $|3\rangle$. The two first states are coherently coupled by the Jaynes-Cummings Hamiltonian as shown previously. The state $|2\rangle = |g, 1\rangle$ decays toward the state $|3\rangle = |g, 0\rangle$ at the rate κ . The evolution of the corresponding density matrix ρ is described by the following rate equations [114]:

$$\frac{d\rho_{11}}{dt} = -\frac{\Omega_1^{(1)}}{2}(\rho_{12} + \rho_{21}) \quad (2.60)$$

$$\frac{d\rho_{22}}{dt} = \frac{\Omega_1^{(1)}}{2}(\rho_{12} + \rho_{21}) - \kappa\rho_{22} \quad (2.61)$$

$$\frac{d}{dt}(\rho_{12} + \rho_{21}) = \Omega_1^{(1)}(\rho_{11} + \rho_{22}) - \frac{\kappa}{2}(\rho_{12} + \rho_{21}) \quad (2.62)$$

$$\frac{d\rho_{33}}{dt} = \kappa\rho_{22} \quad (2.63)$$

This system can be written by changing the variables $x = \rho_{11}$, $y = \rho_{22}$ and $z = \rho_{12} + \rho_{21}$. It takes the form:

$$\frac{d}{dt} \begin{pmatrix} x \\ y \\ z \end{pmatrix} = \begin{pmatrix} 0 & 0 & -\Omega_1^{(1)}/2 \\ 0 & -\kappa & \Omega_1^{(1)}/2 \\ \Omega_1^{(1)} & -\Omega_1^{(1)} & -\kappa/2 \end{pmatrix} \begin{pmatrix} x \\ y \\ z \end{pmatrix} \quad (2.64)$$

When the emitter is in resonance with the cavity ($\delta = 0$), the frequencies λ characterizing the system's evolution are the solutions of the equation:

$$(\kappa/2 + \lambda)(\lambda^2 + \kappa\lambda + (\Omega_1^{(1)})^2) = 0 \quad (2.65)$$

The solutions of 2.65 are:

$$\lambda_0 = -\frac{\kappa}{2}; \quad \lambda_{\pm} = -\frac{\kappa}{2} \pm \frac{\kappa}{2} \sqrt{1 - 4(\Omega_1^{(1)})^2/\kappa^2} \quad (2.66)$$

Depending on the ratio $\Omega_1^{(1)}/\kappa$, two different regimes exist:

- **The strong regime coupling** ($\Omega_1^{(1)} > \kappa/2$): This regime corresponds to the scenario when the cavity damping is weak. As seen before, the losses are small enough as to allow a reabsorption of the emitted photon. However, the Rabi oscillations are now damped with κ as decay constant, as depicted by fig.2.16. Spectrally, the strong regime coupling is characterized by the Rabi splitting around the resonance frequency.
- **The weak regime coupling** ($\Omega_1^{(1)} < \kappa/2$): In this case, the cavity is lossy and the relaxation of the electromagnetic field is efficient. In this regime, the cavity is empty most of the time. Figure 2.16 shows the time signature of the weak coupling regime (bottom left) as well as the spectral signature (top left). The acceleration of the spontaneous emission is spectrally visible by a broadening the radiative emission linewidth.

In the weak coupling regime, assuming that $\Omega_1^{(1)} \ll \kappa$, we can write the decay rate:

$$\Gamma_{CM} = -\lambda_+ \approx (\Omega_1^{(1)})^2/\kappa \quad (2.67)$$

If we consider that the dipole and the mode electric field are along the same direction, the eq. 2.67 reads

$$\Gamma_{CM} = \frac{2|\mu_x|^2}{\epsilon_0 \hbar} \frac{Q}{V_{\text{eff}}} \quad (2.68)$$

The emission rate shown by the eq.2.68 can be compared to the spontaneous emission of the same emitter in bulk given by the eq.2.27. Consequently, the Purcell factor is

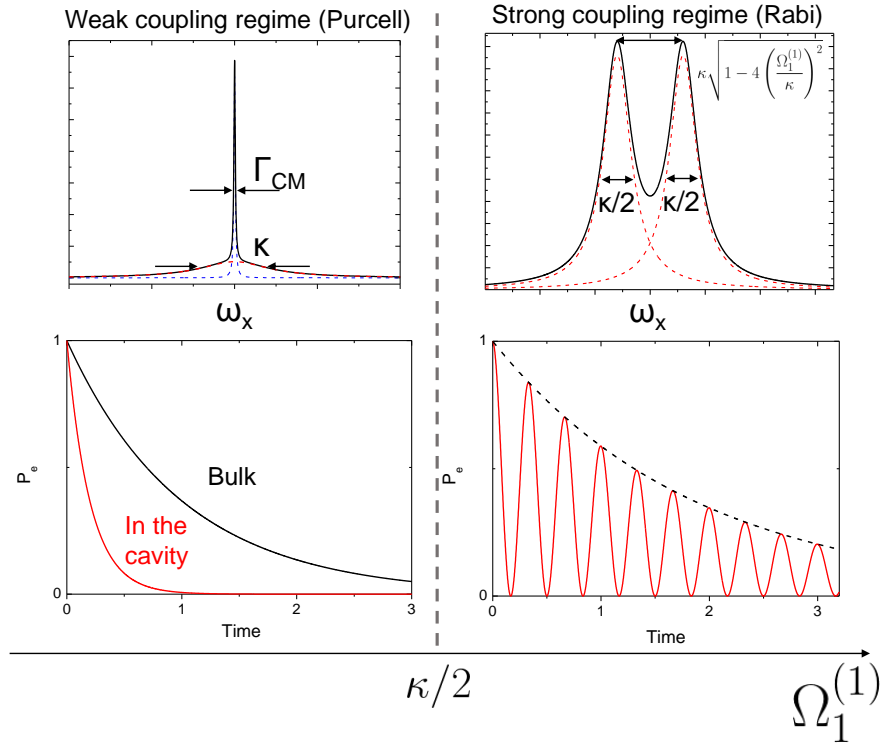


FIGURE 2.16: Temporal and spectral characteristics of both coupling regimes.

defined as the ratio of both rates:

$$F_p = \frac{\Gamma_{CM}}{\Gamma} = \frac{3}{4\pi^2} \frac{Q(\lambda/n)^3}{V_{\text{eff}}} \quad (2.69)$$

The Fermi golden rule method:

In the weak coupling regime, the spontaneous emission decay rate can also be described by the Fermi golden rule:

$$\Gamma_{CM} = \frac{2\pi}{\hbar} |\langle g, 1 | H | X, 0 \rangle|^2 \rho_{cm}(\omega) \quad (2.70)$$

where $\rho_{cm}(\omega)$ is the density of modes per unit energy.

Considering the case where the emitter is spatially located at the maximum of the electric field, its transition is resonant with the energy of the mode ($\omega_X = \omega_m$) and its dipole is parallel to the field, we have:

$$\Gamma_{CM} = \frac{2 |\langle g, 1 | \vec{\mu}_X | X, 0 \rangle|^2 Q}{\hbar n V_{\text{mode}}} \quad (2.71)$$

The Purcell factor F_P gives the maximum acceleration rate that could offer the cavity if the emitter is perfectly matched with the intra-cavity electric field.

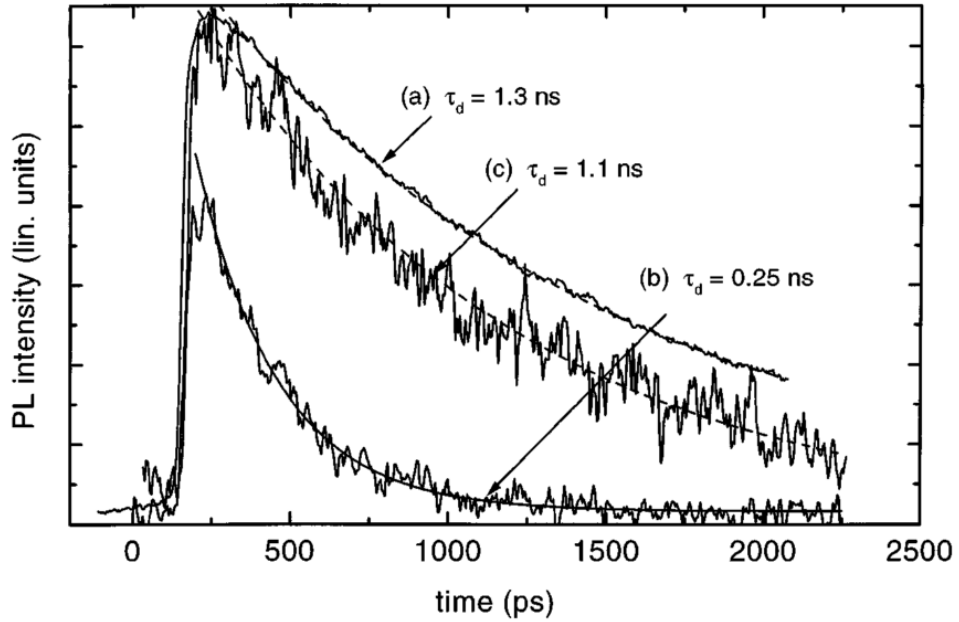


FIGURE 2.17: Figure reproduced from [33]. Time-resolved PL spectra for a QD in bulk (a) and for a QD in a pillar : on resonance (b) and out of resonance (c) with the fundamental mode.

The equations 2.69 and 2.71 show that the spontaneous emission is largely enhanced with cavities exhibiting small losses (high quality factor Q) and small effective volumes. Figure 2.17 shows the first acceleration of the spontaneous emission of a QD ensemble in a pillar cavity (with a diameter equal to $1\mu\text{m}$ and a quality factor $Q\sim 5200$) [33]. The curve (a) shows the time-resolved PL of a QD in bulk GaAs while the lines (b) and (c) show the time-resolved emission of one QD when it is in resonance (b) or out of resonance (c) with the fundamental mode of the pillar.

In the following, we give a short overview of the different semiconductor structures that are used to modify the spontaneous emission of single QDs.

2.3.2 Semiconductor Structures Confining Light

In solid state systems, there are different categories of structures to modify the electromagnetic density of states of a single emitter: some are based on the coupling with plasmons in metals (nanoantennas), and others are based on semiconductor waveguides and cavities. In this overview, we only consider the latter.

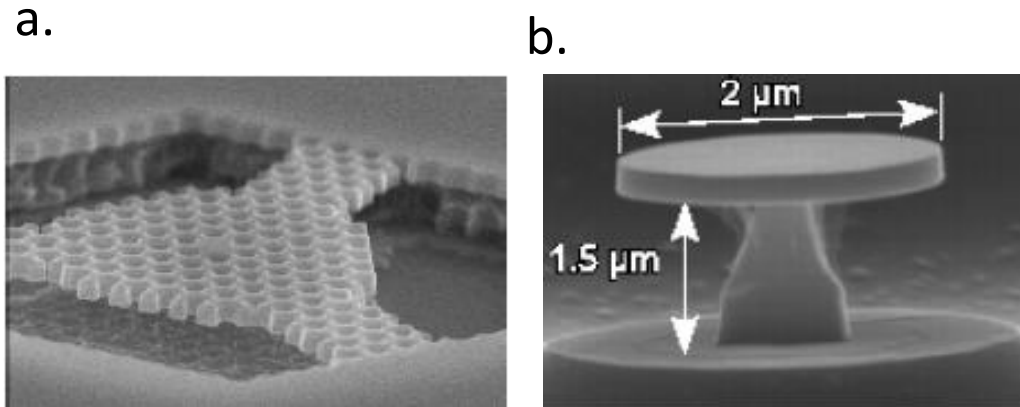


FIGURE 2.18: **a.** Suspended photonic crystal cavity obtained with a missing hole in the center of the image, reproduced from [37]. **b.** SEM image of one microdisk ($2\ \mu\text{m}$ of diameter) reproduced from [118]

2.3.2.1 Cavities

One can tally three main structures of semiconductor cavities to control the spontaneous emission of a single emitter: microdisks, photonic crystals and micropillars. These three structures, where a single QD is coupled with the optical mode of a cavity were used to demonstrate the Purcell effect or the strong coupling regime. In this section, we briefly introduce each structure.

- Microdisks:** Microdisks are disks whose diameter is few microns and with a revolution axis parallel to the growth axis. The typical height of the disk is reduced to its minimum to contain only one mode, λ/n where n is the optical index of semiconductor. Due to internal reflections at the interface with the air, the confinement of the mode is achieved in all three directions of space. Optical quality factors between $5 \cdot 10^5$ and $5 \cdot 10^6$ can be achieved depending on the material [116]. Moreover, microdisks exhibit small effective volumes, leading to high Purcell factors when an emitter is well coupled with the mode. The first control of spontaneous emission in a microdisk was shown by Gayral et al. in 2001 [117]. Later, the strong coupling regime has been demonstrated at the LPN by E. Peter and her coworkers in 2005 [118]. The extraction of photons occurs in the 2D plane parallel to the disk so that, additional techniques, as the evanescent coupling with fibers are needed to optimize the collection of the photons [119].
- Photonic crystals:** A 2D photonic crystal can be made of a suspended membrane with a periodic holes lattice. The periodicity, shape, distribution and size of holes

determine the photonic bandgap that blocks the propagation photons in the structure. By varying locally the position of holes, the optical field is confined locally, giving rise to a cavity. Q -factors are of the order of $5 \cdot 10^4$ with smaller effective volumes than the wavelength to the cube [112, 120, 121]. As with microdisks, the collection is usually in the plane of the membrane. It raises some mismatching issues with external optics that is detrimental to the photon collection.

- **Micropillars:** During my PhD, I worked with micropillar cavities. A micropillar is a cylinder with few micrometer diameter is few micrometers and a 10 micrometers height. Three main parts from the bottom to the top can be distinguished: the bottom mirror, the cavity spacer and the top mirror. The mirrors are Bragg reflectors, made of an alternation of layers with thickness equal to $\lambda/4n$ where n is the optical index in the layer and λ the resonant wavelength. In standard structures, the cavity width is λ/n where n is the optical index in the cavity (which is usually GaAs). Using a top-down process, micropillars are fabricated from a planar cavity where they are etched. The etching process is a crucial step in the fabrication. The roughness on the edges of the micropillars must be as low as possible in order to maintain a high Q at low volume.

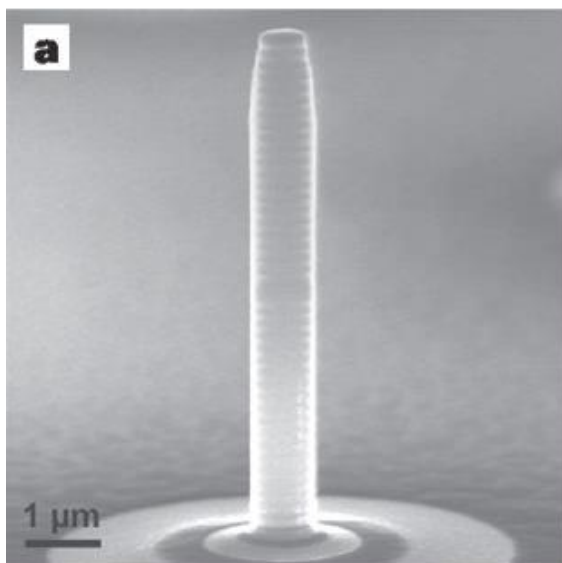
J.-M. Gérard and coworkers used micropillars to demonstrate the first acceleration of the spontaneous emission with an ensemble of QDs in 1998 [33]. In 2001, G. Solomon and coworkers used a single-mode (polarization-non degenerate) micropillar to demonstrate a high coupling efficiency between the emitter and the optical mode [34]. In 2004, A. Forchel and coworkers showed the first strong coupling regime between an InAs QD and the optical mode of a micropillar [35]. All these results were obtained without controlling the position of the QD in the cavity relying on a statistical matching of the QD and the micropillar. In 2008, a technique to control deterministically the position of the micropillar cavity with respect to QD was developed by Dousse and coworkers [45]: the *in situ* lithography technique. This technique led to the fabrication of the current brightest source of polarization-entangled pairs of photons [46] and of indistinguishable photons [31].

We describe the *in situ* lithography technique in section 2.4.

2.3.2.2 Semiconductor waveguides

In 2008, a technique has been proposed to redirect the emission of a QD other than by mean of Purcell effect. Instead of coupling a single QD to a cavity, the emitter is inserted in a monomode optical waveguide. In 2008, P. Lodahl and coworkers showed the coupling of QD with a 1D photonic guide inside a photonic crystal [122]. Later in

a.



b.

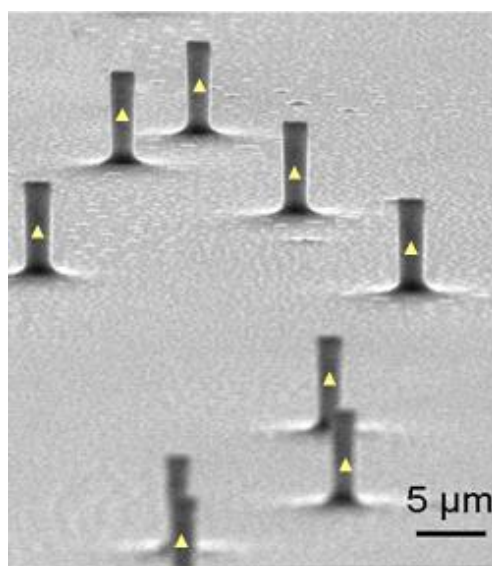


FIGURE 2.19: **a.** SEM image of one micropillar, reproduced from [35] **b.** SEM image of a series of micropillars fabricated by using the *in-situ* lithography [45]. The quantum dots are marked with yellow triangles.

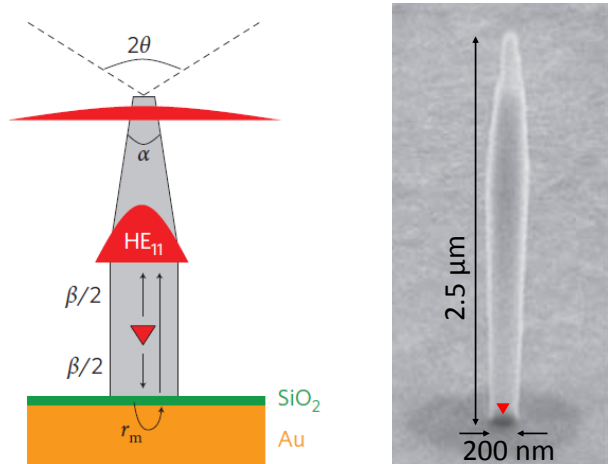


FIGURE 2.20: *Left* : Schematics of a photonic waveguide, the red triangle shows the position of the QD. *Right* : SEM image of one photonic waveguide. The red triangle shows the position of the QD. Figures reproduced from [32]

2010, J. Claudon and coworkers fabricated a bright single-photon source by inserting a single QD in a photonic nanowire on top of a metallic mirror [32]. The only direction permitted for emitted photons is along the wire, toward the top as shown by fig.2.20. The length of the nanowire is equal to $2.5\mu\text{m}$ for a diameter around 200nm.

2.4 Techniques of cavity-QD coupling

The Purcell enhancement of spontaneous emission requires two main criteria:

- **Spatial matching:** The emitter (or dipole) must be located where the electric field of the mode in the cavity is the strongest. This criterion is one of the most critical: after a Stransky-Krastanov growth, the QDs are randomly distributed in the plane.
- **Spectral matching:** The cavity resonance must be at the frequency of the QD optical transition. Typically, the spectral dispersion of the QDs energy is large (about 50meV at 1.3eV), three orders of magnitude broader than the spectral width of a cavity with a Q-factor of 10^4 .

Multiple approaches have been explored to reach these two conditions. A short review is given below before describing the *in situ* lithography technique that we used during this thesis.

2.4.1 Deterministic techniques of coupling of a QD in a cavity

In 2005, the first deterministic coupling between a QD and a cavity was demonstrated by A. Imamoglu's group. They measured the QD position with respect to metallic marks by using a Scanning Electronic Microscope (SEM) or with a Atome Force Microscope (AFM) [123, 124]. Then they defined a photonic crystal cavity centred on the QD using the marks to align the electronic beam lithography. The spectral matching was then adjusted by modifying the holes diameter using iterative digital etching steps. This technique does not allow the fabrication of multiple devices simultaneously and it is so challenging that it was never reproduced.

Another approach is to control the QDs position during the growth. In 2008, a site-controlled QD was coupled to a photonic crystal cavity [125]. The main drawback is the optical quality of QDs: compared to Stranski-Krastanov QDs, site-controlled QDs exhibit a lower quantum efficiency ($\approx 40\%$) with a broader linewidths [126].

In 2009, a new approach consisting in a movable and tunable cavity was implemented in Pr. G. Solomon's team [127]. They developed a technique where one of the cavity mirror

was formerly bonded to a fiber and movable. Using a piezo-electric actuator, they could couple the confine electric field with a single QD. They demonstrated a high Q ($=23000$) but with a high volume ($= 2.3 \mu\text{m}^3$) which is detrimental to get high Purcell effect [75]. With the same technique, Warburton's group showed recently a Purcell enhancement equal to 3 [128].

2.4.2 Coupling a single QD in a cavity using the *in situ* lithography

Principle of the *in situ* lithography technique:

At the LPN, P. Senellart and coworkers developed an original low temperature photolithography technique to deterministically couple a QD to a micropillar cavity. The technique relies on the overlap of three optical paths that are used to excite a target QD (at 850nm), to collect their emission (around 930nm) and to expose a resist layer (at 550nm) deposited on a planar cavity sample. The QD position is measured with a 50 nm accuracy by maximizing its emission. When the QD position is determined, the 550 nm excitation line is used to define a disk shape in the resist centred on the QD. This disk will later be used as a direct mask to etch the micropillar. The disk diameter is adjusted so that the fundamental mode pillar matches the QD emission energy. After the *in situ* lithography step, the resist is developed leading to disks. The planar cavity is then etched except where the resist was exposed in order to get micropillars that are all centred on QDs.

The process starts with a planar cavity sample with a low-density layer of InAs/GaAs QDs. The QDs are randomly distributed at the center of the planar cavity as shown by fig.2.21b. The mirrors of the cavity are made of alternating pairs of AlGaAs/GaAs layers. A silicon nitride SiN_4 layer and a resist layer are deposited at the top of the sample, which is then placed in a cryostat at 4K.

As shown in fig.2.21 a., the cryostat developed in collaboration with attocube is equipped of a three-axis (X,Y and Z) piezo-controlled stage allowing the displacement of the sample with an accuracy better than 1 nm. The excitation laser lines are focused with a fixed microscope objective. The X and Y directions are finely controlled by using capacitive sensors which measure with precision the absolute position of the sample (with a precision of 10 nm). Knowing the absolute position of the sample along X and Y allows to have a feedback on the sample position, avoiding drift effects and providing a good stability. The whole is controlled by a centralized operating system with a user-friendly interface.

1 - Measurement of the position of a single QD:

The QDs in the planar cavity are excited by sending the excitation laser through the fixed

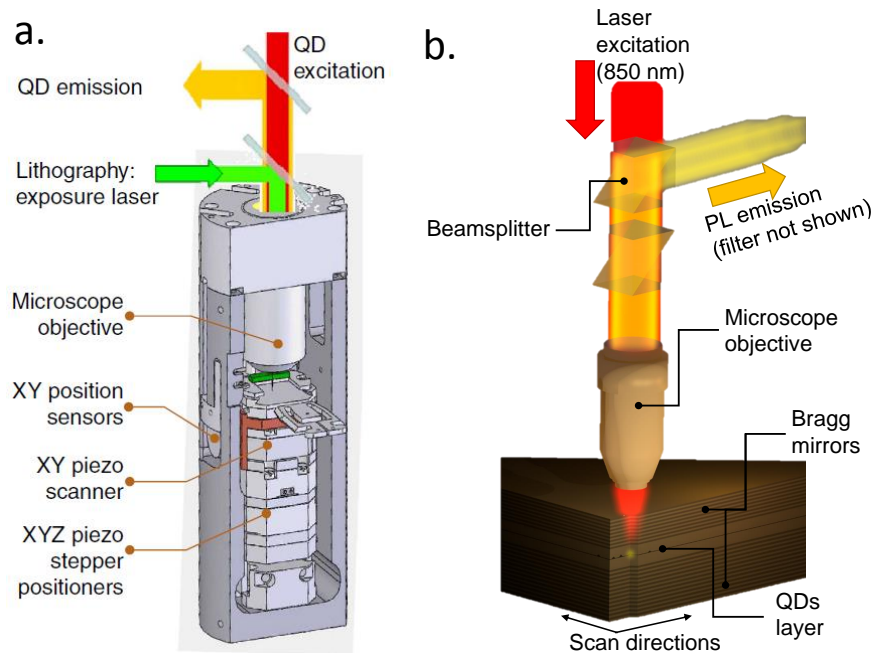


FIGURE 2.21: **a.** Microscope structure used for the *in situ* lithography. **b.** Schematics of the first step consisting in the excitation of InAs QDs in a planar cavity by collecting the photoluminescent light emitted (yellow beam). Scales are not respected.

microscope objective. The QDs are excited non resonantly (at the absorption energy of GaAs or InAs, with a wavelength between 750nm and 850nm). The photoluminescence (PL) signal, filtered by dichroic mirror, is collected through the same objective. To get the maximum of emitted photons from the QD, it is crucial that the detection path is correctly aligned with the excitation laser path. The displacement of the sample (using the XY piezo scanners) allows us to scan the position of the sample. Figure 2.22a. shows an example of PL map measured by scanning a planar cavity sample excited with a laser at 850nm. The Z-axis is the intensity of photoluminescent light emitted by the InAs QDs in the planar cavity. To precisely locate a single QD, we finely displace the sample with respect to the beam and we maximize the collected PL as shown by fig.2.22b. The position of the QD is obtained with an accuracy of 50nm by maximizing the PL from the selected QD. Simultaneously, its emission spectrum is monitored in order to measure the different QD transition energy. By increasing or decreasing the excitation power, we can also identify the different emission lines of the QD. The energy of the targeted QD transition will be used to define the correct parameter for the cavity.

2 - Exposure of the resist :

Once a suitable QD has been chosen and located at the center of the 850 nm excitation line, the photoresist is exposed with the green line. This green laser follows the

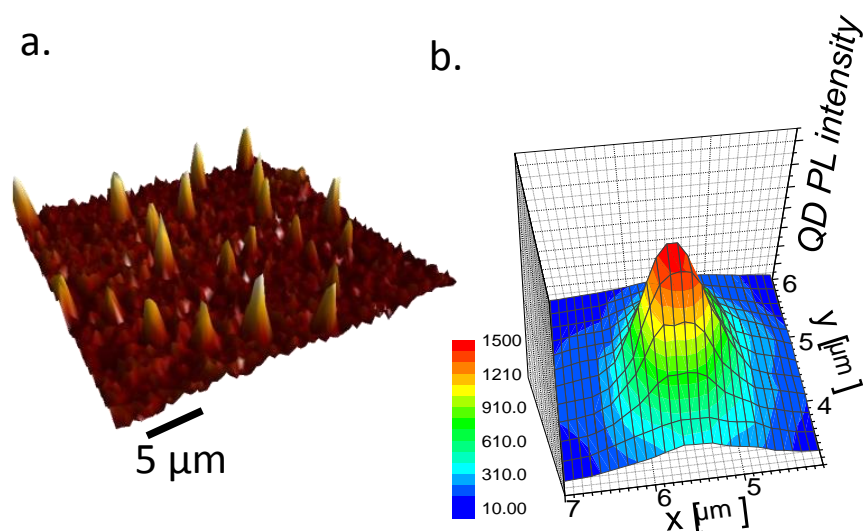


FIGURE 2.22: **a.** Photoluminescent (PL) map of planar cavity sample done by scanning the sample horizontally. **b.** Map of photoluminescent signal from a single QD in a planar cavity.

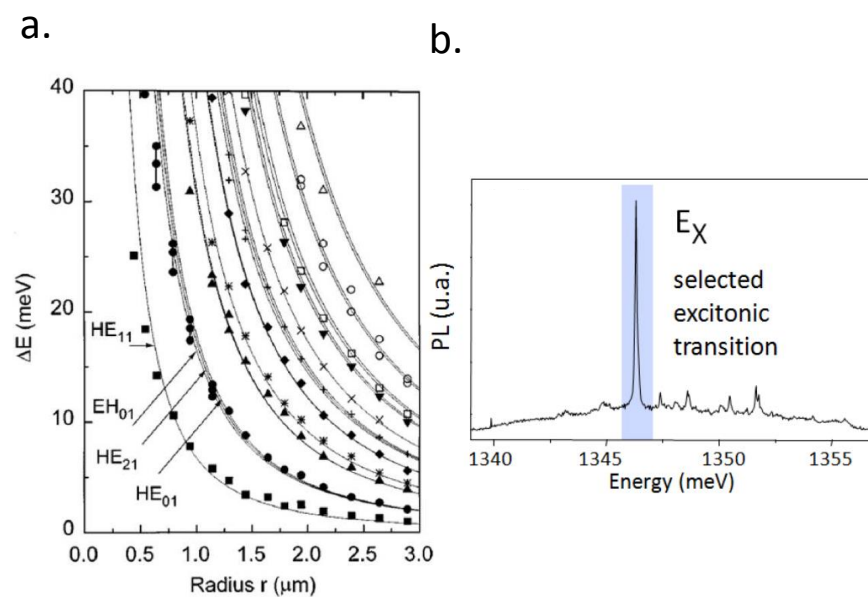


FIGURE 2.23: **a.** Figure reproduced from [129]. Measured evolution of the energies of the optical modes as a function of the radius of a micropillar. **b.** Figure reproduced from [85]. Measured PL spectrum from a single QD in a planar cavity.

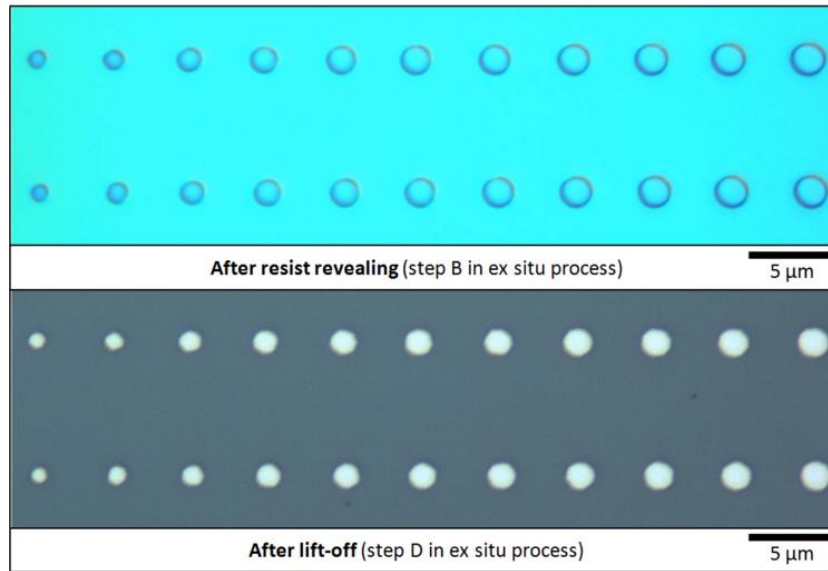


FIGURE 2.24: Figure reproduced from [85]. (top) Optical microscope images of printed disks after the resist revealing. (down) Optical microscope images after the the lift-off step.

same optical path as the excitation laser line (red) and as the collection line (yellow)¹. The overlap of the green spot with the other spots is important to get a good spatial matching. As shown by fig.2.23a., the optical modes energy of a micropillar shifts with the pillar radius. The diameter of the exposed disk is finely chosen (with a precision of 100nm) to adjust the pillar diameter and consequently its fundamental mode energy to the QD transition. There are two ways to change the exposed disk size: by choosing the exposure time of the resist or by drawing a circle with a given diameter. Although the variation of the exposure time was the first chosen solution before 2009, using the attocube setup developed in 2010, we can draw circles and any arbitrary shape around a single QD. To obtain a good control of the pattern size, a calibration curve is usually done before each lithography, as illustrated by fig.2.24.

3 - Ex situ process:

After typically 40-50 QDs have been located and disks exposed centered on each of them, the sample is removed from the cryostat. The next steps take place in the clean room and require some *standard* processes that are depicted in fig.2.25 and described below: First, the resist on the sample is developed (1), dissolving the exposed part. Then, a 40nm thick layer of Nickel is deposited (2) and followed by a lift-off (3). Ni disks are

¹The three lines have been focused and aligned cautiously by measuring the reflections of lines on a metallic grating in the cryostat.

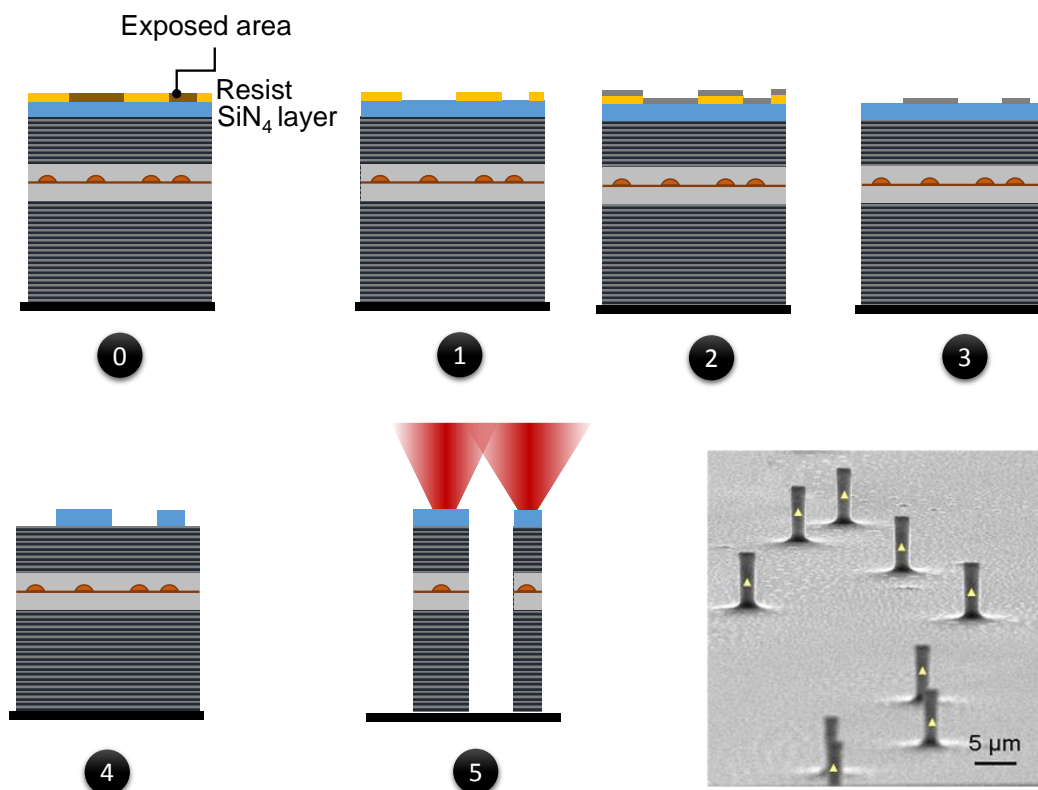


FIGURE 2.25: Schematics of the ex-situ clean room processes for the fabrication of deterministic pillars and SEM image of a series of micropillars, each micropillar contains a single InAs QD (represented by a yellow triangle).

exactly where the resist has been exposed previously, as shown by the microscope image 2.24. These disks protect the underlying silicon nitride SiN₄ layer during the mask transfer using a reactive ion plasma etching (RIE) (4). Finally, the SiN₄ mask protect the exposed areas during the semiconductor etching where all the unprotected surfaces will be etched to obtain the micropillars (5). After this last step, the micropillars are formed and the sample is ready for optical measurements. When needed, like for defining an electrical contact, we can also remove the SiN₄ layer.

2.5 Brightness of a single-photon source

Considering the diversity of single-photon sources that are used or developed in the quantum optics community, we aim at defining a common criteria to characterize the source brightness.

2.5.1 Definition of the brightness

In a pulsed regime, we define the brightness of a single-photon source **as the probability that one excitation pulse results in the effective emission and collection of one and only one photon in the first lens of the photonic path**. Brightness and extraction efficiency get often mixed up. In this definition, the brightness depends not only on the extraction efficiency that defines the probability of collecting an emitted photon but also on the probability that the source emits one photon.

2.5.1.1 Brightness of a parametric down conversion source

Since they feature many advantages (they are compact, cost-effective, robust, operate at room temperature), attenuated lasers and Parametric Down Conversion (PDC) sources are widely used for photonic quantum technologies. Lasers can be attenuated to the limit that on average each pulse contains less than one photon. The probability that one pulse contains exactly k photons knowing that the average number of photons is n is given by the Poisson law:

$$\begin{aligned} P_n(k) &= \frac{n^k}{k!} e^{-n} & P_n(1) &= n e^{-n} \\ P_n(2) &= \frac{n^2}{2} e^{-n} & P_n(k > 1) &= 1 - P_n(0) - P_n(1) \end{aligned} \quad (2.72)$$

Figure 2.26 shows the evolution of the equation 2.72 as a function of the mean number of photons n . The black line represents $P_n(1)$ and we observe that the probability to get one photon per pulse $P_n(1)$ will always be lower than $1/e \approx 0.37$ with an attenuated laser. Moreover, as shown by the probability to get more than one photon per pulse (blue line), the probability to get more than one photon is close to 0.3 for $n = 1$. The generation of multiple photons is detrimental for the measurements at the single-photon scale, so working with lasers requires a strong attenuation of the beam, to keep a reasonable single photon purity. As a consequence, the mean number of photons n is set to $n \ll 1$ so that $P_n(1)$ is generally between 0.001 and 0.01 in most of the linear quantum optics experiments.

Heralded photon sources are the most used sources in experiments needing indistinguishable single photons. By strongly pumping a nonlinear crystal, two down-converted beams are generated, labelled as signal and idler. Since they exhibit perfect correlation in photon number, the detection of the idler beam heralds the presence of the signal. Because the photons are emitted into a multitude of spatial and spectral modes, the heralded signal is not a pure single-photon state. Consequently a strong filter is required leading to low heralding rates. Depending on the detectors efficiency η , the measurement

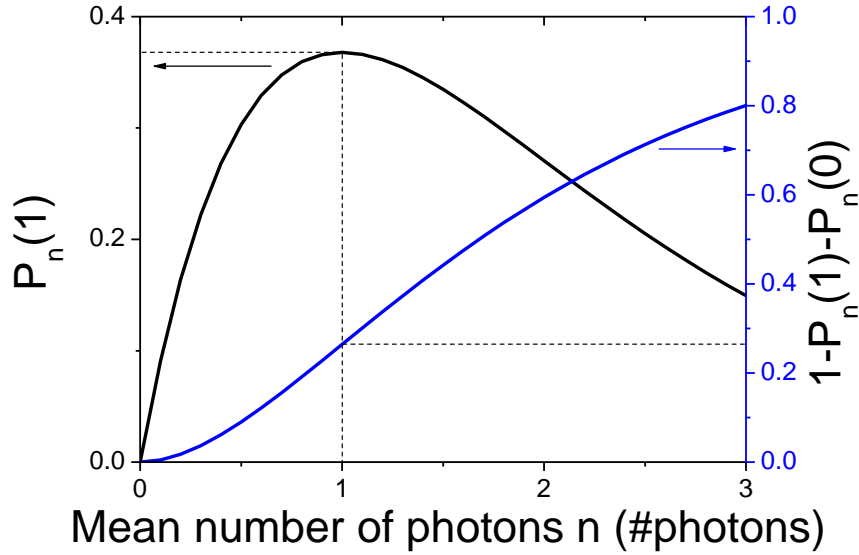


FIGURE 2.26: (*Black line*) Theoretical probability to have only one photon in one pulse emitted by a poissonian source as a function of the mean intensity n (in number of photons). (*blue line*) Calculated probability to have more than 1 photon in a pulse as a function of the mean intensity.

operators are given by [49]

$$\begin{aligned}
 \prod_{\text{NoClick}} &= \sum_{n=0}^{\infty} (1-\eta)^n |n\rangle \langle n| \\
 \prod_{\text{Click}} &= \sum_{n=0}^{\infty} [1 - (1-\eta)^n] |n\rangle \langle n|
 \end{aligned} \tag{2.73}$$

From the equations 2.73, the brightness of the source (seen as the heralding probability) can be calculated as a function of the single-photon purity $1 - g^{(2)}$ and of the detector efficiency η . Figure 2.27 reproduced from [49] shows the calculated heralding probability as a function of the single-photon purity with various detector efficiencies. The shaded region depicts the achievable region. We see that even with an ideal detector, a high purity leads to extremely low heralding rates, and hence low single photon rates.

In the perspective to get pure and deterministic single-photon sources using PDC sources, new techniques emerged as the multiplexing of several PDC sources [48]. A. Christ and C. Silberhorn calculated that an array of at least 17 switched sources is required to build one deterministic (with a brightness higher than 0.99) pure single-photon sources. We see that in this case, this kind of source is no longer compact nor cost-effective any more.

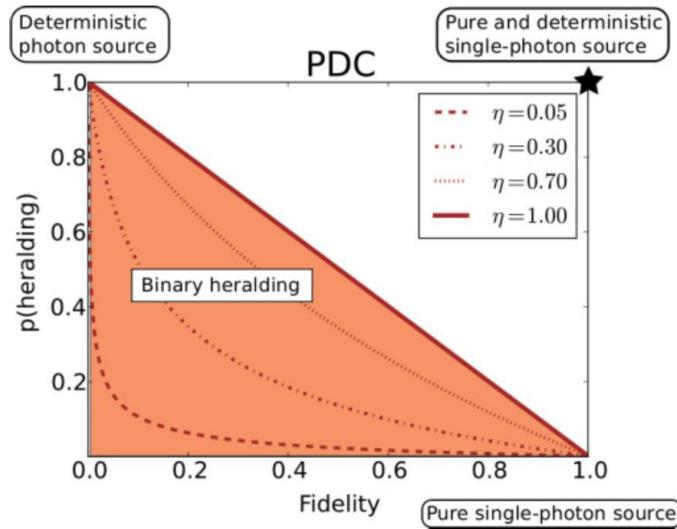


FIGURE 2.27: Figure reproduced from [49]. Heralding probabilities and single-photon Fock-state fidelities ($1 - g^{(2)}$) using a single-mode PDC source in conjunction with a binary detector featuring various detection efficiencies η .

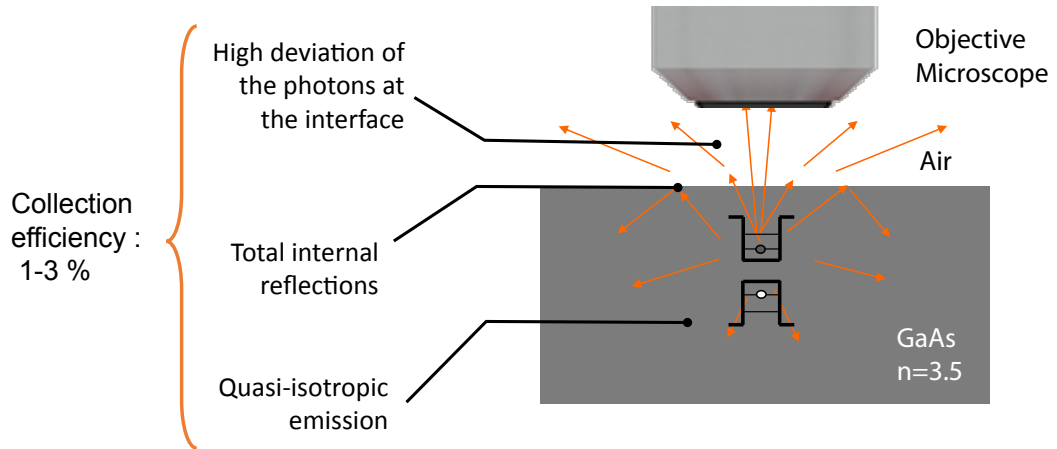


FIGURE 2.28: Schematics of the collection of emitted photons from a QD in bulk. Only a small fraction (few %) of the emission is collected.

2.5.1.2 Brightness of a single QD in a bulk

Contrary to PDC sources, the single-photon purity of a QD source does not degrade with the pump power. Moreover, the probability that a single QD emits a single photon converges to one at the saturation as it was shown previously:

$$p(n=1) \xrightarrow{P \rightarrow P_{\text{sat}}} 1 \quad (2.74)$$

Yet, without any modification of its electromagnetic environment, a QD emits in all the directions inside a semiconductor material presenting a high optical index (equal to 3.5 for GaAs). It can be shown that the fraction of emission exiting the sample in the upper half space is:

$$\eta_{coll} \rightarrow \frac{1}{4n^2} \approx 2\% \quad (2.75)$$

Without any technique to increase the collection efficiency, the probability of collecting a photon emitted by a QD in bulk is extremely low, and as such, does not bring much improvement as compared to PDC sources.

2.5.1.3 Brightness of a single QD in a micropillar

In the case of a semiconductor QD in a micropillar, the brightness of the single-photon source is proportional to the fraction of photons emitted in the cavity mode. Since the QD can still emit in the other electromagnetic modes with a decay rate that is similar to the one observed in bulk as shown in [33], the total emission rate of the QD is:

$$\Gamma_{tot} = \Gamma_{CM} + \Gamma \quad (2.76)$$

The fraction of photons emitted in the cavity mode is then given by the ratio β :

$$\beta = \frac{\Gamma_{CM}}{\Gamma_{tot}} = \frac{F_P}{F_P + 1} \quad (2.77)$$

This fraction of photons emitted in the cavity mode becomes rapidly predominant when F_P increases. For instance, if the QD decay rate is accelerated by a factor 5, the QD emits more than 80% of photons in the mode. Combined to an efficient extraction of the photons from the cavity, this device can be a bright source. Indeed the brightness of the source is then given by:

$$\text{Brightness} = p_x \cdot \beta \cdot \eta \quad (2.78)$$

where p_x is the occupation factor of the QD state and η the probability that one photon emitted in the cavity mode is effectively released by the top mirror of the micropillar and collected by the first lens. Here, because the fundamental mode of a micropillar is highly directional:

$$\eta = \frac{\kappa_{top}}{\kappa_{top} + \kappa_{bottom} + \kappa_{loss}} \quad (2.79)$$

where the coefficients κ_{top} , κ_{bottom} and κ_{loss} correspond respectively to the cavity damping rates through the top mirror, the bottom mirror and the wall losses of the pillar as depicted by fig.2.29 **a**. The probabilities p_x and η are respectively inherent to the QD

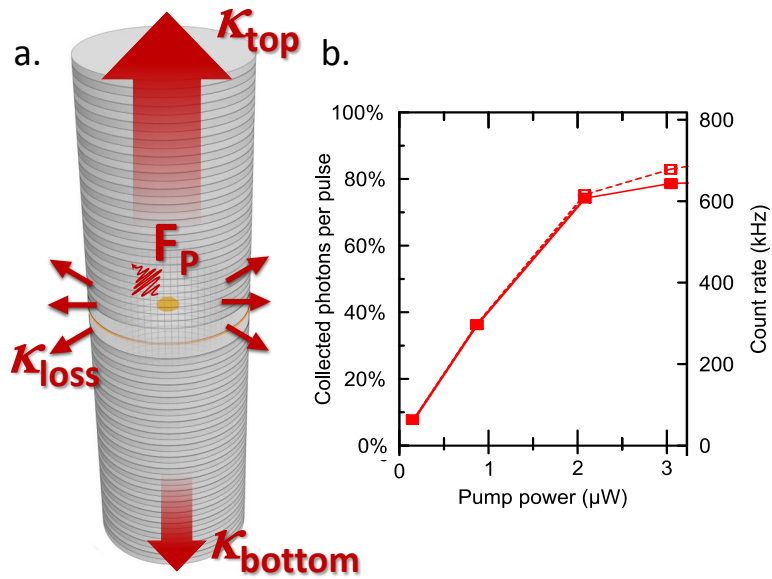


FIGURE 2.29: **a.** Schematics of the extraction of the photons from a pillar cavity. κ_1 (κ_2) corresponds to the cavity damping associated to the top (bottom) mirror of the micropillar while κ_{loss} corresponds to the leaking rates on the walls of the micropillar. **b.** Figure reproduced from [47]. Right (Left) axis: Detected count rate (Measured brightness of a micropillar) as a function of the pump power in pulsed regime. Empty symbols and dashed lines correspond to raw data while full symbols and solid line correspond to multiphoton corrected data.

and to the cavity, while $\beta = \frac{F_P}{F_P+1}$ results from the coupling of the dot with the optical mode of the cavity.

2.5.2 Recent progresses in the extraction of photons emitted by a QD

Due to the excellent coupling with external optics, most of the brightest single-photon sources have been made in micropillar structures.

A brightness of 44% was reported in 2001 by Moreau et al. at the LPN [86]. A few years later, Heindel and coworkers used micropillars electrically connected and measured an extraction efficiency equal to $34 \pm 7\%$ [130].

At the same time, at the LPN, Dousse et al. developed a photonic molecule made of connected pillars. This novel structure allowed to extract very efficiently photons emitted by two QD states: the exciton X and the biexciton XX . They demonstrated a brightness of 30% for both the biexciton and the exciton energies. The whole formed the brightest source of polarization-entangled photons to date [46].

With a QD randomly located in a photonic nanowire as described in 2.3.2.2, Claudon et al. showed a brightness of $72 \pm 9\%$ by collecting the signal within a numerical aperture (NA) of 0.75 [32].

Later at the LPN, O. Gazzano and his coworkers demonstrated a high brightness of 0.79 ± 0.08 in a NA of 0.4 with a QD coupled deterministically to the optical cavity of a

micropillar [31, 45].

In this work, we show that this brightness range has now been measured reproductively using different cavity structures and designs.

Chapter 3

Purity And Indistinguishability of Devices Based on Adiabatic Cavities

In recent years, many important steps in the development of QD based quantum photonic networks have been demonstrated: the fabrication of ultrabright sources of single photons [31, 32] or entangled photon pairs [46], the emission of highly indistinguishable photons [40, 107] as well as the interference between photons emitted from remote quantum dots [131, 132]. In this thesis, we worked on the optimization of the performance of bright single-photon sources. Our objective is to further increase the photon indistinguishability and purity while keeping a high brightness.

In this chapter, we study the purity as well as the indistinguishability of single photons emitted by a first generation of micropillar QD devices where we implemented a high Purcell effect. In a first part, I recall the results demonstrated before my arrival in the group: in 2012 a micropillar based bright source of single and indistinguishable photons was demonstrated by O. Gazzano and his coworkers [31]. Prior to this work, indistinguishability of photons [36, 38, 39, 106] and high brightness [30, 32, 46] had never been combined. Because it was the first demonstration of a bright source of single and indistinguishable photons, this work got the attention of the quantum optics community. Such a device was used to make an entangling quantum logic gate at the LPN in collaboration with the group of Pr. Andrew White from University of Queensland (Australia) [47] and a LPN QD source is now being studied by M. de Almeida and J. Loredó in A. White's laboratory.

At the beginning of my PhD, we decided to optimize the micropillar design to increase the Purcell factor. Based on a study by Lermer et al. [133], we grew a cavity with an adiabatic gradient of the thickness in the Bragg mirrors in order to reduce the optical modal volume while maintaining a large Q factor. This sample is described in detail in

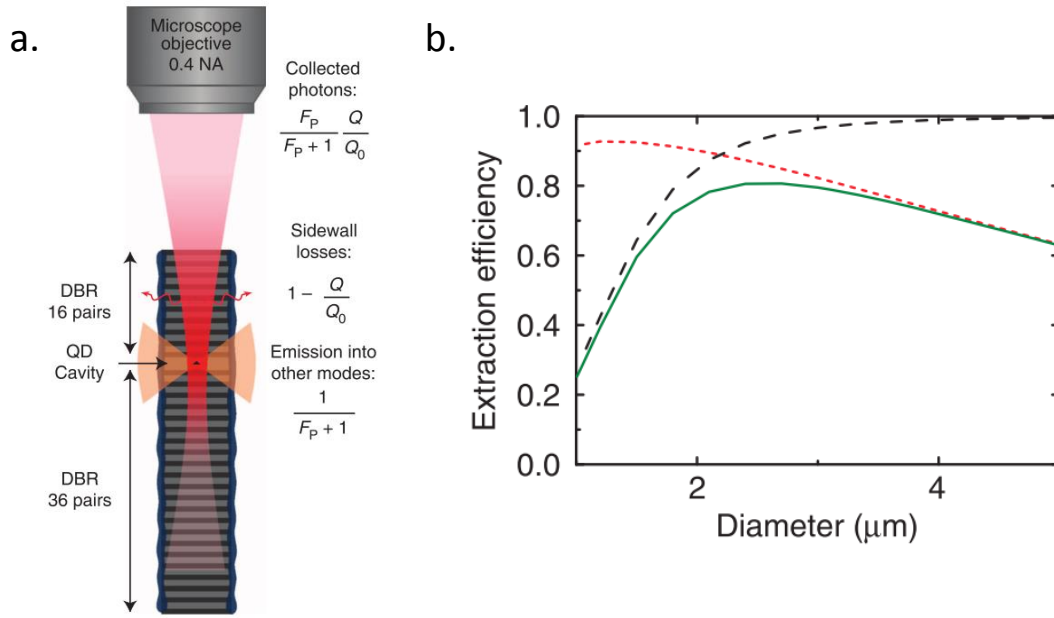


FIGURE 3.1: Figures reproduced from [31]. **a.** Schematics of the device. The QD (designed as a black triangle) is centered in the cavity. **b.** Fit of the measured extraction efficiency $\eta = Q/Q_0$ (black dashed line), calculated $F_P/(F_P + 1)$ (red dotted line) and the maximum brightness $Q/Q_0 \cdot F_P/(F_P + 1)$ (solid green line).

the second part of this chapter.

The experimental characterization of the sources is presented in the third part. We demonstrate the deterministic fabrication of a device operating in the high Purcell effective regime. The brightness of the source is shown to be as high as 0.74, similar to the state of the art in previous structures. In these new devices, we show that the excitation conditions must be chosen very carefully in order to emit single and indistinguishable photons while keeping a low multi-photon emission probability.

3.1 Latest Results in 2012 : Bright Indistinguishable Photons from a Micropillar

Before presenting the work carried out during my PhD, we summarize the results obtained by O. Gazzano and coworkers in 2012 on the bright emission of single and indistinguishable photons.

The sources used in 2011-2012 were fabricated by the *in situ* lithography technique described in section 2.4. The devices have an asymmetric cavity: to collect more photons from the top of the pillar, the top mirror is made of 16 Bragg pairs as compared to 36 pairs for the bottom mirror, as depicted by fig.3.1. This strong unbalance leads to less than 0.1% of the photons escape from the bottom of the pillar. Nevertheless, it does not prevent them from escaping through the rough sidewalls of the pillar. These losses

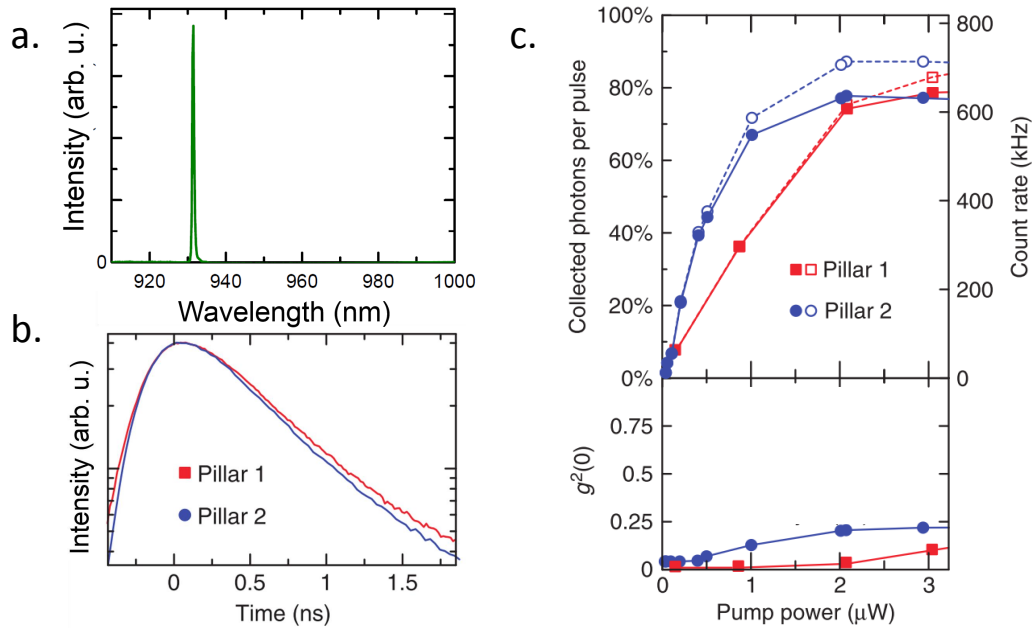


FIGURE 3.2: Figure reproduced from [31]. **a.** PL spectrum of pillar 2 at 10K. The QD resonance is spectrally matched with the cavity mode. **b.** Time-resolved PL intensity for the exciton lines in pillar 1 and 2. After deconvolution with the temporal response of the system, a lifetime around 265-270ps is deduced leading to Purcell factors around 3.9 ± 0.6 . **c.** Top: Raw (open symbols) and multi-photon corrected (full symbols) number of collected photons per laser pulse. Bottom: Measured $g^{(2)}(0)$ values as a function of the pump power.

are quantified by the leaking rate κ_{losses} . The ratio of the quality factor of the pillar Q with the one of the planar cavity Q_0 is thus given by:

$$\eta = \frac{Q}{Q_0} = \frac{\kappa_{\text{top}} + \kappa_{\text{bottom}}}{\kappa_{\text{top}} + \kappa_{\text{bottom}} + \kappa_{\text{losses}}} \approx \frac{\kappa_{\text{top}}}{\kappa_{\text{top}} + \kappa_{\text{losses}}} \text{ considering } \kappa_{\text{bottom}} \ll \kappa_{\text{top}} \quad (3.1)$$

As shown in the thesis of B. Gayral and of A. Dousse [85, 134], the quality factor Q of micropillar with a λ -cavity decreases when its diameter is lower than a critical diameter given by the etching conditions, due to the losses on the sidewalls of the micropillar. With the sample O. Gazzano studied, the critical diameter is typically about $2\mu\text{m}$. O. Gazzano worked with a structure exhibiting a Q -factor around $Q_0 \approx 3000$. The pillar sidewalls losses were estimated to about 5% such that $Q/Q_0 \approx 0.95 \pm 0.05$ for diameters bigger than $2\mu\text{m}$. Figure 3.1b. shows the measured ratio Q/Q_0 (black dashed line), the estimated fraction of photons emitted by the QD in the cavity mode β (red dotted line) and the maximum achievable brightness (solid green line).

In the work reported by Gazzano et al. [31], five bright sources were studied. Figure 3.2a. shows the PL spectrum of one of the pillars at 10K close to saturation showing that all other emission lines marginally contribute to the signal. Figure 3.2b. shows the measured PL intensity as a function of time. It gives the decay time of the devices

(after deconvolution) as well as the Purcell factor. Purcell factors around 3.9 ± 0.6 are measured by comparing these decay times with the one of QDs in bulk. In 2012, O. Gazzano et al. studied devices operating with a Purcell factor around 3-4 leading to a fraction of photons emitted in the fundamental optical mode of the pillar of around 0.6-0.8. Furthermore, the fraction of photons in the cavity emitted through the top mirror was equal to 0.95 ± 0.05 . The exciton occupancy probability p_x was close to 1 since the QD had been chosen to exhibit only one emission line during the *in situ* lithography. Figure 3.2c. shows the brightness reported in [31]. To measure the number of collected photons per pulse, a prerequisite is the precise measurement of the optical losses between the first collecting lens and the detector (including the detection efficiency). For this data set, the overall detection efficiency was about 0.0097 ± 0.001 . The setup efficiency leads to the extraction of the brightness as the probability that one laser pulse results in the collection of a single photon into the first lens. This probability is corrected by the multi-photon emission given by the $g^{(2)}(0)$ as shown at the bottom panel of fig.3.2c. The $g^{(2)}(0)$ slightly increases with the pump power reaching a maximal value lower than 0.25. The full symbols show the corrected brightness by the term $(1 - g^{(2)}(0))^{1/2}$. At saturation, a measured brightness of 0.78 ± 0.08 was obtained, a record value.

Figure 3.3a. summarizes the photon indistinguishability as a function of the excitation conditions. Green squares correspond to an above-band excitation in the wetting layer (at 860nm) while red triangles correspond to a quasi-resonant excitation (at 906nm). A better indistinguishability was observed under an above-band non resonant excitation but it is much more dependent on the pump power than for the quasi-resonant excitation for which the photon indistinguishability is approximately constant around 0.5.

By combining both excitations (with quasi resonant excitation plus 10% of the total intensity using an excitation at 860nm) the indistinguishability was shown to be improved as illustrated by the stars on figs.3.3 a. and d. Particularly a mean wave packet overlap of 0.92 ± 0.11 (corrected from $g^{(2)}$) was measured for a source brightness at 0.53 ± 0.05 collected photons per pulse.

This work showed first that, ultrabright sources of single photons can be fabricated using the control of the spontaneous emission from a QD in a pillar cavity ; and secondly that high indistinguishability can be obtained at high brightness. These results placed the QD-based sources among the most promising system to obtain new sources for optical quantum information processing.

At the beginning of my thesis, we worked on further optimizing the devices by increasing the Purcell effect. By increasing the Purcell effect, the fraction of emitted photons in the cavity mode β is increased leading to a brighter device. Furthermore, since the

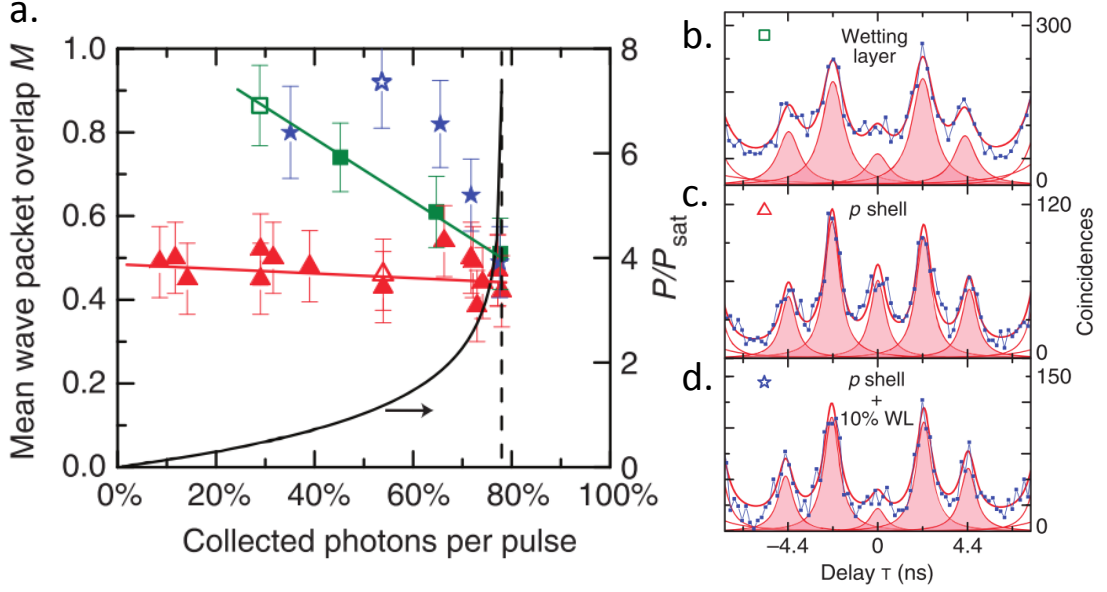


FIGURE 3.3: Figure reproduced from [31]. **a.** Measured mean wave packet overlap as a function of collected photons per pulse with three different excitation conditions. Green squares correspond to a non resonant pulsed excitation at 860nm, red triangles to a quasi-resonant pulsed excitation at 906nm and blue stars to a quasi-resonant pulsed excitation in addition to a slight continuous wave excitation at 860nm (contributing to 10% of the signal). **b.-d.** Measured correlation histograms between the two SPADs for the three excitation conditions indicated by the open symbols in **a.** The extracted mean wave packet overlap is $M=0.86$ for **b.**, $M=0.48$ for **c.** and $M=0.92$ for **d.** from the fitted Lorentzian peaks (shaded curves).

theoretical photon indistinguishability, without considering any spectral diffusion, is given by:

$$M = \frac{\gamma}{\gamma + \gamma^*} = \frac{T_2^*}{T_2^* + 2T_1} \quad (3.2)$$

An acceleration of the spontaneous emission by Purcell effect should also lead to an improved photon indistinguishability.

The Purcell factor is proportional to the pillars quality factor and inversely proportional to the effective volume of the optical mode ($F_P \propto Q/V_{\text{eff}}$), consequently we used a structure allowing to decrease the volume without degrading the pillar quality factor. This structure is described in the following section.

3.2 Fabrication of Devices Operating in the High Purcell Regime

As shown in [85, 134], the quality factor Q of a standard micropillar structure¹ was degraded when the diameter was lower than $2\mu\text{m}$ for the typical etching conditions used

¹made of a λ cavity surrounded by two Bragg mirrors.

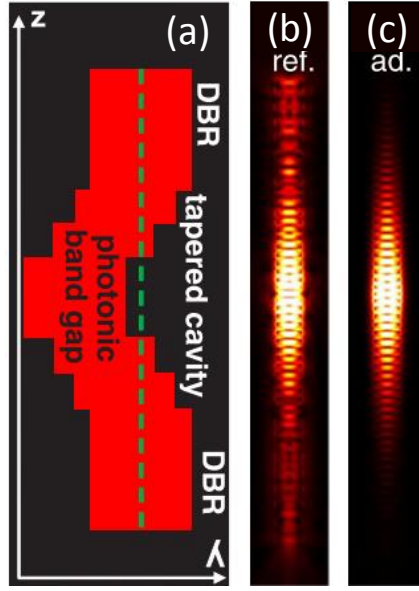


FIGURE 3.4: **a.** Figure reproduced from [133]. (a) Schematics of the tapered cavity surrounded by two Bragg mirrors (DBR). Calculated electric field amplitude profiles in a standard micropillar ($d = 750\text{nm}$) with a standard cavity design (b) and with an adiabatic cavity design (c).

in 2012 at the LPN for a planar Q -factor of 3000. The electromagnetic field is scattered by the sidewall roughness, increasing the losses. As a result, the Purcell factor, being proportional to the Q factor over the effective volume of the mode ($F_P \propto Q/V_{\text{eff}}$), was maximal for a pillar diameter around $1\mu\text{m}$. However, when the diameter is smaller than $2\mu\text{m}$, the quality factor Q gets lowered because of the losses on the sidewall leading to a degradation of the output coupling efficiency η . An optimal compromise for the extraction efficiency $\beta\eta$ was reached for a diameter of $2.5\mu\text{m}$.

3.2.1 Adiabatic Cavity Design

To get a better confinement of the optical mode without any scattering of the electric field on the sidewalls, Lermer et al. proposed in 2012 a structure based on an adiabatic variation of the Bragg mirror layer thickness to form a cavity [133]. Instead of using a λ cavity surrounded by two Bragg mirrors, their design features a tapered cavity in which the fundamental Bloch mode is subject to an adiabatic transition to match the Bragg mirror Bloch mode. They showed both experimentally and theoretically that the 3D mode confinement is improved with respect to λ -cavities and that the pillar quality factor Q is kept unspoiled for smaller diameters. Figure 3.4 shows the typical design of a tapered cavity (**a.**) and the comparison between the calculated profiles of electric fields in a classical design (**b.**) and in an adiabatic design (**c.**) considering a fixed pillar roughness. As a result, it clearly shows that the mode is better confined in the second

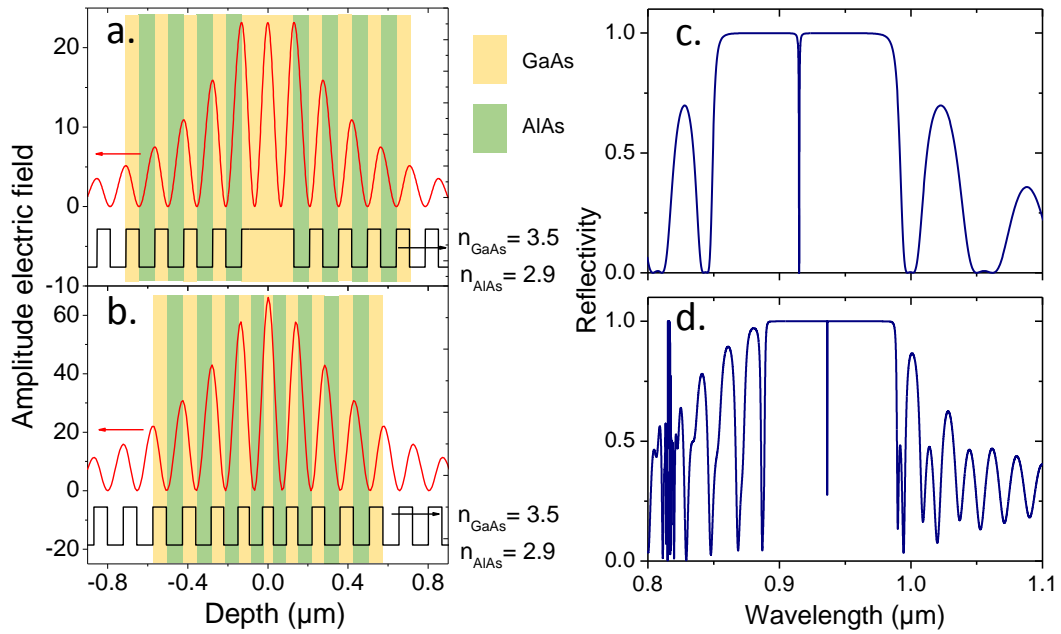


FIGURE 3.5: **a-b.** Red solid line: Calculated electric field distribution in a standard planar cavity (**a.**) and in an adiabatic planar cavity (**b.**); Black solid line: Evolution of the optical index in the structure as a function of the depth in the planar cavity. **c-d.** Calculated reflected spectra by the standard planar cavity (**c.**) and by the adiabatic planar cavity (**d.**) described in **a-b.**

design and is less prone to scatter on the roughness of the pillar walls. This technique allows on to get smaller modal volumes in a cavity with a high quality factor, paving the way to a strong increase of the Purcell factor F_P .

3.2.2 Design and Characterization of the Planar Structure

We designed and grew a planar cavity at the LPN using a tapered cavity between two Bragg mirrors. The structure was calculated by Justin Demory and Loic Lanco. The red solid line in fig.3.5 represents the calculated electric field intensity distribution as function of the relative depth with the center of the cavity (left axis) in a standard structure (**a.**) and in the adiabatic structure (**b.**). The optical index distribution is shown in the black solid lines (right axis). A progressive change of the layer thickness leads to a confinement of the electric field in the center of the structure. The position of the InAs QD layer is positioned at the center of the cavity (at 0nm) where the electric field profile is maximal. Figures 3.5c. and d. show the calculated reflectivity spectra of the planar structure with both designs. The resonance of the adiabatic cavity is calculated to be around 945nm. Compared to a standard cavity (**c.**), the stop-band (defined as the region where the reflectivity is close to 1) is smaller in an adiabatic cavity than in a

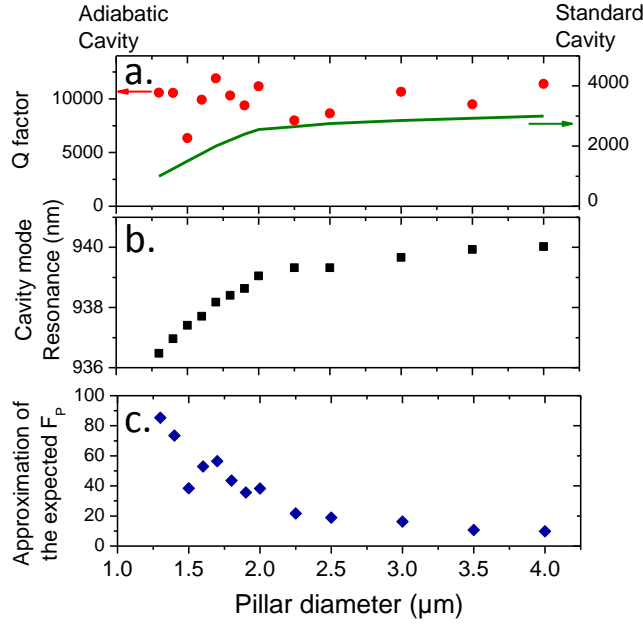


FIGURE 3.6: Measured characteristics of micropillars made of an adiabatic structure as a function of the pillar diameters: **a.** Red points: Q -factor of pillars embedding an adiabatic cavity ; Green line: Q -factor of pillars embedding a standard cavity from [31] **b.** Cavity mode wavelength. **c.** Expected Purcell factor F_P . **d.** Figure from [85]. Evolution of the Q -factor as function of micropillar diameter containing a standard cavity.

standard one.

In order to measure the Q -factor of this new structure, pillars of various diameters were etched after an electronic lithography on a planar cavity containing a high density of QDs. This allowed us to measure the PL of QDs filtered by the mode of the pillars. We measured the quality factors as well as the fundamental mode energy of the pillars as a function of the diameter of the pillars. Figure 3.6a. shows the evolution of the quality factor as a function of the pillar's diameter: red points correspond to the measured Q -factor of the pillar containing an adiabatic cavity, green line shows the measured Q -factor in standard pillars (from [31]). In the case of the adiabatic cavity, the Q -factor does not decrease when the pillar diameter decreases down to $1.5\mu\text{m}$. Fluctuations of $\pm 20\%$ are still observed. Figure 3.6b. shows the shift of the energy of the fundamental mode of the micropillar as a function of the diameter. As with standard structures, when the diameter decreases, the fundamental mode blueshifts by several nm. Figure 3.6c. shows the expected Purcell factors from the measured Q -factor. We approximated of the effective mode volume by [134]:

$$V_{\text{eff}} = L_{\text{eff}} \cdot S_{\text{eff}} = \frac{7\lambda}{4n_{\text{GaAs}}} \cdot \frac{\pi r^2}{3.5} = \frac{\lambda \pi r^2}{2n_{\text{GaAs}}} \quad (3.3)$$

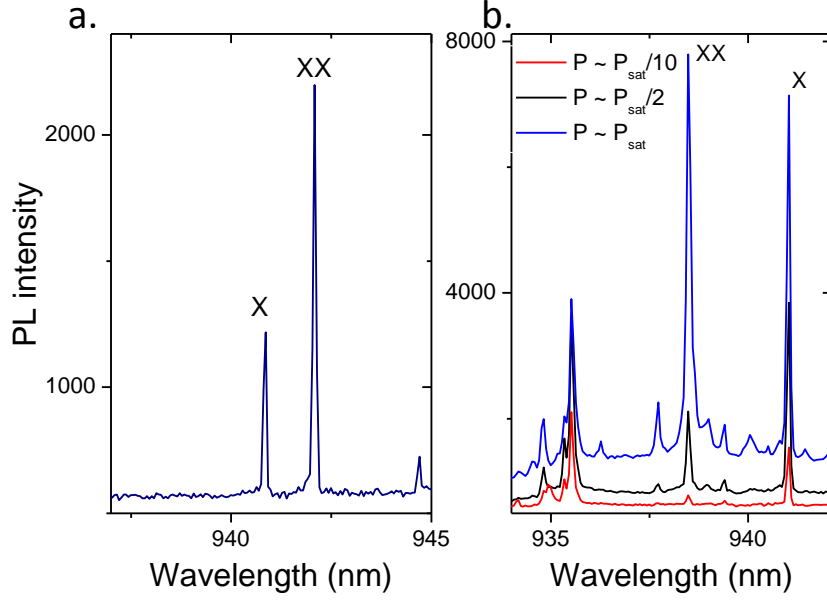


FIGURE 3.7: Measured PL spectra from QDs in planar cavity during the *in situ* lithography. As shown by **b.**, the emission lines are identified by varying the excitation power. The excitation is CW and above-band (850nm).

with r the radius of the micropillar. When the cavity volume decreases, F_P highly increases since the Q -factor is not degraded due to the adiabatic design.

By conserving a Q -factor close to the planar cavity quality factor Q_0 ($\sim 10^4$), such design should lead to a good output coupling $\eta = Q/Q_0$ combined to a high Purcell factor, a very promising situation for the fabrication of ultrabright single photon sources.

3.2.3 Fabrication of QD-Adiabatic Pillar Devices

I used a planar adiabatic cavity with a low density of InAs QDs and performed an *in situ* lithography. Figure 3.7 shows measured spectra from different QDs in the planar cavity. Figure 3.7**b.** shows three spectra from the same QD with different excitation powers. The exciton emission line (X) and the biexciton emission lines (XX) are identified using their respective intensity evolution with the excitation power and observing the FSS of their emission lines.

Two *in situ* lithography steps were performed on this sample, exposing approximately 25 disks for each. After the first lithography, I developed the resist and lifted off the deposited Nickel as shown by fig.3.8**a.** Before the etching, I did another *in situ* lithography on another region of the sample. The two lithographies were done to have two samples with similar properties. Figure 3.8**b.** shows a microscope image of the second part after the second Ni lift off. Then, the sample is etched to define the pillars and cleaved in two pieces.

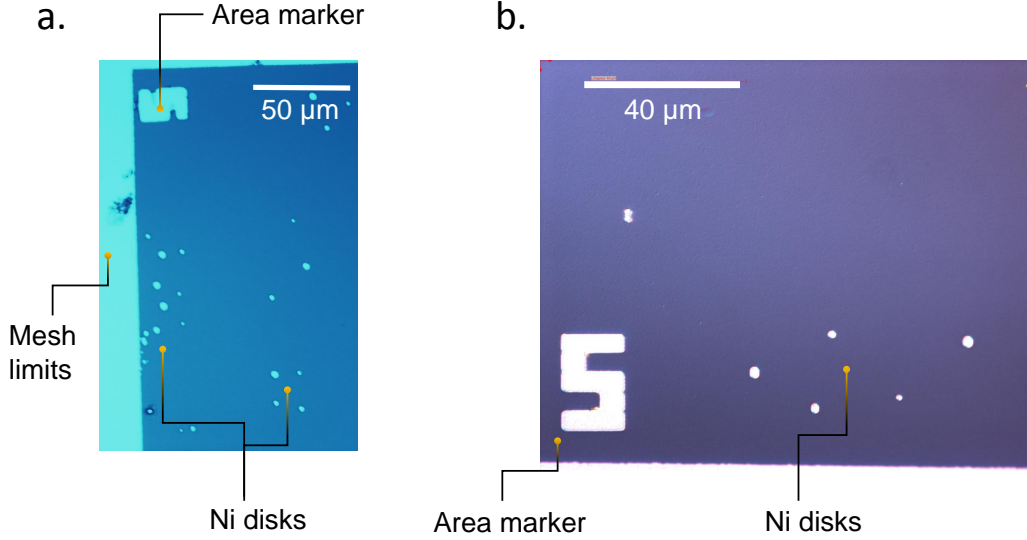


FIGURE 3.8: Optical microscope images of the first part (a.) and of the second part (b.) of the adiabatic cavity after the lift-off step after the *in situ* lithography. White area is nickel (Ni) region protecting the SiN_4 layer during the mask transfer as described in the chapter 2.

Both samples were placed in separated cryostats at 4K where the single photon sources have been intensively studied. These devices were used for studying quantum interferences of single photons emitted by remote sources, as described in chapter 6.

3.3 Experimental Characterization of a QD Coupled to an Adiabatic Pillar Cavity

In this part, we describe the characterization techniques used to study the devices. Because the temperature impacts on many parameters like the detuning between the QD transition with the cavity mode and the phonon emission processes, we characterized our sources as a function of temperature. Finally, the brightness of a source made with an adiabatic design is discussed.

3.3.1 Microphotoluminescence Setup and Thermal Control of the Spectral Detuning δ_{X-CM}

The samples are usually kept in a cryostat to preserve them in an inert atmosphere and avoid oxydation. The experiments are performed at low temperature (4-50K). At the beginning of this thesis, a helium-flow cryostat was used. Everyday, samples were cooled down and warmed up. To avoid these numerous cooling cycles, the group invested in a closed-cycle cryostat that is able to keep the samples at low temperature during several

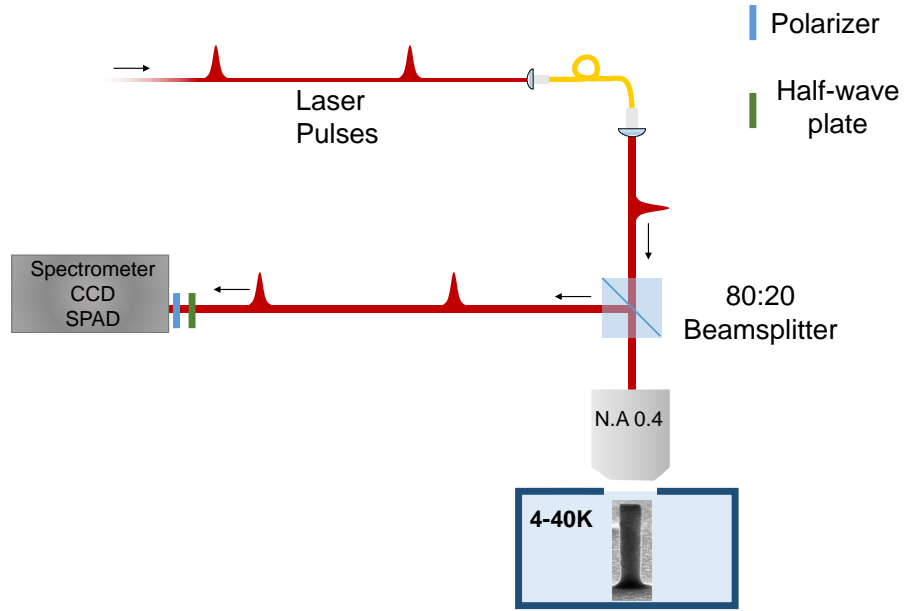


FIGURE 3.9: Schematic of the optical setup used to characterize the sources

weeks.

The experimental setup is depicted in fig.3.9. A tunable mode-locked laser is coupled to a single-mode fiber (SMF) and is used to excite the sources from the top. The PL is collected via the same objective (with a numerical aperture NA equal to 0.4) and sent to an imaging spectrometer with a 1-meter focal length. The spectra are imaged on a nitrogen-cooled CCD² with a spectral resolution of 12.8pm (18 μ eV). Photon correlations are measured by switching the spectrometers's output to single-photon avalanche diodes (SPADs).

For most of the PL measurements, the QD is excited non resonantly, at an above-band energy. Under a nonresonant excitation, one bright line and several other lines are visible in the PL spectrum as shown by fig.3.10a. The bright narrow line (X) is attributed to the exciton emission line since its intensity presents a linear dependence with the pump power. Broad peaks correspond to the emission of the phonon sideband (PSB) through the cavity mode. The temperature of the sample was slightly decreased to detune the QD from the cavity mode at 1.310eV and to measure the fine structure splitting of the exciton. In resonance with the mode, it is difficult to distinguish the splitting of the excitonic fine structure with the splitting of the optical modes. The fine structure splitting of the exciton is measured by rotating the half-wave plate in front of the spectrometer. Figure 3.10b. shows three measured spectra for different positions of the half-wave plate. The change position of the exciton emission line evidences the presence of a very large

²Charge Coupled Device

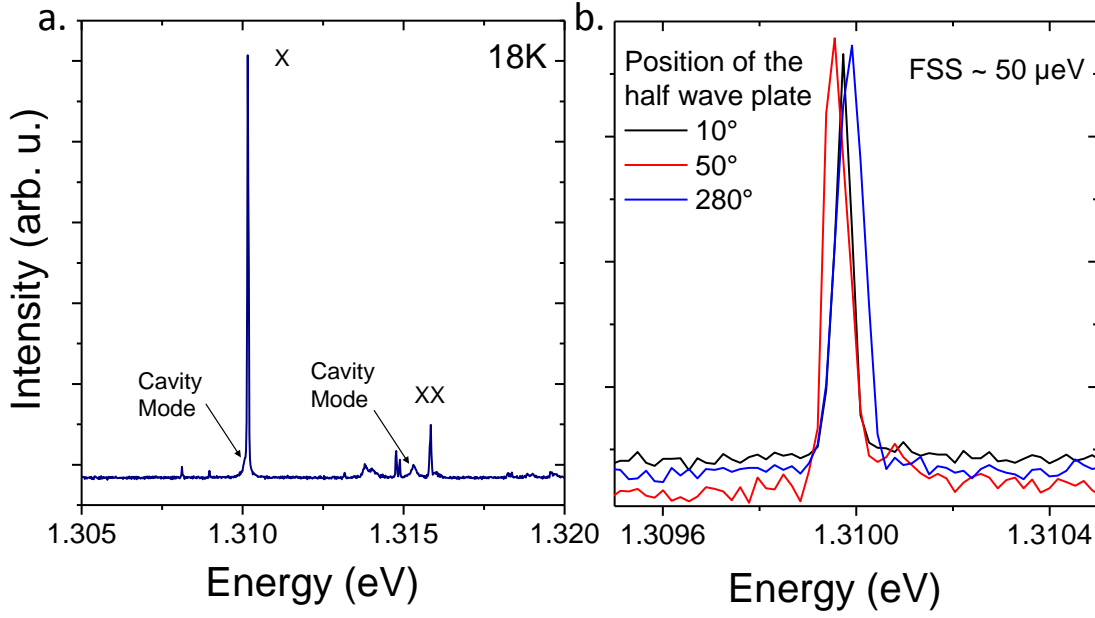


FIGURE 3.10: **a.** Measured PL spectrum of a single QD in a pillar under an above-band excitation at 18K. The brightest emission line corresponds to the exciton (X) transition. The biexciton emission line (XX) is located to a higher energy by about 6meV (corresponding to the Coulomb interactions between two excitons). **b.** Raw measured spectra of the X transition under a quasi-resonant excitation for different half-wave plate position. The dependence of the emission line shows the energy splitting of the exciton line. The observed fine-structure splitting value is around $50\mu\text{eV}$.

fine structure splitting of $50\mu\text{eV}$ for this QD. Moreover, the biexciton (XX) emission line can easily be recognized by its quadratic dependence with the excitation power and equal FSS. The other lines are attributed to trions and most of them disappear under a quasi-resonant excitation.

3.3.2 Influence of Temperature on PL Spectra

In order to measure the impact of temperature, the sample is continuously heated while recording its PL spectra under a non resonant excitation ($\lambda = 865\text{nm}$). Both the cavity mode line and the exciton line redshift but with a different temperature dependence, the exciton (X) emission moving faster with the temperature. The source are then studied as a function of the spectral exciton-mode detuning noted $\delta_{\text{X-CM}} = E_{\text{X}} - E_{\text{CM}}$.

Figure 3.11a. shows the measured PL intensity as a function of temperature and wavelength under a non resonant excitation ($\lambda=850\text{nm}$). The resonance is reached around 23K. Figure 3.11b. shows the energy of the exciton transition (black squares) as well as the energy of the cavity fundamental mode (red points) as a function of the temperature. Close to the resonance, a spectral pulling of the cavity line as described in [135] is observed.

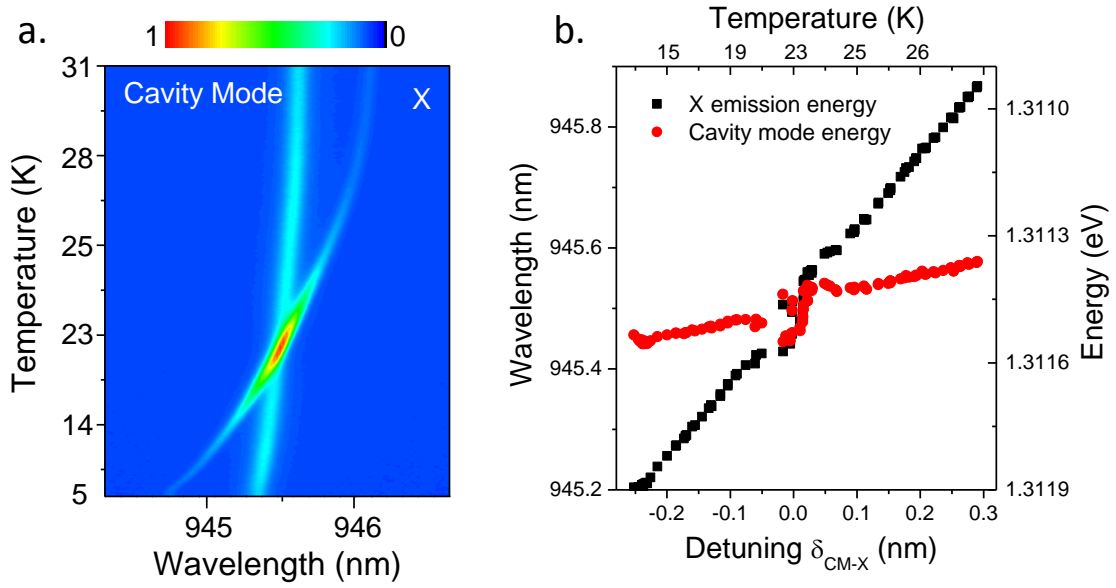


FIGURE 3.11: **a.** Normalized emission intensity of the device as a function of the wavelength (x-axis) and of the sample temperature (y-axis). **b.** Spectral positions of the exciton (X) emission line and of the cavity mode energy (CM) as a function of the spectral detuning $\delta_{\text{X-CM}}$.

At 23K, the spontaneous emission is accelerated by the Purcell effect. Most of the photons emitted by the QD at the exciton energy are emitted in the cavity mode, hence the increase of collected photons as shown by fig.3.11a.

3.3.3 Evolution of the Decay Times With the Spectral Detuning

In this section, we investigate the decay rate of the exciton emission line as a function of the detuning $\delta_{\text{X-CM}}$.

The QD is optically excited with 3 ps pulses from a mode-locked Ti-Sapphire laser through a microscope objective. The QD PL is collected and sent to a SPAD after a spectral filtering through a spectrometer. *Picoquant* photon counters are used to measure the delay between the excitation and the photon detection with a temporal resolution of approximately 120ps.

Figure 3.12a. shows the time-resolved PL of the exciton emission line for two different detunings. When the exciton transition matches the energy of the cavity mode (red line), the spontaneous emission is accelerated with respect to the situation where the X line is detuned by 0.6 meV (black line). Figure 3.12 b. shows the measured decay rate enhancement γ as a function of $\delta_{\text{X-CM}}$. As expected, γ reaches its maximum for $\delta_{\text{X-CM}} = 0$, with a strong enhancement of the decay rate by a factor 10 ± 2 . With such a strong

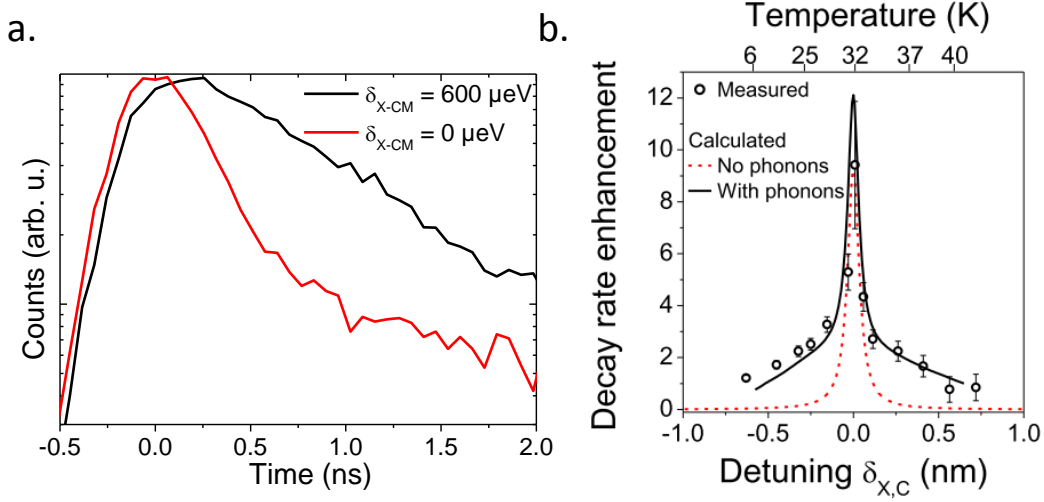


FIGURE 3.12: **a.** Time resolved PL of the exciton emission line for two detunings : red line corresponds to spectral matching of the X line in the cavity ($\delta_{X-CM} = 0\text{meV}$ while the black line corresponds to a detuning equal to $\delta_{X-CM} = 0.6\text{meV}$. **(b.)** Evolution of the decay rate enhancement as a function of the detuning δ_{X-CM} .

Purcell factor, the fraction of photons that are emitted in the mode of the cavity reaches $\beta = 0.91 \pm 0.02$. These results show that we achieved a considerable increase of the Purcell factor with respect to the sources fabricated in 2011. Nevertheless, considering the Q -factor of the pillar (~ 12000) as well as its diameter ($2\mu\text{m}$), a higher enhancement of the Purcell factor is expected as shown by fig.3.6. In collaboration with A. Auffèves, T. Grange and G. Hornecker, we explained this discrepancy by taking into account the coupling of the QD with phonons. For an ideal two-level system, the acceleration of spontaneous emission reads:

$$F_P(\delta_{X-CM}) = F_P \frac{\gamma_c^2}{\gamma_c^2 + 4\delta_{X-CM}^2} \quad (3.4)$$

where γ_c is the cavity linewidth. The red dashed line of fig.3.12**b.** shows this theoretical enhancement of spontaneous emission for $\gamma_c = 80\text{pm}$ and $F_P = 12$. We observe that the measured decay enhancement does not follow a simple Lorentzian dependence as we could have expected by considering that the coupling with the cavity is ruled by the Zero Phonon Line (ZPL) emission only. By considering the influence of the phonon sideband (PSB), we could derive a decay enhancement which reproduces well the experimental observation (black line). The good agreement between the black line and our measurement evidences that the decay rate enhancement is modified by the coupling with phonons. Figure 3.13 shows the calculated emission in the cavity induced by the

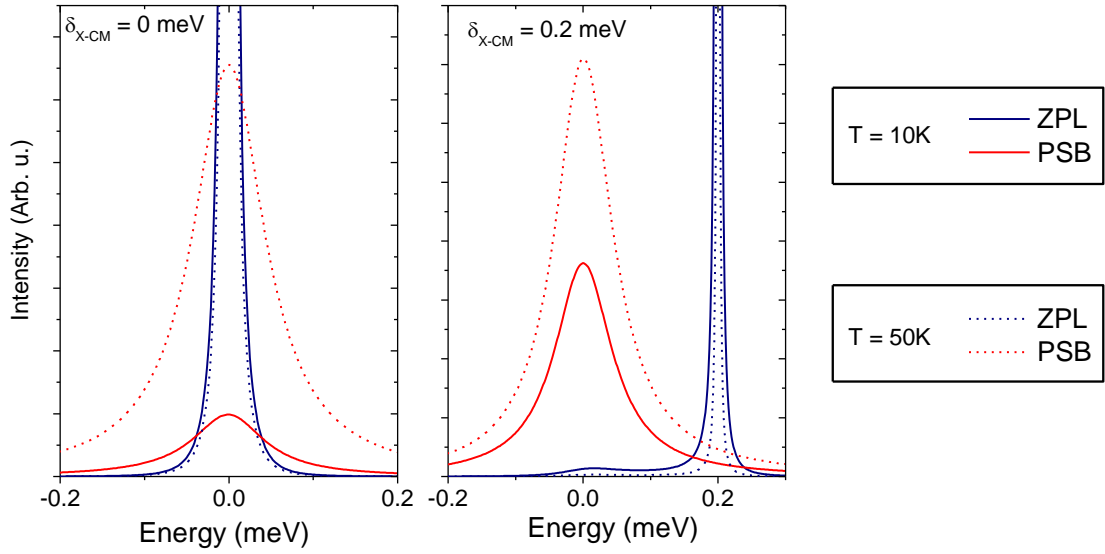


FIGURE 3.13: Calculated emission in the cavity mode through the zero-phonon line (ZPL) channel (blue) and through the phonon-sideband (PSB) (red) for two different detunings (left, $\delta_{X-CM} = 0\text{meV}$ and right, $\delta_{X-CM} = 0.2\text{meV}$) at 10K and at 50K.

ZPL (in blue) and by the PSB (in red) at 10K (solid lines) and at 50K (dashed lines) for two different detunings δ_{X-CM} . More details on this theory can be found in [136].

Depending on the sample temperature and on the exciton-cavity mode detuning, the fraction of photons emitted through the PSB evolves. Figure 3.13 shows the theoretical emission of the ZPL and of the PSB filtered by the cavity in four configurations: at resonance (left panel) with the cavity at 10K (solid lines) and at 50K (dotted lines) and when the exciton is detuned from the cavity (right panel). They show that between 10K and 50K, the fraction of photons emitted in the PSB is largely increased. Since a fraction of photons emitted through the PSB and funnelled out into the cavity is not negligible, we define an effective Purcell factor taking into account the emission through the PSB as well as through the ZPL:

$$F_P^{\text{eff}}(\delta_{X-CM}) = \frac{\gamma^{\text{ZPL}} + \gamma^{\text{PSB}}}{\gamma_0} \quad (3.5)$$

where γ^{ZPL} and γ^{PSB} correspond to the enhanced decay rate into the cavity mode for the emission in the ZPL and in the PSB respectively while γ_0 correspond to the decay rate into the other optical modes of the electromagnetic field, which is close to the emission decay rate in bulk material.

Figure 3.14 shows the theoretical evolution of F_P^{eff} as a function of temperature for two different detunings δ_{X-CM} . Figure 3.14a. corresponds to the situation where the ZPL is

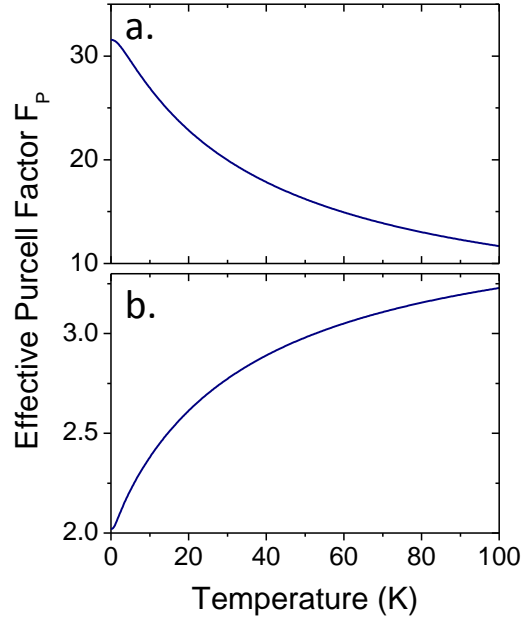


FIGURE 3.14: Theoretical evolution of the effective Purcell factor as a function of temperature when the QD is on resonance (**a.**) or detuned by 0.2 meV (**b.**) with the cavity.

on resonance with the cavity mode ($\delta_{\text{X-CM}} = 0$ meV) while fig.3.14**b.** to the case where the ZPL is slightly detuned ($\delta_{\text{X-CM}} = 0.2$ meV). At $\delta = 0$, when increasing the temperature, the fraction of emission within the ZPL decreases resulting in a decreasing effective Purcell factor. On contrary, in the case of $\delta = 0.2$ meV (**b.**), the effective Purcell factor slightly increases with temperature due to the increase of the coupling of the PSB with the cavity mode.

3.3.4 Brightness of a High Purcell Device

The device that we fabricated exhibits a strong Purcell effect and a potential to be a very bright source of single photons. We describe the measurement of the brightness of one of the best devices.

The brightness is studied as a function of the pump power when the exciton transition is in resonance with the cavity mode ($\delta_{\text{X-CM}} = 0$ meV). The QD is excited non resonantly by laser pulses. The PL is collected and filtered by a spectrometer before a SPAD delivers a count rate. By using a HBT setup, the single-photon purity is also measured under the same excitation conditions.

The transmissions of the optical components are given in table 3.1.

The detection efficiency includes the transmission of the spectrometer as well as the SPAD detection efficiency. With this configuration, the overall setup detection efficiency

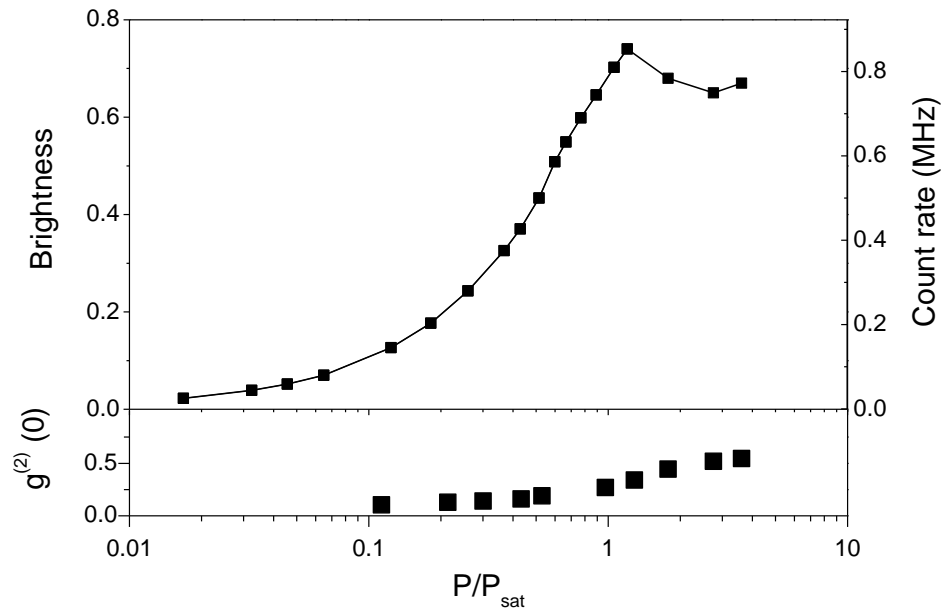


FIGURE 3.15: Top: Measured brightness as a function of the pump power. Bottom: Single photon purity

Component	Transmission/Efficiency	Error bar
Detection	8.8 %	± 0.5 %
HBT NPBS	51 %	± 2 %
Cryostat window	98 %	± 1 %
Polarizer	90 %	± 2 %
Long pass filter	98 %	± 1 %
Half wave plate	98 %	± 1 %
Collection NPBS	40 %	± 2 %
Lens	95 %	± 1 %
Overall setup	1.44%	± 0.1 %

TABLE 3.1: Transmission and overall efficiency of all setup components.

is around 0.0144 ± 0.001 . Fig.3.15 shows the count rate as a function of the pump power. By comparing this rate with the laser repetition rate, we deduce the brightness of the source as the probability to collect a single photon per laser pulse. We correct also the count rate by the multiple photon correction term $\sqrt{1 - g^{(2)}(0)}$ assuming a poissonian noise [30]. At saturation, the measured brightness reaches 0.74 ± 0.07 collected photons per pulse. The brightness of the exciton line as defined in the chapter 2 reads:

$$\text{Brightness} = p_x \eta \frac{F_P}{F_P + 1} \quad (3.6)$$

where p_x are the probability that the QD is occupied by an exciton and η the extraction efficiency. Since the ratio $\beta = \frac{F_P}{F_P + 1}$ is equal to 0.91 ± 0.02 , the ratio $p_x \eta$ is estimated to be around 0.82 ± 0.09 according to fig.3.6. Since we measured different emission lines in

the spectrum it is reasonable to assume that $p_x \sim 0.8$.

These results show the fabrication of state-of-the-art bright single photon sources with an adiabatic cavity design. The adiabatic cavity structure provides a better light confinement in the micropillar and consequently a higher Purcell factor with respect to a λ -cavity.

In the rest of this chapter, we study the influence of the optical excitation on single-photon purity and indistinguishability.

3.4 Purity of a Single-Photon Source

Previous works showed that the single-photon purity is often degraded when a single QD is coupled with an optical microcavity inducing the acceleration of spontaneous emission [130, 137]. In this part, we discuss the mechanisms behind this purity degradation. Different explanations were proposed to describe this effect such as background emission in the cavity mode (cavity feeding effect) [138] or as recapture processes [139].

In the following, we show that the single-photon purity is not related to cavity feeding effects but rather to multiple capture of carriers under non resonant excitation. For this particular study, we used another source coming from the sample studied by O. Gazzano during his PhD. We compare the single-photon purity between a QD in a planar cavity with a QD which has been deterministically coupled to a micropillar structure. In this section, the planar cavity is a standard one: it is constituted of a λ -cavity surrounded by two Bragg mirrors. The planar cavity exhibits a Q -factor about $Q = 3000$. The pillar diameter is equal to $2.5\mu\text{m}$. We study the influence of Purcell effect and the excitation wavelength on the single-photon purity and present a model reproducing our observations considering multiple capture processes.

3.4.1 Temperature Tuning of the Purcell Effect

Figure 3.16a. shows the PL spectrum of the source at 27K when the exciton (X) emission line is detuned from the cavity mode energy. We distinguish the emission peak associated to the exciton transition (noted X) and a bump associated to the emission in the cavity. The signal coming from the cavity is due to the PSB emission in the cavity as shown previously. We fit the cavity line and the exciton line as a function of temperature with two Lorentzian peaks. Figure 3.16b. shows the deduced energy of the exciton emission line (black squares) and the energy of the cavity (red circles) as a function of the temperature (top axis) and of $\delta_{X\text{-CM}}$ (bottom axis). Figure 3.16c. shows the area of the fitted peak associated to the exciton line (black squares) and of the cavity mode

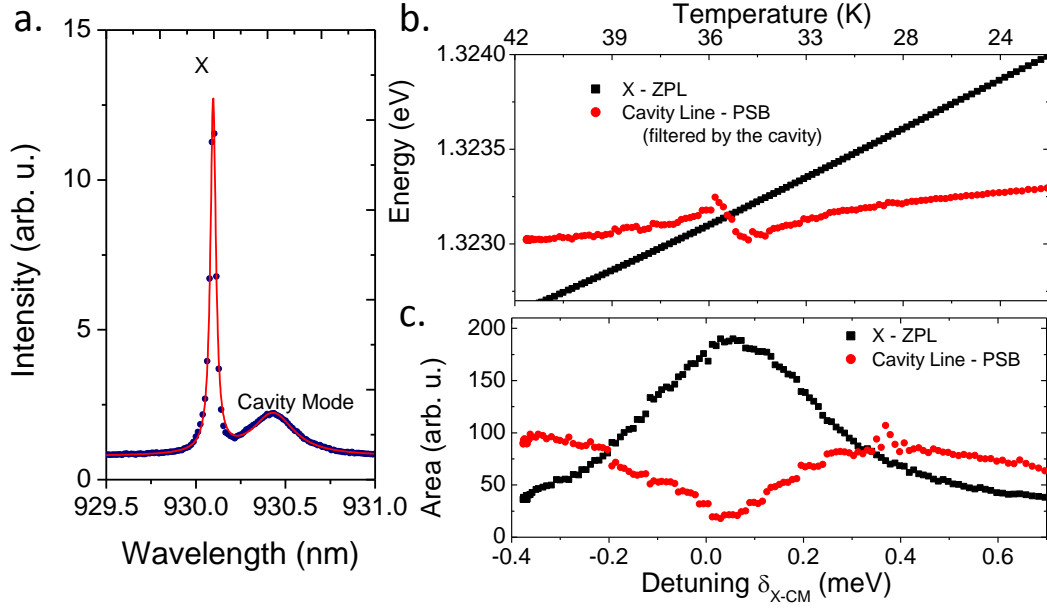


FIGURE 3.16: **a.** Points show the measured spectrum at 27K when the exciton line is detuned from the mode of the cavity. The red solid line is a fit with two Lorentzian peaks. **b.** Black squares (Red points) show the position of the exciton (X) peak (the cavity mode CM) as a function of the spectral detuning $\delta_{X-CM} = E_X - E_{CM}$. **c.** Black points (red points) show the area of the peak associated to the exciton line (cavity mode line) as a function of the detuning.

(red circles). The exciton ZPL intensity increases when the detuning decreases due to the improvement of the coupling in the cavity. On contrary, the cavity line (i.e. the PSB emission in the cavity) intensity is intense when the exciton transition is detuned from the cavity, evidencing the strong coupling with the phonons at these temperature [140]. We show in the annex A that this PSB enhanced emission can actually perform as a bright single photon source [136].

Figure 3.17a. shows the measured decay time of QD emission as a function of temperature. A small decrease of the QD exciton lifetime is observed at resonance. The red points also show the evolution of the radiative lifetime of a QD in a planar cavity (in a non-etched part of the same sample). For QDs in the planar cavity, no decrease of the QD exciton lifetime is observed. The Purcell factor given by the ratio between decay times in the planar cavity structure and in the micropillar:

$$F_p = \frac{\tau_{\text{pillar}}}{\tau_{\text{planar}}} - 1 \quad (3.7)$$

is plotted in fig.3.17b. In resonance, a maximum value of 1.2 is measured, which is lower than the expected Purcell factor in such a micropillar ($Q = 3000$ and a diameter equal to $2.5\mu\text{m}$). This discrepancy finds an explanation in the high coupling with the phonons

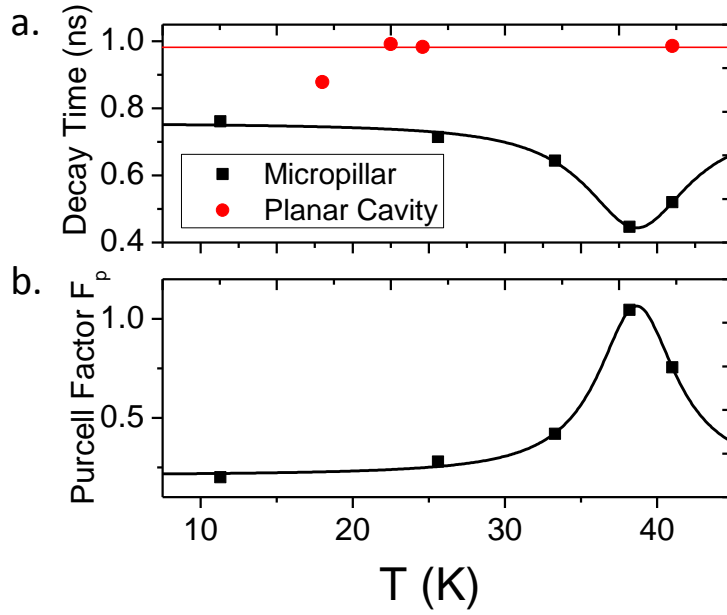


FIGURE 3.17: **a.** Evolution of the decay time of the exciton for the QD in a micropillar τ_{pillar} (black squares) and of a QD in a planar cavity τ_{planar} (red points) as a function of temperature. **b.** Evolution of the Purcell factor of the QD in micropillar as a function of temperature. This Purcell factor is calculated by comparing it with the decay time in planar cavity : $F_p = \frac{\tau_{\text{pillar}}}{\tau_{\text{planar}}} - 1$

at this temperature range.

3.4.2 Single-photon Purity as a function of Purcell Effect

We now study the single-photon purity of the QD emission at different temperatures. Under pulsed excitation, we measured the autocorrelation function for a non-resonant excitation or a quasi resonant excitation.

Measured autocorrelation histograms under non resonant excitation are shown in fig.3.18a. when the QD is detuned from the cavity ($\delta_{\text{X-CM}} = 0.87\text{meV}$) and in fig.3.18b. for $\delta_{\text{X-CM}} = 0$. A detuning of $\delta_{\text{X-CM}} = 0.87\text{meV}$ leads to a noisier experimental curve as well as broader peaks since the width of the peaks is related to the lower Purcell effect experienced by the QD. Interestingly, here the $g^{(2)}(0)$ (given by the central peak) does not increase with the increase of the pump power. On the contrary, on resonance with the cavity (fig.3.18 b.), the exciton line is much brighter and the autocorrelation histogram exhibits a better signal-to-noise ratio with narrower peaks. However, the $g^{(2)}(0)$ gets rapidly high when the power increases. Figure 3.18 c. shows the comparison between the multiple photon emission at resonance (black squares) and detuned from the cavity mode (red points) showing that the single-photon purity is largely degraded when the

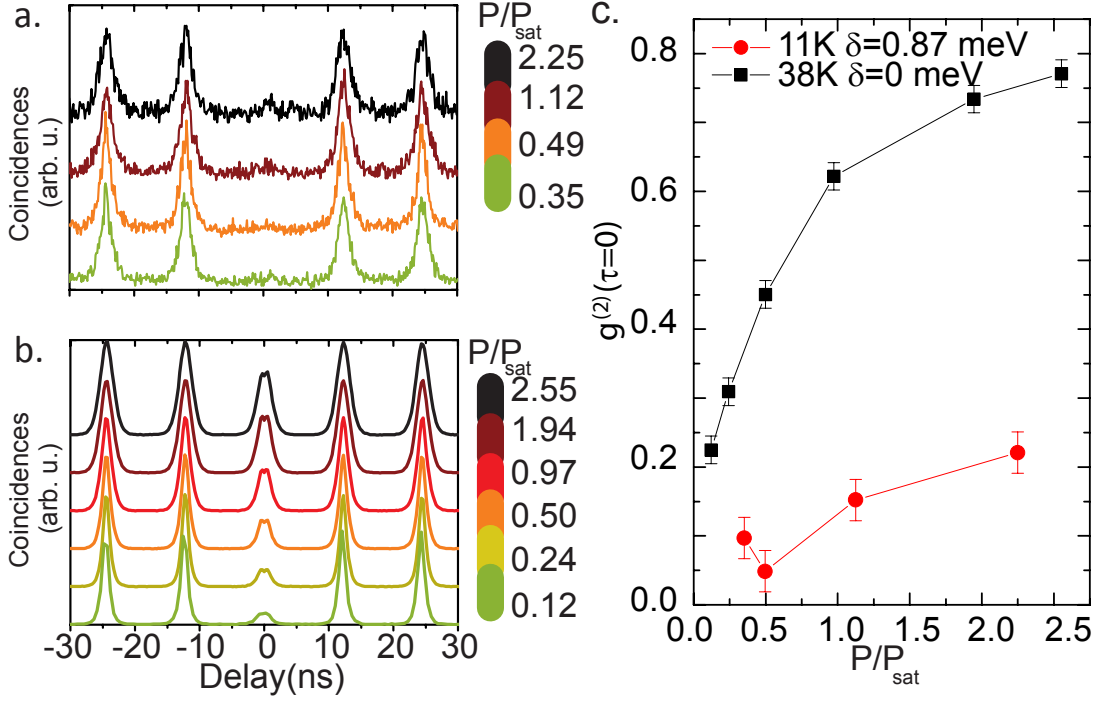


FIGURE 3.18: **a.** and **b.** Measured autocorrelation functions for various excitation powers for the QD in the pillar cavity at different detunings (different temperatures). The QD is excited under non resonant excitation. Curves are vertically shifted for clarity. **c.** Evolution of the $g^{(2)}(0)$ as a function of the excitation power at different detunings ($\delta_{\text{X-CM}} = 0.87$ meV and $\delta_{\text{X-CM}} = 0$ meV) under a non resonant excitation.

spontaneous emission is accelerated by Purcell effect when using an above-band excitation.

Several mechanisms are usually proposed to explain the degradation of the single-photon purity in the presence of a cavity. The first mechanism is related to the emission at the cavity mode energy due to so called cavity feeding effects. As discussed before this emission is related to the coupling with the phonons (see 2.1.8). If the micropillar hosts several QDs, the emission of detuned QDs in the cavity line would certainly degrade the single-photon purity. However, using *in-situ* lithography, the device was deterministically fabricated from a low-density wafer such that only a single QD is coupled to the pillar cavity. Figure 3.19a. shows the measured autocorrelation function on the exciton line as well as the measured cross correlation between the exciton and the cavity emission lines under the same conditions. Both measurements present the same value for the central peak. Figure 3.19b. presents the evolution of $g^{(2)}(0)$ for the X-X and X-C for three different temperatures. These observations show that the emission induced by cavity-feeding presents the same statistic as the exciton emission line. Note that if the cavity mode emission presented a Poisson-like statistic, the X-C cross-correlation would present a higher central peak than the X-X correlation. As a conclusion, our work shows

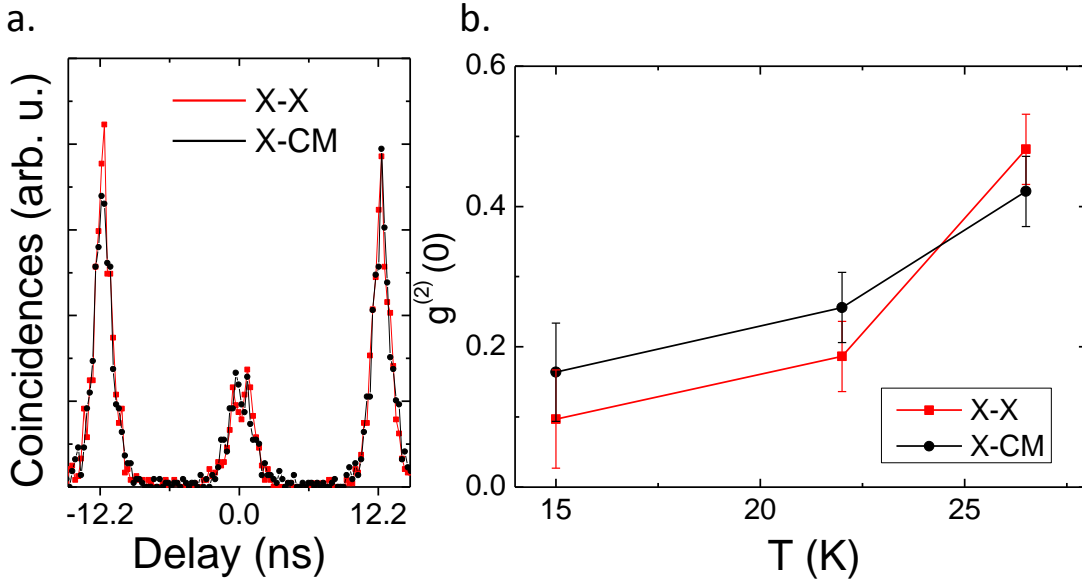


FIGURE 3.19: **a.** Correlation function measured at 27K. The red points correspond to the autocorrelation function of the QD exciton line, the red solid line is a fit. The black points correspond to the cross correlation between the QD exciton line and the cavity-like emission line. **b.** Evolution of the measured $g^{(2)}(0)$ in auto or cross correlation as a function of the temperature.

that the funnelling of the PSB line into the cavity mode presents the same single-photon purity as the ZPL line. This mechanism cannot degrade the single-photon purity of the device when only one QD is embedded in the micropillar.

3.4.3 Recapture Processes Induced by Non Resonant Excitation

Another explanation for the reduced single-photon purity at resonance is the possibility for the QD to capture another electron hole pair after the emission of a photon [141]. Under a pulsed above-band excitation, one laser pulse creates a lot of carriers in the wetting layer surrounding the QD. Pairs of charges must be captured in the QD and relax for the QD to emit a photon.

We compare the single-photon purity of a QD with an enhanced decay rate with the $g^{(2)}(0)$ of a QD that does not experience any Purcell effect. Both are excited under a non resonant excitation (at 850nm). The symbols in fig.3.20 show the measured $g^{(2)}(0)$ as a function of temperature, and as a function of the detuning δ_{X-CM} for the QD in the pillar cavity. Blue diamonds present the evolution of $g^{(2)}(0)$ as function of the temperature under an above-band excitation (at half power from the saturation power). In a planar cavity, where the decay time of the exciton line is close to the ns, the $g^{(2)}(0)$ is constant in the lowest temperature range (10-20K) and increases linearly at temperatures above

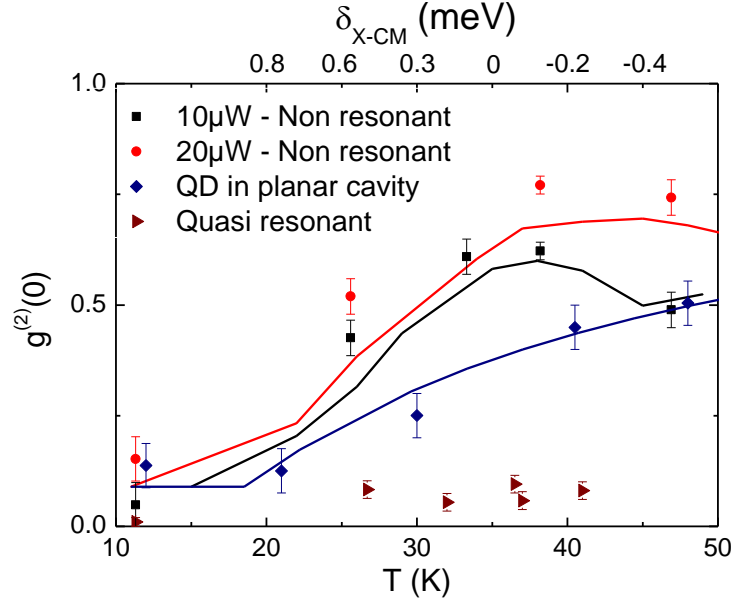


FIGURE 3.20: Evolution of the $g^{(2)}(0)$ as a function of the temperature

25K. We attribute this increase to the increase of the decay time of the residual charges in the wetting layer around the QD with increasing the temperature.

On contrary, the $g^{(2)}(0)$ for the QD in the pillar represented by the red points and by the black squares presents basically the same trend but with a local increase corresponding to the temperature range where the Purcell effect is stronger. The maximum value of the probability that multiple photons have been emitted is reached at the temperature of resonance with the cavity mode (38K). This effect is demonstrated independently of the excitation power ($10\mu\text{W}$ and $20\mu\text{W}$).

The increase of the $g^{(2)}(0)$ with the temperature and with the Purcell effect is related to the surrounding carrier lifetime (noted τ_{QW}) as well as the capture time of the latter into the QD (noted τ_{cap}). Only one pair must be trapped in the QD for the QD to emit one single photon. However, several pairs are created per pump pulse, the number of pairs in the quantum well is noted n_{QW} . If the QD rapidly emits a single photon while the quantum well still hosts charges, the QD can capture another pair resulting in the emission of a second single photon for the same laser pulse. This effect has been observed in GaAs QDs where the radiative lifetime is shown to be shorter than the surrounding carrier lifetime [141].

To confirm our observations, I implemented a rate equation model which calculates the $g^{(2)}(0)$ for both QDs in planar and pillar cavities by taking into account the effects of residual surrounding charges. In this model, we considered two discrete states of the QD

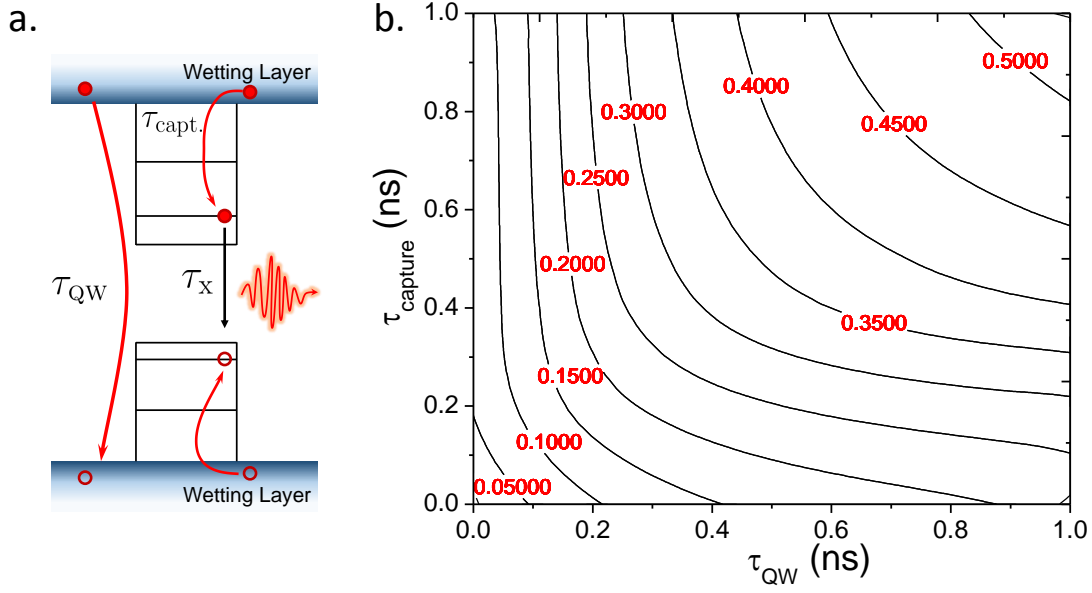


FIGURE 3.21: **a.** Schematic of the QD and QW states and the main decay times. **b.** Calculated $g^{(2)}(0)$ for a QD in a planar cavity ($\tau_{\text{X}} = 1\text{ns}$ and $\tau_{\text{XX}} = 0.5\text{ns}$) as a function of the decay times τ_{QW} and τ_{cap} .

(the exciton X and the biexciton XX) plus the wetting layer reservoir where charges are created and relax into the QD. The probabilities that the QD is empty, occupied by one or two pairs of charges are respectively written p_0 , p_1 and p_2 . For the sake of simplicity, we only consider the neutral states of the QD and the trapping of electron-hole pair and not individual charges. We used the set of equations proposed in the work of Peter et al.[141]:

$$\frac{d}{dt}n_{\text{QW}} = -\frac{n_{\text{QW}}}{\tau_{\text{cap}}}(p_0 + p_1) - \frac{n_{\text{QW}}}{\tau_{\text{QW}}} \quad (3.8)$$

$$\frac{d}{dt}p_1 = \frac{n_{\text{QW}}}{\tau_{\text{cap}}}p_0 + \frac{p_2}{\tau_{\text{XX}}} - \frac{p_1}{\tau_{\text{X}}} - \frac{n_{\text{QW}}}{\tau_{\text{cap}}}p_1 \quad (3.9)$$

$$\frac{d}{dt}p_2 = \frac{n_{\text{QW}}}{\tau_{\text{cap}}}p_1 - \frac{p_2}{\tau_{\text{XX}}} \quad (3.10)$$

where τ_{cap} is the capture time of the charges in the QD, τ_{QW} the decay time of the charges in the quantum well (QW) formed by the wetting layer, τ_{X} the radiative decay time for the X and τ_{XX} the biexciton radiative decay time.

At time $t=0$, the pump pulse is modelled by an initial population n_{QW} in the wetting layer. As described by fig.3.21 **a.**, the QW excitons can be either captured in the QD or recombine radiatively with a typical decay time τ_{QW} . For those that are captured in the QD, depending on the number of pairs in the QD, they recombine with the exciton decay rate τ_{X} or to the biexciton decay rate τ_{XX} . Figure 3.21**b.** shows the calculated

$g^{(2)}(0)$ as a function of τ_{QW} and of τ_{cap} for a QD in a planar cavity. We consider typical radiative decay times $\tau_x = 1$ ns and $\tau_{\text{XX}} = 0.5$ ns. We see that both the capture rate as well as the decay rate of the carriers impact similarly the single-photon purity. When both are much shorter than the exciton radiative lifetime (left bottom corner), we expect a low $g^{(2)}(0)$ as it is the case at low temperatures. Yet, when they are both longer (right top corner), the $g^{(2)}(0)$ considerably increases, as experimentally observed around 50K. Although the exciton and biexciton decay times in a InAs QD are well known, the decay rate of charges in the wetting layer and the capture rate in a QD are more difficult to measure. Therefore, we determined them by considering the measured $g^{(2)}(0)$ of the QD in planar cavity with constant radiative decay times τ_x and τ_{XX} . Since they exhibit the same effect on the single-photon purity, we assume that they are equal for the sake of simplicity: $\tau_{\text{QW}} = \tau_{\text{cap}}$. The blue solid line in fig.3.20 shows the multiple-photon probability calculated with our model for the QD in the planar cavity where we fitted the parameters $\tau_{\text{QW}} = \tau_{\text{cap}}$ as a function of the temperature.

To model the impact of the Purcell effect, we considered the same evolution of the parameters $\tau_{\text{QW}} = \tau_{\text{cap}}$ with the temperature for the QD coupled to the pillar cavity. Then, we adjusted the exciton decay time τ_x following the measurement shown in fig.3.17. The black and red lines in fig.3.20 show the calculated $g^{(2)}(0)$ with two different initial number of charges in the quantum well. The black (red) line is given for $n_{\text{QW}} = 4$ ($n_{\text{QW}} = 10$) while we take $n_{\text{QW}} = 10$ for the red line. We see that both reproduce well the trend given by the measured $g^{(2)}(0)$ as well as the local increase of $g^{(2)}(0)$ that we highlighted at resonance.

As a result, we showed that the cavity feeding is not detrimental to the single-photon purity, on contrary it is shown to be useful for the fabrication of tunable bright single-photon sources by using the phonon coupling as explained in [136] and in the annexe A. Moreover these results show that the degradation of the single-photon purity is mostly due to the recaptures of residual charges in the WL, especially when the exciton lifetime is decreased by Purcell effect. To overcome this mechanism, we demonstrate that the quasi-resonant excitation is an excellent alternative: in this case, the charges are directly created in the QD and there is no risk of recaptures after the exciton recombined. We measured the single-photon purity of the QD coupled to the pillar (triangles in fig.3.20) as a function of temperature under quasi resonant excitation. We observe that the probability that the QD emits multiple photons stays lower than 0.1 at any radiative rate. In the following, most of the results have been obtained under a quasi-resonant excitation in order to minimize the recapture processes.

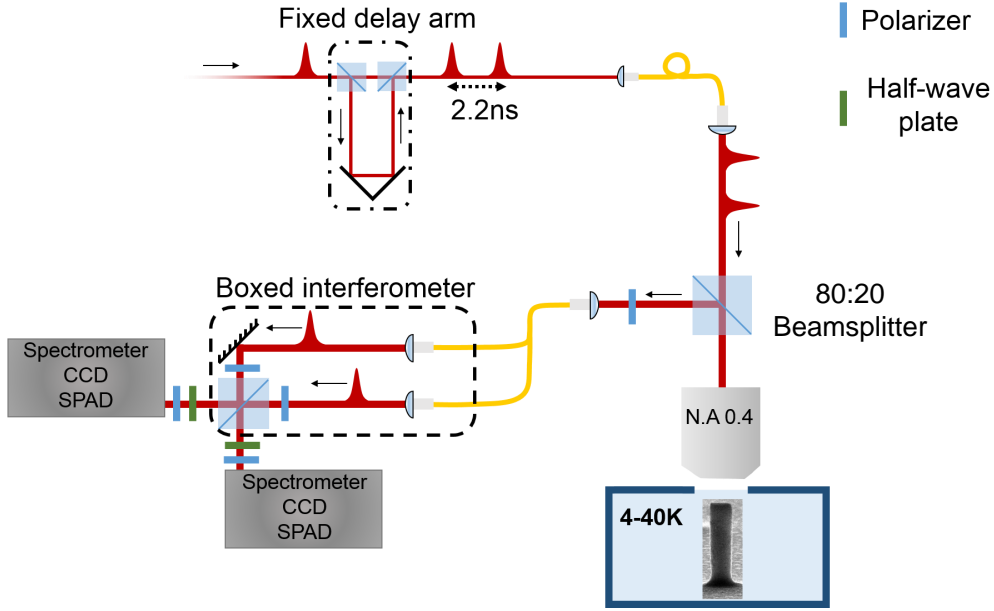


FIGURE 3.22: Schematic of the full setup to measure the mean wavepacket overlap between successively emitted photons from a QD device.

3.5 Characterization of the Photon Indistinguishability

In the following, we measure the mean overlap between photons that are emitted by sources exhibiting a high Purcell factor ($F_P = 10 \pm 2$). A new interferometer for the HOM experiment has been developed in order to measure the overlap of photons that are coupled to single-mode fibers (SMF). First, we describe this interferometer and the experimental procedure to align it. Then, we measure the mean photon overlap for various devices for different excitations. Finally, we conclude by highlighting the role of the electronic environment on the mean photon overlap between successively emitted photons.

3.5.1 Description of the HOM-Interferometer

The measurement of the mean wave packet overlap between photons requires that they reach the beamsplitter *simultaneously* with the exact *same spatial mode* and *same polarization*.

During his thesis, Gazzano used a Michelson-type free-space interferometer [142]. In order to get rid of the unstable spatial overlap of the photons, I decided to develop a Mach-Zender interferometer with fibered inputs.

As depicted by the schematics of the setup in fig.3.22, the source is in a cryostat at 5-50K and 3ps Ti-Sapphire laser pulses excite the source. The mode-locked laser generates

pulses every 12.2 ns at a tunable wavelength (750-1000nm). Each pulse is split to create two similar pulses with a delay of 2.3ns³. The delayed path is always set and one arm is blocked when we wish to excite the QD once per period only (for an autocorrelation measurement for instance).

Both the direct and the delayed paths are coupled to a single mode fiber (SMF). The fiber is then connected to a collimator that sends the light to the microscope objective. The coupling into a SMF makes the first and the second pulses follow exactly the same spatial mode. Therefore, the sample is excited twice per laser pulse with the same excitation power and emits two single photons with a delay of 2.3 ns.

The QD is excited quasi-resonantly using $\lambda \approx 890 - 910$ nm in order to get a good single-photon purity. Since the pump wavelength is rather close to the QD emission, we reduce the scattered laser light with a longpass filter. Among the emitted photons, it is important to select the photons with polarization along one of the QD axis fine structure. The signal is then coupled into a SMF. The coupling efficiency of the source emission into a SMF varies typically from 0.4 to 0.8 depending on the pillar size and the optics used between the sample and the SMF. In order to maximize the coupling between the fiber and the pillar, we use a beam reducer with a factor 1.2-1.8 before the fiber depending on the pillar size. The fibered signal is then sent into the interferometer with a delay of 2.3 ns in such a way that the photons will arrive simultaneously on the recombining cube. The interferometer that has been used under non resonant excitation during this work is shown in fig.3.23. Before the cube, two Glan-Thompson prisms make both photons arrive with the same polarization on the cube. As a common polarization, we chose a vertical linear polarization in order to minimize the birefringent effects in the cube that could be detrimental for the visibility of the interference.

The outputs of the interferometer are sent to two spectrometers. Both are equipped with SPADs.

Spatial alignment of the interferometer:

The usual process for aligning the interferometer shown in fig.3.23 and optimize the spatial overlap given by ϵ is described below:

- As a preliminary step, we check the axis of the Glan-Thompson prisms using the Malus law. We monitor the transmission of a laser beam at 940nm on our detector (a CCD in our case) with a polarization analyzer. By using one Glan-Thompson as analyser, the other prism is easily set to be parallel to the first one.

³The delay on the excitation is variable and fixed by the position of a mechanical delay line.

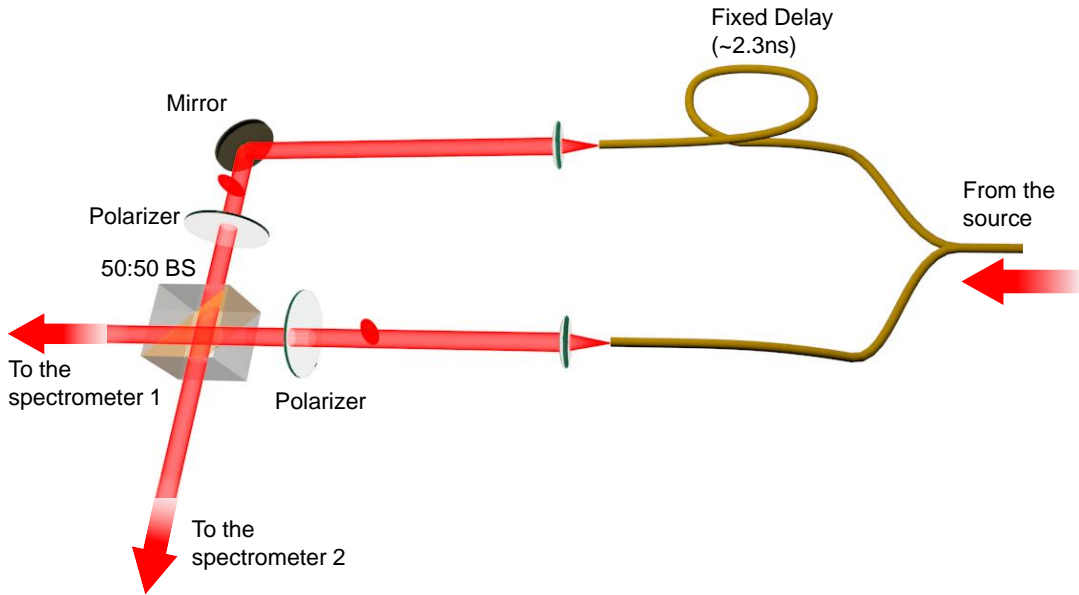


FIGURE 3.23: Schematics of the interferometer setup.

- The positioning of the optical components is first done by using a visible (633nm) low power laser. Without the cube, the collimator 1 is aligned in such a way that the beam goes to one of the spectrometers along the optical axis of the latter. Then the cube is positioned in order to get the cube faces perpendicular to the beam. The second collimator and a mirror are positioned to reach an overlap of the two beams as shown in fig.3.23. Once they overlap fringes appear, indicating that a slight angle exists between both beams. By slightly adjusting the mirror, the angle between the beams is minimized by increasing the fringe spacing. The second output of the cube is then aligned to the optical path of the second spectrometer.
- The final alignment is done by using a coherent CW laser at 930nm. The beam overlap is ensured by imaging the beams on both spectrometers (without the focalization lens in front of the spectrometer, with the slits fully open). Afterwards, with the lens in front of the spectrometer, the angle of the second beam is precisely adjusted by overlapping the two focused points. Since there are some air fluctuations, the phase between the interferometers arms oscillate randomly. By measuring the oscillations contrast, the interferometer visibility is extracted:

$$(1 - \epsilon) = \frac{I_{\max} - I_{\min}}{I_{\max} + I_{\min}} \quad (3.11)$$

The parameter ϵ reflects the spatial overlap between the two paths and is given by the visibility of classical interferences such that it is equal to 0 when the overlap is

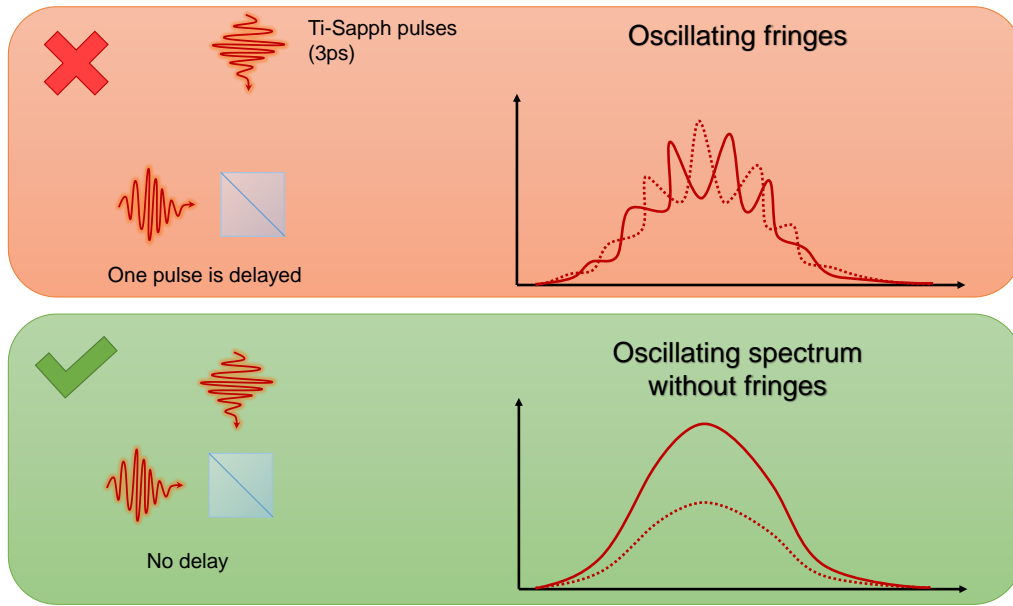


FIGURE 3.24: Temporal overlap of two 3-ps pulses from the Ti-Sapphire laser. The delay line on the excitation is finely adjusted by increasing the fringes spacing of the interfering spectrum.

perfect and that the contrast of classical interferences is equal to 1. The parameter ϵ is then taken into account to deduce the photon indistinguishability. The interferometer visibility must take into account the temporal overlap and the spatial matching (polarization overlap included) but it is independent from the cube coefficients. Otherwise, the imperfections of the cube will be considered twice in the data analysis. So the visibility is measured by *detecting* (in opposition to *sending*) the same intensities from both arms.

At the end of the spatial alignment, the measured ϵ is supposed to be the lowest. With this interferometer, ϵ is typically around 0.08 ± 0.03 (corresponding to a contrast of 0.92 ± 0.03).

The temporal overlap of the single photons on the recombining cube is achieved by adjusting finely the delay on the excitation (shown in fig.3.22). Once the spatial overlap in the interferometer is optimized, we send the 3ps pulses from the Ti-Sapphire laser in the interferometer. Since the phase between two waves depends on the wavelength and that the spectrum of the pulses is spectrally wide, fringes appear on the spectrum as sketched in fig.3.24. The fringes spacing increases when the delay decreases. As soon as the spectrum oscillates as a whole, we consider that the excitation delay is equal to the difference in length between the two arms of the interferometer with a precision of 3ps (corresponding to displacement of 1 mm in the delay line). Compared to the decay

time of the QDs, this value is negligible and we do not take it into account to deduce the photon indistinguishability.

After these steps, single photons from both arms will meet the cube with a good spatial and spectral matching ($92 \pm 3\%$). To measure the indistinguishability of the photons, it is important that the indistinguishability of the paths is preserved up to the detectors. If any information (as any information introduced by birefringence) is added to one of the paths, the interference is erased [143] and the photon coalescence is not observed anymore, independently of the coherence of the source. To ensure the indistinguishability of the paths, we work exclusively with silver mirrors at 45° and we place two polarization analysers in front of the spectrometers. The analysers axis is chosen such that the beam are sent on the blazed grating with a TM polarization⁴.

3.5.2 Measurement and Extraction of the Mean Photon Overlap

The QD is excited by two successive and similar pulses. Two single photons are emitted with a delay equal to the interferometer's delay. The first photon is noted (A) and the second photon (B). Due to the presence of a 50:50 BS, different scenarios for the photons path in the interferometer are possible. The table 3.2 summarizes the different cases:

Description	Classical probability	Detection delay
Both photons take the same path (short and long)	1/2	$\pm 2.2\text{ns}$
The photon (A) takes the short path while the photon (B) takes the long path	1/4	$\pm 4.4\text{ns}$
The photon (A) takes the long path while the photon (B) takes the short path	1/4	0 ns

TABLE 3.2: Different scenarios when a pair of photons crosses the interferometer

One drawback of the interferometer appears here: not all the pairs of photons can interfere, only one pair over four is used for the HOM experiment (when (A) takes the long path and (B) the short path). Nevertheless, since no quantum interferences occurs with $\pm 2\text{ns}$ and $\pm 4\text{ns}$ signals, these peaks are useful to deduce the quantum interference at zero delay.

The table 3.3 shows the events that are associated to each peaks considering the actual reflected intensity R and the transmitted intensity T of the cube. The area of the peaks

⁴The blazed grating of the spectrometer is more efficient with a incident TM polarization.

Peak	Description	Start	Stop	Detection probability
-4.4	(A) took the short path and (B) the long one	(B)	(A)	R^2
-2.2	(A) and (B) took the short path (A) and (B) took the long path One pulse contained 2 photons	(B) (B)	(A) (A)	RT RT $2R^2g^{(2)}(0)$
0	(A) took the long path and (B) took the short path The pulse (A) contained 2 photons The pulse (B) contained 2 photons	(A) (B)	(A) (B)	$P_c = T^2 - 2RTM + R^2$ $2RTg^{(2)}(0)$ $2RTg^{(2)}(0)$
+2.2	(A) and (B) took the short path (A) and (B) took the long path One pulse contained 2 photons	(A) (A)	(B) (B)	RT RT $2T^2g^{(2)}(0)$
+4.4	(A) took the short path and (B) the long one	(A)	(B)	T^2

TABLE 3.3: Weight of the peaks as a function of the different possible scenarios. The probability of detection when two photons meet simultaneously the beam splitter is $P_c = T^2 - 2RTM + R^2$ where M is the photon overlap.

around -2.2, 0 and 2.2 ns depend on the $g^{(2)}(0)$ while only the peak at 0 ns depends on the mean photon overlap. When the sources emit pure single photons that are fully indistinguishable, the peak at 0 ns should vanish only for $R = T = 0.5$ and $g^{(2)}(0) = 0$. Knowing the interferometer characteristics and the single-photon purity $g^{(2)}(0)$ of the source, the mean photon overlap is given by:

$$M = \frac{1}{(1-\epsilon)^2} \left[2g^{(2)}(0) + \frac{R^2 + T^2}{2RT} - \frac{A_0}{A_{-2.2\text{ns}} + A_{+2.2\text{ns}}} \left(2 + g^{(2)}(0) \frac{(R^2 + T^2)}{RT} \right) \right] \quad (3.12)$$

where $(1-\epsilon)$ is interferometer visibility measured with a continuous and coherent source and R and T are the beamsplitter coefficients. To measure the mean wave packet overlap of successively emitted photons, we begin by finding the best conditions to excite quasi-resonantly the source in order to get a high single-photon purity. Figure 3.25a. shows the measured autocorrelation function of the emission from one source under a quasi-resonant excitation ($\lambda = 905\text{nm}$). The measured $g^{(2)}(0)$ is extremely low, showing that the probability that the source emits more than one photon under these conditions is lower than 0.01.

Then, without changing the excitation wavelength, the delay line on the excitation path is unblocked in order to excite the device twice a period and the collected PL is sent into the interferometer. The points in fig.3.25 b. show the measured histogram resulting from the correlation between the two SPADs at the output of the HOM interferometer. From the measured points, we fit the peaks with double-sided exponential decays. The fitting peaks are shown with the grey lines while the cumulative fit is shown with the

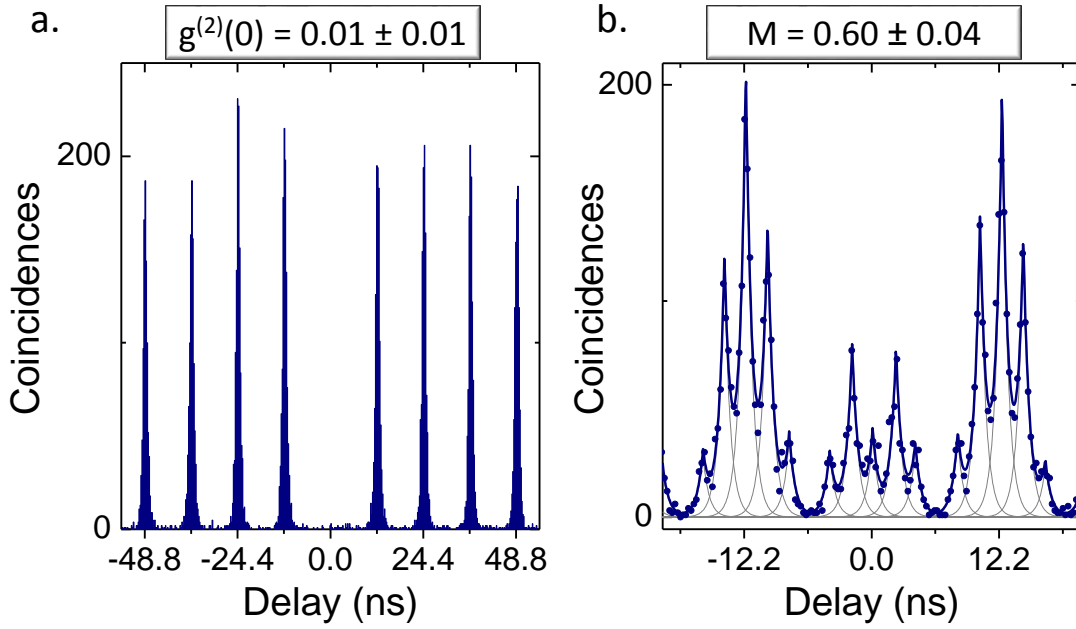


FIGURE 3.25: **a.** Measured autocorrelation function under a pulsed quasi-resonant excitation (laser excitation at 920nm) for an acquisition time equal to 8 minutes. The ratio of the area at zero delay with the lateral peak areas gives $g^{(2)}(0) = 0.01 \pm 0.01$. **b.** Points : Pulsed correlation histograms between the two SPADs with an acquisition time equal to 9 minutes. The source is excited twice a period under the same conditions as **a.**. Grey lines are the individual fits of the peaks. The blue line is the cumulative fit with all the peaks. The normalized central peak gives a mean photon overlap equal to $M = 0.68 \pm 0.03$.

blue thick line. An offset is adjusted to account for the small background due to dark counts on the SPADs. This offset is adjusted to obtain the closest fit to the classical ratio shown in the table 3.3. Once the offset has been correctly set, the mean photon overlap is calculated from the ratio of the central peak with the lateral peaks (according to the eq.3.12). For the measurement shown in fig.3.25, the extracted indistinguishability is equal to 0.60 ± 0.03 with a $g^{(2)}(0)$ equal to 0.01 ± 0.01 as shown by fig.3.25a. This result is corrected from the setup imperfections: considering a classical visibility of 0.93 ± 0.03 and for the ($R=0.55$, $T=0.45$) recombining beam splitter. The raw measured photon overlap not corrected from the setup imperfections and from the single-photon purity is 0.52 ± 0.01 .

In the following, we discuss the excitation conditions that allow maximizing the source quality.

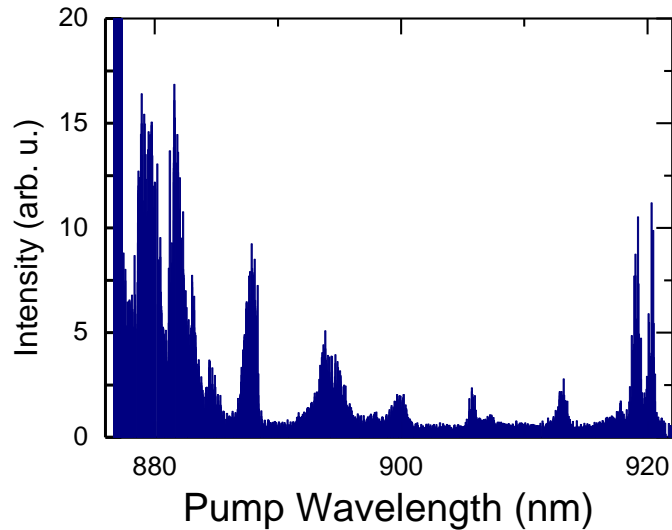


FIGURE 3.26: Measured PL signal from a source as a function of the wavelength of the pump

3.5.3 Influence of Excitation Conditions on the Mean Wave Packet Overlap

Previously, we highlighted the importance of the quasi-resonant excitation to emit single photons by reducing the recapture processes. Gazzano and coworkers also showed that a quasi-resonant excitation was not always the best excitation condition to emit highly indistinguishable photons [31]. They found that the quasi-resonant excitation needed to be combined with a slight continuous-wave excitation at higher energy (around 850nm) in order to stabilize the electronic environment of the QD.

Here we show that the technique that was implemented is unfortunately not universal. Various excitation energies appear as resonances in the excitation of a QD in a cavity. Figure 3.26 shows the integrated intensity of the exciton line as a function of the excitation wavelength. Between 890 nm and 920 nm, at least five pump wavelengths allow to excite the QDs in quasi-resonance efficiently. Even if most of the wavelengths higher than 890 nm provide a good single-photon purity, a slight change of few nanometers can make the emitted photons switch from indistinguishable to distinguishable.

We measured the mean wave packet overlap of photons that are successively emitted for various λ_{exc} . First, the mode-locked laser is set to emit pulses around 900 ± 0.5 nm and we measure the photons indistinguishability. Figure 3.27a. shows the corresponding histogram. Then the same measurement is repeated after a slight increase of the pump wavelength to 902 ± 0.5 nm (fig.3.27b.) the peak at 0 ns is much smaller in the case where the QD is excited at 902 nm.

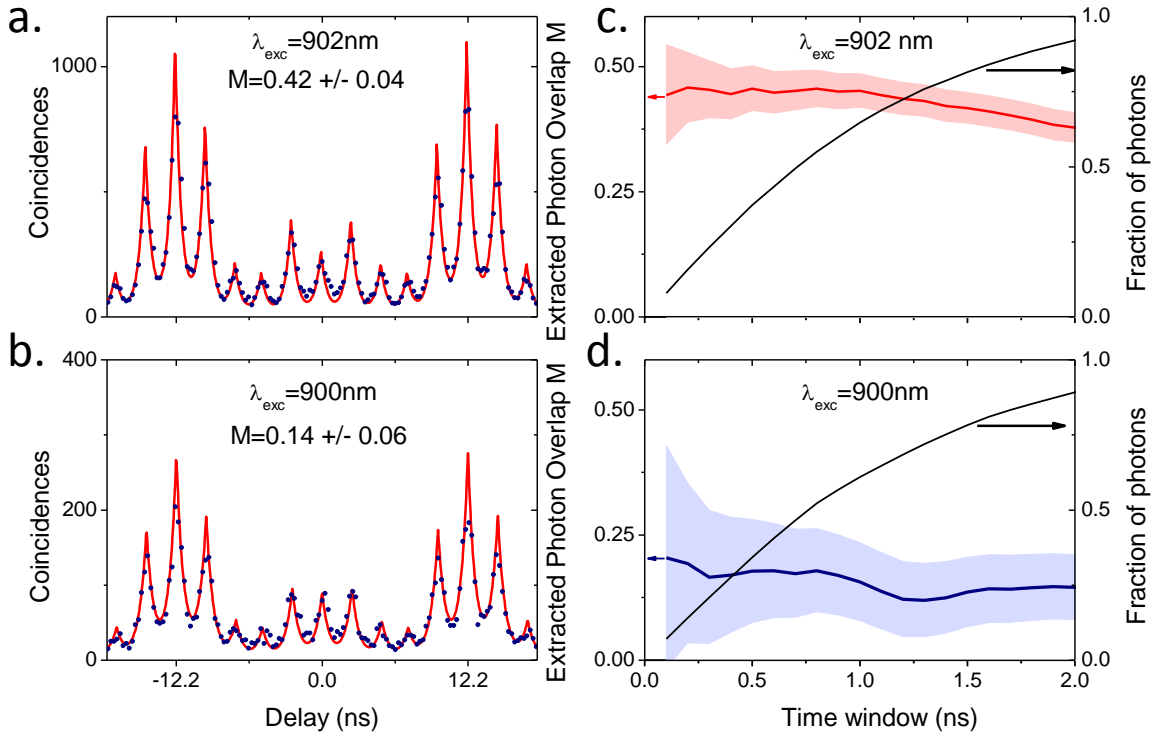


FIGURE 3.27: Influence on the wavelength of the excitation. **a.** **b.** Pulsed correlation histogram between the output of the HOM interferometer when the device is excited quasi-resonantly by laser pulses at 900 nm (**a.**) or at 902 nm (**b.**) The respective acquisition times are 19 min. (**a.**) and 24 min. (**b.**) **c.** Measured mean wave packet overlaps of successively emitted photons as a function of the width of the detection temporal window considered. The red line corresponds to the excitation at 902 nm (**a.**) while the blue line corresponds to the excitation at 900 nm (**b.**)

Figures 3.27c. and d. show the extracted mean wave packet overlap (left axis) and the fraction of coincidences taken into account (right axis) as a function of the width of the time window used to extract M . The photon overlap is calculated by considering only the counts in a window centered on the peaks. The window width corresponds to the full temporal range where the coincidences are considered. A small width leads to a strong temporal postselection considering a small fraction of the acquired coincidences while a width larger than the decay time corresponds to take into account all the coincidences without any temporal postselection. Figure 3.27c. corresponds to the indistinguishability for $\lambda_{\text{exc}} = 902$ nm while fig.3.27d. corresponds to $\lambda_{\text{exc}} = 900$ nm. As expected, both indistinguishabilities decrease when the time window width gets broader.

Depending on the excitation wavelength, the mean wave packet overlap is $M_{902 \text{ nm}} = 0.42 \pm 0.04$ and, $M_{900 \text{ nm}} = 0.14 \pm 0.06$, respectively considering all the events in a 1.5 ns window.

These results show the strong dependence on the excitation wavelength to obtain indistinguishable photons.

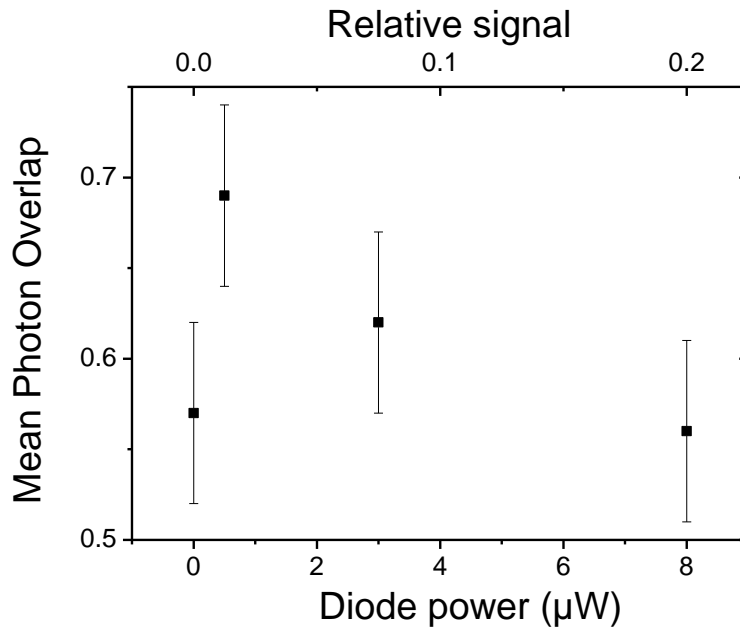


FIGURE 3.28: Measured mean wave packet overlap under a quasi-resonant excitation as a function of the diode power at 850nm.

In order to increase the photon indistinguishability, we tested whether the QD electronic environment can be stabilized by using a slight CW illumination at high energy [144, 145]. This technique previously allowed a considerable increase of the photon indistinguishability when the QD was illuminated by an additional CW beam which lead to 10% of the total intensity from the source.

Here, we introduce a low power CW excitation power at 850 nm for a device that is excited at 906 nm. The points in fig.3.28 show the evolution of the mean wave packet overlap as a function of the beam power at 850 nm. Interestingly, the photon indistinguishability does not vary monotonically but first increases before decreasing at higher powers. The highest indistinguishability is observed under a very small 850 nm illumination, corresponding to few percent of the total signal. In this particular case, the use of an additional CW illumination improves the photon indistinguishability. Nevertheless, the same illumination leads to a degradation of the photon indistinguishability in other cases.

We now present the mean wave packet overlap of the photons emitted by the ultrabright single photon source ($F_P = 10$) described in section 3.3. Figure 3.29a. shows the correlation histograms when the device is excited quasi-resonantly with the additional CW beam ($\lambda = 850$ nm) while the panel b. shows the data corresponding to the case where the QD is only excited with the pulsed excitation. With the CW beam, the count rates is much higher than without it showing a higher population of the state for the same

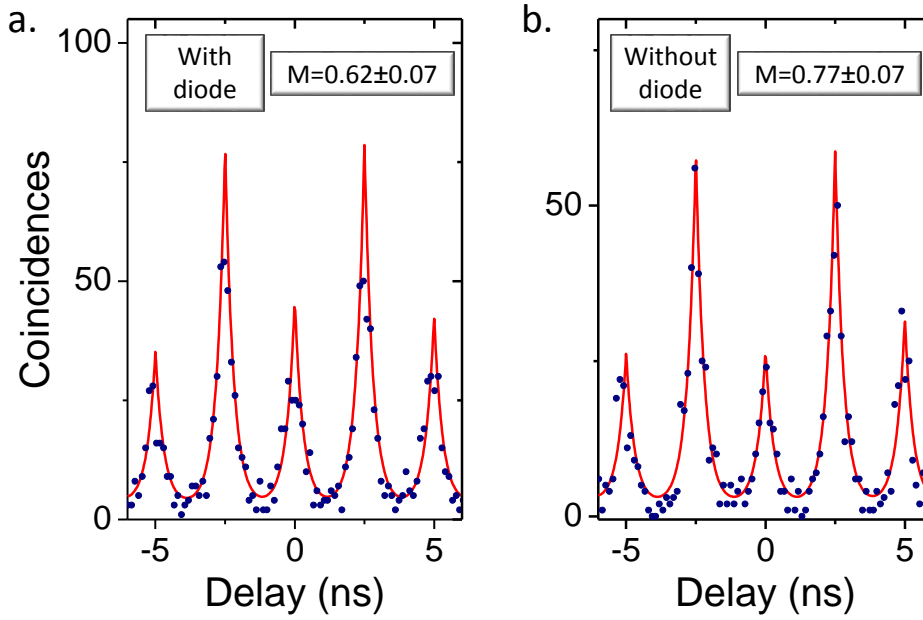


FIGURE 3.29: Pulsed correlation histograms under the same pulsed excitation with **a.** and without **b.** additional CW beam at 850nm. The acquisition times are 5 min. for the measurement (**a.**) and 9 min. for the measurement (**b.**).

excitation power at 906 nm. The acquisition time of the histogram shown by fig.3.29a. is 5 minutes compared to 10 minutes for the histogram corresponding to the fig.3.29b. In comparison to the lateral peaks, the peak at 0ns is smaller in **b.** than in **a.** In fig.3.30a., the extracted mean wave packet overlap is plotted as a function of the detection time window with or without the CW laser. With a small temporal window, the two photon indistinguishabilities are equal but the one corresponding to the case where a CW beam is used drops rapidly when more coincidences are considered. Considering a temporal window of 1 ns (corresponding to more than 80% of the coincidences), we extract a mean photon overlap equal to $M = 0.77 \pm 0.07$ without any additional excitation compared to $M = 0.62 \pm 0.07$ with an additional excitation.

As a consequence, for this bright source, the photon indistinguishability could not be further improved using a CW non resonant excitation.

Observing different QDs in this sample, we can conclude that there is not universal recipe to get indistinguishable photons. We observed that the photon indistinguishability can be rapidly degraded if the excitation is not at the correct wavelength or if an additional illumination modifying the QD surroundings is used or not. On average on all the studied pillars, it was difficult to get a mean wave packet higher than 0.6-0.7. We evidenced that the devices on this sample are very prone to the charge noise. As shown previously by fig.3.5, in this adiabatic structure, the InAs layer is separated from the AlAs layer by only 27 nm compared to about 150 nm in a standard structure. It is reasonable to think that this enhanced the charge noise since defects are well known to accumulate

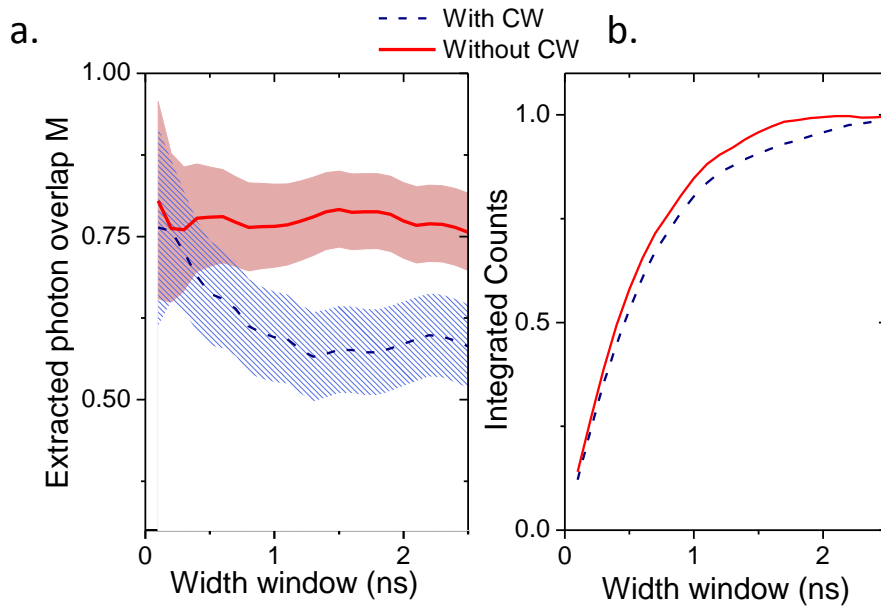


FIGURE 3.30: **a.** Measured mean wave packet overlaps of successively emitted photons and **b.** integrated counts as a function of the width of the detection temporal window considered.

in Al rich layers [146]. In the following, we further evidence the presence of charge noise by analyzing the memory effects that are visible in the autocorrelation histograms measured from a pillar.

3.5.4 Memory Effects and Influence of Electronic Charges

Often, it is assumed that each pulse corresponds to a new trial of an experiment with the same initial conditions. If this were fully true, results from each excitation pulse would be independent, and the side peaks in the photon correlation histograms would have the same area (that would be normalized to 1). However, in some cases, the peaks in the histograms follow an envelop for long delays. Figure 3.31 shows two measured autocorrelation functions. They are measured with the same QD but the histogram **a.** is obtained with a quiresonant excitation following a decreasing exponential while the histogram **b.** is obtained with an above-band excitation evidencing an increasing exponential.

This phenomenon is attributed to memory effects, each pulse does not correspond to a new trial with the same initial conditions. Among these effects, one can report some blinking effects due to surrounding defects [147, 148], the capture of single carriers instead of electron-hole pairs [79] or spectral diffusion [149, 150]. Here, we use a rate equation model described in the PhD thesis of C. Santori [151] and show that these effects are commonly observed with the adiabatic cavities where the QDs are close to the AlAs layer.

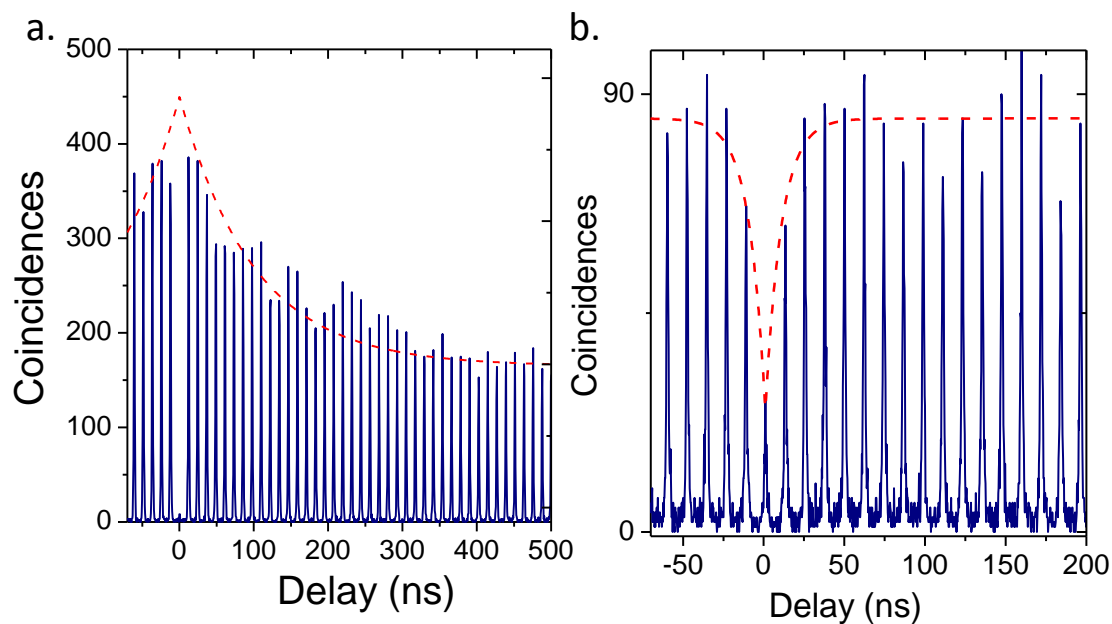


FIGURE 3.31: Measured autocorrelation functions : **a.** under a pulsed quasiresonant excitation (acquisition time: 6 minutes) and **b.** under a pulsed non resonant excitation (acquisition time: 11 minutes). Blue solid line shows the coincidences histogram and the red dashed line shows a exponential fit of the envelop of the autocorrelation function.

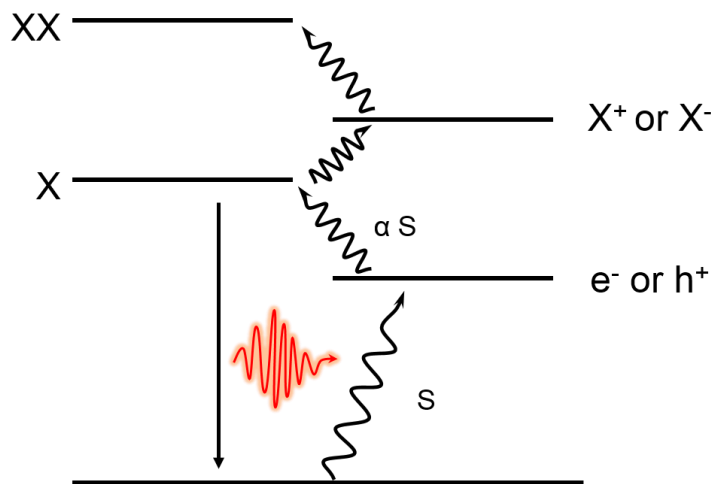


FIGURE 3.32: Schematics of the blinking model

3.5.4.1 Blinking Effect

Blinking describes a behavior when the emitter oscillates between two configurations *on*, the QD emits one photon at the detected energy, and *off*, the QD does not emit light at this energy. This change of configuration is mainly attributed to the presence of single carriers. The system is described schematically in fig.3.32. The bottom level

corresponds to the empty occupancy state of the QD. The diagonal transitions show the capture of single charges in the QD. The capture of one single charge considering that the initial state is not charged follows the rate s . Similarly, the capture of one charge considering that the QD is initially charged follows the rate αs . The levels on the left correspond to neutral states and the levels on the right correspond to charged (\pm) states.

Before the interaction with an excitation pulse, the QD is empty or occupied by a single charge. When a quasi-resonant (or resonant) pulse is applied, two charges are injected into the QD and relax. We measure only the photon emitted by the exciton recombination using a spectral filtering. In other words, the detection of one photon at this energy is synonymous of the detection when the QD ends up in the empty occupancy state.

We denote P_n the probability that the QD is in a neutral state (X, XX,...) and P_c the probability that the QD is in a charged state (X^+ , X^- ,...). Their evolution is ruled by the following equations:

$$\begin{aligned}\frac{d}{dt}P_n &= s(\alpha P_c(t) - P_n(t)) \\ \frac{d}{dt}P_c &= s(-\alpha P_c(t) + P_n(t))\end{aligned}\quad (3.13)$$

Considering that the state is initially neutral, we denote the probability that it is neutral (resp. charged) $P_{(0,n)}$ (resp. $P_{(0,c)}$). Furthermore, we denote the probabilities $P_{(\pm,n)}$ or $P_{(\pm,c)}$ that the QD is neutral or charged given that it is initially charged. Depending on the initial state of the QD (neutral or charged), the occupancy probabilities read:

$$\text{Initial neutral state: } \begin{cases} P_{(0,n)}(t) = \frac{1}{1+\alpha}(\alpha + e^{-(1+\alpha)st}) \\ P_{(0,c)}(t) = \frac{1}{1+\alpha}(1 - e^{-(1+\alpha)st}) \end{cases}\quad (3.14)$$

$$\text{Initial charged state: } \begin{cases} P_{(\pm,n)}(t) = \frac{1}{1+\alpha}(\alpha - e^{-(1+\alpha)st}) \\ P_{(\pm,c)}(t) = \frac{1}{1+\alpha}(1 + e^{-(1+\alpha)st}) \end{cases}\quad (3.15)$$

If we consider that a photon associated to the neutral exciton is emitted (and detected) at the time t , then the probability that the QD will emit another photon at the same energy at a time $t + \tau$ is proportional to the probability that the QD is neutral given that it was neutral at the time t :

$$P(\tau) \propto P_{(0,n)}(|\tau|) = \frac{1}{1+\alpha}(\alpha + e^{-(1+\alpha)s|\tau|})\quad (3.16)$$

Since the probability that the QD stays in a neutral state decreases with the time, the probability to detect one photon at the time $t + \tau$ knowing that we detected one photon

at the time t decreases exponentially with τ . This justifies the fitting of our data in fig.3.31 by a two-sided exponential function. Our model shows that in the example shown by the fig.a., the typical time for the QD to be in a charged state from a neutral state is approximately 100ns.

3.5.4.2 Long-term Antibunching

Under a non resonant (above-band) excitation, the mechanism is not different. As shown by fig.3.31, the opposite of blinking is observed: the lateral correlation peaks decrease near the central peak. The loading of charges in the QD as described by our model explains this trend.

After an exciton has recombined and a photon has been emitted, another electron-hole pair must be trapped before the QD emits another photon. However, as it was explained previously, the probability that the QD is occupied by a single charge after a time τ is $P_{(0,c)}(\tau)$. If a single electron or hole occupies the QD, only a single hole or electron must be captured for a photon to be emitted. When charges are created in the wetting layer, they can be trapped one-by-one in the QD, in opposition to the resonant excitation where the charges are inserted in pairs. Consequently, the detection of a first photon decreases the probability to detect another photon at a time τ .

These memory effects surely affects the capacity for the emitter to behave as bright source of indistinguishable photons since they correspond to charge fluctuations in the QD leading to a lower coherence. Furthermore, since the probability to emit single photons evolve in time, it surely degrades the brightness of the device. These effects are considered in the factor p_x in the expression of the brightness (eq.3.6).

3.6 Conclusion

In this chapter, we developed sources operating in a high Purcell regime in order to increase the device brightness and the photon indistinguishability. We reported the fabrication of sources embedding tapered pillar cavities. The diameters of the pillars based on adiabatic structure can be decreased leading to a smaller effective volume of the mode. We fabricated sources with small effective volume and obtained a high Purcell enhancement of the spontaneous emission. A bright single photon sources with an effective Purcell effect equal to 10 ± 2 was reported. It was also shown that the measured Purcell effect is lower than the theoretical one because of the coupling to phonons. Finally, at saturation the measured brightness reached 0.74 ± 0.07 .

We demonstrated that a good single-photon purity is obtained by exciting quasi-resonantly a discrete state of the QD. Typical values $g^{(2)}(0)$ around 0.01 are obtained in a high

Purcell regime.

Nevertheless, it was difficult to get a photon indistinguishability higher than 0.6-0.7 on average. This phenomenon is attributed to the high charge noise that is due to the proximity between the AlAs layer of the Bragg mirrors and the QDs. Even the use of additional beams to stabilize the charges was not enough to provide higher indistinguishabilities.

These measurements confirmed that the electronic environment was a crucial parameter to control in order to obtain highly indistinguishable photons. As a consequence, we developed an advanced technique to fabricate electrically controlled sources. Such control can provide two main assets for the sources: the fine tuning of the QD transition in order to replace the temperature tuning and the stabilization of the electronic surrounding of the QDs. The next chapter is dedicated to the study of electrically controlled sources.

Chapter 4

Indistinguishability of Electrically Controlled Sources

In the last chapter, we showed the importance to control the electronic environment close to QDs to further increase the indistinguishability of the photons. In this context, strong technological efforts were successively made by two post-docs in the group Anna Nowak and Niccolo Somaschi to develop electrically controlled sources.

In this chapter, we present the new generation of devices obtained with an advanced *in situ* lithography technique in order to couple a single QD to a pillar on which an electrical field is applied. The first part of this chapter is dedicated to the fabrication of this new generation of sources as well as their optical characterization. The second part focuses on their performance for quantum information processing applications: the bright emission of single and highly indistinguishable photons is demonstrated in a reproducible way.

4.1 Fabrication of Electrically Controlled Devices

To build a scalable solid-state quantum network, it is essential that several sources are tuned to the same emission wavelength. The possibility to tune the QD transition to a target wavelength is a key feature and the temperature control used in the previous chapters is not a long term and practical solution. By inserting the QDs in doped structures and by applying an electric field, this tuning can be achieved through the Stark effect [152–154]. To get a bright source, the QD must also be efficiently coupled to a photonic structure.

Establishing electrical contacts on photonic structures like nanowires or micropillars presenting sizes of a few microns is challenging. After a short review of other works, we present the photonic structure developed at the LPN to address this problem during the postdoc of Anna Nowak in 2012-2013. This new design allows combining the

deterministic coupling between a single QD and a microcavity with electrical contacts. It is shown that the micropillar can be connected through four 1D wires while confining efficiently the optical mode in the cavity. Then the procedure of advanced *in situ* lithography used to couple the connected pillar with a single QD is described. We demonstrate the fabrication of bright, tunable single-photon sources with high photon indistinguishability.

4.1.1 State-of-the-art

The modification of the QD emission properties by applying an electric field in a doped structure has been experimentally studied by several groups. It was shown that applying an electric field to a diode containing QDs allows controlling efficiently the QD transition energy as well as the level of the fine structure splitting.

In 2001, Findeis et al. [152] studied the dependence of the photocurrent and of the photoluminescence of single QDs as a function of the applied electric field. The electrical control of the spin in a single QD has been shown by Sabine Laurent et al. in the group of O. Krebs at the LPN in 2005 [155]. The manipulation of the fine structure splitting of the exciton was also demonstrated by Kowalik et al. [77, 156]. In 2010, Bennett et al. [157] used this key feature to study the coherent coupling of the exciton states in single QDs in a doped structure and the generation of entangled photon pairs. In addition, numerous works based on the emission properties of QDs in *p-i-n* diode have been published [74, 158, 159]. An important challenge is then to combine these results with the control of spontaneous emission by the Purcell effect.

Only a few works have demonstrated an electrical control of a QD coupled to a cavity, showing how challenging such a fabrication is. In 2007, Strauf et al. showed the first coupling of a QD in a high- Q microcavity with electrical contacts [160]. Figure 4.1 shows a schematic of the device they fabricated. By defining trenches in the planar cavity (as shown by fig.4.1b.), they used a controlled AlO_x oxidation to confine the light in the cavity providing an enhancement of the spontaneous emission and a photon extraction as high as 0.38. In 2008, an electrically driven QD coupled to micropillar with a Purcell enhancement of about 10 was demonstrated by Bockler et al. [161]. To fabricate these devices, extremely delicate processing steps are necessary. Starting from a planar structure, they first fabricated micropillars by means of electron-beam lithography relying on statistics to find one pillar containing one QD. The sample is then planarized using benzocyclobutene (BCB) which acts as a insulator, and a ring-shaped gold contact is patterned on top of the pillar as shown by fig.4.2. The contact quality relies on a very small area within 100 nm from the pillar edge. In 2010, Heindel et al. from the same group used this technique to fabricate an electrically injected

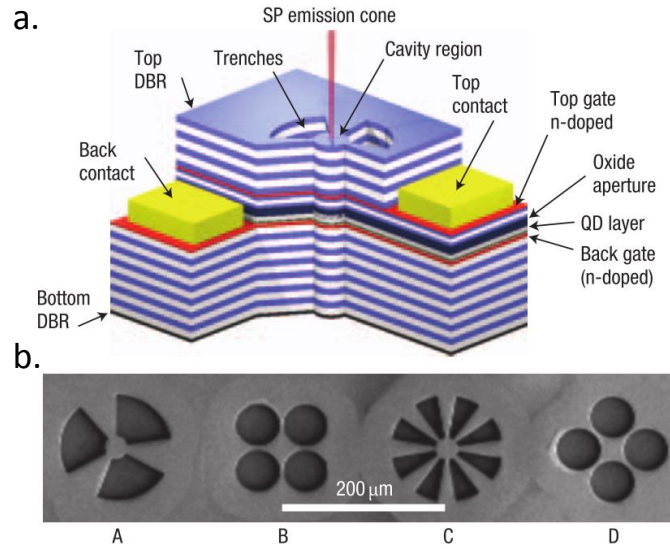


FIGURE 4.1: Figure reproduced from [160]. **a.** Three-dimensional schematic view of the fabricated device by Strauf et al. A λ -cavity is embedded between AlGaAs/GaAs DBR. Two contacts allow to apply an electric field gradient inside the cavity. **b.** SEM images of various geometries used to confine the light. The electrical contact is provided by the small lateral contacts.

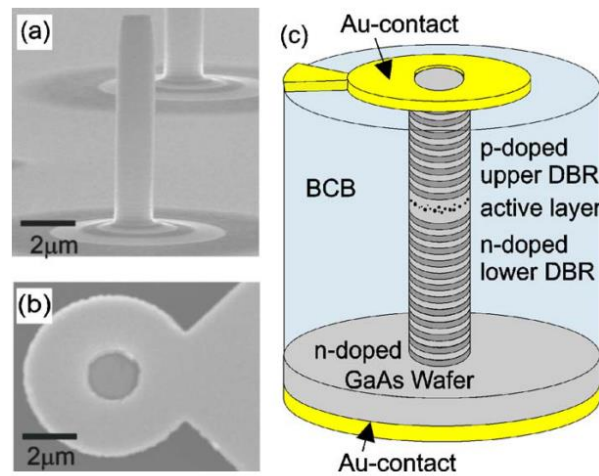


FIGURE 4.2: Figure reproduced from [161]. **a.** SEM image showing a micropillar before the planarization **b.** Top view of a fully processed device showing the uncapped upper surface of the micropillar at the center of the gold ring. **c.** Schematic view of the electrically driven micropillar fabricated in [161]

single photon source with a brightness equal to 0.34 ± 0.07 [130]. Later, Schneider et al. integrated site controlled QDs into electrically driven micropillars [137]. Although this strategy can provide a good spatial matching of the QD emission in the cavity mode, the spectral matching remains random.

No group had demonstrated the fully deterministic fabrication of an electrically driven QD in a cavity. Yet, the repeatability of such fabrication is an important step towards

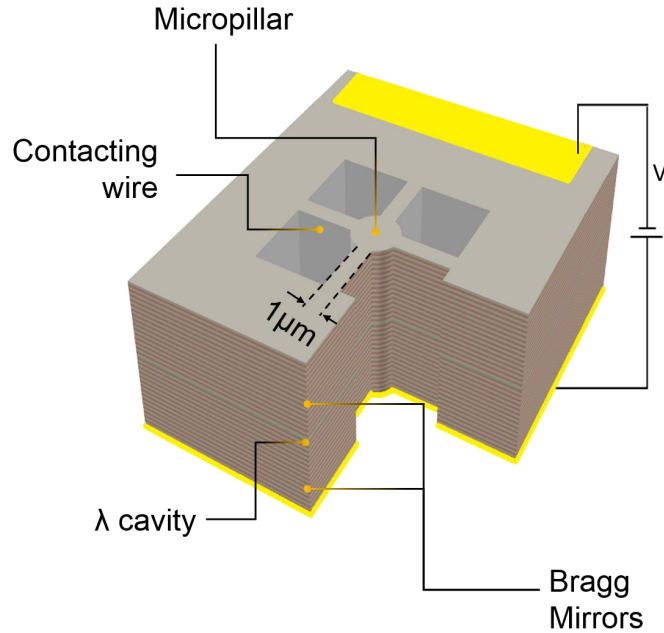


FIGURE 4.3: 3D schematic of the device: a micropillar is connected to a surrounding frame through four $1\text{-}\mu\text{m}$ wide 1D wires. The electrical contacts are defined on the frame (yellow contacts).

the development of a scalable solid-state quantum network based on QDs.

In the following, we describe the cavity design proposed at the LPN to allow the deterministic and repeatable fabrication of electrically driven sources.

4.1.2 First Deterministic Fabrication of a Bright Tunable QD Based Source

The cavity proposed by the group is sketched in fig.4.3. It consists of a micropillar connected to a surrounding frame by 1D wires with typical width of $1\ \mu\text{m}$. The electrical contacts are defined on a diode connected to the frame. The optical modes in this new cavity design was first studied on devices obtained through electron-beam lithography. A planar cavity made of a standard λ -cavity spacer surrounded by two Bragg mirrors was grown. The top (bottom) mirror consists of 30 (30) pairs of alternating AlGaAs/GaAs $\lambda/4$ thick layers to obtain a high quality factor for the planar cavity. To characterize the optical properties of the cavities, a large density QD layer was embedded in the structure and a electronic-beam lithography was used to define connected pillars as well as standard "isolated" pillars. The objective was to compare the mode volume and Q -factors of connected pillars to those of isolated ones.

Figure 4.4a. shows measured PL spectra from connected pillars. The width of the wire was fixed to $1\ \mu\text{m}$. Arrows show the optical modes of the connected pillars. With a

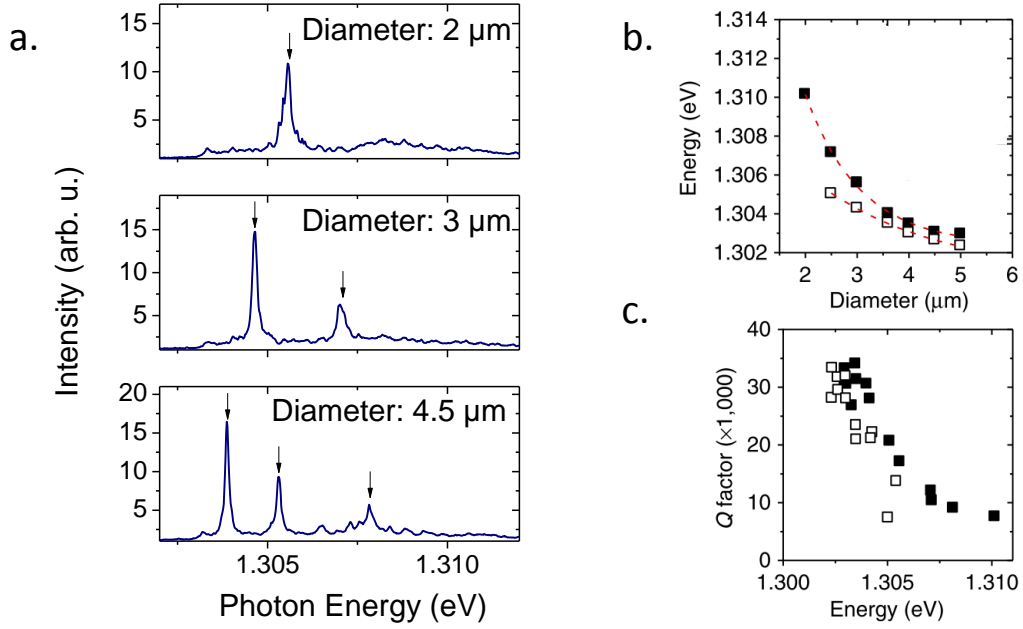


FIGURE 4.4: **a.** Measured PL spectra of the connected pillars with different diameters. Arrows show the cavity mode resonances. **b.** Energy of the fundamental mode in standard pillars (solid symbols) and connected pillars (open symbols). The dashed lines are guides to the eyes. **c.** Measured quality factors of the fundamental mode for the standard (solid) and connected pillars (open).

large diameter, several optical modes are measured. We see that all the optical modes are broader and shifted to higher energies when the pillar diameter is decreased. Figure 4.3b. shows a comparison of the energy of the fundamental modes for standard cylindrical pillars (solid symbols) and for connected pillars (open symbols) as a function of the diameter. We see that for a given diameter, the energy of the fundamental mode is slightly lower in the connected pillar compared to the corresponding standard pillar. This indicates a slight penetration of the electric field in the connecting wires leading to a larger effective volume. For instance, a connected pillar with a diameter equal to 3 microns presents the same volume as a pillar with diameter of 3.5 microns. To compare their Q -factor for a given mode volume, fig.4.4c. shows the measured evolution of the Q -factor as a function of the fundamental mode energy. As expected, the Q -factor of connected pillars is slightly lower than standard ones indicating small leakage in the wire. Despite of the field penetration into the wires, the connected pillars exhibit very high Q -factors ($10^4 - 3.5 \cdot 10^4$).

This study shows that this new structure provides a very efficient confinement of light. The fact that the effective volume of the mode is larger for connected pillars is not detrimental since the diameter is carefully chosen during the *in situ* lithography. The additional inplane photon escape is also not a limitation to get a good photon extraction, one just needs to use a larger top mirror escape rate by decreasing the number

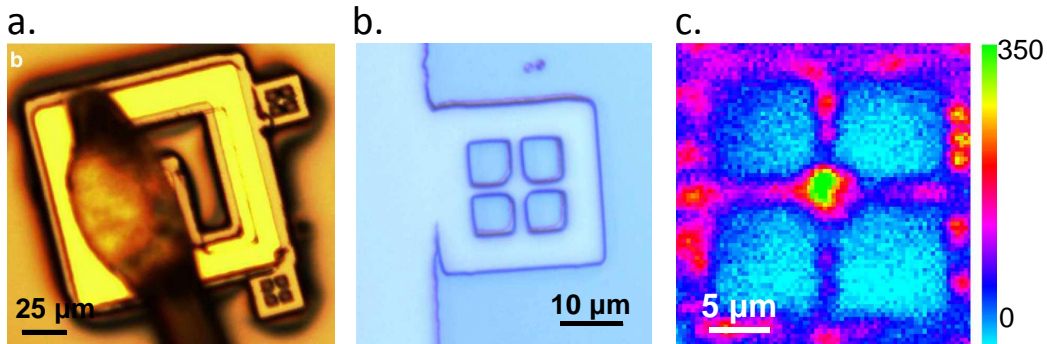


FIGURE 4.5: **a.** Microscope photograph of the bonded sample : two connected devices are visible. **b.** Optical image of a pattern defined in the photoresist. Using *in situ* lithography, it is centered on a single QD. **c.** PL map measured by horizontally scanning the sample in the *in situ* cryostat.

of pairs for the top mirror. In the following, we explain the fabrication of bright single photon sources using this structure developed by Anna Nowak, post doc in the group in 2012-2013.

The advanced *in situ* lithography used to fabricate electrically tunable sources is similar to the *in situ* lithography used previously and described in 2.4. One QD is precisely localized by collecting the PL under non resonant excitation and an exposure laser expose the resist on top of the planar cavity. To be able to write any pattern in the resist, a new *in situ* lithography setup was developed in collaboration with the company attocube providing an absolute measure of the sample with a 10nm repeatability. A software for the exposure process was developed. A standard optical lithography is first done in the clean room to define the ohmic contacts where the electrical bonding will be done. QDs are selected in a region within 20 μm from this contact. Once a QD is localized, instead of exposing a disk as for standard micropillars, we expose the shape of the studied structure (including the surrounding frame) as shown by fig.4.5b. Then, the first *ex situ* steps are the same as for the *standard* process. After the structure etching, the SiN_4 hard mask is removed and the top p-contacts are defined on the large frame using a standard optical lithography step plus a contact deposition and lift off. Finally, a bonding is done to connect the ohmic contacts to a ceramic. Figure 4.5a. shows a photograph at the end of the process: the square ohmic contact and the bonding are

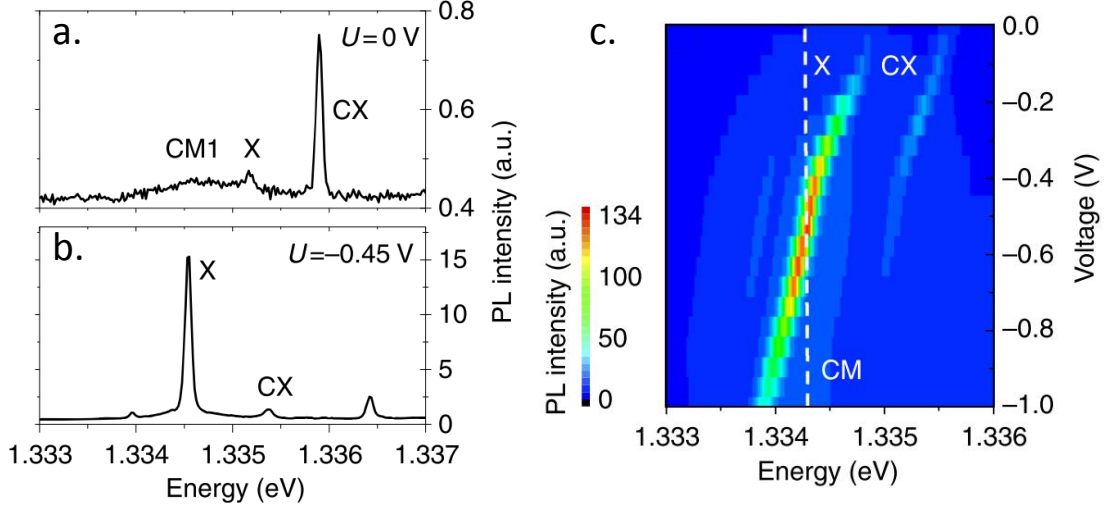


FIGURE 4.6: Measured PL spectra at 35K under a non resonant excitation for 0V (a.) and for -0.45V(b.) c. PL intensity map as a function of energy and applied voltage at 35K.

shown on the bottom left side. Two connected pillars presenting the shape of a small cross in a square are visible on the right side.

Figure 4.5c. shows a PL map after etching the structure. The PL is spectrally filtered in a 5-nm wavelength range around the pillar fundamental mode. A high intensity signal is collected from the QD positioned at the center of the pillar structure, signature of the efficient collection through the Purcell effect. Emission from other QDs is visible on the sides of the structure.

We first show the tunability of the source at a constant temperature. Under a CW non resonant excitation, we collect the PL from the center of the pillar. Figure 4.6c. shows the PL intensity map as a function of the photon energy and of the applied voltage at 35K. By application of a negative voltage, the QD transitions redshift, with an increase of the signal when the exciton energy transition (X) is in resonance with the fundamental mode. Figures 4.6a. and 4.6b. show the PL spectra for 0V and -0.45V. By comparing the exciton lifetime for these two voltages, a Purcell factor of $F_P = 0.8 \pm 0.08$ was deduced in agreement with the quality factor ($Q = 1300$) of the cavity mode. At resonance, a brightness of 0.37 ± 0.07 was demonstrated. This brightness was partially limited by the presence of a charged exciton (visible in fig.4.6) as well as by the low value of the Q -factor.

In the third year of my PhD, a new generation of devices was fabricated by Niccolo

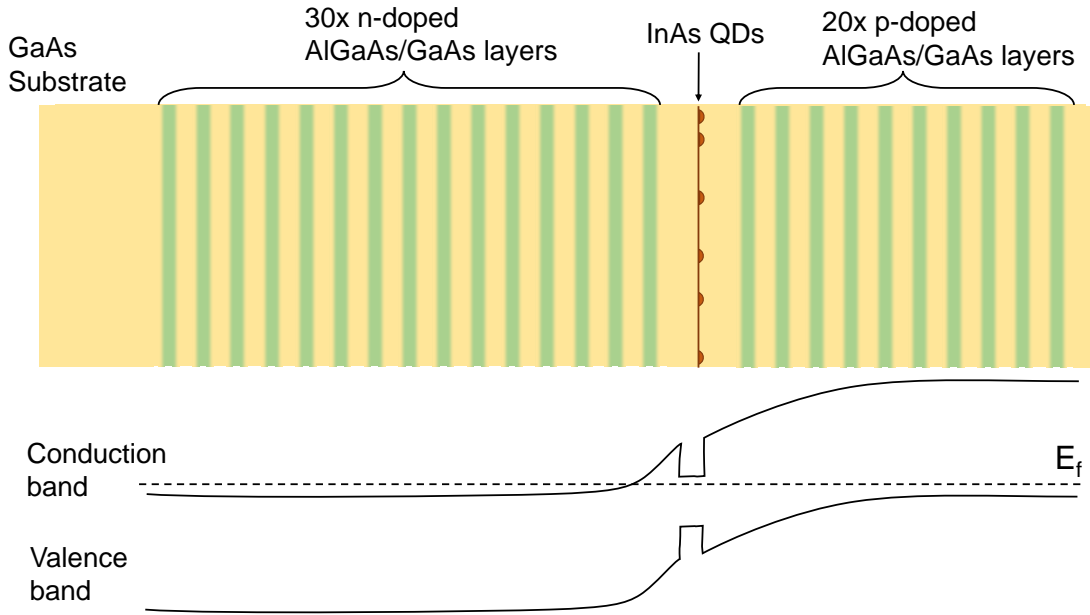


FIGURE 4.7: Top: Simplified description of the doped planar structure used to control the electronic environment of the QDs. Bottom: Simplified evolution of the conduction and valence in the planar structure. Fermi sea level is denoted E_f .

Somaschi. These new devices present a much higher Q -factor and a doping of the layers optimized to have a control of the charge in the QD.

4.1.3 Optimized Sample for the Control of Charges

Compared to the first generation of tunable sources, this generation is made with a higher Q -factor by increasing the number of pairs in the Bragg mirror in order to enhance the Purcell effect and the brightness. Moreover, since this new generation of devices is designed to emit single and indistinguishable photons under a pulsed excitation, we changed the structure of the doping in order to improve the charge control and to stabilize the Fermi level close to the QD. Figure 4.7 shows a simplified schematic of the doped structure and a simplified evolution of the conduction and valence bands. The bottom mirror is made of 30 $\text{Al}_{0.95}\text{Ga}_{0.05}\text{As}/\text{GaAs}$ pairs. These pairs are gradually Si n-doped (from $1 \cdot 10^{18} \text{cm}^{-3}$ to $2 \cdot 10^{18} \text{cm}^{-3}$). Similarly, the top mirror is made of 20 $\text{Al}_{0.95}\text{Ga}_{0.05}\text{As}/\text{GaAs}$ pairs, with a varying p-doping concentration up to $2 \cdot 10^{18} \text{cm}^{-3}$.

After the growth, an *in situ* lithography was performed. The main difference with the previously studied samples relies on the shape of the surrounding frame. To obtain cavities with minimized polarization splitting, we used another pattern: the surrounding frame is now circular and the wires are at 45° from the crystal axis as shown by fig.4.8. The geometry plays an important role for resonant fluorescence measurements as described in chapter 5.

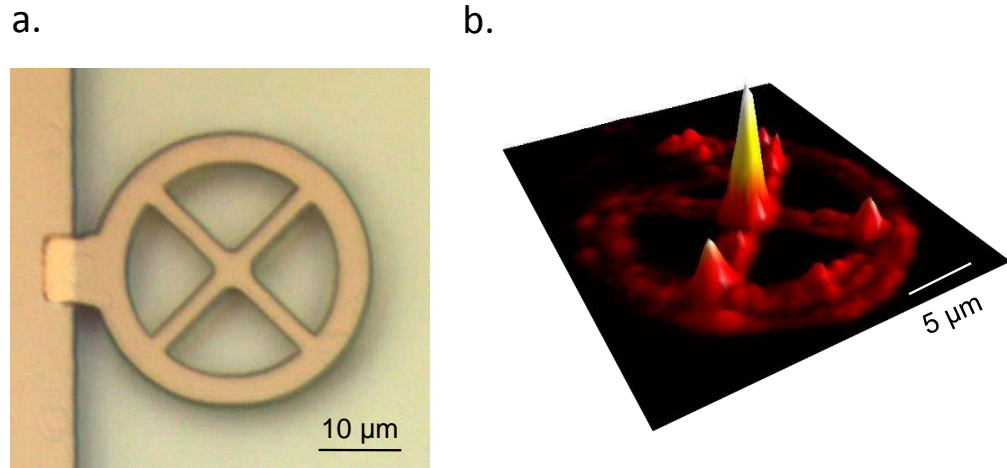


FIGURE 4.8: **a.** Optical image of one source from the second generation. **b.** PL map measured by horizontally scanning the sample in the *in situ* cryostat.

Once the connected pillars are etched and the ohmic contacts bonded, one can optically characterize the samples. Figure 4.9 shows a microscope photograph of the devices before the bonding. Three diodes (A, B and C) are made on this sample and 25 pillars in total are connected to the diodes. In the following, we show briefly the PL measurements of sources connected to diodes A and B.

4.1.4 Voltage Tunable PL

Figure 4.10**a.** shows the PL intensity as a function of the photon energy and of the voltage at 4K. All QD transitions evidence a shift over 0.5meV when the applied voltage changes. The quality factor of the fundamental mode of the cavity is $Q \sim 12000$, one order of magnitude higher than the first generation of devices. This Q -factor value is also of the same order of magnitude as the adiabatic source (chapter 3). Figure 4.10**b.** shows three PL spectra for various applied voltages. At -3V, the exciton emission line (X) is tuned to higher energies with respect to the cavity mode (CM). Other emission lines corresponding to other electronic states (CX) are visible.

Figure 4.11 shows the spectral positions of the exciton transition and of the fundamental mode of the cavity as a function of the voltage. As a dipole in an electric field, the exciton line position E_x evolves quadratically with the electric field F [74, 159]:

$$E_x(F) = E_0 - pF + \beta F^2 \quad (4.1)$$

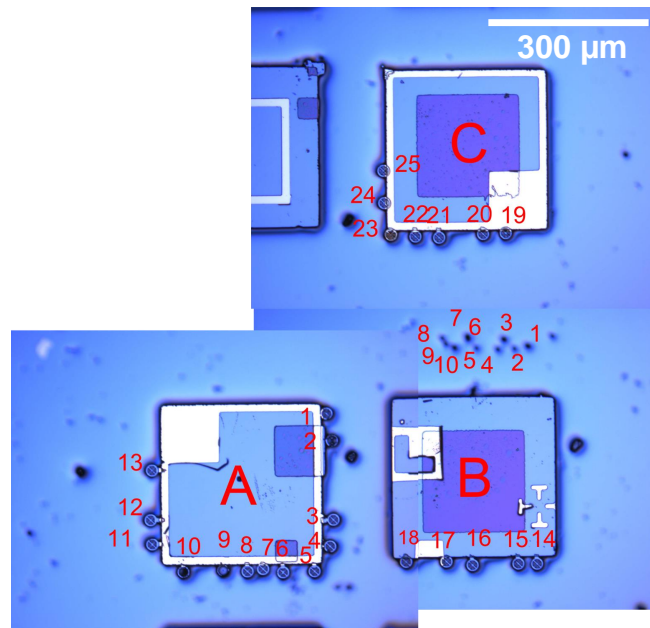


FIGURE 4.9: Microscope photograph of the three diodes denoted A, B and C. Each diode is connected to several devices made of a surrounding frame contacting the diode and a micropillar embedding a single QD.

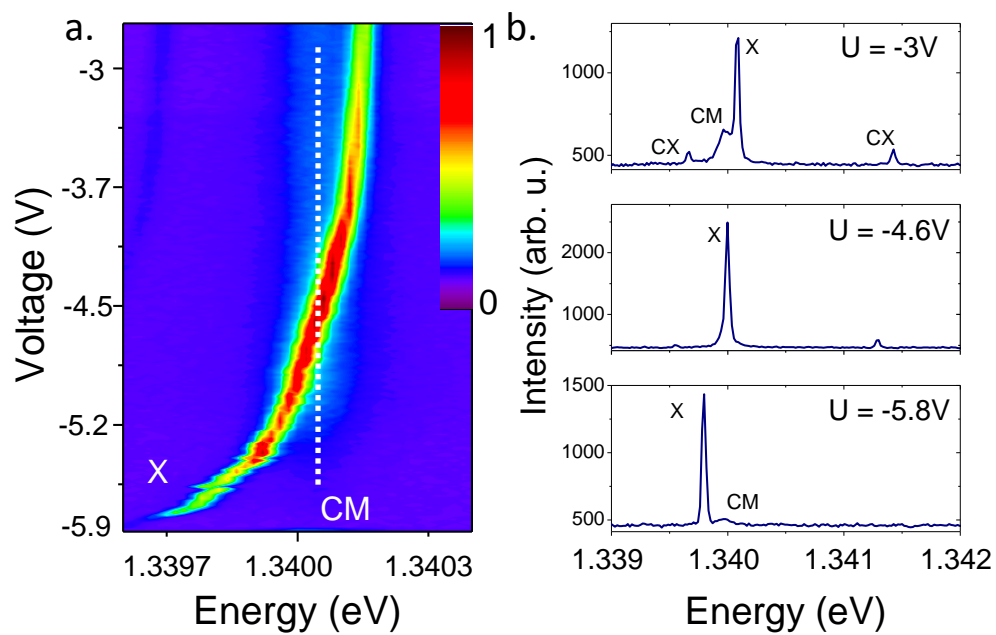


FIGURE 4.10: **a.** PL Intensity map as a function of the energy and of the voltage at 4K. **b.** PL spectra for different voltages at 4K.

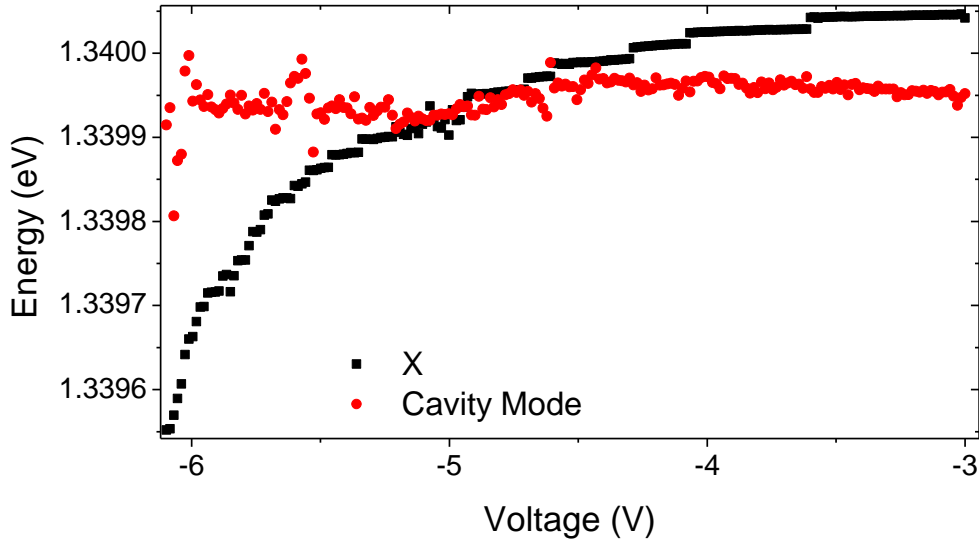


FIGURE 4.11: Measured energy of the exciton transition (black squares) and of the fundamental mode of the cavity (red points) as a function of the applied voltage.

where p is the permanent dipole moment and β the polarizability. Usually, the dipole moment p is neglected assuming an in-plane rotational symmetry confinement potential.

4.2 Full characterization of the Pillar 13A

4.2.1 Setup Transmission

To measure the PL from the electrically tunable sources, we used the helium bath cryostat that is usually used for the *in situ* lithography process in lab 2. As shown by fig.4.12, the laser used to excite the devices was located in lab 1. Laser pulses were coupled into a long single-mode fiber (SMF) which links the two labs. Then the PL is collimated by a microscope objective in the cryostat, it is filtered by a long pass filter and a polarizer and is coupled into another long SMF going to lab 1. There, the single photons are sent into a HBT interferometer as depicted by fig.4.12 or into the HOM interferometer described in chapter 3. Table 4.1 summarizes all the components and their losses at the wavelength of the emitted photons ; showing a total detection efficiency of 1.3 %.

4.2.2 Single-Photon Purity and Measured Brightness

The electrically tunable sources are quasi-resonantly excited by a mode-locked laser. Figure 4.13a. shows the time-resolved spontaneous emission when the QD transition is

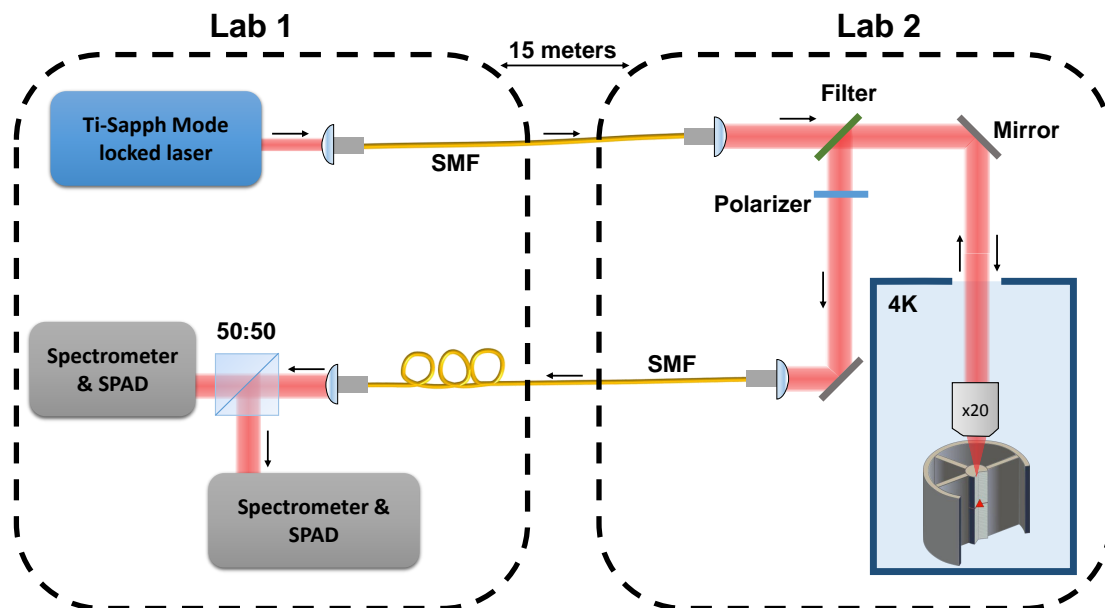


FIGURE 4.12: Schematic of the optical setup used to characterize the sample placed in the helium bath cryostat in lab 2.

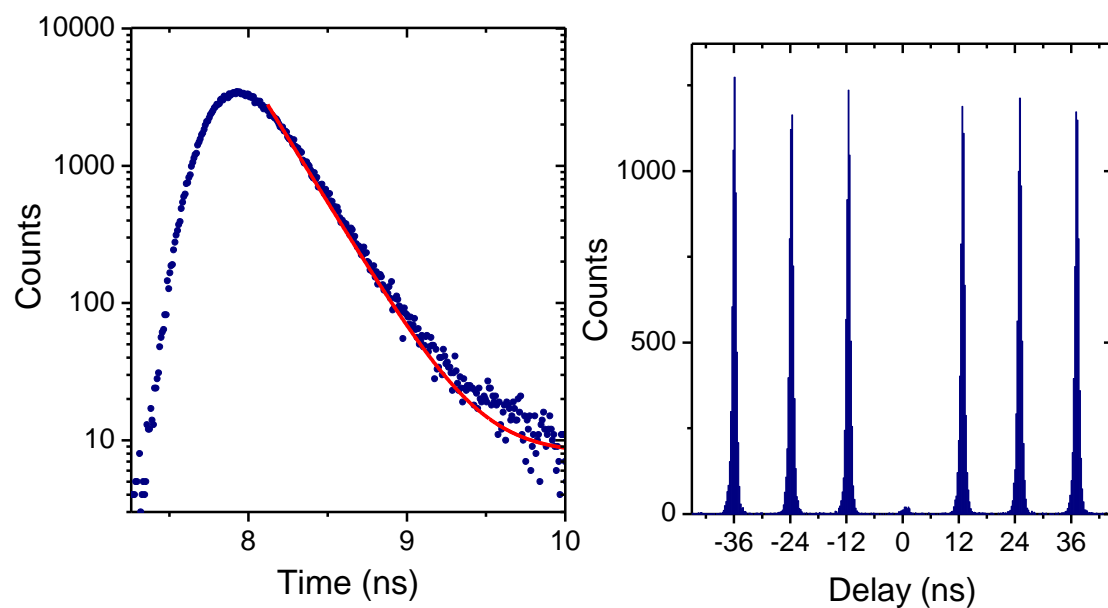


FIGURE 4.13: **a.** Time resolved PL when the exciton emission line is tuned in the cavity ($\delta_{X-CM} = 0\text{meV}$). The measured decay time after deconvolution by the time response of the setup is $190 \pm 20\text{ps}$. **b.** Pulsed autocorrelation function under a quasiresonant excitation. Here the extracted single-photon purity is $g^{(2)} = 0.04 \pm 0.01$. The acquisition time is equal to 1min30s.

Component	Transmission/Efficiency
Collection microscope objective	0.53
Cryostat window	0.9
Mirrors	0.70
Green dichroic mirror	0.95
Polarizer	0.85
Long pass filter	0.95
Coupling objective	0.69
Coupling efficiency	0.9
Fiber transmission	0.9
Detection	0.088
Overall setup	$1.3 \cdot 10^{-2}$

TABLE 4.1: Transmission and overall efficiency of all setup components. The detection refers to the transmission of the spectrometer with the detection efficiency.

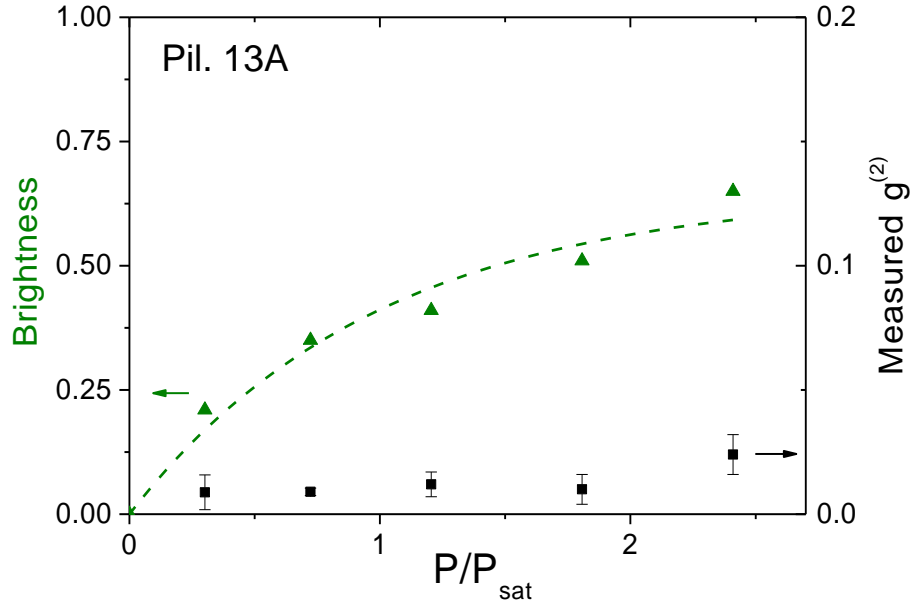


FIGURE 4.14: Pillar 13A: (Left axis) Measured and corrected brightness of the source under a pulsed quasi-resonant excitation. (Right axis) Measured $g^{(2)}$ under the same conditions

tuned on resonance with the cavity. After deconvolution with the response time of the setup, we extract a decay time equal to 190 ± 30 ps corresponding to a Purcell factor of 7 ± 2 . Such high Purcell factor leads to the emission of a large fraction of photons by the QD in the mode of the optical cavity ($\beta \approx 0.85$).

Figure 4.13b. shows a measured autocorrelation function of the pulsed emission from the device 13A corresponding to a $g^{(2)}(0)$ of 0.04 ± 0.01 .

Figure 4.14 summarizes our measurements as a function of the excitation power at 898 nm: black squares show the measured evolution of the single-photon purity $g^{(2)}$.

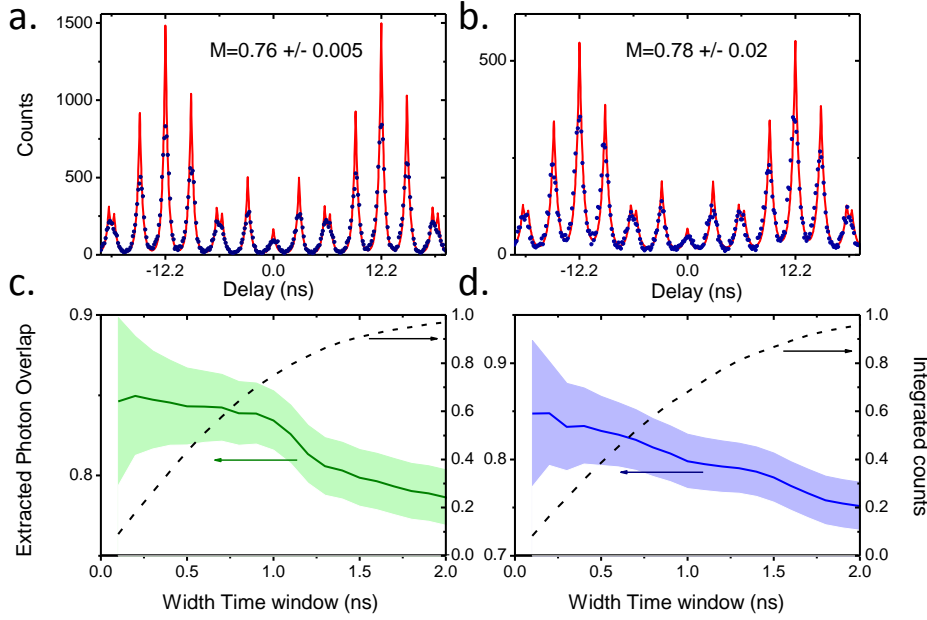


FIGURE 4.15: **a.-b.** Measured correlation histograms between the output of the HOM interferometer using the device 13A two consecutive days. The acquisition times are respectively $t_{\text{acq}}=17\text{min}$ and $t_{\text{acq}}=10\text{min}$. **c.-d.** Solid lines: Extracted mean photon overlap as a function of the size of the temporal windows considered to extract M . Dashed lines: Normalized fraction of the integrated counts as a function of the width of the window considered.

Up to saturation, the measured $g^{(2)}$ is around below 0.08. Green triangles show the derived brightness from the count rate and from the calibration given by the table 4.1. The dashed green line shows the theoretical behaviour of the exciton integrated intensity. The brightness is corrected by the multiphoton correction term $\sqrt{1 - g^{(2)}}$ assuming a poissonian noise. At saturation, the brightness of the source reaches 0.65 ± 0.07 showing that this device is the brightest electrically tunable single-photon sources to date. It corresponds to a fraction of emission in the mode $\beta=0.85$ and $\eta \cdot p_x \approx 0.8$. Considering the observation of charged exciton lines in fig.4.10b., we conclude that $p_x < 1$.

4.2.3 Indistinguishability of Successively Emitted Photons

To measure the photon indistinguishability, we use the HOM interferometer described in chapter 3.

Blue points on fig.4.15a. shows a measured histogram correlation between the two SPADs after the interferometer. For this experiment, the delay between the photons is 3.1 ns instead of 2.2 ns. As a consequence, the outside peaks of distinct periods overlap. The extracted mean photon overlap M is given by the peak area at 0ns using the same method as previously. Figure 4.15c. shows the evolution of the photon overlap M

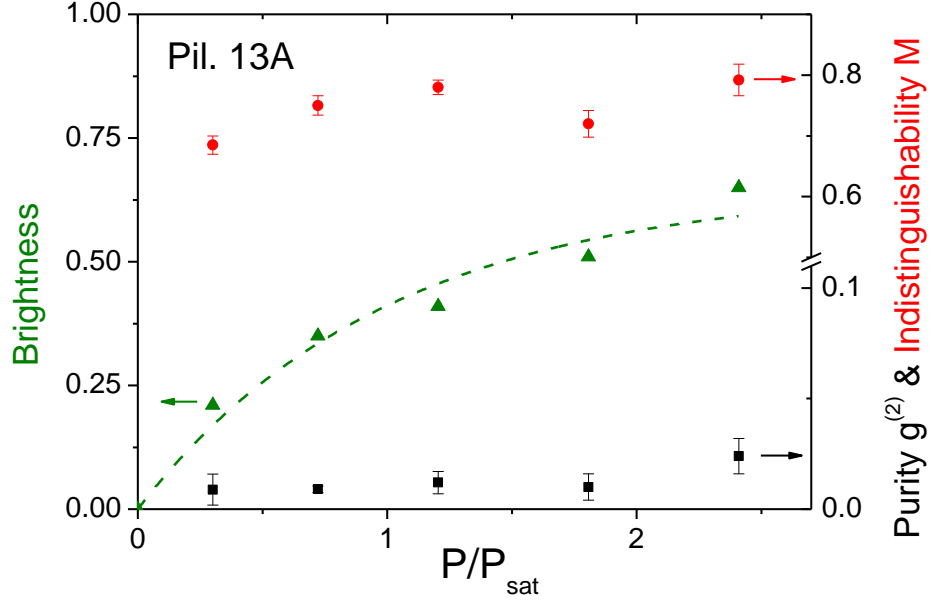


FIGURE 4.16: Measured evolution of the $g^{(2)}$ (black squares, right axis) of the photon indistinguishability M (red points, right axis) and of the brightness (green triangles, left axis) as a function of the pump power for pillar 13A.

(solid green line) and the normalized fraction of integrated counts (black dashed line) as a function of the temporal width considered for the analysis. By considering 80% of the integrated counts corresponding to a temporal width equal to 1.2ns, the extracted indistinguishability is $M=0.81\pm 0.02$ (fig.4.15a.). We repeated this measurement two consecutive days and we observed that the photon indistinguishability was stable as illustrated by fig.4.15b. and fig.4.15d. Considering a temporal window equal to 1.2ns, we extracted a photon indistinguishability $M=0.83\pm 0.02$. The red line in fig.4.15a. (b.) shows the theoretical correlation histogram considering $M=0.81$ ($M=0.83$).

This measurement was performed with an excitation power close to the saturation of the QD corresponding to a brightness of 0.65. The fast acquisition of a histogram with thousands of coincidences per peak is possible in order to measure the mean photon overlap with a high accuracy.

Figure 4.16 summarizes the measured mean wave packet of photons (red points) as a function of the excitation power. We observe that the measurement of photon indistinguishability is repeatable and it does not depend on the pump power. More interestingly, a mean photon overlap equal to 0.83 ± 0.02 is reached for maximum brightness (shown by the green triangles). Such indistinguishability is similar to the best M obtained by Gazzano et al. with a standard micropillar cavity using a two-color excitation scheme [31]. Yet, as shown in chapter 3, a such method was not universal and did not allow to get a high M at the maximum of brightness. Here, we measure a

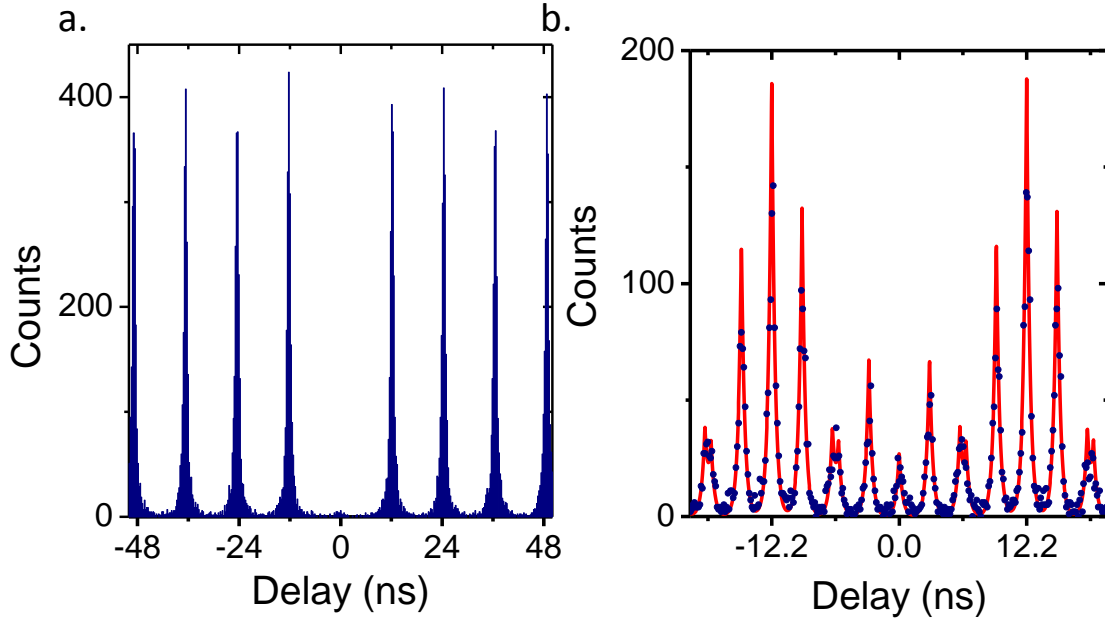


FIGURE 4.17: **a.** Measured autocorrelation function at the output of the HBT setup in order to measure the single-photon purity from the pillar 15B. The area of the central peak normalized by the lateral peaks gives $g^{(2)} = 0.01 \pm 0.005$. The acquisition time is equal to $t_{\text{acq}}=7\text{min}30\text{s}$. **b.** Measured autocorrelation function at the output of the interferometer. The area of the peak at 0ns gives the mean photon overlap. Acquisition time: $t_{\text{acq}}=8\text{min}$

high indistinguishability at saturation without any optical stabilization. It appears that the electronic environment is stabilized by the diode structure which sweeps the free carrier away from the QD. Such observations are consistent with transmission measurements obtained on gated sample that showed spectral linewidths close to the radiative limit[158].

4.3 Results on Another Device: 15B

Getting multiple bright source of indistinguishable sources is important for the development of a reliable quantum solid-state network.

The measured characteristics of another pillar (15B) are presented in this section.

The device is excited quasi-resonantly. Figure 4.17**a.** shows a measured autocorrelation function and a good single-photon purity ($g^{(2)} = 0.01 \pm 0.005$) is extracted. Figure 4.17**b.** shows a measured correlation histograms at the output of the HOM interferometer. As with the pillar 13A, a high mean wave packet overlap of $M=0.75 \pm 0.012$ is observed.

The measured performance of the pillar 15B is shown in fig.4.18. Green triangles show the measured brightness (left axis) while the red points and the black squares show the mean photon overlap and the $g^{(2)}$ (right axis) respectively. By exciting with a

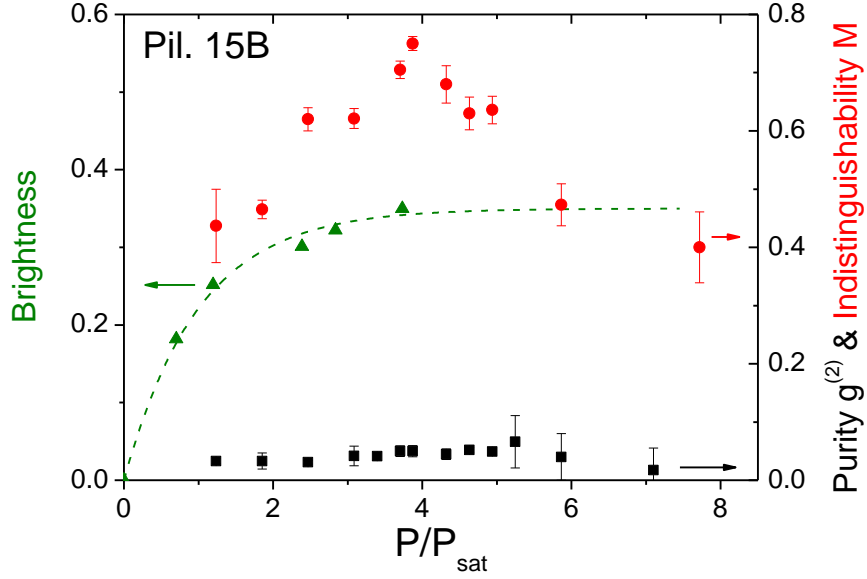


FIGURE 4.18: Measured evolution of the $g^{(2)}$ (blue diamonds, right axis) of the photon indistinguishability M (red circles, right axis) and of the brightness (black squares, left axis) as a function of the pump power for pillar 15B.

wavelength close to 900 nm, the probability for the QD to emit multiple photons stays low (with $g^{(2)}$ lower than 0.06 ± 0.02) as shown by the blue diamonds. The brightness at saturation reached about 0.35, lower than for the device 13A because of the QD state which is statistically in two states X and CX. At maximum brightness, we measured an indistinguishability as high as 0.81 ± 0.05 .

4.3.1 Excitation-Jitter-limited Indistinguishability

We studied two sources showing high photon indistinguishability at high brightness without the need of another light beam to stabilize the surrounding environment. Moreover, the fine tuning of the exciton transition in resonance with the mode allowed us to perform measurements at 4K, which reduces the effect of the phonons bath.

At this point, the fact that all measured indistinguishabilities reach a maximum value in the 75-85% range questions the limits imposed by the excitation scheme. Indeed, charges created at a higher discrete levels than the exciton energy level take some time to relax τ_{relax} . At 4K, this time is about few dozens of picoseconds [78]. This relaxation mechanisms introduce an uncertainty on the starting time of the photon emission, an uncertainty sometimes referred to as a "time-jitter".

The effect of the time-jitter has been theoretically studied by Kiraz, Atature and Imamoglu in 2004 [162]. Considering a phonon assisted relaxation process, they showed that the two-photon interference is degraded by the information about the photon arrival time

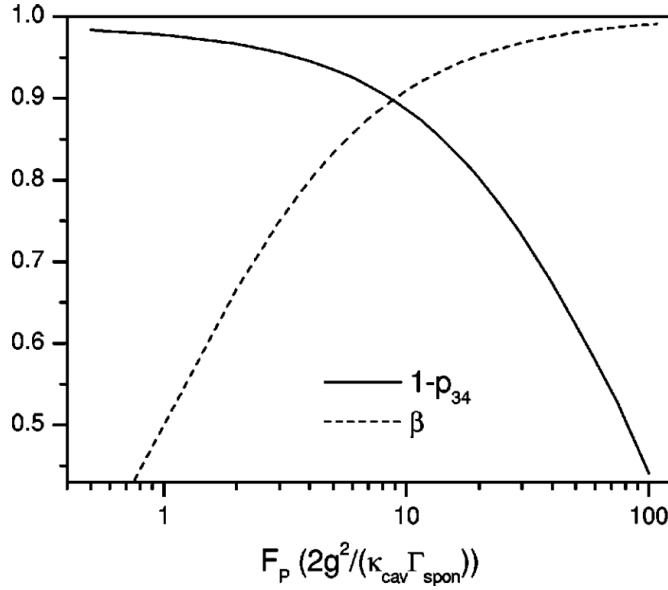


FIGURE 4.19: Figure reproduced from [162]. Calculated evolution of the mean photon overlap (solid line) and of the fraction of emitted photons in the cavity (dashed line) as a function of the Purcell effect F_P .

carried by the phonon reservoir. They showed that this time-jitter was more detrimental when the spontaneous emission is accelerated with the Purcell effect, as illustrated by the theoretical curve shown on fig.4.19. The solid line represents the evolution of the indistinguishability as a function of the Purcell factor (logarithmic scale). The dashed line represents the fraction of photons that are emitted in the cavity mode $\beta = F_P/(F_P + 1)$. This calculation evidences that a relaxation time must be much shorter than the radiative time to preserve a good two-photon interference independently of the photon coherence. For instance, if the photon decay time is similar to the relaxation time τ_{relax} , the maximum achievable indistinguishability is lower than 0.45.

In our case, if we consider that the relaxation time is about $\tau_{\text{relax}} \sim 10\text{ps}$ at 4K and a Purcell factor around 10, the predicted maximum indistinguishability is around 0.85. This value is extremely close to our experimental observations indicating that the two-photon interference visibility is probably limited by the incoherent intra-dot relaxation of the charges and not by the coherence of the photons.

We present in the next chapter the implementation of the resonant excitation on these devices.

4.4 Conclusion

This chapter presented the deterministic fabrication of electrically controlled single-photon sources using an advanced *in situ* lithography technique. Two generations of

samples were fabricated, the first one presented a Q -factor around 1000, a Purcell factor of $F_P = 0.8$ and a brightness of 0.37 ± 0.07 [163]. The second one exhibits a Q -factor around 12000 and a Purcell factor as high as 10 ± 2 leading to a brightness as high as 0.65 ± 0.07 . Furthermore, a high photon indistinguishability with 75-85% was measured for two devices under only one quasi-resonant excitation at maximum brightness, evidencing the efficient control of the electronic surrounding via the diode structure. This new generation of single and highly indistinguishable photon sources with a brightness at the state-of-the-art is already very appealing for some quantum optics applications. As explained in chapter 7, boson sampling experiments do not require very high degrees of indistinguishability, but high brightness is really critical.

Comparing our measurements with theoretical studies indicates that the photon indistinguishability is now limited by the time jitter. In the carrier generation process, this effect introduces an uncertainty on the time of photon emission that is all the more important than the spontaneous emission is accelerated. The next chapter will present the resonant excitation of the same devices, confirming this analysis.

Chapter 5

High Indistinguishability and High Brightness from Resonant Fluorescence Spectroscopy

5.1 Introduction

In the previous chapters, two different designs of sources operating in a high Purcell regime were studied. In chapter **3**, the indistinguishability of photons emitted by QD-pillar devices was limited by the charge noise. In chapter **4**, the photon indistinguishability was improved with respect to devices in chapter **3** by implementing an electronic control of the charge. However it was limited by the time-jitter induced by the quasi-resonant excitation [162]. In both cases, a state-of-the-art brightness in the 60-80% range was combined with a photon indistinguishability of 75-80%.

To reach higher photon indistinguishability, we decided to implement a resonant optical excitation of the QD transition. In the last few years, the resonant excitation of a single QD has been demonstrated and the resonance fluorescence of QDs was measured [164–166]. The Mollow triplet of the resonant fluorescence was also observed [167] and studied [168]. In 2013, Monniello et al. [169] studied the dephasing induced by a pulsed resonant excitation. The challenge for resonant pumping is to separate the exciting laser light from the fluorescence. To get a good signal-to-noise ratio between the excitation and the emitted photons, an orthogonal excitation geometry was implemented where the QD was excited by the laser perpendicularly to the collection axis.

In 2009, a high degree of photon indistinguishability was demonstrated under a continuous-wave (CW) excitation by Ates et al. [39]. The QDs fluorescence was collected vertically along the axis of the pillar as illustrated by fig.5.1**a-b**. Using a CW excitation, a visibility of 0.90 ± 0.05 was extracted by post-selecting the coincidences at zero delay with

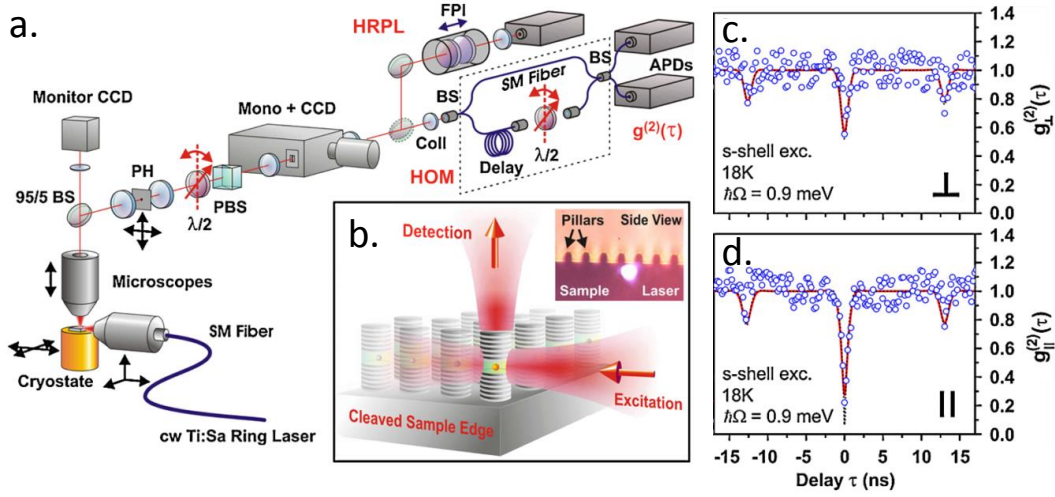


FIGURE 5.1: Figure reproduced from [39]. **a.** Schematic of the experimental setups for photoluminescence (PL) and photon statistics. **b.** Orthogonal excitation-detection geometry on individual micropillars. Inset: sideview of micropillars at the cleaved sample edge. **c.** (**d.**) Two-photon interference data under orthogonal (parallel) polarizations of the interferometer arms.

a low excitation power. Due to the low excitation power, the results were quite noisy as seen in fig.5.1c. and d. and the value of the indistinguishability after the deconvolution from the detector time jitter was 0.9 ± 0.05 .

In 2014, Monniello et al. [41] used a similar excitation scheme for a QD in a waveguide (as shown in fig.5.2c.) to study the photon indistinguishability emitted by a QD. Under a pulsed excitation, a photon indistinguishability greater than 0.7 was reported without any postselection. Figure 5.2a. shows the difference of radiative lifetimes under non resonant (red stars) and resonant excitation (black squares). The observed difference was due to the relaxation of charges induced by non resonant excitation. By using a Michelson interferometer with a variable path length δt (FTIR), the impact of the non resonant excitation on the degradation of coherence was measured and given by T_2 as shown in fig.5.2b. This degradation was attributed to the creation of multiple charges around the QD during the non resonant excitation.

In 2013, He et al. used a pulsed resonant excitation to demonstrate a near-unity photon indistinguishability of 0.97 ± 0.02 in a pulsed regime [40]. Contrary to previous works, the laser excitation was separated from the PL by using a cross-polarization configuration: in a planar structure, a single QD was excited from the top of the sample along one polarization axis while the detection polarization was chosen to be orthogonal in order to extinct the laser light. To increase the signal-to-background ratio, a 20 GHz etalon

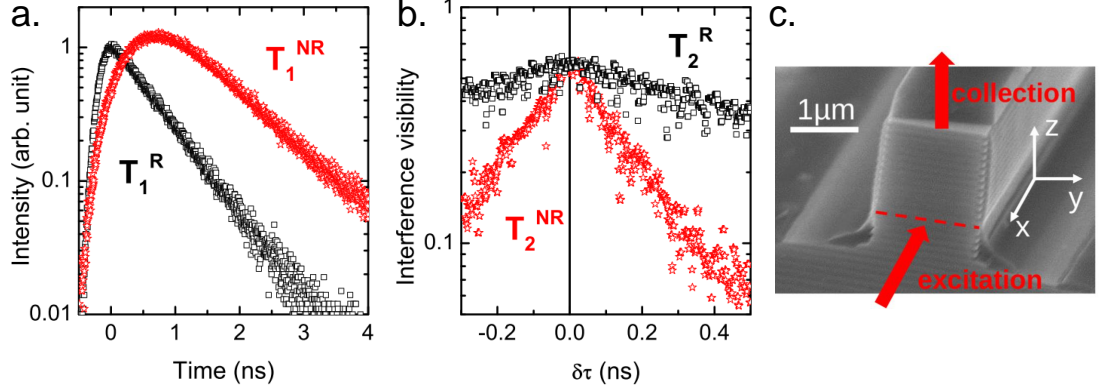


FIGURE 5.2: Figure reproduced from [41]. **a.** Lifetime measurements (semilog scale) for resonant (black squares) and nonresonant (red stars) excitation. The decays give $T_1^R = 670$ ps and $T_1^{NR} = 850$ ps. **b.** Fourier transform spectra (semilog scale) for resonant (black square) and non resonant (red stars) excitation yielding the coherence times $T_2^R = 950$ ps and $T_2^{NR} = 200$ ps.

was added on the detection line in order to eliminate the residual laser background. This result was very promising for applications that would require highly indistinguishable photons. Nevertheless, the QDs were embedded in a planar cavity providing a low Q -factor (~ 200) hence a low photon extraction and a low brightness estimated to be below 3%.

In this chapter, we use the electrically tunable sources presented in chapter 4 and perform a pulsed resonant excitation of the QD. By collecting the PL in a crossed-polarization configuration, we measure the indistinguishability of the photons that are successively emitted.

5.2 Setup Used for the Resonant Excitation

In this section, we describe the experimental setup used in order to perform the resonant excitation of our connected pillar sources.

Figure 5.3 shows a simplified schematic of the setup. To get the highest signal-to-background ratio, defined as the ratio between the collected PL from the device to the collected scattered laser light, the excitation and collection path are in a crossed-polarization configuration like in He et al.[40]. The excitation beam, sent from the top of the pillar, is linearly polarized along one direction. As explained later, due to a finite fine structure splitting of the QD transition, the QD emits PL along all polarizations.

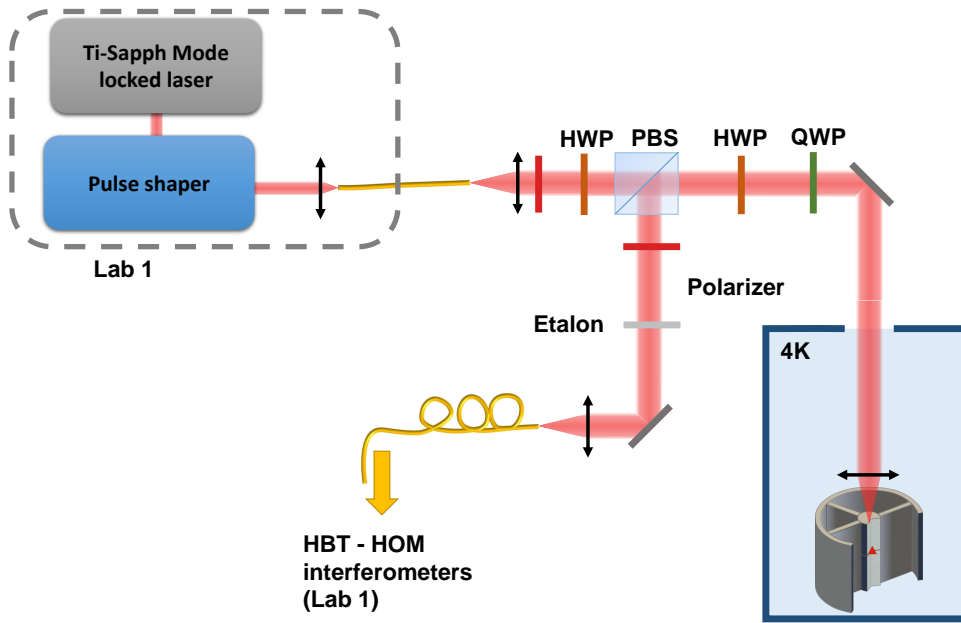


FIGURE 5.3: Schematic of the crossed-polarization configuration. The device is excited along one linear polarization while the signal is collected along the orthogonal polarization. **PBS**: Polarization Beamsplitter, **HWP**: Half-wave plate, **QWP**: Quarter-wave plate

Only the polarization orthogonal to the excitation is collected. The excitation beam is coupled to a SMF in lab 1 as in chapter 4 and is collimated by using a microscope objective in the setup located in lab 2. A polarizer, a half-wave plate (HWP) and a polarizing beamsplitter (PBS) are used to select a linear polarization. This polarization is rotated using a second HWP after the PBS in order to be parallel with respect to the cavity modes axes. The effects of possible birefringent optical elements (mirrors, cryostat window,...) are compensated using a quarter-wave plate (QWP). The signal emitted by the sample is reflected by the PBS and filtered by an additional polarizer in order to improve the signal-to-laser ratio. This signal is finally coupled to a SMF in a confocal geometry. An extinction ratio of the laser light of around 10^{-5} is measured using this configuration.

Our objective is to excite the QD by sending resonant pulses through the optical mode of the pillar. However, the pulses of the mode-locked laser are 3ps-long, shorter than the cavity decay time (~ 10 ps for a Q -factor around 10^4). In the spectral domain, the pulse spectrum, three times wider than the cavity linewidth, results in a large fraction of reflected light by the cavity. To match the pulses to the cavity mode, laser pulses are temporally shaped using of a monochromator and a fixed Fabry-Perot cavity (etalon). This etalon is a few millimeter thick glass with reflection coating. It presents a nominal FWHM of $11\mu\text{eV}$ and a free spectral range of $200\mu\text{eV}$, much smaller than the spectral width of the 3ps pulsed as shown by fig.5.4a., where the spectrum of the light transmitted

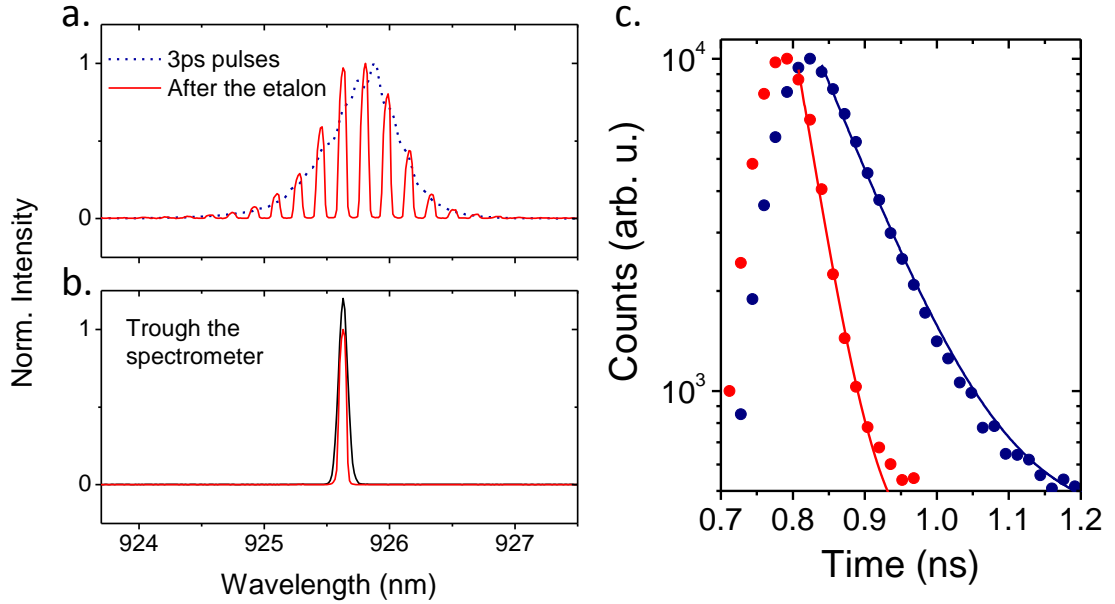


FIGURE 5.4: **a.** Measured spectra of the laser pulses (blue dashed line) and of the transmitted pulses through the etalon (red solid line). **b.** Spectra of the pulses after the spectrometer (black line) and after the spectrometer plus the etalon (red line). **c.** Measured temporal profile of the pulses after the spectrometer (red points) and after the spectrometer and the etalon (blue points). Solid lines are exponential fits.

by the etalon is composed of several peaks. We use a monochromator made of a dispersive grating and a slit to implement a first spectral filtering of the laser pulse (up to 10ps). Figure 5.4**b.** shows the laser spectrum after the spectrometer with or without the etalon. Figure 5.4**c.** shows the temporal profile of the pulses after the spectrometer only (red points) and after the spectrometer and the etalon (blue points) measured with SPAD with a 30ps resolution. Using both temporal and spectral informations, we can estimate that for the example of fig.5.4, the pulse after the spectrometer is 25ps long while after the etalon, the pulse is 75ps long before the cavity. The pulse duration can be modified on demand by tilting the etalon or by focusing or defocusing the lenses focusing on the spectrometer's slit.

In this experiment, the polarization axis of the excitation and of the collection are orthogonal. Exciting the QD through the cavity mode demands that both axis are aligned along the cavity axis. Indeed, if the cavity is not perfectly circular, it behaves as a waveplate for a laser polarization not aligned along one of its axis. Due to the 1D wires connecting the pillar with the surrounding frame, the cavity optical modes are linearly polarized.

We study the pillar 18 from diode B under non resonant excitation. Figure 5.5**a.** shows two PL spectra under a non-resonant excitation for two different PL polarizations. The cavity mode is splitted in the two linear polarizations of the collection. Figure 5.5**b.**

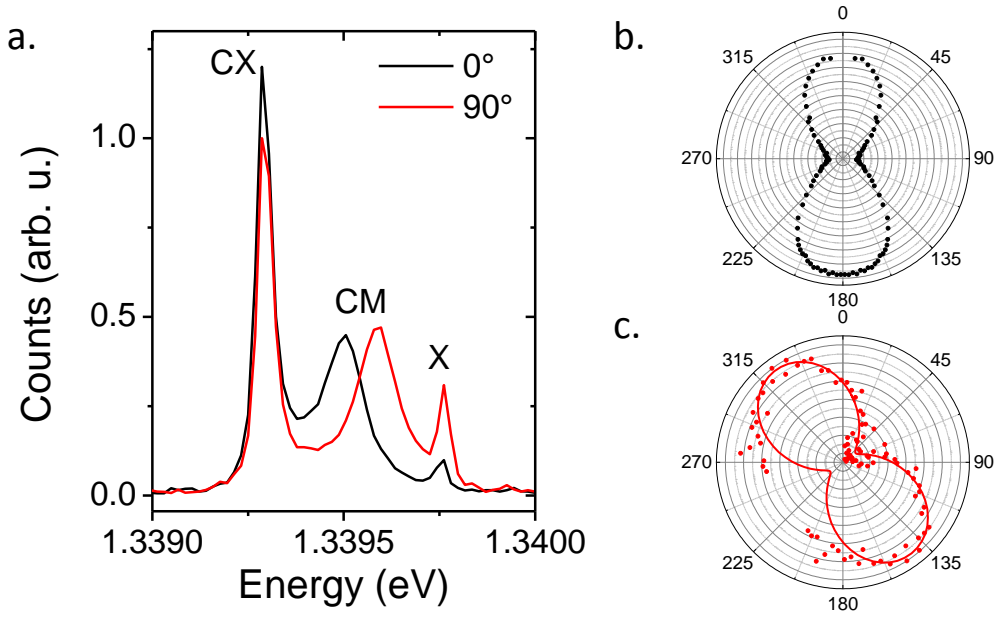


FIGURE 5.5: **a.** PL spectra of the device 18B under a non-resonant excitation as a function of the linear polarization. **b-c.** Relative spectral position of the cavity mode **b.** and of the exciton line **c.** as a function of the polarization angle. The zero has been chosen to be along the higher energy mode of the cavity.

shows the spectral position of the cavity emission line as a function of the polarization axis of the collected PL relative to its average energy. We define the horizontal (H) mode (0° - 180°) as the polarization of the higher energy mode and the polarization of the vertical (V) mode (90° - 270°) as the lower energy mode. The measured difference of energy between the two modes is equal to $71 \pm 2 \mu\text{eV}$ for a cavity linewidth of $120 \mu\text{eV}$. Under the same experimental conditions, the fine structure splitting of the exciton transition is also observed. Figure 5.5c. shows the relative spectral position of the exciton emission line as a function of the polarization axis. Comparing with fig.5.5b., we see that the fine structure axis of the QD is shifted by an angle approximately equal to 35° from the cavity axis. This observation is not a coincidence, but is related to the fact that the 1D wires are $\sim 5^\circ$ from the crystal axes. The spectral amplitude of this splitting, measured around $13 \pm 3 \mu\text{eV}$, is much smaller than the cavity one. The QD axis are later called $|X\rangle$ and $|Y\rangle$.

In the following, the laser emission energy is always tuned in resonance with the H mode of the cavity and is linearly polarized along this mode. Exciting along one of the cavity axis ensures that a linear polarization is maintained in the cavity. Moreover, a H polarized excitation excites a linear superposition of the $|X\rangle$ and $|Y\rangle$ exciton states. The beating between $|X\rangle$ and $|Y\rangle$ states leads to an emission collected along the V-axis. The electrical bias applied to the device is used to tune the QD transition in resonance with the laser and the H cavity mode. Figure 5.6a. shows a series of PL spectra under

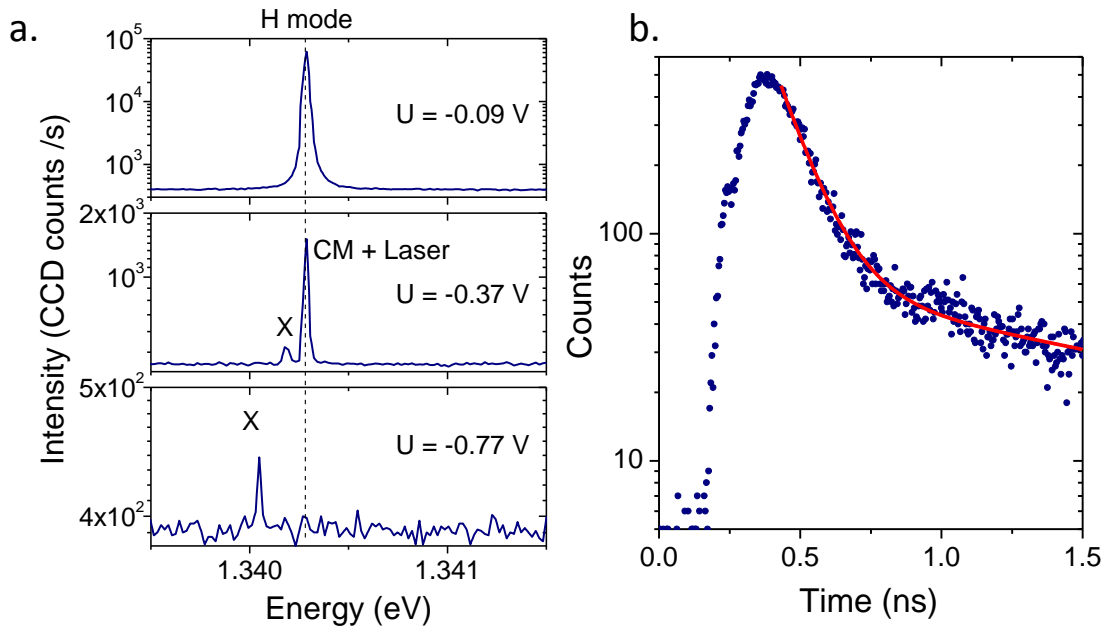


FIGURE 5.6: **a.** PL spectra under a CW resonant excitation (at 1.3403 eV) for various applied voltage. Emission line associated to the exciton transition is marked as X. **b.** Blue points: Measure time-resolved PL of the exciton emission line in resonance with the laser. Red solid line: Double exponential fit with a decay time equal to 112ps and to 1.6ns.

a CW excitation for different applied voltages. For an applied voltage $U=-0.77V$, signal from the scattered laser around 1.3403eV is in the noise while the exciton emission line is visible around 1.340eV. The QD transition is then tuned in resonance with the laser controlling the voltage.

In order to increase the ratio between the collected light and the scattered laser light, the HWP and QWP angles are very finely adjusted.

Figure 5.7 shows an example of PL intensity map when the polarizing elements are optimally aligned. The collected PL intensity along the V mode is plotted as a function of the photon energy and of the electrical bias voltage. At a very negative voltage, the QD exciton (X) transition is far detuned from the excitation and the scattered laser light is in the noise. When the X transition is brought in resonance with the laser and with the cavity mode (around -0.1V), the collected signal increases by four orders of magnitude. Note that the observation of a QD signal far from the QD-laser resonance is a signature of the coupling of the exciton with phonons leading to a phonon assisted QD emission at different energy from the laser.

Using a 15ps pulse, we measure the time-resolved PL emission when the QD is on resonance with the laser (blue solid line) with $U=-0.09V$ as shown in fig.5.6b. By fitting it with an exponential decay (red dashed line), we extract a decay composed of two

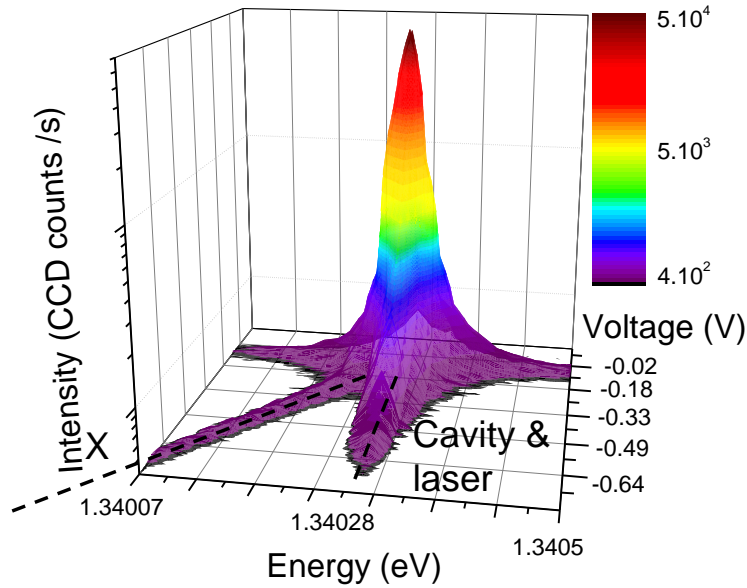


FIGURE 5.7: Collected PL intensity map under a resonant excitation as a function of the photon energy and of the applied voltage.

exponentials: the first decay time is 112 ± 10 ps evidencing a Purcell factor of around 12 ± 2 and the second decay is about 1.6 ns. There is not clear explanation for the second decay but it might be related to the response of the detector.

5.2.1 Reflectivity Measurements

In this part, we fully characterize the parameters of the pillar 18B using reflectivity measurements.

Measuring the reflectivity of one pillar embedding a QD allows extracting precisely the cavity parameters, the input coupling of the beam into the cavity and the QD-cavity coupling. The first reflectivity setup was developed in the group during the PhD of Vivien Loo under the supervision of Loic Lanco [170]. It allowed demonstrating the optical nonlinearity by sending laser pulses containing only few photons on a QD-pillar device in 2012 [171] and to measure the Faraday rotation induced by a single spin [172]. The same principle is used here and illustrated by fig.5.8a. A CW tunable laser focused on the pillar, is reflected by the cavity and sent to a detector. The intensity of the reflected light is collected and measured as a function of the laser energy. Figure 5.8b. shows the measured signal when the QD is detuned from the cavity (top panel). A reflectivity dip is observed corresponding to the cavity resonance. From the value of the reflectivity at the cavity energy, we can measure the coupling of the pillar through the

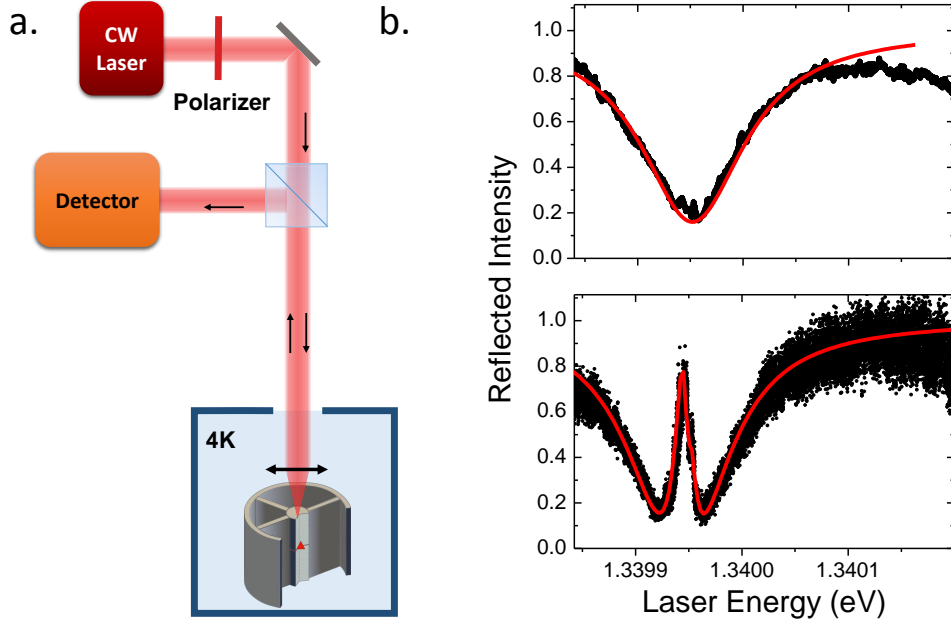


FIGURE 5.8: **a.** Simplified schematic of the setup to measure the reflectivity of one device. **b.** Measured reflectivity at low power (black points) and theoretical fit (red line).

top mirror $\kappa_{\text{top}}/\kappa$ (see section 2.5 in chapter 2) [170]:

$$R_{\text{min}} = \left(1 - \frac{2\kappa_{\text{top}}}{\kappa}\right)^2 \quad (5.1)$$

We extract two possible values for the output coupling: $\kappa_{\text{top}}/\kappa = 0.7 \pm 0.05$ or $\kappa_{\text{top}}/\kappa = 0.3 \pm 0.05$. Considering that the mirrors of the cavity are highly asymmetric (with 30/20 pairs) and that a high brightness value was measured previously (corresponding to a large fraction of photons being released by the top), we deduce that $\eta = \kappa_{\text{top}}/\kappa = 0.7 \pm 0.05$. The width of the cavity mode gives an accurate value of the cavity damping $\kappa = 120 \mu\text{eV}$ corresponding to a Q -factor equal to $Q = \omega_c/\kappa = 11000$ where ω_c is the fundamental mode energy of the cavity.

By changing the electrical applied bias, the exciton transition is tuned into resonance with the cavity. The exciton transition appears as the narrow peak in the middle of the cavity resonance as shown by the bottom panel in fig.5.8. The height of the peak depends on the coupling strength between the QD and the cavity Ω_1 and on the coherence rate $\gamma_{\text{refl}} = \gamma_{\perp}/2 + \gamma^*$ [171], where γ_{\perp} is the spontaneous emission rate in the other modes and γ^* the pure dephasing rate as defined previously. By fitting the measured reflectivity with a model developed by Justin Demory during his PhD, a coupling strength equal to $\Omega_1 = 21 \pm 2 \mu\text{eV}$ and a coherence rate equal to $\gamma_{\text{refl}} = 0.35 \pm 0.15 \mu\text{eV}$ are extracted. This value corresponds to a radiative lifetime in the other radiative channels that are not coupled with the mode of cavity of 1 ns [33] and a negligible pure dephasing of the

state. The device cooperativity defined as $C = \Omega_1^2/\kappa\gamma$ reached the very high value of $C=13$ in a regime of strong Purcell effect.

Furthermore, the measured reflectivity presents a little shoulder on the higher energy side of the peak. This shoulder is attributed to the energy splitting of the exciton fine structure. By taking into account the fine structure splitting, the fit (red line) is in an excellent agreement with the measurement with a splitting of $4 \pm 1\mu\text{eV}$. The splitting value is different from the measured splitting value in fig.5.5. Indeed, we observe that the fine structure differs from one experimental condition to another for the same QD. Depending on the excitation conditions, we observed that the applied voltage to tune the QD in resonance with the mode is different. Under a CW non resonant excitation, a CW resonant excitation or a pulsed resonant excitation, the electric field seen by the QD is always different. This can be attributed to a charge screening or to a flattening of the bands induced by the excitation: excited electrons and holes are swept in opposite directions and screen the field as observed in [74]. This effective field leads to a modification of the fine structure splitting and to a spectral shift of the exciton transition as shown in [157].

5.3 Emission Mechanisms in Crossed Polarization

We discuss here the emission mechanisms under resonant excitation in a configuration where the emitted signal is orthogonal to the excitation. We first describe them qualitatively and then we describe the used theoretical model.

5.3.1 Qualitative Discussion

To simplify, we assume that the QD axis are at 45° from the cavity axis. When exciting the QD with a H polarized light, we create an exciton state $|H\rangle = \frac{|X\rangle+|Y\rangle}{\sqrt{2}}$. Collecting a signal in V polarization corresponds to an exciton state $|V\rangle = \frac{|X\rangle-|Y\rangle}{\sqrt{2}}$. In the absence of a fine structure splitting, the $|H\rangle$ state is an eigenstate of the system which does not evolve over time. As a result, no signal is expected in V polarization for $\Delta_{FSS} = 0$. In the presence of a fine structure splitting ($\Delta_{FSS} \neq 0$), the exciton state $|\phi(t=0)\rangle = \frac{1}{\sqrt{2}}(|X\rangle+|Y\rangle)$ evolves into $|\phi(t)\rangle = \frac{1}{\sqrt{2}}(e^{i\omega_X t}|X\rangle+e^{i\omega_Y t}|Y\rangle) = \frac{e^{i\omega_X t}}{\sqrt{2}}(|X\rangle+e^{i\Delta_{FSS}t/\hbar}|Y\rangle)$ with $\Delta_{FSS} = \hbar(\omega_X - \omega_Y)$. After a time $t \propto \frac{\pi}{\Delta_{FSS}}$, the $|\phi(t)\rangle$ presents a maximal overlap with the $|V\rangle$ state. Both $|H\rangle$ and $|V\rangle$ exciton states can radiatively decay in the cavity H and V modes respectively. The collected PL is thus related to the spontaneous emission of the $|V\rangle$ exciton state in the V mode of the pillar. The higher the splitting, the faster the evolution of the state is. In practice, the polarization rotation time induced by the

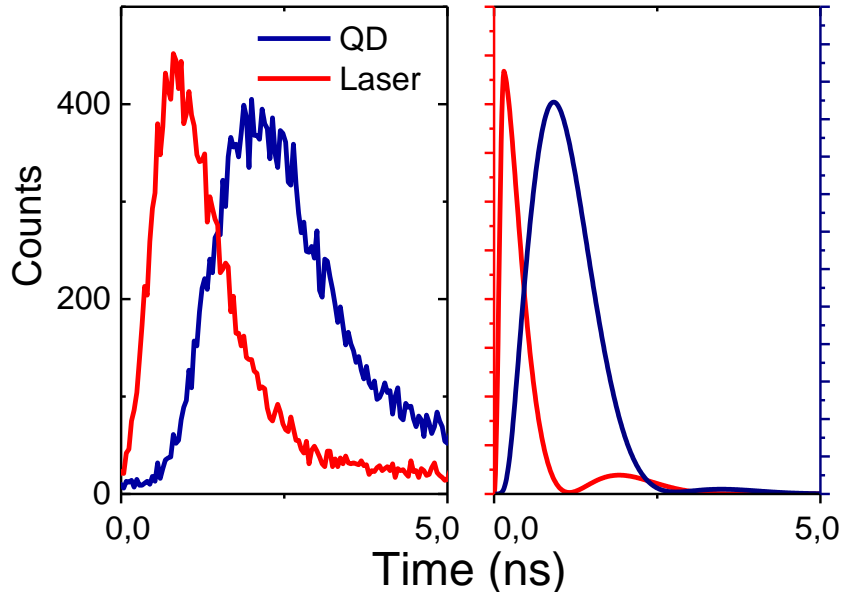


FIGURE 5.9: **a.** Measured time resolved photoluminescence from the QD in crossed polarization (blue line) and reflected laser pulse (red line). **b.** Calculated temporal evolution of the photon emission in the mode V (blue line) and evolution of the population of the state $|H\rangle$ (red line) with $\Delta_{FSS} = 15\mu\text{eV}$

FSS is of the same order as the accelerated radiative decay time. Thus, no oscillations of the $|V\rangle$ population are observed.

Figure 5.9a. shows the measured time-resolved PL in the V polarisation (blue line) and the reflection of the laser on the sample (red line). An important delay between the laser excitation (red solid line) is observed showing the delay of the rotation of the polarization. In comparison, fig.5.9b. shows the calculated evolution of the population of the state $|H\rangle$ (red solid line) and the evolution of the emission from the V mode (blue solid line) for a 15ps-long excitation pulse. A splitting of $\Delta_{FSS} = 15\mu\text{eV}$ is considered corresponding to a typical time of 80 ps which is a good order of magnitude with the observed delay. This value is different from previously because of the different effective field induced by the excitation in pulsed regime. This model has been developed by Gaston Hornecker in Alexia Auffèves's group in Grenoble and is described in the next part.

5.3.2 Theoretical Model of the Emission in Crossed Polarization

A three-level system ($|X\rangle$, $|Y\rangle$ and $|0\rangle$) is considered for the exciton states. They are coupled to two cavity modes $|H\rangle$ and $|V\rangle$ as illustrated in fig.5.10. The populations corresponding to a $|X\rangle$, $|Y\rangle$, $|H\rangle$ or $|V\rangle$ exciton states are noted P_X , P_Y , P_H and P_V . The

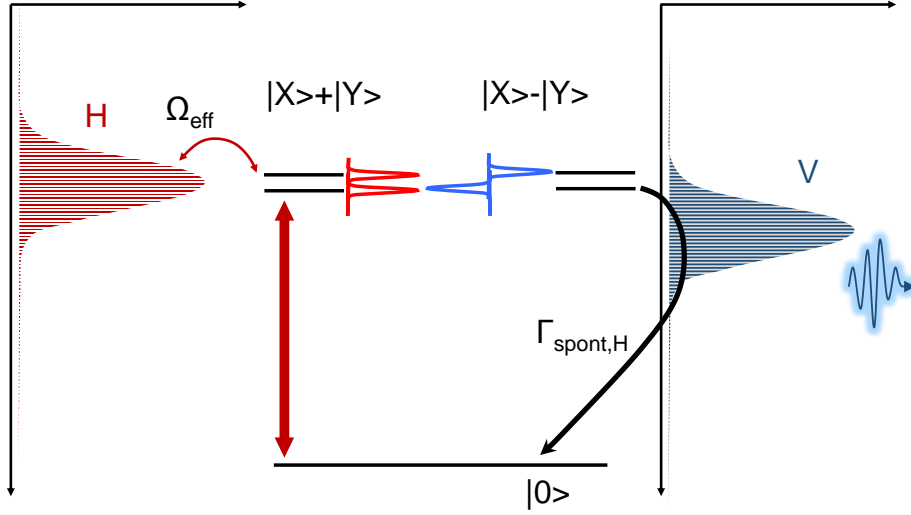


FIGURE 5.10: Schematic of the theoretical model used to calculate the resonant PL.

states $|X\rangle$ and $|Y\rangle$ are tilted by an angle θ to the cavity axis such that

$$\begin{aligned} |H\rangle &= \cos\theta|X\rangle + \sin\theta|Y\rangle \\ |V\rangle &= -\sin\theta|X\rangle + \cos\theta|Y\rangle \end{aligned} \quad (5.2)$$

In the following, the angle between the fine structure axis with the cavity modes is considered as equal to 45° . We observe negligible influence of this parameter in the $35\text{-}55^\circ$ range. The average energy of the QD $|X\rangle$ and $|Y\rangle$ states is resonant with the H mode of the cavity and detuned from the V mode of the cavity by $70\mu\text{eV}$.

The excitation is a monochromatic laser coherent state presenting a step time dependence. Figure 5.11 shows the theoretical evolutions of P_X , P_Y , P_H and P_V with a pulse duration $T_{\text{pump}}=15\text{ps}$. The first column corresponds to an average number of photons $n_{\text{in}} = 10$ photons ($< \pi$ pulse) and the second column to $n_{\text{in}} = 80$ photons ($> 3\pi/2$ pulse). At $t = 0$, the system is in its fundamental state ($P_X = P_Y = P_H = P_V = 0$). From $t = 0$ up to the time T_{pump} (grey region in fig.5.11), the state $|H\rangle$ is coherently driven with an effective Rabi frequency Ω_{eff} . The driving field is related to the input number of photons n_{in} using the emission rate of the QD in the cavity $4\Omega_1^2/\kappa$ where $\Omega_1 = 20\mu\text{eV}$ and $\kappa = 120\mu\text{eV}$ being respectively the coupling strength of the QD with the fundamental mode of the cavity and the cavity damping.

Under the influence of the field, the population P_H of $|H\rangle$ reaches a value around 0.95 at the π -pulse. Then, the state evolves and flip into the $|V\rangle$ state due to the energy

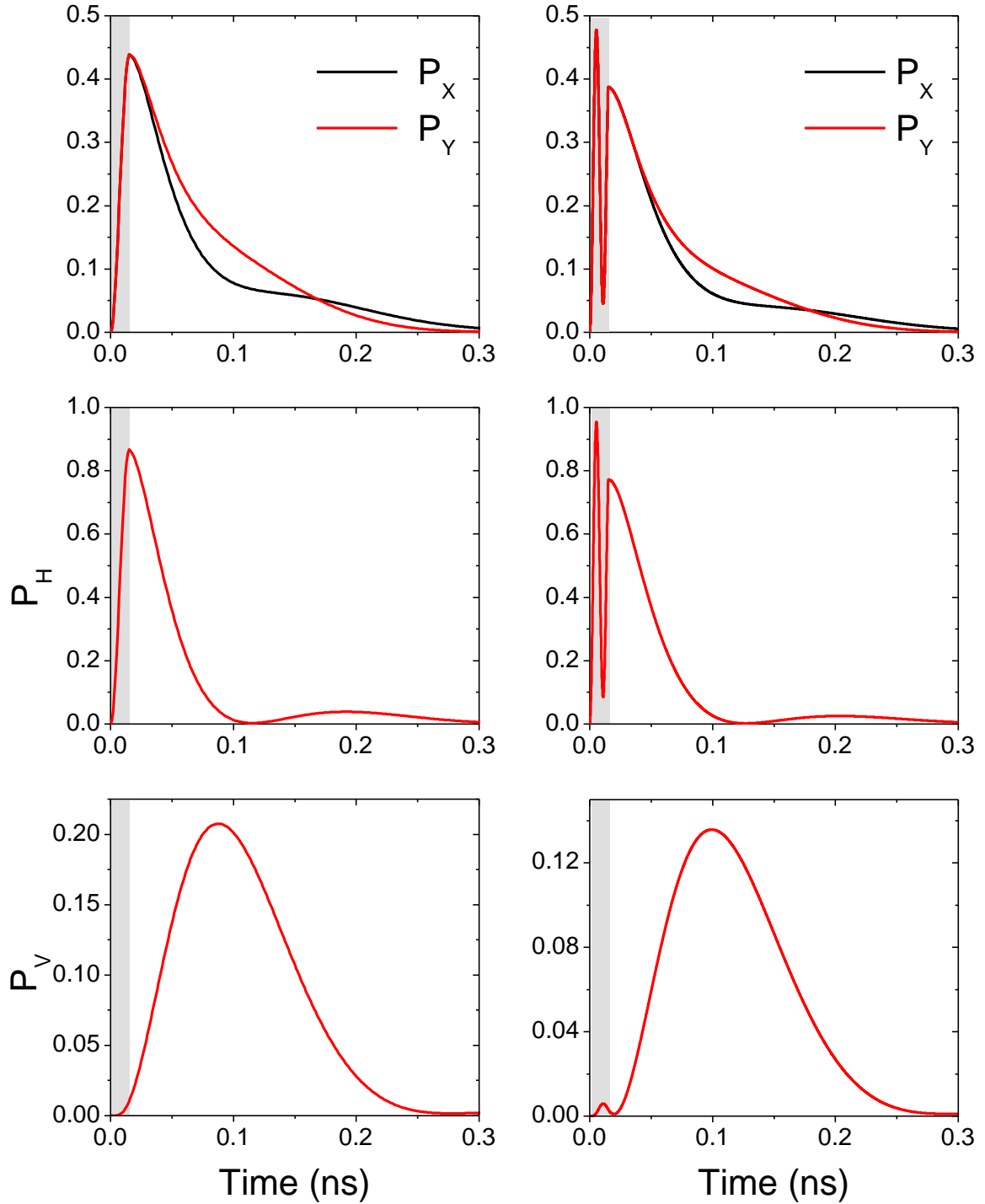


FIGURE 5.11: Calculated state populations of the states $|X\rangle$, $|Y\rangle$, $|H\rangle$ and $|V\rangle$ for a pulse duration $T_{\text{pump}} = 15\text{ps}$. The device parameters are $\Delta_{FSS} = 15\mu\text{eV}$, $\kappa = 120\mu\text{eV}$, $\gamma = 0.3\mu\text{eV}$. The detuning with the V mode is $70\mu\text{eV}$

splitting Δ_{FSS} . As a consequence the population P_V of the state $|V\rangle$ increases slowly. Finally, the photons are efficiently released from the pillar through the top mirror with a good output coupling ($\kappa_{\text{top}}/\kappa.\beta = 0.7 \pm 0.05$ with $\beta = \frac{F_P^V}{F_P^V+1}$). The measured PL in crossed polarization corresponds to the total emission collected in V polarization outside the cavity

5.4 Coherent Control With Few Photon Pulses

In this section, we explore the coherent control of an exciton state coupled with a cavity. We first qualitatively explain how Rabi oscillations are observed here through power measurements. In the second part, the observation of Rabi oscillations by sending few photons per pulse on the pillar 18B is reported.

5.4.1 Observation of Rabi oscillations under a pulsed excitation

For the sake of simplicity, we disregard here the effects related to the exciton fine structure splitting. In the presence of an oscillatory driving field, a two-state quantum system follows a cyclic behaviour called Rabi oscillations. When the two-level system (with a transition pulsation ω_0) is illuminated by a coherent beam of photons (of pulsation ω), it cyclically absorbs photons and emits them by stimulated emission. Assuming that the system is in its ground state at $t < 0$ and coupled to an oscillatory driving field for $t > 0$, the probability of it being found in the excited state is [113]:

$$P_e(t) = \frac{\Omega_1^2}{\delta^2 + \Omega_1^2} \sin^2 \left(\frac{(\sqrt{\Omega_1^2 + \delta^2})t}{2} \right) \quad (5.3)$$

where $\delta = \omega_0 - \omega$ is the pulsation detuning between the photon and the two-level transition and $\Omega_1 \propto -\mu.E$ is the Rabi frequency as defined in chapter 2. The period of the temporal oscillation varies with the detuning δ and with the amplitude of the electric field E . Considering the case where the pump is in resonance with the two-level system ($\delta = 0$), the probability of finding the excited state oscillates with a unitary contrast with a pulsation Ω_1 :

$$P_e(t) = \sin^2 \left(\frac{\Omega_1 t}{2} \right) \quad (5.4)$$

For the sake of simplicity, we neglect any dephasing term leading to a damping of the oscillations. As soon as the driving field is switched off (for $t > T_{\text{pump}}$), the two-level system returns to its ground state by spontaneously emitting a photon. The Rabi oscillations thus take place during the pulse, which in our case lasts from 10 to 50 ps. Fast detectors would be needed to monitor the Rabi oscillations in real time.

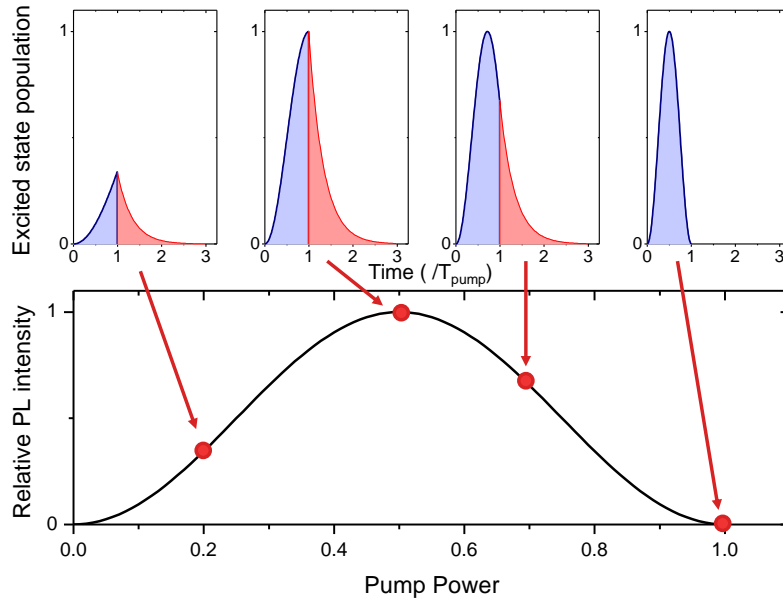


FIGURE 5.12: Schematics of the observation of the Rabi oscillations observed by changing the excitation power given a fixed pulse duration.

Rabi oscillations can be indirectly measured through power measurements. Since the pulsation of the oscillation depends on the pump power ($\Omega_1 \propto E = \sqrt{P_{pump}}$), the evolution of the PL as a function of the pump power reflects the Rabi oscillations as illustrated by fig.5.12. The top row shows a schematic of the temporal evolution of the exciton population in a QD when the pump power is increased (from the left to the right) given a fixed pulse duration. During the pulse (blue shaded region), the population oscillates due to the interaction with the driving field. After the pulse, the system relaxes to its ground state by emitting spontaneously a photon as shown by the red shaded region. The red shaded integrated area thus oscillates with the probability $P_e(T_{pump})$. Since $P_e(T_{pump}) \propto \sin^2\left(\frac{A\sqrt{P}T_{pump}}{2}\right)$ (where A is a fixed coefficient), the integrated emitted intensity oscillates with the square root of the pump power \sqrt{P} as shown by the bottom row of fig.5.12. The π -pulse is defined as the lowest pump power associated to the first intensity maximum in a power dependent measurement.

Rabi oscillations were first indirectly observed in QDs by using various techniques [173–175] such as measuring the photocurrent from QDs in a photodiode [176]. First observations of Rabi oscillations using the direct resonant fluorescence signal were reported in 2007 [164–166] by using an orthogonal excitation and collection configuration: QDs were excited by the side and resonant fluorescence is collected perpendicularly to sample's surface.

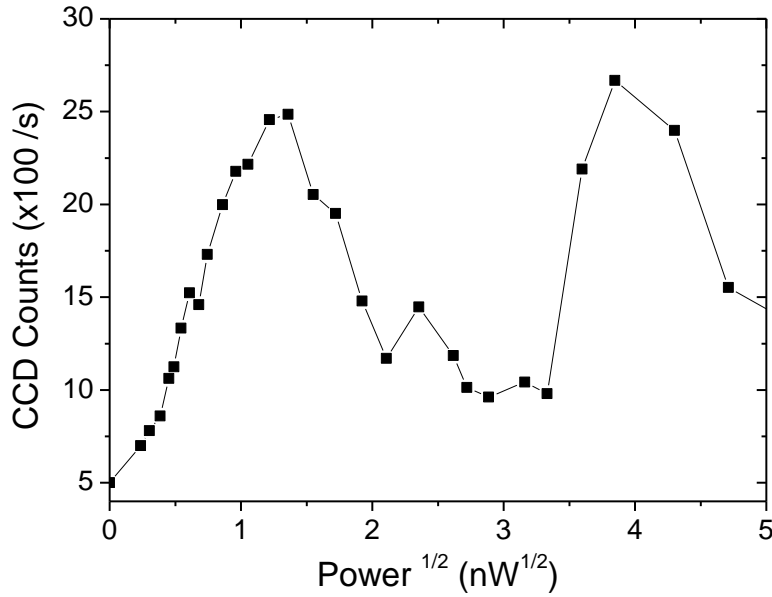


FIGURE 5.13: Measured collected PL from a single QD under resonant excitation as a function of the square root of the excitation power.

5.4.2 Connecting Flying Qubit with Quantum Nodes

In the prospect of quantum networks where the information is carried by single photons, it is necessary to develop devices allowing an efficient interaction between the flying single photons and a stationary quantum node [177]. The development of a very efficient interface between single photons and stationary qubits is a milestone in this context. In the QD community, such switching relies on the possibility of saturating the QD transition with only one photon. The record value in terms of few photon non linearity was obtained at the LPN in 2012 during V. Loo's PhD. Several groups studied the optical switching of a node containing a single QD [18, 171, 178]. Similar experiments were also conducted for atomic qubits with atoms coupled to optical microstructures [179, 180]. In 2012, a single-photon based elementary network made of atoms in cavity was implemented by Ritter et al. [181]. The exchange of single photons from one atom to another was studied with a success rate of 2.10^{-4} and a fidelity of $84 \pm 1\%$. Note that the success rate was mainly limited by the brightness of one of the atoms ($\eta \sim 0.03$ for one hyperfine state). Recently, the coherent control spin of a single atom using a single photon was studied by Reiserer et al. [182].

5.4.3 Coherent Control With Few Photon Pulses

In the following, we measure the coherent control of the QD exciton from pillar 18 B.

Figure 5.13 shows the measured PL from a QD under resonant excitation. The number of collected counts is plotted as a function of the square root of the excitation power such that Rabi oscillation resolved in power are visible. Using a short pulse (13 ps), several oscillations are visible. The indicated power is the one measured in the optical path. The power received by the pillar is derived from the optical losses on the excitation line.

The table 5.1 shows the transmissions of the optical elements of the setup.

Optical elements	Transmission
Fiber Coupler	0.9
Fiber Collimator	0.75
Polarizer	0.85
Half-Wave Plate	0.7
Polarizing Beam Splitter	0.995
Quarter-Wave Plate	0.9
Half-Wave Plate	0.7
Mirrors	0.78
Red Filter (Imaging line)	0.95
Green Filter (Exposure line)	0.95
Cryostat Window	0.9
Microscope Objective	0.52
Transmission of the Excitation Line	0.0832

TABLE 5.1: Transmission of the optical elements used for the coherent control of the QD

The transmission of the excitation path is measured to 0.0832. The average number of photons per pulse sent on the device is deduced considering that the excitation is pulsed with a period of 12 ns at a wavelength of 925 nm. For a measured power of 1 nW, the transmitted power is equal to 0.0832 nW corresponding to a mean number of photons n equal to 4.65.

Figure 5.14 shows the Rabi oscillations as a function of $\langle n \rangle$ for two pulse durations: 12 ps and 56 ps. With a 12 ps pulse, the π -pulse is obtained using a mean of 8.6 photons per pulse. With a longer pulse of 56 ps, the π -pulse is reached by sending only 3.8 photons per pulse. To reach the π -pulse, we observe that more photons are required using a shorter pulse. This is related to the fact that the population must increase faster in order to be maximal when the pulse ends. As explained previously, the speed for the exciton state to be populated increases with the square root of the excitation power (only for the first period of the oscillations).

Figure 5.15 shows the fraction of the QD total emission calculated in the V mode of the cavity as a function of the number of photons per excitation pulse for two different pulse durations (**a.** 15 ps and **b.** 56 ps) and different energy splitting Δ_{FSS} . Figure 5.15 is deduced from calculations like those presented in fig.5.11 by integrating the instantaneous signal over the time. We observe that the theoretical spontaneous emission

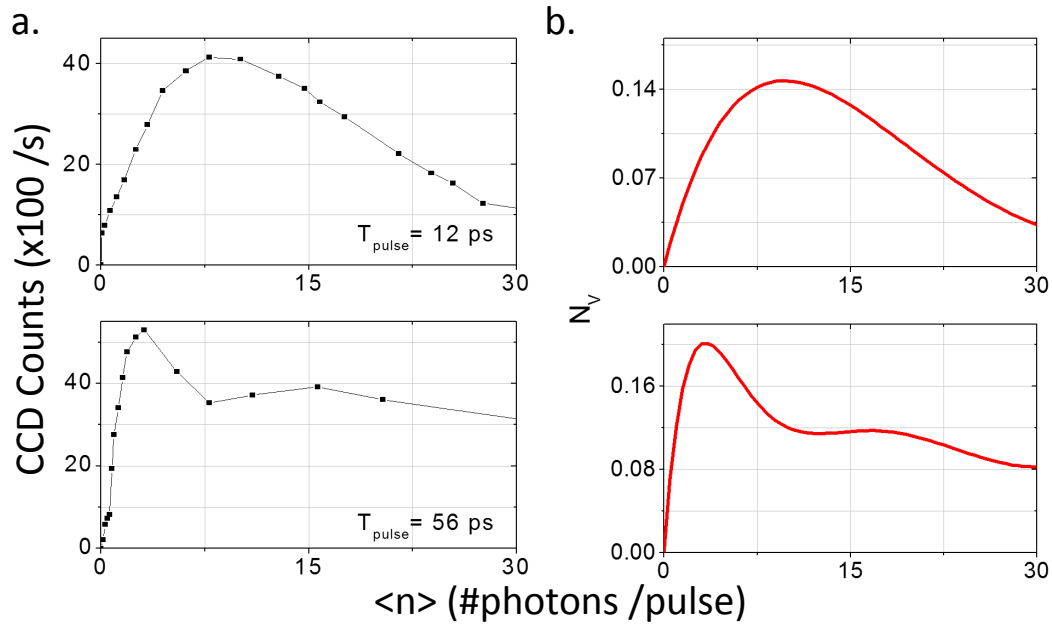


FIGURE 5.14: **a.** Measured collected PL from a single QD under resonant excitation as a function of the measured number of photons per pulse. **b.** Calculated PL as a function of the mean number of photons.

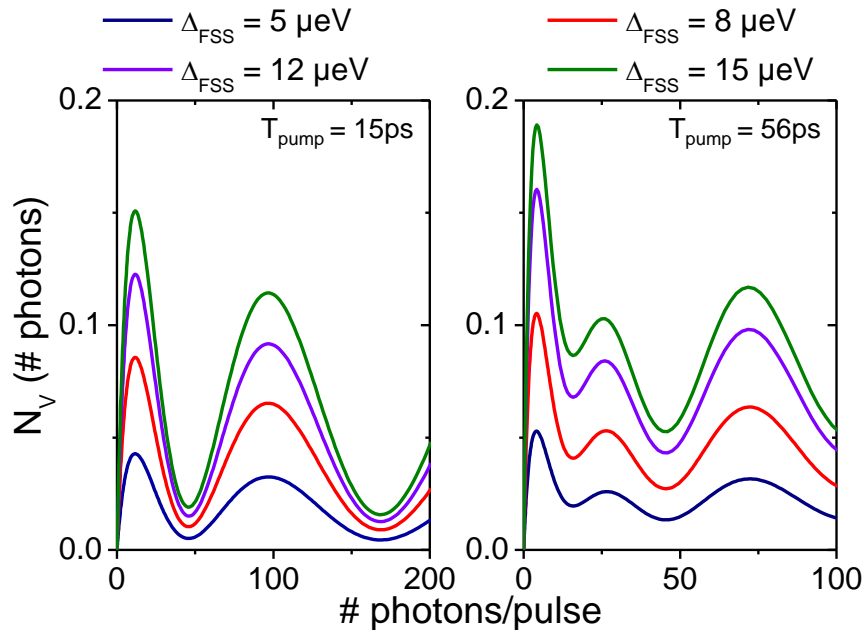


FIGURE 5.15: Calculated integrated fraction of emitted photons into the V mode of the cavity as a function of the number of injected photons for different pulse durations (**a.** 15 ps and **b.** 56 ps) and different energy splittings Δ_{FSS}

in the V mode oscillates evidencing Rabi oscillations. The shape of the oscillations depends on the pulse duration and their amplitude mostly depends on the exciton fine structure splitting Δ_{FSS} . The value of Δ_{FSS} thus determines the number of photons emitted in the V mode of the optical cavity, i.e, the source brightness that we measure in the next section.

Our results are in very good qualitative agreement with the calculated emission of photons as a function of the number of input photons for $\Delta_{FSS} = 15 \mu\text{eV}$ as shown in fig.5.14**b**. Note that some discrepancy can arise from the simplified square shape of the excitation used in the model. These results show the excellent interface between the photons and the QD in the micropillar due to the efficient input coupling of the pillar (~ 1) and the excellent coupling between the QD and the mode of the cavity characterized by the cooperativity parameter $C = \frac{g^2}{\kappa\gamma_{\text{ref}}} \sim 13$.

These measurements show that the QD state can be deterministically initialized to the excited state with a probability close to 0.95 by sending only few photons on the device. Using true Fock states of light, the same device should allow initializing the state with only one photon with a high probability. Theoretical models are currently under development to fully qualify this efficiency. These results are very promising for interconnecting flying qubits to stationary ones. Indeed, the coherent control of a trion transition has been used to initialize a single spin [19], a qubit with a coherence time as long as few microseconds.

5.5 Characterization of the Device 18B under Resonant Excitation

In the following, we show how the same device 18B resonantly excited is an excellent single photon source.

5.5.1 Single Photons Emission under Resonant Excitation

Figure 5.16**a**. shows a measured autocorrelation histogram under a pulsed excitation corresponding to the π -pulse with a pulse duration of 40ps. The collected emission is directly connected into a fiber based HBT consisting of two SPADs at the outputs of a fibered 50:50 beamsplitter. A single photon purity of $g^{(2)}(0) = 0.15$ is observed. By placing an etalon filter (FWHM=11 μeV) on the collection path, we filter out the residual laser light. Figure 5.16**b**. evidenced a high single photon purity in the same conditions. The extracted $g^{(2)}(0)$ is equal to 0.01 ± 0.01 . In the following, the etalon is always used unless the contrary is indicated.

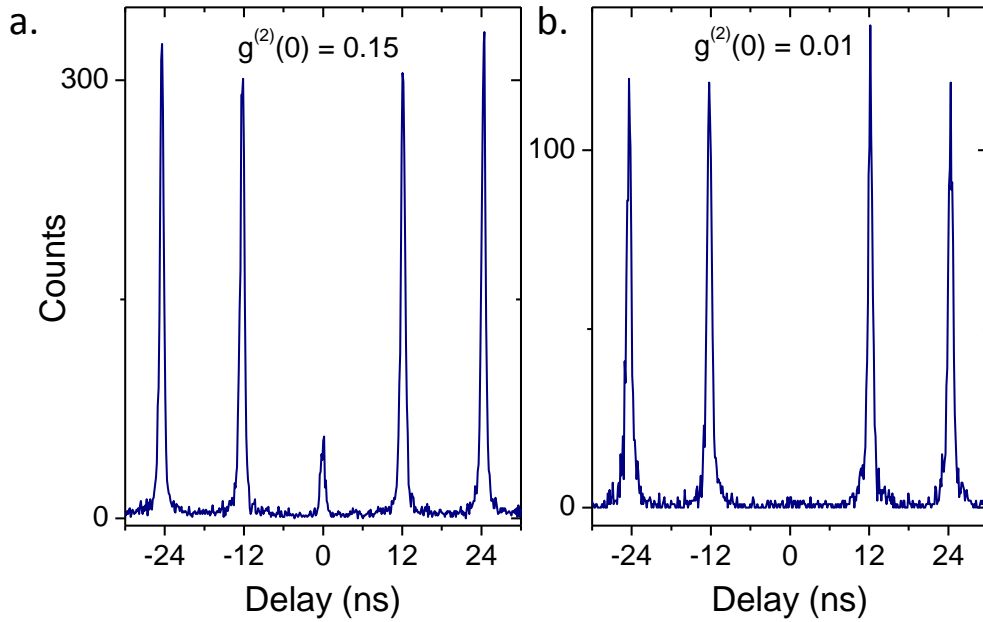


FIGURE 5.16: Measured autocorrelation histogram under resonant excitation without any spectral filtering (**a.**) and by filtering using a Fabry Perot etalon **b.** Excitation power is equal to 1.5nW corresponding to π -pulse and pulse duration is about 40ps. Acquisition times are respectively $t_{\text{acq}} = 1\text{min}$ and $t_{\text{acq}} = 3\text{min } 40\text{s}$.

Figure 5.17 shows a measured autocorrelation functions using a shorter pulse excitation ($\sim 15\text{ps}$) at a power very close to the π -pulse. It is plotted in a linear scale (**a.**) and in a logarithmic scale (**b.**). The absence of peak at zero delay evidences that the collected photons are perfect single photon Fock states. The measured $g^{(2)}(0)$ is estimated to 0 ± 0.003 .

Figure 5.18 shows the evolution of the measured $g^{(2)}(0)$ as a function of the excitation power under the same conditions previously used. A very good photon purity ($g^{(2)}(0) < 0.02$) is observed up to the π -pulse.

5.5.2 Two-photon Interference with Near-Unity Photon Indistinguishability

As in the previous cases, the mean photon overlap is measured by collecting two successively emitted photons with a temporal delay of about 2.3 ns. The sample is excited twice per laser period by using a delay path after the pulse shaper. Collected photons from the device (in the V mode) are sent into a fully fibered interferometer developed by Lorenzo de Santis. Figure 5.19 shows a schematic of the interferometer. The collected signal is polarized and sent into a calcite that plays the role of a 50:50 beamsplitter by setting the input polarization at 45° from calcite axis. Then, the polarization of each arm

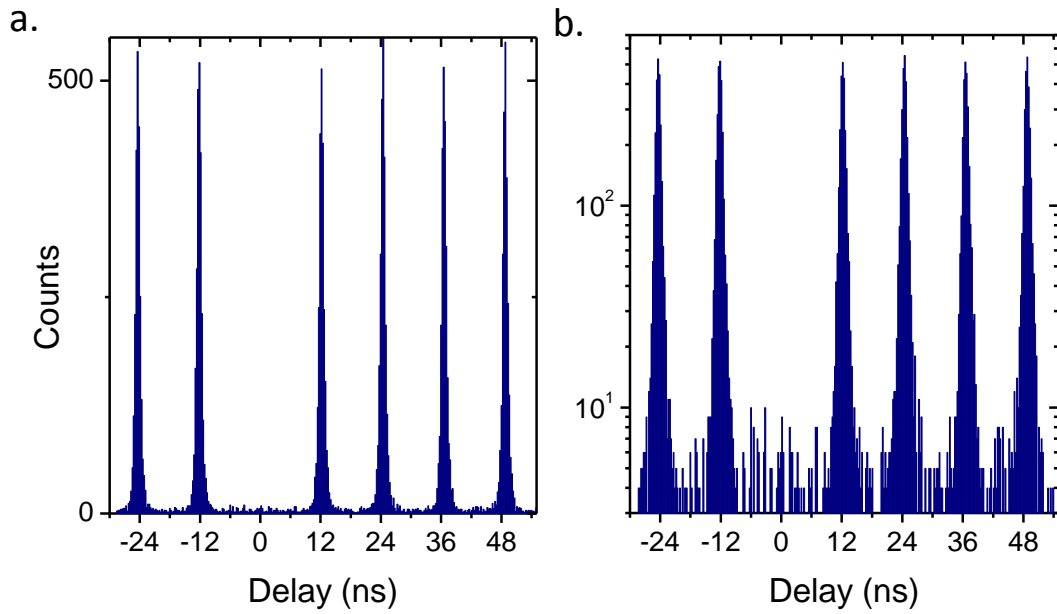


FIGURE 5.17: Measured autocorrelation histogram under resonant excitation in linear scale **a.** and in logarithmic scale **b.** The extracted $g^{(2)}$ is equal to 0.005 ± 0.005 . Acquisition time is $t_{\text{acq}} = 14$ min.

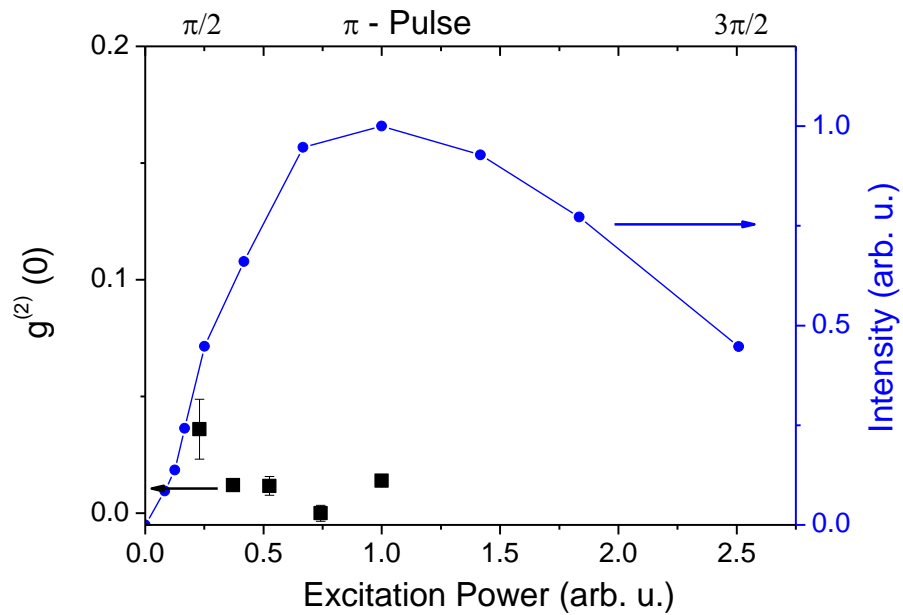


FIGURE 5.18: Measured $g^{(2)}(0)$ and brightness as a function of the excitation power.

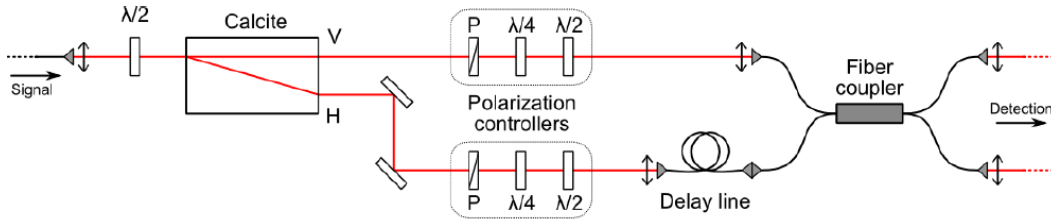


FIGURE 5.19: Schematic of the fibered interferometer used to measure the mean wavepacket overlap.

of the interferometer is rotated in order to reach the same polarization state before coupling to a 50:50 fibered beamsplitter where the quantum interference takes place. At the output of the fibered recombining beamsplitter, the paths are highly indistinguishable. The classical interferometer visibility ($1 - \epsilon$) is measured to be $1 - \epsilon = 0.9988 \pm 2.10^{-5}$ evidencing the close to perfect overlap provided by this setup. Finally, the beamsplitter outputs are plugged to fibered SPADs.

Figure 5.20 shows a measured correlation histograms between the SPADs at the output of the interferometer. With a linear scale (**a.**), the peak at zero delay is not visible evidencing an extremely good two-photon interference. Figure 5.20**b.** shows the same data in logarithmic scale. Red solid line shows the theoretical correlation peaks in the case of a perfectly indistinguishable source with $\epsilon = 0$. Considering the area between the points and the red line over a time windows, we extract the wavepacket overlap between successively emitted photons of $M=0.995 \pm 0.01$.

As a test, two-photon interferences were measured in crossed polarization (red points in fig.5.21) and in parallel polarization (green squares in fig.5.21). In crossed polarizations, the photons do not interference hence a peak at 0 ns appears. Once the photon indistinguishability is restored in parallel polarizations, the peak at 0 ns vanishes evidencing the high mean wavepacket overlap between the photons.

The photon indistinguishability does not depend significantly on the pump power. We measured the $g^{(2)}$ and the photon indistinguishability for different powers (see fig.5.22). A photon indistinguishability higher than 0.98 (corrected from $g^{(2)}$) is evidenced over

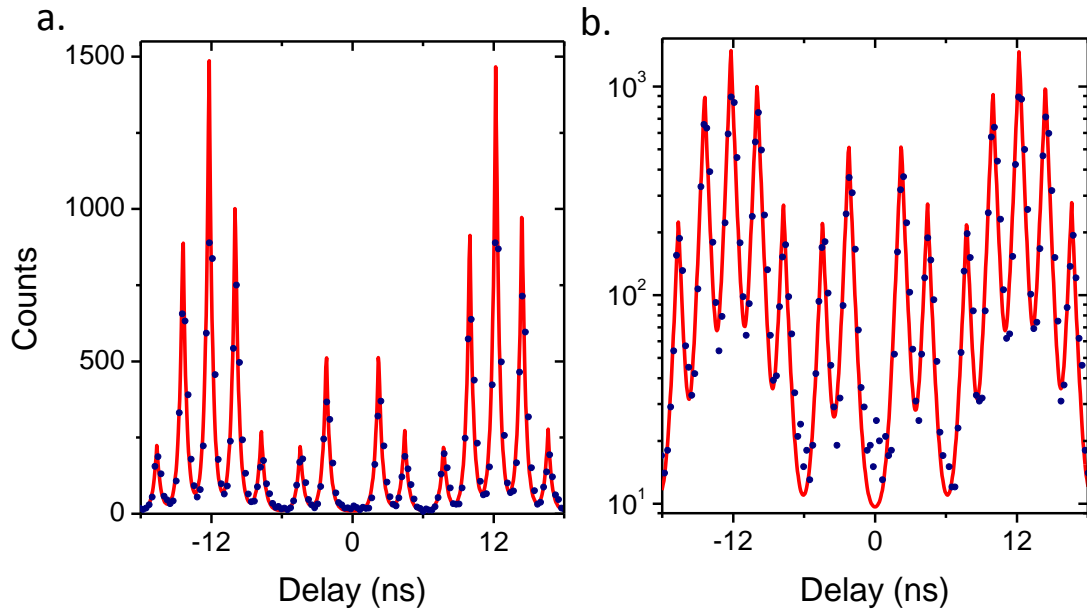


FIGURE 5.20: Measured correlation histogram between the HOM outputs in linear scale (a.) and in logarithmic scale (b.). Acquisition time is around $t_{\text{acq}} = 11\text{min}$. The red line shows the theoretical histogram for a perfect two-photon interference.

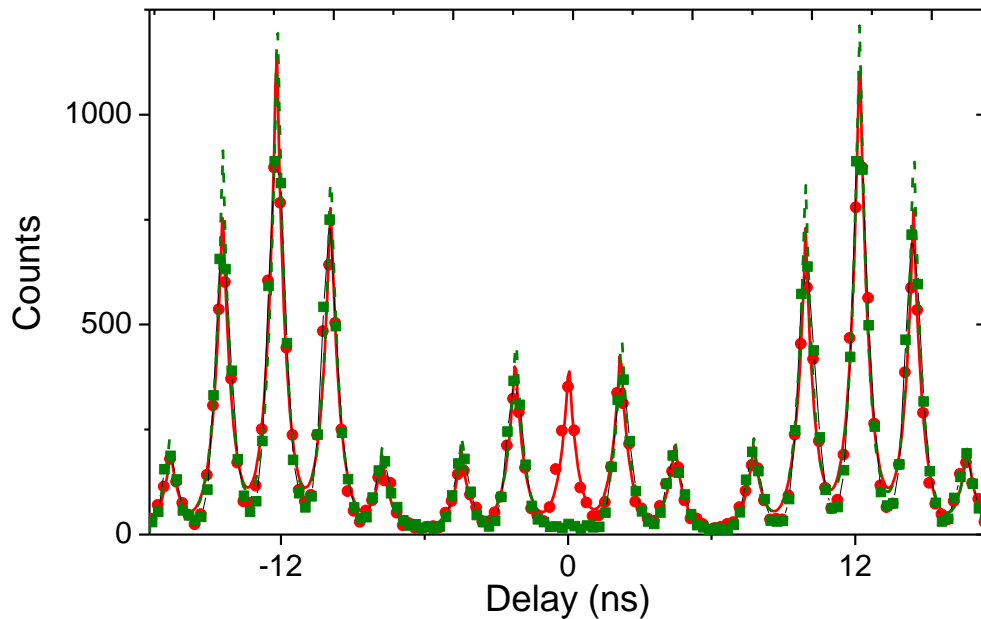


FIGURE 5.21: Measured correlation histograms between the HOM outputs when the photon polarizations are parallel (green squares) and orthogonal (red points). Acquisition times are 17 min. 30s. (crossed polarization) and 10 min. 30s. (parallel polarizations).

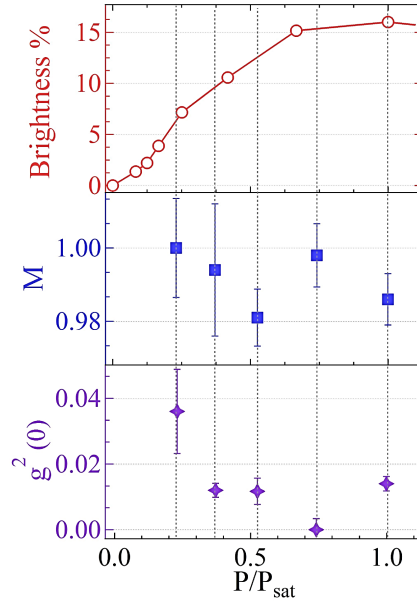


FIGURE 5.22: Evolution of the brightness (red open circles, top panel), of the measured photon indistinguishability M (blue squares, middle panel) and of the $g_s^{(2)}(0)$ (purple diamond, bottom panel) as a function of the excitation power

the whole power range. At the π -pulse corresponding to the maximum of counts, a photon indistinguishability is measured to 0.986 ± 0.007 .

5.5.3 Brightness

We calibrated our experimental setup in order to convert the count rates to the brightness in the first lens. Figure 5.23 summarizes all the device characteristics. The best single photon purity is combined with very high degrees of indistinguishability at a brightness of 16%.

We can fully account for the brightness theoretically: with an outcoupling efficiency of 70%, the brightness cannot exceed 35% in a crossed polarization configuration. Moreover, during the emission process, the created $|H\rangle$ exciton radiatively recombines in the H mode or evolved to the $|V\rangle$ exciton state with a time scale inversely proportional to the fine structure splitting (FSS). As a result, the larger the FSS, the larger the fraction of emission into V mode is. This is shown by the calculation presented fig.5.15 that fully account for the observed brightness. The brightness observed here is therefore limited by the use of an excitonic transition and could reach the limit of 35% using a trion state. Compared to previous works, this is the first time that a brightness higher than very few percent and a full photon indistinguishability are demonstrated simultaneously.

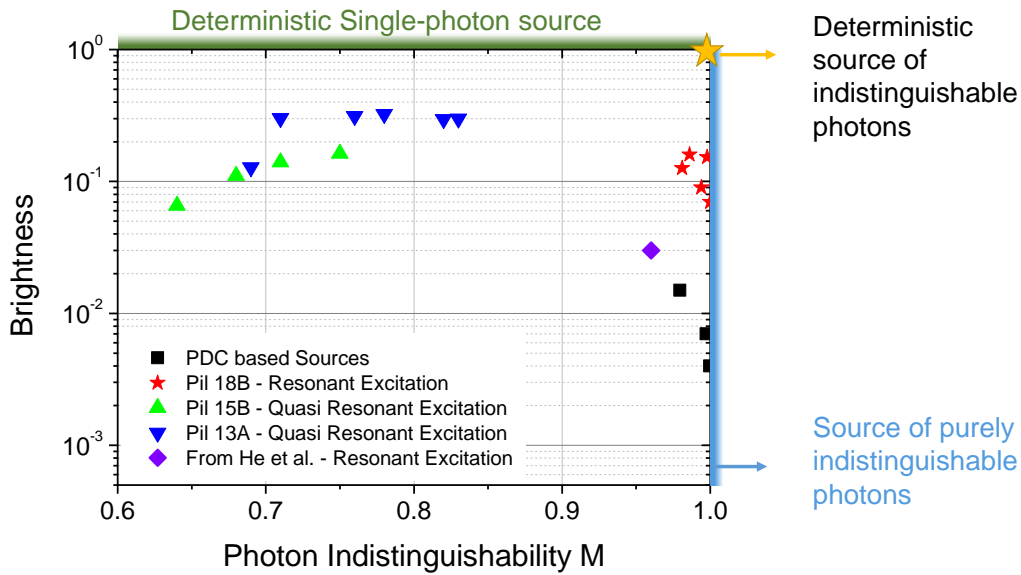


FIGURE 5.23: Comparison of the sources developed in this work with heralded single photon sources based on Parametric Down Conversion (PDC) sources (black points, data from Juan Loredo in Queensland University)

5.6 Comparison With State-Of-The-Art and Conclusion

To conclude on the potential of the devices presented in this work, we propose to compare our results with other QDs and SPDC sources. The sources are fully characterized by three figures of merit: single-photon purity given by $g^{(2)}$, photon indistinguishability given by M and brightness. A 3D diagram would not be appropriate to provide a fair and clear comparison, as a consequence we only plotted in fig.5.23 the brightness as a function of the photon indistinguishability with the different sources studied here, the previous state-of-the-art reported by He et al.[40] (purple diamond) and data from high quality SPDC sources (black points). These last measurements were done by our collaborators Juan Loredo, Marcelo de Almeida and Pr. Andrew White in Brisbane. For all data, the $g^{(2)}(0)$ is below 0.05 limiting the brightness of SPDC sources below 0.015. Since a single-photon source should provide photons with a well-defined polarization, the source brightness is divided by a factor of 2 for the unpolarized devices under a non-resonant excitation.

Figure 5.23 provides strong evidence that the QD sources developed during this PhD bring the single-photon generation technology to a new level. Compared to SPDC sources of the same quality, the brightness of QD sources under strictly resonant excitation is enhanced by a factor 40. The single-photon purity and indistinguishability reach ultimate values of $g^{(2)} = 0.0017 \pm 0.0017$ and $M = 0.986 \pm 0.007$ evidencing a quality that is perfectly adapted for highly demanding applications.

As a conclusion, embedded quantum dots in connected pillars offer a new generation of nearly-ideal single-photon sources. They offer a unique combination of high brightness with perfect single-photon purity and indistinguishability. Depending on the purpose, they can be excited either quasi-resonantly to emit high rate of photons that are highly (70-80%) indistinguishable or resonantly to provide fully indistinguishable photons with a brightness which is 2-3 orders of magnitude greater than the sources that are currently used in the quantum optics laboratories.

Chapter 6

Cavity Enhanced Two-Photon Interferences Using Remote Sources

The sources developed in the group gather high brightness with high single-photon purity and indistinguishability. The implementation of such source could be a promising step in the improvement of performance in quantum information processing protocols. As discussed in chapter 7, possible perspectives are for instance the use of these devices in experiments measuring the boson sampling of single photons.

In the future, an important challenge is the development of a photonic solid-state quantum network. In this context, photons emitted by remote sources should interact efficiently. The quantum interference between photons emitted by remote sources was studied using various sources including QDs in the recent years. All these works were done in a low-brightness regime without the possibility to control the QDs spontaneous emission. In this chapter, we implement an elementary photonic network based on bright remote sources and study the role of a high Purcell regime.

6.1 Introduction

The two-photon interference with remote sources has been reported using various sources based on ions, atoms or parametric downconversion sources as well as QDs. We give a very short and non exhaustive overview of the pioneering works involving remote single-photon sources:

- **Quantum interferences with remote parametric down conversion single-photon sources:** In 2003, the group of Pr. Gisin from University of Geneva studied the quantum interference between photons emitted by spatially separated

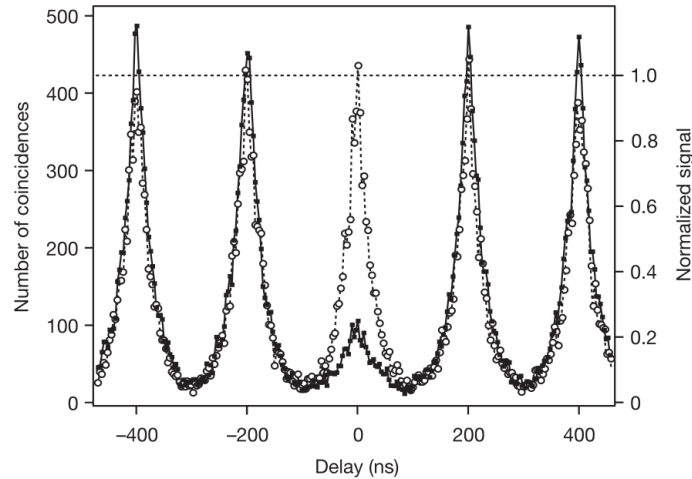


FIGURE 6.1: Figure reproduced from [183]. Correlations of photons emitted by remote trapped atoms. The central peak is lower due to the quantum interferences that occur when two indistinguishable photons simultaneously arrive on the beamsplitter.

sources [184]. A contrast of 83% in the telecommunication wavelength range was demonstrated. Later, the group of Pr. Zeilinger from University of Vienna used synchronized lasers and separate nonlinear crystals to study the quantum interferences between the photons emitted by each source [185]. An electronic synchronization was developed in order to precisely control the cavities of two mode-locked lasers, each laser exciting nonlinear crystals in order to generate two pairs of heralded photons in parallel. One photon of each pair interfere with the other one in a fibered beam-splitter (FBS). A measured interference contrast of $M=0.83 \pm 0.04$ was evidenced by adjusting the photon polarizations. This value was mainly limited by the time jitter between the pulses and the bandwidth of the used filters.

- Atom-based quantum interferences:** In 2006, the group of Pr. Grangier from LCFIO in Orsay, Beugnon et al. studied the quantum interference between two single photons emitted by two remote atoms [183]. Two single rubidium-86 atoms were studied, confined in separate optical dipole traps, in the same chamber, at an effective temperature of 1.5 mK. Both atoms were excited simultaneously by the same laser pulse in resonance with their transition. Both atoms relaxed into their ground states by emitting single photons, with a decay time of 26 ns. The two single photons interfered with a maximal probability equal to 0.78 ± 0.03 . Figure 6.1 shows two measured correlation histograms: black squares correspond to the interference configuration while open circles correspond to the case where beams are fully independent. The residual peak is attributed to an imperfect spatial overlap between the two photons.

- **Ion-based quantum interferences:** Maunz et al. [186] studied in 2007 the quantum interferences between single photons emitted from remote ions. Two Yb ions were used and stored in independent traps in separated vacuum chambers. By comparing the autocorrelation measurements in cross and parallel polarizations under pulsed regime, a high interference contrast of 95% was demonstrated.

More recently, two-photon quantum interferences using remote sources were studied using solid-state emitters. In comparison with atoms, ions or PDC based sources, solid-state emitters are spectrally spread. Consequently, it is more challenging to find two emitters with similar emission properties than for atoms, ions or PDC based sources.

- **Organic molecules based quantum interferences:** In 2010, Lettow et al. [187] demonstrated the same quantum effects using indistinguishable photons emitted by remote organic molecules. Two single molecules were continuously excited and a fine tunability of the emission was used to analyse the contrast of the quantum interferences with a maximum overlap $M=0.5$.

- **Nitrogen Vacancy (NV) centers based quantum interferences:** In 2012, Bernien et al. [188] reported the observation of quantum interferences of the emission from two separate NV centers in diamond. Similarly to Beugnon and coworkers [183], they collected light from two emitters in the same cryostat using a single lens. A two-photon interference with a contrast of $66 \pm 10\%$ was obtained using a strong spectral filtering (to get rid of the phonon sideband emission) and strong temporal filtering (to reduce influence of dephasing).

- **Quantum dots based quantum interferences:** The first quantum interferences using remote QD sources were achieved in parallel in the group of Pr. Solomon from NIST, USA [131] and in the group of Pr. Shields in Toshiba, UK [132] in 2010. Each group used different techniques to implement the quantum interferences. In Shields group, Patel and coworkers developed a CW electrically tunable single photon source embedded in a p-i-n diode. By applying a voltage on one of the samples, they measured the photon overlap as a function of the spectral detuning. Figure 6.2a. shows a measured PL map as a function of the photon energy and applied electric field to one of the QDs. The points on fig.6.2b. show the extracted photon overlap (visibility) as a function of the spectral detuning between the photons emitted by the two QDs. Tuning both sources to the same energy, the measured contrast is equal to 0.33 ± 0.01 .

In parallel, Flagg et al. [131] performed similar measurements by placing one of the samples on a piezo-electric transducer in such a way that the emission energy of one of the QD is tuned by applying a strain. Both samples were excited by

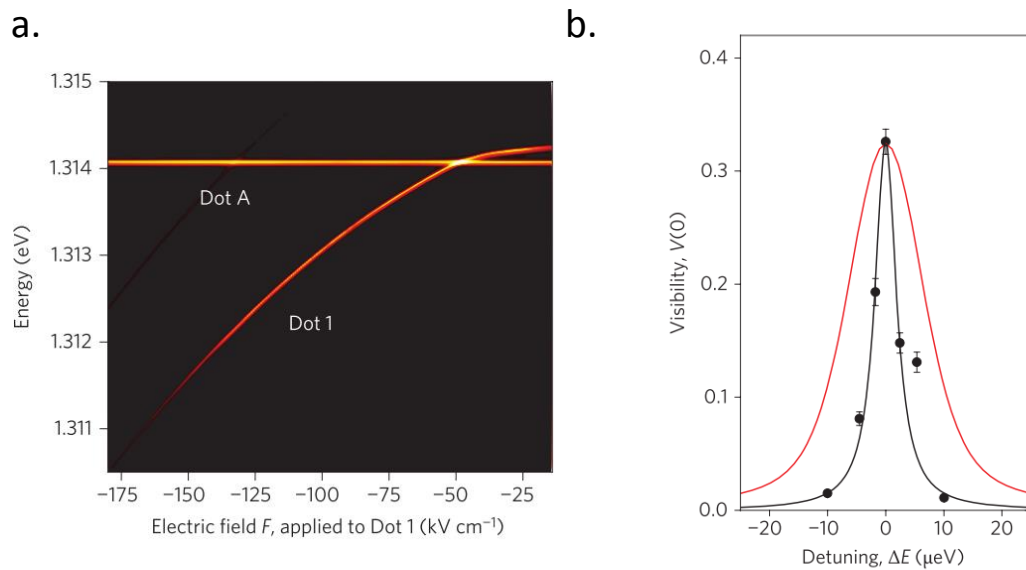


FIGURE 6.2: Figure reproduced from [132]. **a.** Photoluminescence map of two quantum dots simultaneously as a function of the applied voltage to QD 1. **b.** Measurement of the visibility extracted as a function of the detuning.

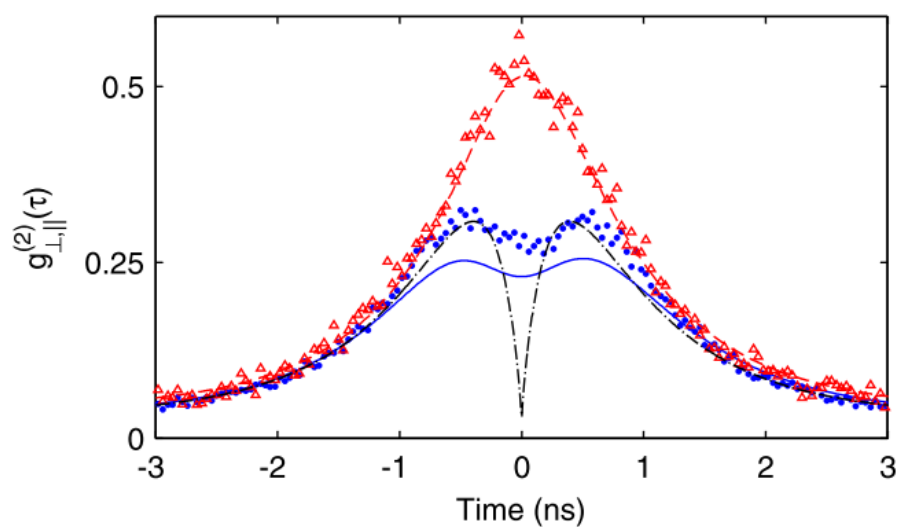


FIGURE 6.3: Figure reproduced from [131]. Correlation peak at zero delay in two different configurations: in crossed polarizations (red triangles) and in parallel polarizations (blue points). These measurements show a clear decrease in the number of coincidences from detectors at the two output ports of the BS.

the same pulsed excitation at high energy (above the GaAs gap). The contrast of interferences was measured by comparing the number of coincidences at zero delay when the photons are in parallel or crossed polarizations. Figure 6.3 shows the measured correlations when the polarizations are parallel (blue) and when the polarizations are crossed (red). A coalescence probability of 0.180 ± 0.004 below the classical limit was reported which reached 0.47 ± 0.06 by post-selecting temporally the photons.

In 2013, Gao and coworkers [189] showed the coalescence of photons emitted by remote QDs using a common strictly resonant excitation. Such scheme is similar to the one used with ions and atoms. Using a ns excitation pulse duration, temporally post-selected photons demonstrate an interference visibility of 0.82 ± 0.02 . Their result shows that resonant excitation in a low excitation regime allows a high interference visibility between photons emitted from remote QDs. Note that in this regime, the light scattered by the QDs presents the coherence of the laser.

Recently, Gold et al. [190] demonstrated a contrast of 0.39 ± 0.02 by using a quasi resonant excitation of remote QDs. However, it must be noted that, surprisingly, the measured two-photon interferences visibility was not zero for high detuning of the sources.

The quantum interferences using remote sources -of any kind- has not been investigated placing the emitters in a cavity to (i) efficiently collect the photons (ii) have an additional parameter, the Purcell factor, to control the interferences.

In this chapter, we report on such a study for photons emitted by QDs in micropillars operating in a high Purcell regime. First, we describe the two sources chosen for this experiment. They both exhibit a bright emission of photons at the same energy. The properties of each source are studied using the same excitation laser, this will impose an experimental limitation, as discussed later. The results of the two-photon interference between photons emitted by the two sources are then discussed.

6.2 Photons Emitted With a Common Excitation

The sample under study is the one studied in chapter 3. During the fabrication, we processed two parts of the sample and cleaved it to get two pieces. We chose a device on each piece presenting the same pillar diameter. We will refer to them as QD A and QD B. QD A is the source presented in chapter 3 with a brightness of 0.74. Since both pillars present the same diameter, their fundamental optical mode are at the same energy (of 1.3115 eV). Each sample is placed in a different cryostat so their temperature

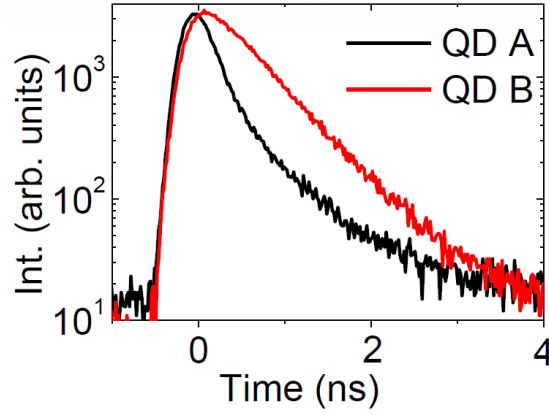


FIGURE 6.4: Measured time resolved exciton emission coresponding to QD A (black line) in QD B (red line) in resonance with the cavity resonance ($\delta_{CM-X} = 0$). The decaytime of the QD A (QD B) T_1^A (T_1^B) is equal to 140 ± 40 ps ($T_1^B = 470 \pm 30$ ps).

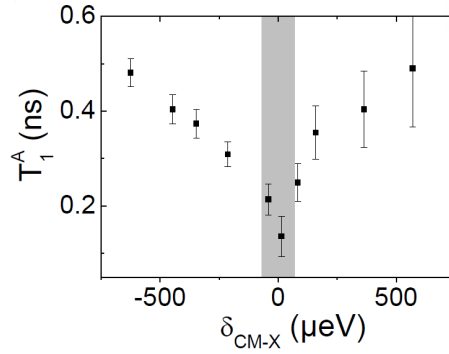


FIGURE 6.5: Decay time of QD A exciton line (T_1^A) as a function of the spectral detuning between the cavity and the exciton. Decay times have been deconvoluted from the temporal resolution of the setup. The grey vertical stripe shows the range of temperature used for the two-source interference.

can be independently controlled. The measured decays of QD A and QD B are shown in fig.6.4 (with the exciton transition resonant with the cavity mode of the micropillar). The red line (black line) corresponds to the decay of QD A (QD B). In resonance, the QD A exhibits a decay time $T_1^A = 140 \pm 40$ ps evidencing a Purcell factor as high as $F_P = 10 \pm 2$ (considering a radiative lifetime in bulk equal to 1.3 ns). QD B lifetime is $T_1^B = 470 \pm 30$ ps. We see that the QD B exhibits a smaller effective Purcell factor: this difference might be due to a stronger coupling to phonons or to the influence of charges around the QDs. The temperature of QD A is tuned in order to study the two-photon interferences. The evolution of decay times as a function of the temperature and of the spectral detuning between the exciton line and the cavity mode δ_{CM-X} is shown in fig.6.5. The grey vertical stripe corresponds to the temperature range explored for the interference described in this chapter.

6.2.1 Synchronisation of Emission from Remote Sources

To ensure that the photon wavepackets simultaneously reach the beamsplitter with a precision lower than the typical sources decay time, we synchronise the emission of photons from both sources. This can be achieved via the excitation or via the collection paths. Because the coupling of the emitted photons from the pillar into a single-mode fiber (SMF) ensures the setup stability, it is convenient to use an adjustable delay line on the excitation path rather than on the collection path. Nevertheless, the installation of an adjustable delay line before one QD with respect to the other does not solve the issue of the repetition rate. A first requirement for remote source interference is that both QDs emits single photons with the same repetition rate. Two possible solutions are:

- **Synchronization of two excitation lasers:** It is possible to tune dynamically the length of a laser cavity to synchronize its repetition rate with an electronic signal input. This *slave* laser repetition rate is tuned using a piezo actuator located in the cavity. The actuator is controlled by a electronic rack (*Lock-to-Clock* by *Spectra Physics*) which finely drives the piezo actuator according to the electronic signal and the measured repetition of the *slave* cavity. If the electronic signal input comes from a fast photodiode detecting the pulses from another mode-locked *master* laser, the *slave* cavity will be synchronized to the latter. This solution allows the synchronized emission of laser pulsed at independent wavelengths allowing the synchronized excitation of two sources in their best excitation conditions respectively. This technique is very promising as long as the *master* laser is stable enough. In our case, it was difficult to run experiments for more than 1hour due to the limited stability of the *master* laser.
- **Use of a common laser:** An alternative solution is to use a common mode-locked laser splitted into two beams to excite both sources. It is the easiest way to ensure that photons are generated at the same repetition rate. By delaying precisely the excitation of one QD compared to the other, the single photons generated by the two sources can reach the beamsplitter simultaneously. The main drawback of this method is that both QDs are excited with the same wavelength. A challenging part of this measurement was to find a common excitation energy for both QDs that features good properties of emission. The results that we present here have been obtained using this technique.

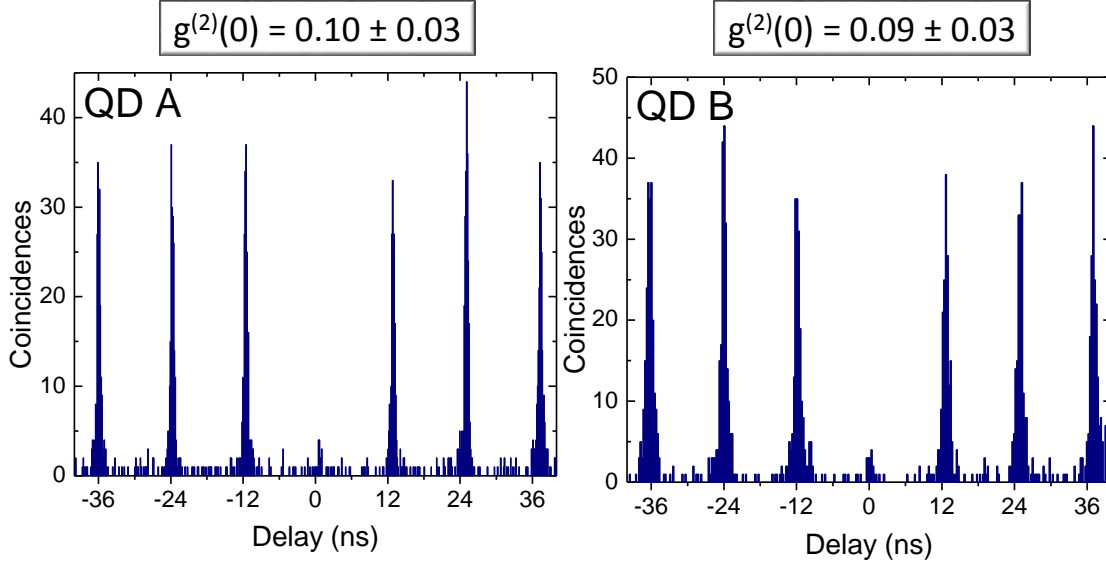


FIGURE 6.6: **a.** Autocorrelation measurement of the QD A under a pulsed excitation below the wetting layer gap, at 1.370 eV ($t_{acq} = 10$ min.) **b.** Autocorrelation measurement of the QD B under the same conditions of excitation used for **a.** ($t_{acq} = 24$ min.)

6.2.2 Single-Photon Properties Using a Common Excitation

Once both QD emission lines are set at the same energy using the temperature of each source as fine tuning knob, we find a common quasi resonant state to use a single excitation wavelength, provided by a single Ti-Sapphire mode-locked laser. To obtain a good single-photon purity in a regime of strong Purcell effect, the laser wavelength is chosen below the wetting layer gap, in order to create charges directly in the QD.

We measure the single-photon purity by sending the photons emitted by each device in the HBT interferometer. Figure 6.6 shows the autocorrelation measurements of each source: QD A (**a.**) and QD B (**b.**) A reasonably good single-photon purity is obtained for both devices: the QD A presents $g_A^{(2)}(0) = 0.10 \pm 0.03$ while the QD B $g_B^{(2)}(0) = 0.09 \pm 0.03$. Both sources are operated with an excitation power close to the saturation of the QD transition. As shown in chapter 3, the brightness of the QD A is equal to 0.74 ± 0.07 . Due to a lower Purcell enhancement of the spontaneous emission and a non optimal excitation wavelength, the QD B brightness is evaluated around 0.3 ± 0.1 .

In the following, we measure the degree of indistinguishability between photons that are successively emitted by each device.

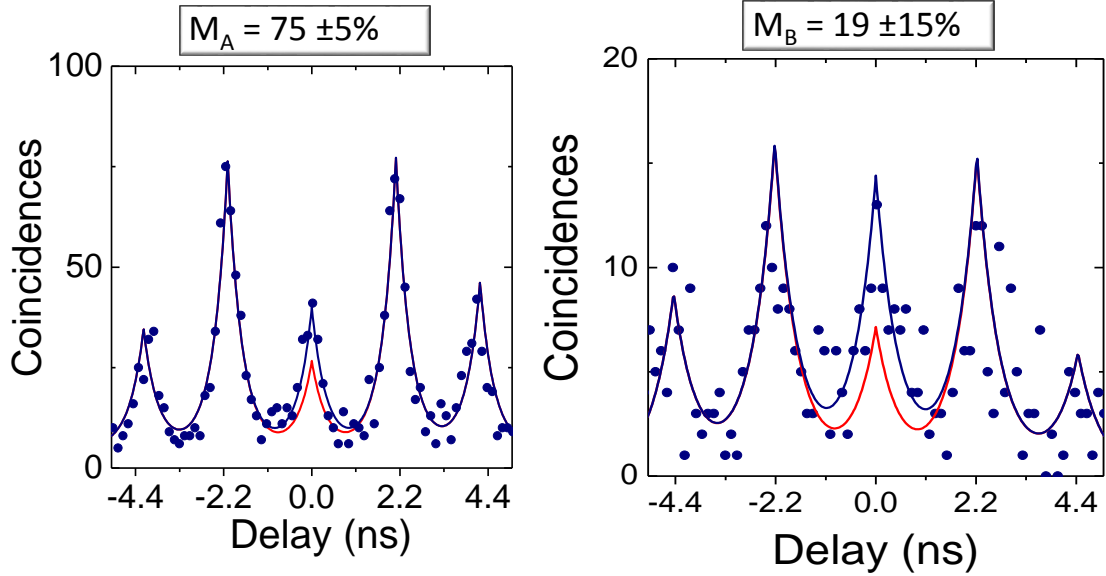


FIGURE 6.7: **a. b.** Correlation histograms between the outputs of the HOM interferometer. The 0 ns peak area gives the interference probability between successively emitted photons from QD A (**a.**) and from QD B (**b.**) under the same excitation conditions. Blue lines are fittings to the experimental data with $M_A = 0.77$ for QD A and $M_B = 0.19$. Acquisition times are 10 minutes and 30 minutes, respectively. Red lines are theoretical correlations for $M = 1$ considering the measured single-photon purity, ϵ and the BS coefficients R and T .

6.2.3 Indistinguishability between Photons Successively Emitted from the same Source

To study the indistinguishability, each QD is excited twice every 12 ns using a delay line of 2.2 ns. The emitted photons are sent into the HOM interferometer described in the chapter 3. Figure 6.7 shows the correlations between the two detectors at the output of the HOM interferometer. By using a single laser to excite both QDs, we were not able to simultaneously optimize the indistinguishability of both sources. We chose an excitation wavelength to maximize the degree of indistinguishability of the photons emitted by QD A. We measure a mean wavepacket overlap M for each source: $M_A = 0.77 \pm 0.07$ for QD A and $M_B = 0.19 \pm 0.15$ for QD B.

Assuming that the effect of time jitter is negligible as compared to pure dephasing term on the photon indistinguishability, we can extract the pure dephasing rate with the following relation:

$$M = \frac{\gamma}{\gamma + \gamma^*} = \frac{T_2^*}{T_2^* + 2T_1} \quad (6.1)$$

where T_1 (γ) is the decay time (decay rate) and T_2^* (γ^*) is the pure dephasing time (dephasing rate). Figure 6.8 shows the theoretical photon overlap M given by equation

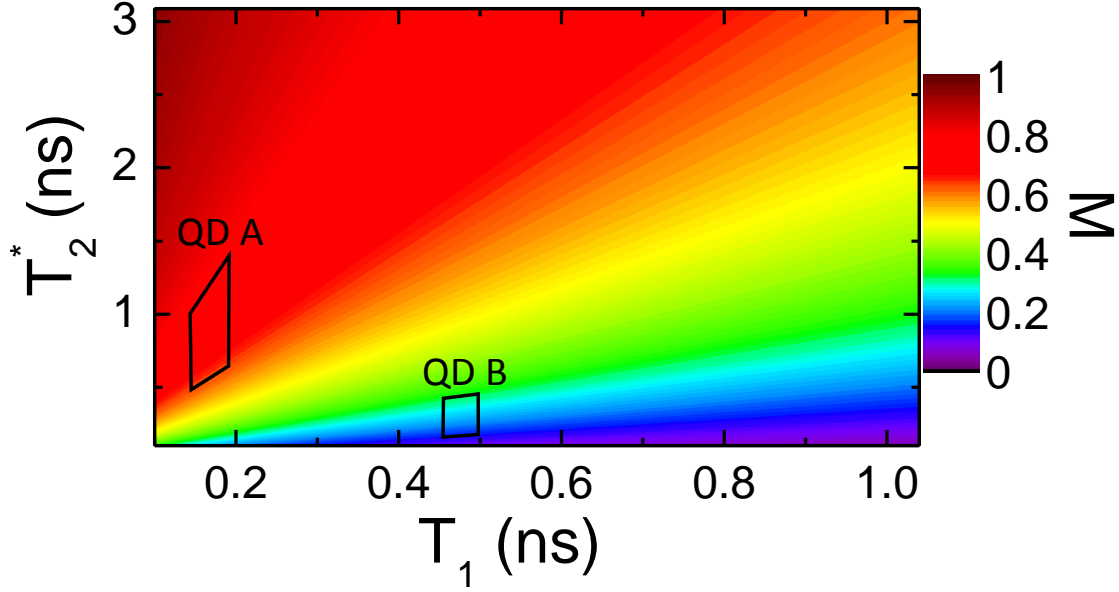


FIGURE 6.8: Colormap of the theoretical indistinguishability (photon overlap) M as a function of the decay time T_1 and the pure dephasing time T_2^* .

6.1 as a function of the decay time T_1 and the pure dephasing time T_2^* . For a given pure dephasing time T_2^* , the photon overlap M increases as the decay time T_1 decreases. The areas on fig.6.8 show the T_1, T_2^* of each QD accounting for the measured photon overlap. The difference of photon indistinguishability between both sources is mainly due to the different enhancement of spontaneous emission. If the QD B were suffering from the same pure dephasing, the photon indistinguishability would be around 0.5-0.7. As expected, the dephasing processes affecting the QD B are stronger since the excitation is optimized for QD A.

The table 6.1 summarizes the parameters characterizing the devices QD A and QD B:

	QD A	QD B
Brightness	0.74 ± 0.07	0.3 ± 0.1
Decay Time at resonance	$T_1^A = 140 \pm 40\text{ps}$	$T_1^B = 470 \pm 30\text{ps}$
Purcell Factor F_P	10 ± 2	2 ± 1
$g^{(2)}(0)$ under the same excitation	0.10 ± 0.03	0.09 ± 0.03
Successive photon indistinguishability	$M_A = 75 \pm 5\%$	$M_B = 19 \pm 15\%$
Pure dephasing Time	500 - 1500 ps	50 - 450 ps

TABLE 6.1: Measured characteristics of QD A and QD B used for the measurement of quantum interferences using remote single photon sources

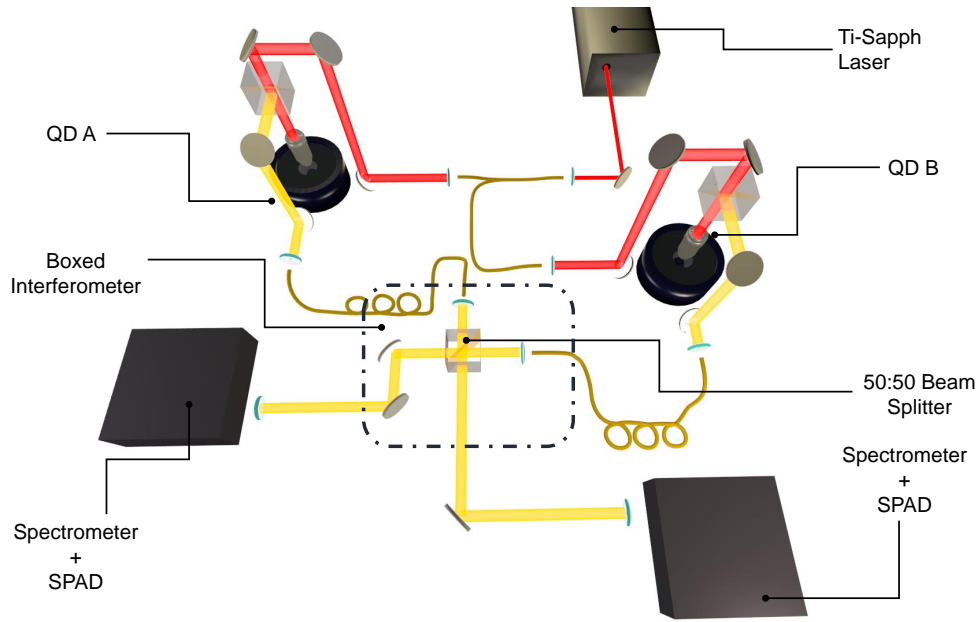


FIGURE 6.9: Schematics of the optical setup using the common excitation technique

6.3 Measurement of the Two-Sources Interference

One of the QD emits highly indistinguishable photons with a fast radiative decay, while the other emits less indistinguishable photons. In this section, we show that the coalescence probability between the photons emitted by these two sources is still high.

6.3.1 Simultaneous Emission of Remote Sources for the Interference

Figure 6.4 shows the emission from QD A (black line) and QD B (red line) after their emission has been synchronized. The delay between excitation has been chosen to synchronize their rising time (with a temporal resolution of 16 ps). In this case, the simultaneity of the photons arriving on the beamsplitter is mainly limited by the incoherent relaxation of charges induced by the quasi-resonant excitation. The order of magnitude of the time jitter is about 50 ps.

Both sources are operated at maximum brightness ; since QD A is brighter than the QD B, the single photon beam emitted by QD A is attenuated to match QD B brightness. Figure 6.9 shows a 3D schematic of the optical setup. Red paths correspond to the excitation laser while yellow lines to collection paths. The free space interferometer is the same as the one described in chapter 3.

6.3.2 Spectral Tuning using the Temperature

The interference is measured as a function of the spectral detuning between the photons emitted by QD A and the photons emitted by QD B. In order to achieve a spectral

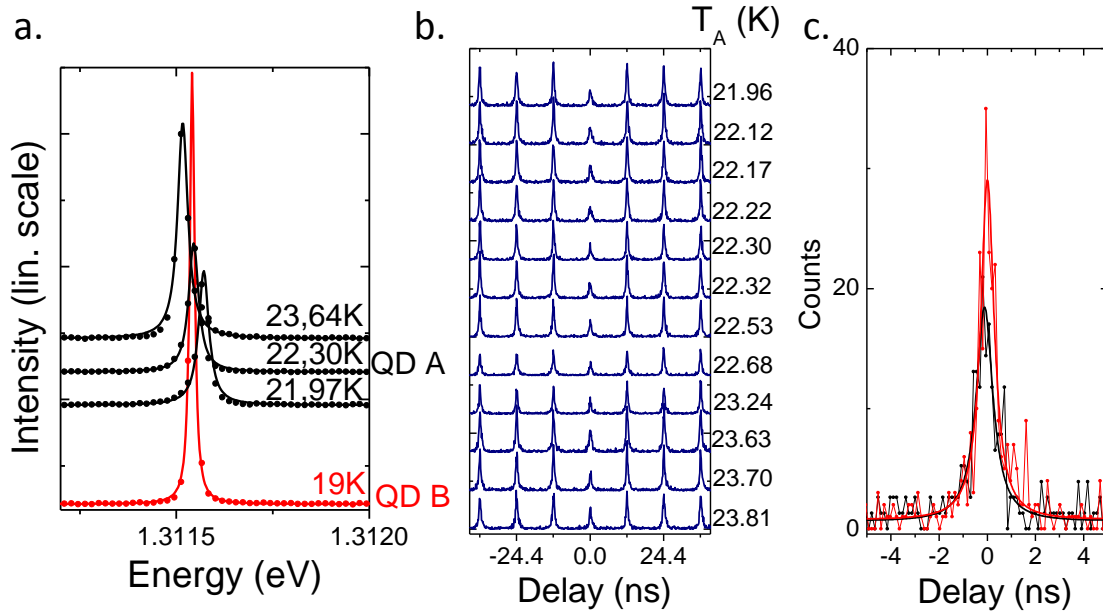


FIGURE 6.10: **a.** PL spectra of QD A at different temperatures and of QD B at a fixed temperature $T=19\text{K}$. Spectra are vertically shifted for clarity. **b.** Measured correlation histograms of the interferences between QD A and QD B. **c.** In black (red): normalized correlation histograms for a detuning equal to $-3 \mu\text{eV}$ ($87 \mu\text{eV}$). On average, the acquisition time for each correlation measurement is about 13 minutes.

matching between the two sources, we changed the temperature of QD A while QD B's temperature is fixed. QD A is in a closed-cycle helium cryostat whose temperature is finely controlled by the system, with a stability of about 5mK. The whole temperature detuning for QD A does not exceed 1K, so that QD A detuning with its cavity does not change by more than 10%. The temperature of QD B is fixed at 19K with a stability of about 2 mK. Figure 6.10a. shows the PL emission spectra of QD A at different temperatures (black points) and of QD B at 19K (red points). We define the detuning $\Delta E = E_X^B - E_X^A$ between the sources where E_X^A (E_X^B) is the measured photon energy from QD A (B) by fitting the measured spectra with two lorentzian peaks (solid lines in fig.6.10 are the corresponding lorentzian fits).

6.3.3 Measurement of the Correlations

For every pulse emitted by the excitation laser (every 12.2ns), each source emits one single photon that temporally overlaps at the HOM beamsplitter. Considering the excitation periodicity, the correlation histogram presents only one peak every 12 ns. Figure 6.10b. shows the measured histograms for different temperatures of QD A. On average, each correlation was measured with an acquisition time of about dozen minutes. As previously stated, the height of the central peak compared to lateral peaks gives the

probability that the photons interfere. For distinguishable photons, its height is given by $(g_A^{(2)}(0) + g_B^{(2)}(0))/2 + R^2 + T^2$. The central peak area decreases when the two sources are tuned to the same energy as seen by fig.6.10c. where the black points correspond to $\Delta E = -3\mu\text{eV}$ compared to the red points where $\Delta E = 87\mu\text{eV}$.

6.3.4 Measured Photon Overlap

One coincidence at zero delay corresponds to different situations, as explained now:

- Two single photons arrive simultaneously on the beamsplitter (BS), but do not interfere. In a perfectly aligned interferometer (with a perfect visibility), this event probability reads

$$p = R^2 - 2RTM_{(A+B)} + T^2 \quad (6.2)$$

where $M_{(A+B)}$ is the photon overlap, R and T the intensity coefficients of the BS.

- The QD A emitted more than one photon per pulse. The associated probability is $p = g_A^{(2)}(0)/2$.
- The QD B emitted more than one photon per pulse. The associated probability is $p = g_B^{(2)}(0)/2$.

The normalized central peak area is given by the contribution of all these events:

$$\frac{A_0}{A_{12.2\text{ns}}} = \frac{g_A^{(2)}(0) + g_B^{(2)}(0)}{2} + R^2 - 2RTM_{(A+B)} + T^2 \quad (6.3)$$

The photon overlap $M_{(A+B)}$ is therefore derived as follow:

$$M_{(A+B)} = \frac{1}{(1-\epsilon)^2} \left[\frac{g_A^{(2)}(0) + g_B^{(2)}(0)}{2} + \frac{R^2 + T^2}{2RT} - \frac{(R+T)^2}{2RT} \frac{A_0}{A_{12.2\text{ns}}} \right] \quad (6.4)$$

where $(1-\epsilon)$ is the interferometer visibility, $g_A^{(2)}(0)$ ($g_B^{(2)}(0)$) the single-photon purity of QD A (QD B), R and T the reflection and transmission intensity coefficients of the beamsplitter and A_0 ($A_{12.2\text{ns}}$) the area of the zero delay (12.2 ns) peak.

Points on fig.6.11 shows the measured photon overlap $M_{(A+B)}$ as a function of ΔE . At high detuning, the measured photon overlap is equal to zero as one could expect since the photons are distinguishable due to the spectral detuning. The photon overlap increases to reach a maximum equal to $M_{(A+B)} = 0.40 \pm 0.04$ at $\Delta E = 0$ without any temporal filtering. Such interference contrast constitutes the current state-of-the-art for a remote-QD interference under a non-resonant excitation. Note that such contrast is higher than the one observed for photons successively emitted by QD B. Moreover the

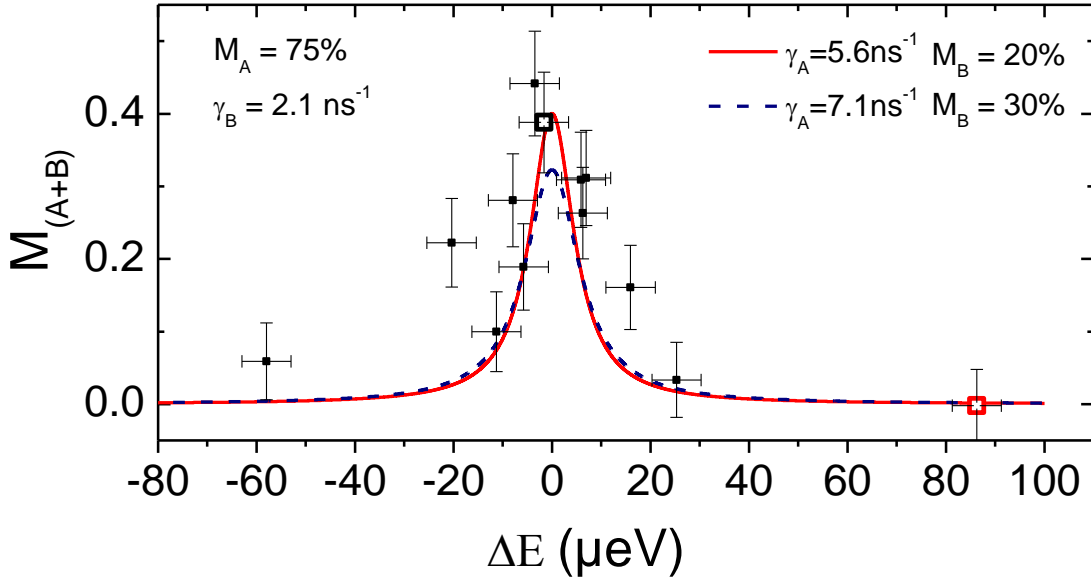


FIGURE 6.11: Measured photon overlap $M_{(A+B)}$ as a function of the detuning between the emission of QD A and QD B ΔE . Lines correspond to the calculated photon overlap using the parameters indicated.

two-photon interference takes place over a large spectral band, with a full width at half maximum (FWHM) as high as $15 \pm 5 \mu\text{eV}$. Patel et al. [132] reported a FWHM for a two source interference of $5 \mu\text{eV}$ with QDs in planar cavity. In our case, the enhancement of the spontaneous emission leads to a broadening of the interfering spectral range due to the broadening of the radiative emission lines by the Purcell effect.

6.4 Cavity Enhanced Interference

The quantum interference between remote sources is investigated in a situation where it is possible to control the sources decay time. Such possibility opens interesting perspectives to optimize a two-source interference as we will discuss in the following section. We first present the theoretical framework developed to account for this experiment by our collaborators in the group of Alexia Auffèves at the Institut Néel.

6.4.1 Theoretical Model - Overlap of Distinct Photons

Different theories about the two-photon interference have been published in the past. Kiraz et al. [162] studied the effect of time-jitter of the charges relaxation in the QD on the two-photon interference using one source. In 2010, Patel et al. [132] proposed a model accounting for the spectral diffusion of independent remote sources. The model developed here consider different emitters with different decay rates, experiencing pure dephasing phenomena [191]. Note that a model based on spectral diffusion was also

developed and could equally account for our observations. In both cases, the time-jitter of the exciton creation in the QD was neglected.

We consider a pair of two-level emitters. We note the associated annihilation operators \hat{a}_A and \hat{a}_B that respectively arrive on the two input ports of a beam splitter. The output annihilation operators (\hat{a}_C, \hat{a}_D) are defined by the unitary operation:

$$\begin{pmatrix} \hat{a}_C \\ \hat{a}_D \end{pmatrix} = \begin{pmatrix} \sqrt{T} & -\sqrt{R}e^{-i\phi} \\ \sqrt{R}e^{i\phi} & \sqrt{T} \end{pmatrix} \begin{pmatrix} \hat{a}_A \\ \hat{a}_B \end{pmatrix} \quad (6.5)$$

The probability to measure two clicks in the two output ports P_c reads

$$P_c = \frac{\int dt_1 \int dt_2 g_{CD}^{(2)}(t_1, t_2)}{\left[\int dt \langle \hat{a}_C^\dagger(t) \hat{a}_C(t) \rangle \right] \left[\int dt \langle \hat{a}_D^\dagger(t) \hat{a}_D(t) \rangle \right]} \quad (6.6)$$

where the function $g_{CD}^{(2)}(t_1, t_2)$ is

$$\begin{aligned} g_{CD}^{(2)}(t_1, t_2) &= \langle \hat{a}_C^\dagger(t_1) \hat{a}_D^\dagger(t_2) \hat{a}_D(t_2) \hat{a}_C(t_1) \rangle \quad (6.7) \\ g_{CD}^{(2)}(t, t + \tau) &= T^2 \langle \hat{a}_A^\dagger(t) \hat{a}_A(t) \rangle \langle \hat{a}_B^\dagger(t + \tau) \hat{a}_B(t + \tau) \rangle + R^2 \langle \hat{a}_A^\dagger(t + \tau) \hat{a}_A(t + \tau) \rangle \langle \hat{a}_B^\dagger(t) \hat{a}_B(t) \rangle \\ &\quad - TR \langle \hat{a}_A^\dagger(t) \hat{a}_A(t + \tau) \rangle \langle \hat{a}_B^\dagger(t + \tau) \hat{a}_B(t) \rangle - \langle \hat{a}_A^\dagger(t + \tau) \hat{a}_A(t) \rangle \langle \hat{a}_B^\dagger(t) \hat{a}_B(t + \tau) \rangle \end{aligned}$$

Assuming a temporal invariance of the $g_{CD}^{(2)}(t_1, t_2)$, the time dependence t_1 and t_2 is replaced by t and $t + \tau$ where τ is the delay between the two detections. The above expression only links the probability of coincidence to the input photons and to the beamsplitter characteristics. Considering that the photon wavepackets are emitted by two independent two-level systems, we have:

$$\langle \hat{a}_A^\dagger(t) \hat{a}_A(t + \tau) \rangle = n_A \gamma_A e^{-\gamma_A t} e^{-i\omega_A \tau} e^{-(\gamma_A + \gamma_A^*)\tau/2} \quad (6.8)$$

$$\langle \hat{a}_B^\dagger(t) \hat{a}_B(t + \tau) \rangle = n_B \gamma_B e^{-\gamma_B t} e^{-i\omega_B \tau} e^{-(\gamma_B + \gamma_B^*)\tau/2} \quad (6.9)$$

where γ_A (resp. γ_B) is the radiative decay rate of the two-level emitter A (resp. B), ω_A (resp. ω_B) is the photon angular frequency, $\gamma_A^*/2$ (resp. $\gamma_B^*/2$) is the pure dephasing rate, and n_A (resp. n_B) is the probability of photon emission per wave packet for each emitter.

For perfect single photon wavepackets:

$$g_{AA}^{(2)} = g_{BB}^{(2)} = 0 \quad (6.10)$$

Hence the correlation between the two output ports $g_{CD}^{(2)}(t, t + \tau)$ reads

$$g_{CD}^{(2)}(t, t + \tau) = n_A n_B T^2 e^{-(\gamma_A + \gamma_B)t} e^{-\gamma_B \tau} + n_A n_B R^2 e^{-(\gamma_A + \gamma_B)t} e^{-\gamma_A \tau} - n_A n_B T R e^{-(\gamma_A + \gamma_B)t} e^{-(\gamma_A + \gamma_A^* + \gamma_B + \gamma_B^*)\tau/2} [e^{i\Delta\omega\tau} + e^{-i\Delta\omega\tau}] \quad (6.11)$$

where $\Delta\omega = \omega_B - \omega_A$. We are interested in the interferences in pulsed regime without any temporal post-selection, we thus integrate over the two time variables:

$$\begin{aligned} \int_0^\infty dt \int_{-\infty}^{+\infty} d\tau g_{CD}^{(2)}(t, t + \tau) &= 2 \int_0^\infty dt \int_0^{+\infty} d\tau g_{CD}^{(2)}(t, t + \tau) \\ &= \frac{2n_A n_B}{\gamma_A + \gamma_B} \int_0^{+\infty} d\tau \left[T^2 e^{-\gamma_B \tau} + R^2 e^{-\gamma_A \tau} - T R e^{-(\gamma_A + \gamma_A^* + \gamma_B + \gamma_B^*)\tau/2} (e^{i\Delta\omega\tau} + e^{-i\Delta\omega\tau}) \right] \\ &= \frac{2n_A n_B}{\gamma_A + \gamma_B} \left[\frac{T^2}{\gamma_B} + \frac{R^2}{\gamma_A} - T R \frac{\gamma_A + \gamma_B + \gamma_A^* + \gamma_B^*}{\Delta\omega^2 + [(\gamma_A + \gamma_B + \gamma_A^* + \gamma_B^*)/2]^2} \right] \end{aligned} \quad (6.12)$$

In parallel, the terms of the denominator of eq.6.6 read

$$\begin{aligned} \int_0^{+\infty} dt \langle \hat{a}_C^\dagger(t) \hat{a}_C(t) \rangle &= \int_0^{+\infty} dt \left[T \langle \hat{a}_A^\dagger(t) \hat{a}_A(t) \rangle + R \langle \hat{a}_B^\dagger(t) \hat{a}_B(t) \rangle \right] \\ &= \frac{T n_A}{\gamma_A} + \frac{R n_B}{\gamma_B} \\ \int_0^{+\infty} dt \langle \hat{a}_D^\dagger(t) \hat{a}_D(t) \rangle &= \frac{R n_A}{\gamma_A} + \frac{T n_B}{\gamma_B} \end{aligned} \quad (6.13)$$

In the following, we consider an equal probability of photon emission ($n_A = n_B$). Then the normalized probability to detect coincidences is

$$P_c = R^2 + T^2 - 2RTM_{(A+B)} \quad (6.14)$$

with

$$M_{(A+B)} = \frac{\gamma_A \gamma_B}{\gamma_A + \gamma_B} \frac{\gamma_A + \gamma_B + \gamma_A^* + \gamma_B^*}{\Delta E / \hbar^2 + [(\gamma_A + \gamma_B + \gamma_A^* + \gamma_B^*)/2]^2} \quad (6.15)$$

where $\Delta E = \hbar\omega$ is the detuning between the emission lines of the QD.

6.4.2 Comparison with the Measured Photon Overlap

Solid lines in fig.6.11 show the theoretical evolution of $M_{(A+B)}$ as a function of ΔE given by the eq.6.15. The best fit to the data are obtained for parameters (see table 6.2) that are compatible with the one derived from the individual source characterization (see table 6.1).

As shown in the eq.6.15, the spectral width of the two-photon interference is determined by the mean value of the decay rates (γ) of both sources and by their pure dephasing

	Red solid line		Blue dashed line	
	QD A	QD B	QD A	QD B
Decay Rate γ	7.1 ns ⁻¹	2.1 ns ⁻¹	5.6 ns ⁻¹	2.1 ns ⁻¹
Equivalent Decay Time T_1	140ps	470ps	180ps	470ps
Pure dephasing Rate γ^*	2.5 ns ⁻¹	8 ns ⁻¹	1.8 ns ⁻¹	5 ns ⁻¹
Equivalent pure dephasing time T_2^*	800 ps	250 ps	1100 ps	400 ps
Corresponding successive photon indistinguishability $M = \frac{\gamma}{\gamma+\gamma^*}$	75 %	20 %	75 %	30 %

TABLE 6.2: Parameters of QD A and QD B used to calculate the wavepacket overlap between the photons emitted by both QDs

rates (γ^*): the wavepackets overlap over a detuning range given by $\frac{\gamma_A + \gamma_A^* + \gamma_B + \gamma_B^*}{2}$. The FWHM of 15 μ eV observed experimentally results both from the Purcell enhancement of γ_A and γ_B , as well as from the pure dephasing on QD B partly.

The two-source interference reaches a value 0.4 ± 0.04 although successively emitted photons by the QD B present a poor overlap (only $M_B = 0.19 \pm 0.15$). In the following, we discuss the details of how the interference using remote sources can be enhanced by the acceleration of spontaneous emission of one source.

A striking feature of our experimental results is the maximum contrast of 0.40 ± 0.04 , provided that QD B emits photons exhibiting an overlap of $M_B = 0.19 \pm 0.15$. In other words, although photons successively emitted by the same emitter hardly overlap, they overlap more efficiently with photons presenting different properties. These observations show that the overlap between remote sources can be optimized through the Purcell effect. For each M_B , there is an optimal value for T_1^A maximizing the interference contrast. Depending on the degree de decoherence of QD B, the decay time of QD A can be optimized in order to maximize the contrast of interference.

The black solid lines in fig.6.12a. show the calculated photon overlap at zero detuning $M_{(A+B)}(\Delta E = 0)$ as a function of T_1^A for different degrees of photon indistinguishability M_B (i.e. different pure dephasing rate γ_B^*). The decay time of QD B is fixed to $T_1^B = 470$ ps and the photon indistinguishability of QD A to $M_A = 0.75$. For a given M_B , we can observe a general trend of the evolution of $M_{(A+B)}$ as a function of T_1^A . If the decay time T_1^A of QD A is too short compared to the one of QD B T_1^B , the overlap is not maximized due to the important mismatch between the wavepacket envelopes. Then $M_{(A+B)}$ increases and reaches a maximum for $T_1^A = T_{1,opt}^A$ which is strongly dependent of the QD B indistinguishability degree M_B .

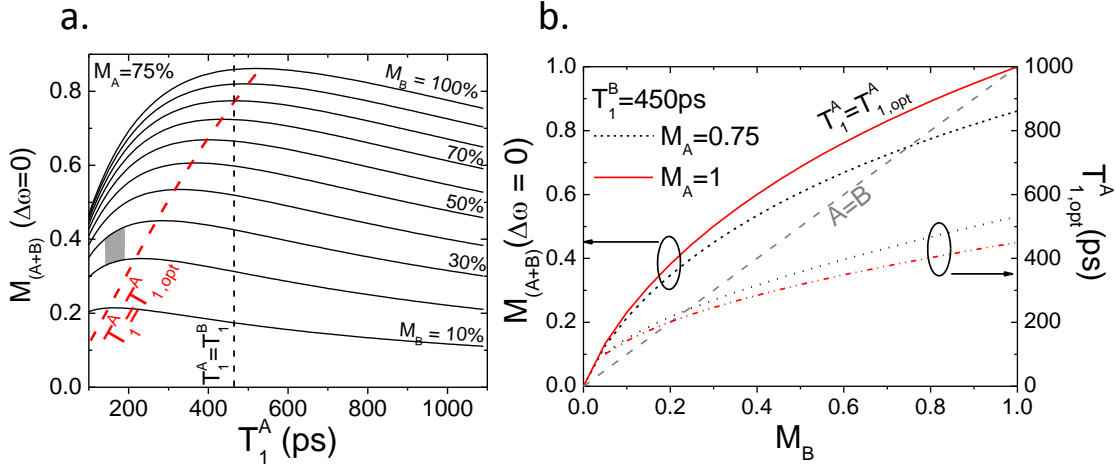


FIGURE 6.12: **a.** Calculated photon overlap $M_{(A+B)}$ at zero detuning ($\Delta E = 0$) as a function of T_1^A , the decay time of QD A, with a fixed $M_A = 75\%$ and different values of M_B . The decay time of QD B is fixed at $T_1^B = 470\text{ps}$. The red dashed line indicates the optimal value of $T_{1,opt}^A$ defined as the optimal decay time where $M_{(A+B)}(\Delta E = 0)$ is maximum. The vertical dashed line indicates the situation where $T_1^A = T_1^B$. Grey area shows the region of parameters for our devices. **b.** (Left axis) Optimal photon overlap $M_{(A+B)}(\Delta E = 0)$ obtained with $T_1^A = T_{1,opt}^A$ and $T_1^B = 470\text{ps}$ in a solid, red (dashed, black) line for $M_A = 1$ ($M_A = 0.75$). The grey dashed line indicated the photon overlap when both sources are identical. (Right axis) Evolution of the optimal decay time $T_{1,opt}^A$ for a value of $M_A = 1$ ($M_A = 0.75$) in a red dot-dashed (black dotted) line.

From eq.6.4, we calculate the optimal decay time of QD A $T_{1,opt}^A$ as a function of the characteristics of QD A and QD B:

$$T_{1,opt}^A = \frac{2}{\left(\left(\frac{\gamma_B(1-M_A)}{M_A} \right)^2 + 4\gamma_B(\gamma_B + \gamma_B^*) \right)^{1/2} - \gamma_B \frac{1-M_A}{M_A}} \quad (6.16)$$

The red dashed line in fig.6.12b. shows the evolution of $T_{1,opt}^A$ as a function of M_B . As expected, the maximum contrast is obtained with $T_{1,opt}^A = T_1^B$ when the sources present the same mean wave packet overlap ($M_B = M_A$). In this scenario, $M_{(A+B)}$ is only limited by the pure dephasing rates.

The left axis of fig.6.12b. shows the evolution of the maximum contrast when the decay time of QD A is always optimized $M_{(A+B)}(\Delta E = 0, T_1^A = T_{1,opt}^A)$ as a function of the indistinguishability degree of QD B M_B . The red solid line corresponds to a perfect indistinguishability of QD A ($M_A = 1$) while the black dashed line to the indistinguishability of QD A that we measured ($M_A = 0.75$). We observe that the optimization of the decay

time of one of the sources (from 100 ps to 500 ps as illustrated by the right vertical axis) allows us to increase the interference probability of the photons compared to the successively emitted photon interference (gray dashed line). The right vertical axis shows the evolution of the optimal decay time $T_{1,opt}^A$ as a function of M_B with $M_A = 1$ (red dashed-dotted line) and with $M_A = 0.75$ (black dotted line). The lower the coherence of the QD B, the faster must be the QD A decay time in order to overcome the dephasing processes.

The Purcell effect was known to improve the indistinguishability of photons successively emitted by limiting the influence of the environment. In a network made of remote sources, the Purcell enhancement of the spontaneous emission of one of the sources was demonstrated here to overcome the pure dephasing that one source suffers and partially restore the two-photon interferences.

6.4.3 Conclusion

In this chapter, we reported the two-photon interference using two bright independent QD sources. We demonstrate a record high interference contrast of 0.40 ± 0.04 with a FWHM of 15 ± 5 , values corresponding to better photon-photon interactions with respect to previous results using QDs in planar structures under non-resonant excitation [132]. We discussed both theoretically and experimentally that the Purcell effect can enhance the two-photon interferences. We also showed that the best photon overlap between remote sources is not always obtained by choosing similar decays. The acceleration of one of the sources allows to overcome the dephasing effects induced by the surrounding electronic noise, or by the interaction with the phonon bath, on the other source. This effect is interesting for the development of a photonic solid-state quantum network since it potentially increases the number of single-photon sources that could interact taking advantage of the radiative broadening of one device.

As in chapter 3, here the interference contrast was mainly limited by the charge noise that the source is exposed to. By benefiting from the performance provided by the sources of chapters 4 and 5 and from electrical control of the emission wavelength, one could expect much better interference using remote contacted sources.

Chapter 7

Conclusion and Perspectives

In this thesis, we developed solid-state sources of quantum light based on QD in micro-cavities. All devices were fabricated using a deterministic technology allowing to fully control the QD-cavity coupling both spatially and spectrally. We demonstrated the fabrication of bright single-photon sources by using an adiabatic cavity design in order to reach a high Purcell factor. Yet we showed that the indistinguishability of the photons was limited by the electronic noise of the QD surrounding.

To overcome these electronic fluctuations, electrically controlled devices were developed in 2013. By embedding the QD layer in a diode structure, the tunability of a bright single-photon source was demonstrated. With a such structure, a clear improvement of the photon indistinguishability was evidenced in a reproducible way. It was particularly demonstrated that the mean photon overlap was not limited by the environment anymore but by the incoherent relaxation processes due to the non resonant excitation.

Using a resonant excitation for a QD in a connected cavity, we demonstrated the coherent control of the QD transition. Under such excitation, the mean photon overlap between successively emitted photons was shown to be close to unity with a brightness of 16% exceeding by almost two orders of magnitude the one of SPDC sources of the same quality.

Finally, we implemented the first two-photon interference using two remote bright sources whose spontaneous emission is controlled by the Purcell effect. We demonstrated that CQED brings a new tool for the scalability and the feasibility of a quantum optical network based on solid-state devices.

Fabricating pure and efficient single photon sources has been an important motivation of the QD community in the last decade, with many progresses obtained in various groups in the last few years. Benefiting from the experience developed in the group of Pascale Senellart at the LPN, the results obtained during this last year bring the QD sources to a level where they can significantly surpass the SPDC sources currently used in optical quantum technologies. Moreover, we demonstrated an extremely good coupling between

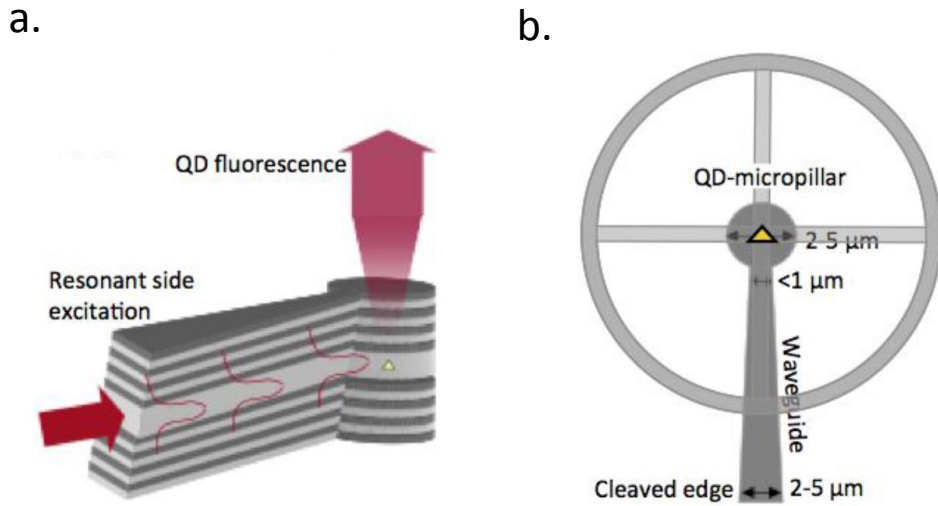


FIGURE 7.1: **a.** Schematic of a micropillar containing a single QD (yellow triangle). A 1D wire is connected to the pillar in a such way that a laser pulse is sent through this wire to resonantly excite the QD in the pillar. **b.** Top view of the schemed structure of the electrically controlled source with a waveguide for the lateral excitation

flying quantum bits (photons) and the single QD in a micropillar, such that coherent control of the exciton transition is now possible by sending only few photons on the device.

These results pave the way to many interesting experiments in quantum optics. In the following, we first discuss some solutions to further improve the sources brightness. Then, we propose several experiments that could directly benefit from the high quality of the sources presented in chapters 4 and 5.

7.1 Strategies to Improve the Sources

The measured brightness of the connected pillar is around 0.65 with an output coupling of the photons through the top mirror around 0.7. By slightly decreasing the number of DBR pairs of the top mirror of the pillars, one could operate the source in a regime of Purcell effect in the $F_P = 6 - 8$ range, while bringing the output coupling efficiency to 0.8-0.85. Moreover, in the connected pillar geometry, the side losses are mostly related to leaky modes in the wires. The precise geometry of the wires (width, shape, number) has not been optimized yet to reduce these losses.

Using strictly resonant excitation, the emission of fully indistinguishable photons was demonstrated with a brightness around 0.16. Under the same excitation conditions, a

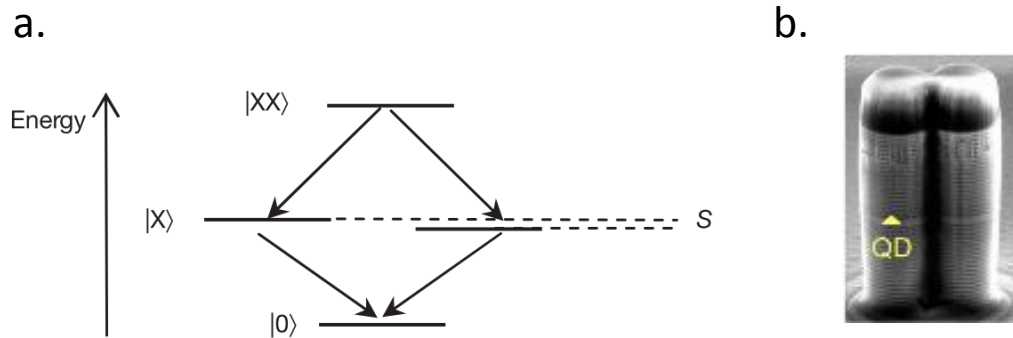


FIGURE 7.2: Figure reproduced from [46] **a.** Sketch of the radiative cascade in a single quantum dot. **b.** SEM image of the photonic molecule containing a single QD (yellow triangle).

brightness as high as 60-70% could in principle be reached by changing the excitation configuration such that the collection path and the excitation path are separated. Such excitation schemes were first demonstrated in planar cavities [164, 166] and one once with micropillar cavities [39] and formed a promising solution to reach brightnesses in the 0.6-0.8 range under resonant excitation. Considering the new design of micropillars connected to a surrounding frame, an attractive possibility would be to take advantage of 1D wires to guide the light to the micropillar as illustrated in fig.7.1. Carlos Anton joined the group as a post-doc in 2015 and will address this challenge in collaboration with the group of Pr. Peter Michler from the University of Stuttgart in Germany.

7.2 Toward Ultrabright and Highly Indistinguishable Sources of Entangled Photon Pairs

A source of triggered entangled photon pairs is a key component in quantum information processing protocols. Polarization entangled photon pairs can be generated using PDC sources or by making use of the radiative cascade of a biexciton trapped in a QD. A biexciton (XX) recombines radiatively through a two-photon cascade. As shown by fig.7.2a., two radiative recombination paths are possible through two exciton states (XX) of orthogonal polarization. The two paths are indistinguishable if the exciton fine structure splitting is negligible with respect to its linewidth leading to the emission of a polarization entangled photon pair. In 2010, Dousse et al. [46] used the *in*

situ lithography technique to fabricate a bright source of polarization entangled photon pairs constituted of a photonic molecule in which a QD is deterministically coupled as shown by fig.7.2. The key feature of the photonic molecule is that two cavity resonances correspond to both XX and X photons, consequently, the collection efficiency of both XX and X photons was considerably improved, leading to a brightness of 0.35 for both photons.

An interesting perspective to emit **indistinguishable** pairs of entangled photons is the resonance fluorescence from the biexciton state. Two solutions are then possible: (i) exciting the QD using a set of two laser excitation at the wavelengths of the exciton λ_x and of the biexciton λ_{xx} or (ii) using the two-photon absorption of a laser at an energy $(E_x + E_{xx})/2$.

In most of the works reported the resonant excitation of the biexcitonic transition, the excitation scheme using one laser is implemented. In 2006, Stuffer et al. [192] reported the two-photon Rabi oscillation of the biexciton by monitoring the current. In 2013, Jayakumar et al. [193] focused pulsed and shaped laser excitation from the side of the sample and collected the resonant fluorescence of both the biexciton and the exciton lines from the top of the sample. In 2014, Muller et al. [42] used a similar method to demonstrate the emission of indistinguishable and polarization-entangled photon pairs by using a two-photon excitation scheme. Indistinguishabilities of $M_x = 0.71 \pm 0.04$ and of $M_{xx} = 0.86 \pm 0.03$ were demonstrated for the exciton and the biexciton photons, respectively.

These works are very promising since they combine entanglement in polarization and high indistinguishability allowed by the resonant excitation of the biexciton. The next step is obviously to combine these techniques with efficient photon collection, using electrically controlled photonic molecules [46].

7.3 Generation of a High Photonic NOON States using QDs

With the already developed sources, 40 times brighter than PDC-based sources of the same quality, many exciting experiments can be foreseen.

A NOON state is a multiphoton state that can be written as $\frac{|N0\rangle + |0N\rangle}{\sqrt{2}}$. In a context of quantum metrology [195] or quantum sensing, replacing single photons by maximally entangled N -photon NOON state in an interferometer leads to a strong enhancement of the phase uncertainty. For instance, it offers the possibility to obtain a higher precision

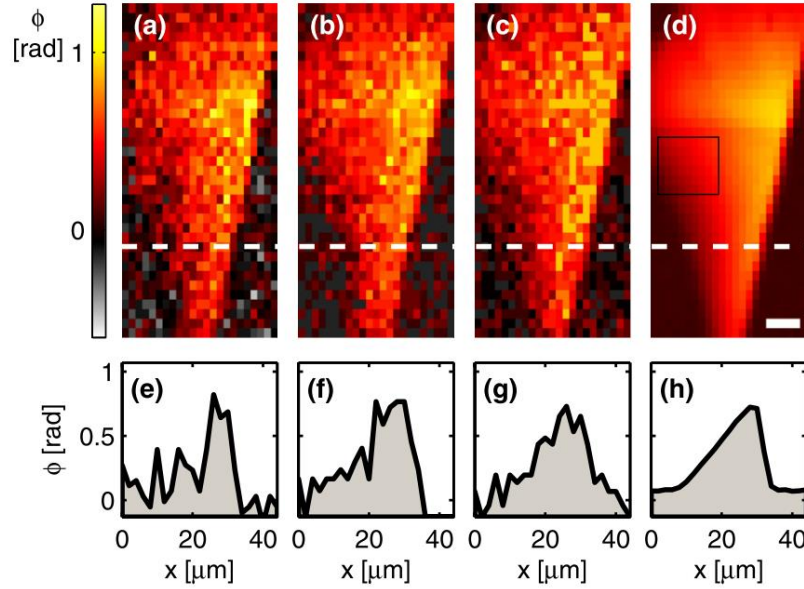


FIGURE 7.3: Figure reproduced from [194]. **a.-d.** Comparison of phase microscopy sensitivity for quantum and classical illumination of single quartz crystal: **a.** using a coherent state only, **b.** using a $N=2$ and **c.** using a $N=3$ NOON states using exactly 50 single photons for **a-c.** **d.** Reference image using bright illumination. The scale bar is $10\mu\text{m}$. **e.-h.** Cross sections marked by dashed white in **a.-d.**

on the phase measurement than the one that could be obtained with a coherent light. If initially the state reads $(|N0\rangle + |0N\rangle)\sqrt{2}$, the state is sent into an interferometer and evolves into $(|N0\rangle + e^{iN\phi}|0N\rangle)\sqrt{2}$ with ϕ the phase shift due to the interferometer difference of paths. This phase shift results in an uncertainty $\Delta\phi \propto 1/N$ corresponding to an improvement of $1/\sqrt{N}$ over the standard quantum limit. NOON states can also allow the realization of super-sensitivity experiments such as supersensitive polarization microscopy as shown by fig.7.3 reproduced from [194].

Historically, the first NOON state was studied in 1990 by Ou et al. [197] with $N=2$ after the demonstration of the Hong-Ou-Mandel (HOM) experiment. Indeed, after the beam-splitter where the two-photon interference takes place, the two photon state $\frac{|20\rangle + |02\rangle}{\sqrt{2}}$ is a path entangled state since both photons exit by either one or the other output. Later, NOON states were studied with $N=3$ and $N=4$ [22, 23, 198]. To our knowledge, Afek et al. [196] measured the highest NOON state ($N=5$) in 2010. Figure 7.4 shows the measured coincidences for $N=2, 3, 4$ and 5 as a function of the phase in a Mach-Zender (MZ) interferometer. As predicted, the phase shifts increases linearly with the number of photons N used for the NOON state. All these works used SPDC sources or coherent sources. In their conclusions, Afek et al. [196] highlight the need for bright and pure sources and efficient single-photon detectors in order to extend the number of photons in the NOON states.

One of the objectives of Lorenzo de Santis who started his PhD in the group in 2014, is to prepare an experiment to measure the NOON state tomography at the output of a HOM interferometer [199] using QD-based sources. A sketch of the developed setup is shown in fig.7.5.

7.4 Boson Sampling Experiments with QD sources

In a context where computing performances must always increase, the development of an universal quantum computer is a major challenge. An universal quantum computer is expected to solve problems that are unsolvable for a classical one.

Nevertheless, its full-size realization remains very challenging. Therefore, intermediate quantum computing schemes have been proposed. Aaronson and Arkhipov showed that the interferences of single photons in a random network can give a measurement of the output of a boson sampling problem, a prediction that is not possible with a classical computer. The problem consists in predicting the output distribution of n single and indistinguishable photons that travelled through a photonic circuit with m modes. An optical circuit can be modelled by an unitary $m \times m$ matrix U . The probability of finding a given state at the output is given by the square of the permanent of the $n \times n$ submatrices U_{IO} related to the output and input states. More precisely, if the input state is noted $I = (I_1, \dots, I_m)$ and the output state is noted $O = (O_1, \dots, O_m)$ where I_k and O_k are the boson occupation numbers, a first $n \times m$ matrix is produced by taking O_k copies of the k^{th} column of U . Then the submatrix U_{IO} is obtained by taking I_k copies of the k^{th} row of the last submatrix. The probability of finding the output state O given the input state I reads:

$$P_Q = |\text{Perm}(U_{IO})|^2 \quad (7.1)$$

For example, the HOM interference used to extract the photon indistinguishability is one particular case of boson sampling with $n = m = 2$. The probability to measure a click at the two outputs is given by:

$$P_Q = |\text{Perm}(U_{IO})|^2 = \left| \text{Perm} \begin{pmatrix} T & iR \\ iR & T \end{pmatrix} \right|^2 = |T^2 - R^2| \quad (7.2)$$

In the case of a 50:50 beamsplitter, the permanent is obviously zero which is coherent with the previous considerations. In the case where the photons are completely distinguishable, the classical scattering probabilities are given by:

$$P_C = |\text{Perm}(|U_{IO}|^2)| = T^2 + R^2 \quad (7.3)$$

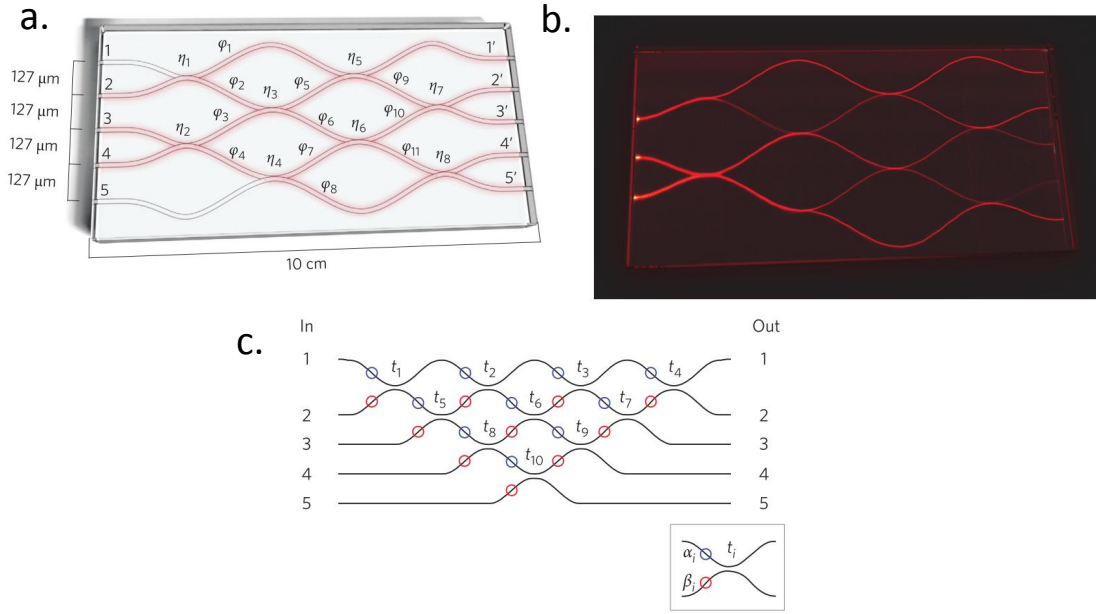


FIGURE 7.6: **a.** **b.** Figures reproduced from [200]. **a.** Schematic of the photonic circuit. It consists of five input modes, five output modes, eight directional couplers and eleven phase shifters. Each output mode is connected to a single-photon detector. **b.** Fluorescence image, a laser light at a wavelength of 633nm was launched into input modes 2 to 4 of an optical network. Colour centre are excited by the propagating beam and emit fluorescent light at 650nm. **c.** Figure reproduced from [201]. Schematic of an arbitrary 5×5 mode transformation. The blue and red circles indicate different phase shifters.

It is interesting to note that the effect of classical events can be removed by measuring the non-classical interference visibility:

$$V = \frac{P_C - P_Q}{P_C} \quad (7.4)$$

In the case of the HOM experiment with photons presenting an indistinguishability M , the probability to detect coincidences reads

$$P_Q = T^2 - 2RTM + R^2 \quad (7.5)$$

So the visibility is

$$V = \frac{2RTM}{R^2 + T^2} = M \quad \text{if } R=T=0.5 \quad (7.6)$$

The first boson sampling is the HOM experiment that was demonstrated by Hong, Ou and Mandel in 1986 with two photons and two modes [98]. We had to wait up to the end of 2012 to see the first demonstration of boson sampling with three photons. This experiment has been simultaneously done by three groups: in Pr. Andrew G. White's group, three photons were sent in 6 optical modes by using fibers [202] while in the groups of Pr. Philip Walther and Pr. Fabio Sciarrino, photonic circuit on chips were

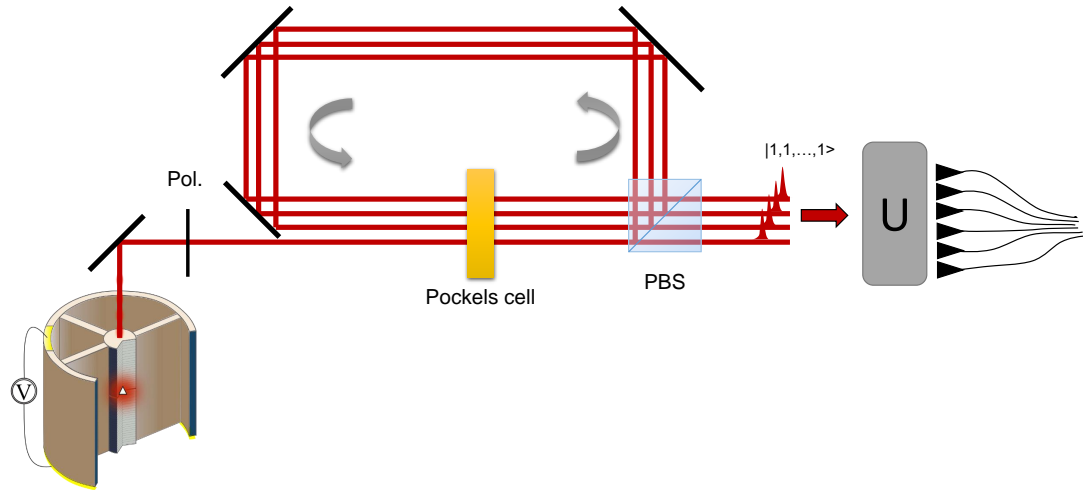


FIGURE 7.7: Schematic of a possible experiment with one electrically controlled device as a single-photon source used to emit single photon before a Fock state is prepared and is sent into a unitary transformer.

developed [200, 201].

To demonstrate that the extended Church-Turing thesis is wrong and the utility of a quantum computer, a large-size system would be necessary. This would require about $n \sim 20 - 30$ photons with a large ($m \gg n$) number of modes. Although it seems easy to largely increase the number of modes [203], it is very difficult to increase the number of input photons because of the limited brightness of SPDC sources. We discussed this point with the group of Pr. Andrew White, authors of [202]. To measure the three-photon boson sampling (fig. 3 of [202]), the acquisition time was about 3 hours and 20 minutes. Considering the 60 visibility points, this corresponds to a full week of continuous acquisition. During such a long acquisition time, the optical alignment drifts and needs constant readjustment.

In the same conditions, the acquisition time with eight photons is assessed about 50 hours for one point. Considering a continuous acquisition of the 60 visibility points, the total acquisition time would be around 3 months.

Since 2012, our group collaborates with the group of Pr. Andrew White in order to combine their expertise in quantum technologies with the performance of our sources. With a brightness of 0.7 typically, a considerable increase of the number of input photons should be reached. Since this collaboration started, a setup using the successively emitted photons by a QD-based source was implemented in order to create a multi-Fock state emitter. This setup is based on the storage of single photons as illustrated by

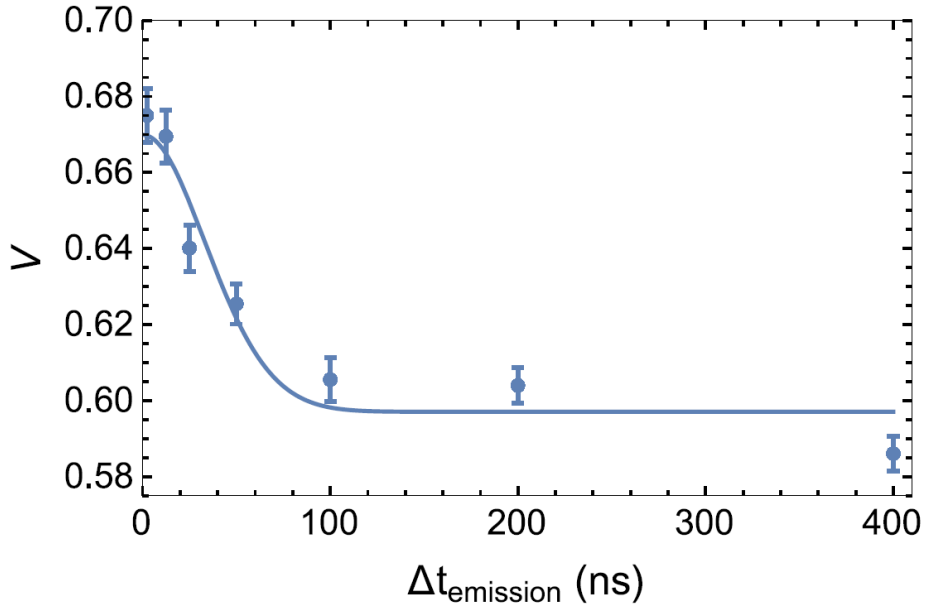


FIGURE 7.8: Data from Juan Loredo et al. Two-photon interference visibility between successively emitted photons as a function of the delay between the emission of these photons. Points are the mean of the all visibilities taken for excitation powers $P < 0.65P_{\text{sat}}$. Solid line corresponds to theoretical predictions from [204].

fig.7.7. Single photons successively emitted from one QD based source are stored into the photon storage as long as the Pockels cell does not flip the polarization of the stored photons. Once the photon polarization is flipped, stored photons are simultaneously emitted and sent into a boson sampling setup.

In this experiment, it is required that photons emitted are indistinguishable whatever the delay separating these photons. Our collaborators Juan Loredo et al. in Brisbane studied the degradation of the two-photon overlap when the temporal delay between the photons is increased. The results were obtained with an old generation of QD-cavity devices (developed in 2011) and are shown in fig.7.8. Thoma et al. [204] developed a model to account for this effect based on a non-Markovian noise induced by the charges surrounding the QD. With the new generation of devices described in chapter 4, the measured reflectivity of the QD in resonance with the cavity evidenced the absence of pure dephasing due to the control of the QD environment in a continuous wave experiment. This suggests that the mean wavepacket overlap is preserved in these devices between successively emitted photons whatever the delay.

Note that, at the LPN, strong efforts have been made on the sources themselves. Yet, our optical setups are still very lossy and should be optimized. In the experiment mounted by Juan Loredo in the university of Queensland, they focused on the optimization of the

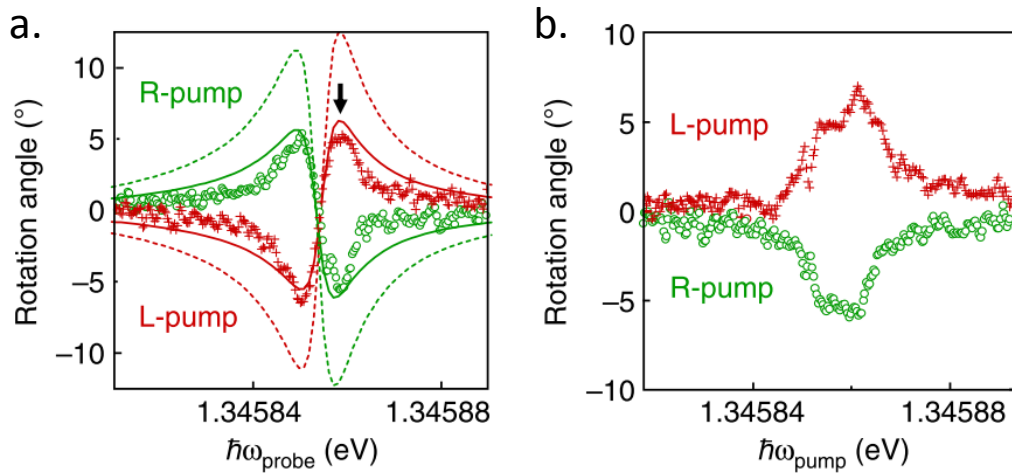


FIGURE 7.9: Figure reproduced from [172]. Symbols: measurement of the Kerr rotation angle as a function of the probe laser energy. Macroscopic Kerr rotation angles up to $\pm 6^\circ$ are obtained by pumping a single spin. Solid lines correspond to theoretical fits.

collection path in order to fully benefit from the brightness of the QD sources. Their efficiency is about 10 times better than the one of setups at the LPN.

7.5 A Step Closer to the Quantum Repeater and the Single-Photon Router ?

The realization of an efficient and scalable interface between a single photon and a stationary qubit is an elementary step for the development of a quantum network composed of many nodes and channels [177]. In chapter 5, we demonstrated the coherent control of the exciton by sending coherent states containing only few photons per pulse. We showed that the combination of the near-unity input coupling with a high cooperativity in our device provides an excellent prospect for the coherent control of the QDs with pure Fock states. Such result is promising for the implementation of an elementary quantum network entirely based on QD devices.

The same devices as those presented in chapter 5 are currently studied by Lorenzo de Santis to measure the nonlinearity at the single photon level. Sending coherent state of light, one expects that only single photons are reflected, so that the device effectively acts as a Fock state filter.

Such device could also be used to create a deterministic two photon beam splitter that

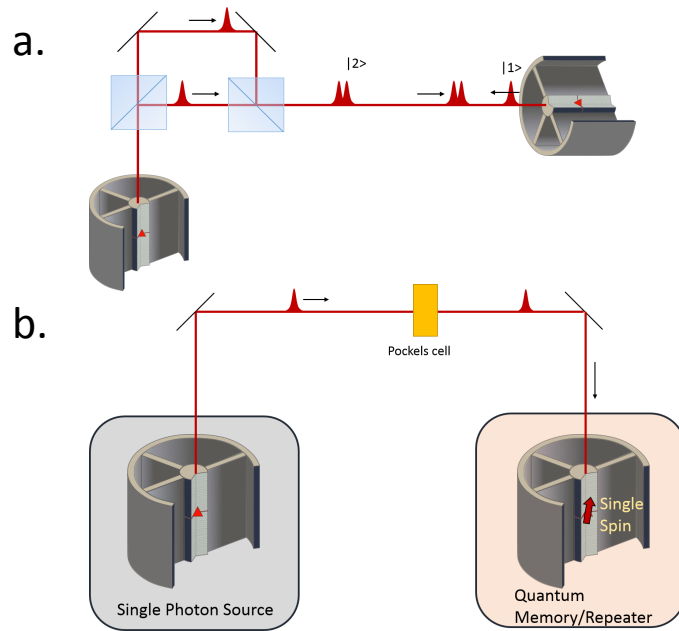


FIGURE 7.10: Schematics of an elementary quantum network using the devices described in this work as a single photon router **a.** or as a quantum memory **b.**

ensures that two photons exit from different outputs. This could be tested by generating a $N = 2$ NOON state with a first source and a HOM interferometer and sending it to another QD in a pillar as sketched in fig.7.10**a.**

Finally, an interesting stationary qubit is the spin of a hole that can have a coherence time as long as a few microseconds [205]. In 2015, a $\pm 6^\circ$ Faraday rotation induced by a single spin in a micropillar cavity was reported at the LPN by Arnold et al. under the supervision of Loic Lanco [172].

These results were obtained with an old generation of QD-based devices with limited cooperativity and output coupling. Strong efforts are made in order to increase the Faraday rotation up to 45° . With the new generation of devices developed in the group, the injection of charges in the QD should allow to deterministically control the charge state of a QD. With the cooperativity and output coupling demonstrated with electrically controlled devices, we expect to reach the situation where the spin can rotate the photon polarization to $\pm 45^\circ$ depending on the spin state. Such situation is ideal to create a maximally entangled spin-photon state by sending a single photon to a spin in a cavity as sketched in fig.7.10**b.**

List of Publications

- **Influence of the Purcell effect on the purity of bright single phoson sources**
V. Giesz, O. Gazzano, A. K. Nowak, S. L. Portalupi, A. Lemaître, I. Sagnes, L. Lanco and P. Senellart
Appl. Phys. Lett. **103**, 033113 (2013)
- **Deterministic and electrically tunable bright single-photon source**
A. K. Nowak, S. L. Portalupi, V. Giesz, O. Gazzano, C. Dal Savia, P.-F. Braun, K. Karrai, C. Arnold, L. Lanco, I. Sagnes, A. Lemaître and P. Senellart
Nature Comm **5**, 3240 (2013)
- **Bright Phonon-Tuned Single-Photon Source**
S. L. Portalupi, G. Hornecker, V. Giesz, T. Grange, A. Lemaître, J. Demory, I. Sagnes, N. D. Lanzillotti-Kimura, L. Lanco, A. Auffèves and P. Senellart
Nano Letters, Accepted (2015)
- **Cavity-enhanced two-photon interference using remote quantum dot sources**
V. Giesz, S. L. Portalupi, T. Grange, C. Anton, L. De Santis, J. Demory, N. Somaschi, I. Sagnes, A. Lemaître, L. Lanco, A. Auffèves and P. Senellart
Phys. Rev. B, **92**, 161302(R) (2015)
- **Near-Optimal Single-Photon Sources in the Solid-State**
N. Somaschi, V. Giesz, L. De Santis, J. C. Loredó, M. P. de Almeida, G. Hornecker, S. L. Portalupi, T. Grange, C. Anton, J. Demory, C. Gomez, I. Sagnes, N. D. Lanzillotti-Kimura, A. Lemaître, A. Auffèves, A. G. White, L. Lanco and P. Senellart
Accepted for publication in *Nature Photonics*
- **Few-Photon Coherent Control of a QD**
V. Giesz, N. Somaschi, L. De Santis, G. Hornecker, T. Grange, J. Demory, C. Anton, C. Gomez, I. Sagnes, A. Lemaître, N. D. Lanzillotti-Kimura, L. Lanco, A.

Auffèves and P. Senellart

Under review for publication in *Nature Materials*

- **Light amplification in a one dimensional artificial atom**

V. Giesz, N. Somaschi, L. De Santis, G. Hornecker, T. Grange, J. Demory, C. Anton, C. Gomez, I. Sagnes, A. Lemaître, N. D. Lanzillotti-Kimura, L. Lanco, A.

Auffèves and P. Senellart

To be submitted

Appendix A

Phonon influence on the emission of a QD coupled to a cavity

We showed how a QD can be coupled with the optical mode of a cavity and how the electromagnetic confinement modifies its spontaneous emission. In parallel, vibrations of the semiconductor lattice make the QD emission associated with the emission or absorption of phonons, via the presence of phonon side bands (PSB) on the emission spectra.

In this section, we see how the coupling bath is modified when the spontaneous emission of a QD is modified due to the coupling with a cavity (in the weak coupling regime).

A.1 Spontaneous emission of a quantum dot in a cavity assisted by phonons bath

In 2009, Hohenester et al. showed that the exciton transition could be assisted by phonons, even when the cavity-exciton is few meV [206]. In 2013, Madsen et al. used this property to measure the effective phonon density [207]. Furthermore, phonons has been shown as a strong link between the cavity and the emitter which can pull the cavity energy through the phonon coupling [135].

Compared to the previous section 2.3.1.3, we consider that the two-level system (QD) is coupled to a continuum of longitudinal acoustic phonons (LA) and to the electromagnetic modes (EM) of the cavity (as shown by the schematics in the fig.A.1). The total Hamiltonian (under the Rotating Wave approximation) associated to the system reads

$$H = \hbar\omega_x |X\rangle\langle X| + H_{phonons} + H_{EM} \quad (\text{A.1})$$

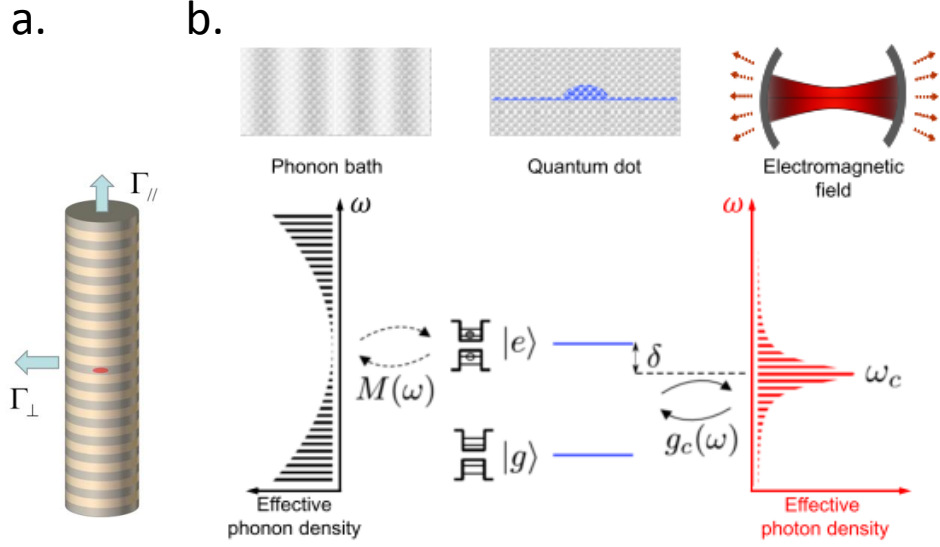


FIGURE A.1: Figures from [?] **a.** Schematic of the pillar with a single QD coupled to optical mode of the cavity. The QD can emit in the optical mode (Γ_{\parallel}) or along the plane (Γ_{\perp}). **b.** Schematics of the model of coupling taking into account the QD, the continuum of LA phonons and the continuum of EM of the cavity.

where ω_x is the pulsation of the exciton transition, $H_{phonons}$ and H_{EM} are respectively the Hamiltonian involving respectively the phononic and the EM modes.

$$H_{phonons} = \int d\omega_{\mathbf{q}} \rho_{ph}(\omega_{\mathbf{q}}) \hbar \omega_{\mathbf{q}} b_{\mathbf{q}}^{\dagger} b_{\mathbf{q}} + \int d\omega_{\mathbf{q}} \rho_{ph}(\omega_{\mathbf{q}}) \hbar M(\omega_{\mathbf{q}}) |X\rangle \langle X| (b_{\mathbf{q}}^{\dagger} + b_{\mathbf{q}}) \quad (\text{A.2})$$

where $b_{\mathbf{q}}$ and $\rho_{ph}(\omega_{\mathbf{q}})$ are the ladder operator and the density of states (DOS) of the LA phonon mode of wavevector \mathbf{q} respectively ; $M(\omega_{\mathbf{q}})$ is the deformation potential coupling between this phonon mode and the exciton. Considering a linear dispersion relation for the LA phonons, and a spherical wave functions for the electron (hole) with a gaussian shape, one can write the DOS and coupling terms respectively:

$$\rho_{ph} = \frac{V \omega_{\mathbf{q}}^2}{2\pi^2 c_s^3} \quad (\text{A.3})$$

$$M(\omega_{\mathbf{q}}) = \sqrt{\frac{\omega_{\mathbf{q}}}{2\hbar c_s^2 \rho_m V_c}} |D_e e^{\sigma_e^2 \omega^2 / c_s^2} + D_h e^{\sigma_h^2 \omega^2 / c_s^2}| \quad (\text{A.4})$$

by taking a sound velocity $c_s = 5000 \text{ m/s}$, a density of mass $\rho_m = 5320 \text{ kg/m}^3$, a deformation potential $D_e = D_h = 9 \text{ eV}$, $\sigma_e = \sigma_h = 3 \text{ nm}$, $V_c = 7.6 \mu\text{m}^3$.

By calculating the DOS of the EM modes and the QD spectrum modified by the polaron shift ($\omega_{QD}^X = 2\pi c / \lambda_X = \omega_0 - \int d\omega_{\mathbf{q}} \rho_{ph}(\omega_{\mathbf{q}}) M(\omega_{\mathbf{q}}) / \omega_{\mathbf{q}}$), the spectrum of the QD reads

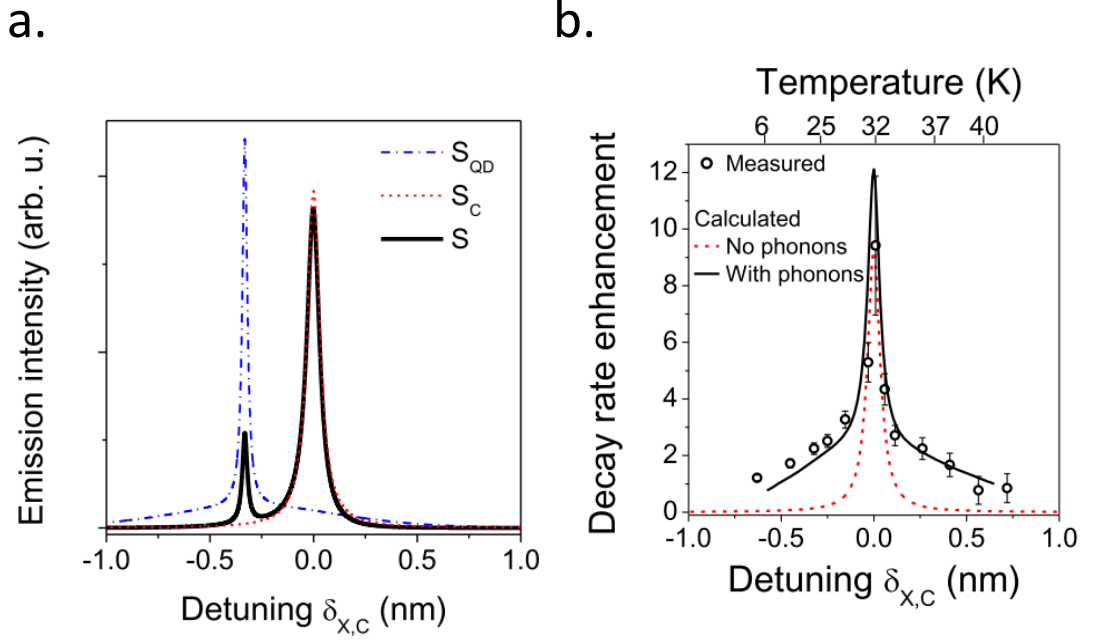


FIGURE A.2: Figures from [?] **a.** Calculated emission spectrum $S(\lambda)$ for a exciton line coupled to cavity line. The blue line is the QD spectrum (coupled to the phonon bath but not coupled to the cavity), the red line is the cavity spectrum. **b.** Measured radiative decay rate normalized to the rate in the planar cavity $\tau_X^0/\tau_X - 1$ as a function of temperature (top axis) and detuning $\delta_{X,C}$ (bottom axis)

$$S_{QD}(\omega) = S_{QD}^{ZPL}(\omega) + S_{QD}^{PSB}(\omega) \quad (\text{A.5})$$

where the first term designates the emission in the Zero Phonon Line (ZPL) and the second corresponds to the emission through the phonon side band (PSB). The fig.A.2 (a) is a plot of three theoretical spectra from the model of coupling we used. When we compare the blue line and the black line, we observe that the height of the ZPL is lower. The cavity mode acts as a filter of the PSB. Moreover, the cavity concentrates the emission of the PSB in order to have a bright emission at the mode energy. This is why one can define an effective Purcell factor taking into account this phenomenon :

$$F_P^{eff} = \frac{\tau_X^0}{\tau_X} - 1 = \frac{\Gamma_{||}^{ZPL} + \Gamma_{||}^{PSB}}{\Gamma_{\perp}} \quad (\text{A.6})$$

τ_X (τ_X^0) being the decay time of the QD in the cavity mode (planar cavity). The symbols \parallel and \perp designates the two possible channels for the QD relaxation : in the cavity mode or the plane mode.

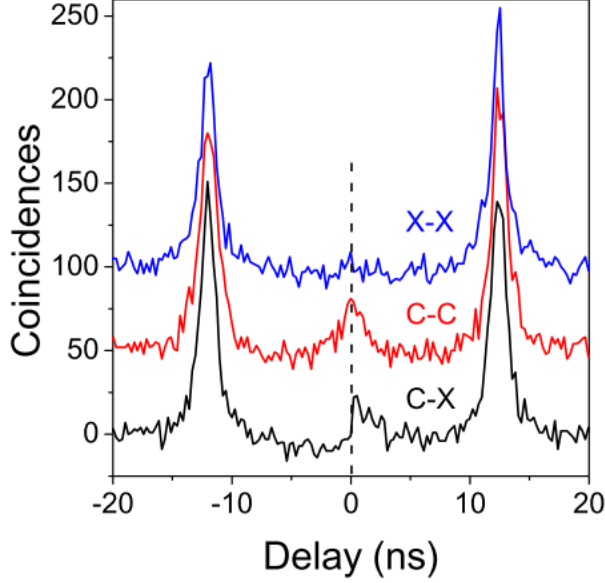


FIGURE A.3: Photon correlation measurements under pulsed excitation, from top to down : blue line, exciton autocorrelation measurement ; red line, cavity line autocorrelation ; black line, exciton-cavity cross correlation. Curves have been vertically shifted for clarity.

The figure.A.2 (b) represents the enhancement of the decay rate F_P^{eff} as a function of the spectral shift between the exciton transition and the cavity line. The points represents the measurements we did by measuring the emission decay times as a function of the detuning with the cavity. The black line is the theoretical result from the equation A.6. Finally, when the detuning between the exciton transition and the cavity mode is larger than the cavity linewidth, we showed that the phonon bath assist and even enhances the coupling between the emitter and the optical mode.

A.2 Photon statistics

We measured the correlations of the photons emitted at the energy of the optical mode of the cavity with the QD. This is done by spectrally filtering the signal impinging both SPADs with different spectrometers filtering different wavelengths. We tuned one of the spectrometer on the cavity line while the other spectrometer was set to send the ZPL emission on the SPAD, as shown by the fig. A.2.

The figure A.3 shows the photon correlation measurements in the three possible configurations : the autocorrelations X-X (blue) and C-C (red) and the cross-correlation X-C (black). First we see that the autocorrelation X-X shows a strong antibunching at zero delay as predicted ($g^{(2)}_{X-X} = 0.03 \pm 0.02$). The main point comes from the

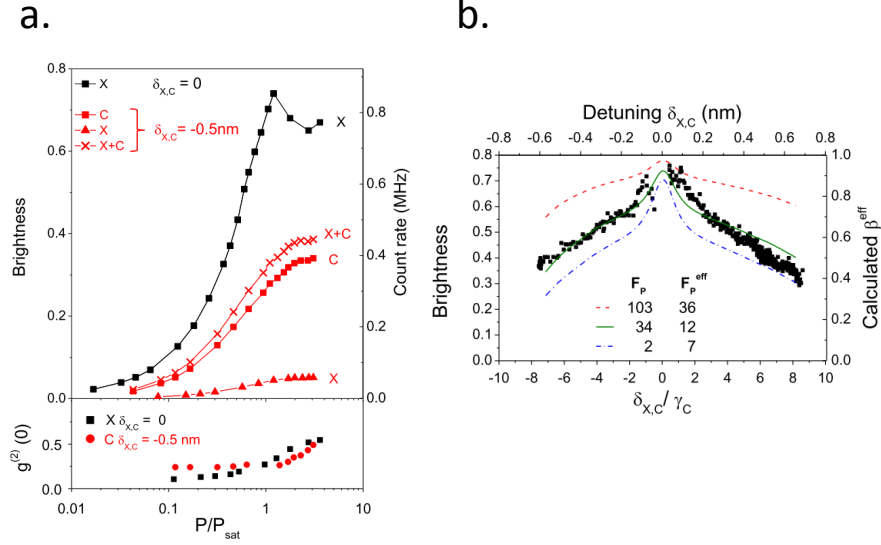


FIGURE A.4: **a.** Evolution of the brightness as a function of the excitation power P , normalized to the power at saturation P_{sat} . **b.** Total brightness (black squares, left scale) compared to calculated mode coupling β (right scale) as a function of the detuning for different values of Purcell factors F_P .

cross-correlation X-C (black line) : the coincidences at zero delay are low ($g^{(2)}_{X-C} = 0.15 \pm 0.05$). A strong antibunching is measured and shows that the photons emitted at the cavity energy are raised by the exciton (X) line. The autocorrelation C-C (blue line) shows a strong antibunching as well ($g^{(2)}_{C-C} = 0.25 \pm 0.05$). The photon statistics of the photon emitted in the cavity line is subpoissonian. The peak at zero delay is slightly higher than the X-X correlation due to a small contribution of other electronic states (as the biexciton XX) in the cavity mode.

A.3 Phonon assisted bright single-photon source

From all the previous considerations we made, a good coupling between the QD and the cavity means that the spontaneous emission of the QD is accelerated in the mode. As a consequence, the brightness of the latter is high when the QD line is centered with the cavity line.

The fig. A.4 shows the measurement of the brightness when the X transition is spectrally matched with the cavity or when it is detuned. The fig. A.4 (a) shows the number of photons collected as a function of the excitation power at two different detunings ($\delta_{X,C} = 0$ in black and $\delta_{X,C} = -0.5$ nm in red). The red curves show the separate contribution of the exciton line (X) and the cavity line (C). It shows that the

main contribution of the signal is from the cavity which is fed by the phonon side bands (PSB) of the QD. The total brightness of the source is now studied as a function of the coupling. The panel **(b)** shows the total brightness (exciton and cavity) as a function of the detuning $\delta_{X,C}$. Solid lines are the calculated fractions of emission into the mode using the model exposed previously ($\beta^{eff} = \frac{\Gamma_{//}^{ZPL} + \Gamma_{//}^{PBS}}{\Gamma_{tot}}$). β^{eff} is plotted for various Purcell factors F_P . The experimental results match well the curve with an effective Purcell factor around 12. The other lines show that the larger the Purcell factor, the broader the wavelength range where the device is a bright single-photon source.

These results show that, even if the phonon side bands can be detrimental to the source coherence [89, 90], it does also assist the coupling to fabricate a bright single-photon source. They are also a good proof of principle that can be applied to other solid-state emitters : for example with NV centers. Actually the PSB of NV centers represent 90% of the emission over 100nm [208].

Bibliography

- [1] Jeremy L. O'Brien, Akira Furusawa, and Jelena Vučković. Photonic quantum technologies. *Nat. Photonics*, 3(12):687–695, dec 2009. ISSN 1749-4885. doi: 10.1038/nphoton.2009.229. URL <http://dx.doi.org/10.1038/nphoton.2009.229>.
- [2] T. E. Northup and R. Blatt. Quantum information transfer using photons. *Nat. Photonics*, 8(5):356–363, apr 2014. ISSN 1749-4885. doi: 10.1038/nphoton.2014.53. URL <http://dx.doi.org/10.1038/nphoton.2014.53>.
- [3] D. Leibfried, R. Blatt, C. Monroe, and D. Wineland. Quantum dynamics of single trapped ions. *Rev. Mod. Phys.*, 75(1):281–324, mar 2003. ISSN 0034-6861. doi: 10.1103/RevModPhys.75.281. URL <http://link.aps.org/doi/10.1103/RevModPhys.75.281>.
- [4] L.-M. Duan and C. Monroe. Colloquium : Quantum networks with trapped ions. *Rev. Mod. Phys.*, 82(2):1209–1224, apr 2010. ISSN 0034-6861. doi: 10.1103/RevModPhys.82.1209. URL <http://link.aps.org/doi/10.1103/RevModPhys.82.1209>.
- [5] M H Devoret and R J Schoelkopf. Superconducting circuits for quantum information: an outlook. *Science*, 339(6124):1169–74, mar 2013. ISSN 1095-9203. doi: 10.1126/science.1231930. URL <http://www.sciencemag.org/content/339/6124/1169.abstract>.
- [6] Igor Aharonovich, Andrew D. Greentree, and Steven Prawer. Diamond photonics. *Nat. Photonics*, 5(7):397–405, jun 2011. ISSN 1749-4885. doi: 10.1038/nphoton.2011.54. URL <http://dx.doi.org/10.1038/nphoton.2011.54>.
- [7] Serge Haroche. Controlling photons in a box and exploring the quantum to classical boundary (Nobel Lecture). *Rev. Mod. Phys.*, 52(39):10158–10178, 2013. ISSN 14337851. doi: <http://dx.doi.org/10.1103/RevModPhys.85.1083>. URL <http://journals.aps.org/rmp/abstract/10.1103/RevModPhys.85.1083>.
- [8] Peter Lodahl, Sahand Mahmoodian, and Søren Stobbe. Interfacing single photons and single quantum dots with photonic nanostructures. *Rev. Mod. Phys.*, 87(2):

- 347–400, may 2015. ISSN 0034-6861. doi: 10.1103/RevModPhys.87.347. URL <http://link.aps.org/doi/10.1103/RevModPhys.87.347>.
- [9] Thomas Monz, Philipp Schindler, Julio T. Barreiro, Michael Chwalla, Daniel Nigg, William A. Coish, Maximilian Harlander, Wolfgang Hänsel, Markus Hennrich, and Rainer Blatt. 14-Qubit Entanglement: Creation and Coherence. *Phys. Rev. Lett.*, 106(13):130506, mar 2011. ISSN 0031-9007. doi: 10.1103/PhysRevLett.106.130506. URL <http://link.aps.org/doi/10.1103/PhysRevLett.106.130506>.
- [10] J. Kelly, R. Barends, A. G. Fowler, A. Megrant, E. Jeffrey, T. C. White, D. Sank, J. Y. Mutus, B. Campbell, Yu Chen, Z. Chen, B. Chiaro, A. Dunsworth, I.-C. Hoi, C. Neill, P. J. J. O’Malley, C. Quintana, P. Roushan, A. Vainsencher, J. Wenner, A. N. Cleland, and John M. Martinis. State preservation by repetitive error detection in a superconducting quantum circuit. *Nature*, 519(7541):66–69, mar 2015. ISSN 0028-0836. doi: 10.1038/nature14270. URL <http://dx.doi.org/10.1038/nature14270>.
- [11] E Knill, R Laflamme, and G J Milburn. A scheme for efficient quantum computation with linear optics. *Nature*, 409(6816):46–52, jan 2001. ISSN 0028-0836. doi: 10.1038/35051009. URL <http://dx.doi.org/10.1038/35051009>.
- [12] Nicolas Gisin and R Thew. Quantum communication. *Nat. Photonics*, 1:165–171, 2007. ISSN 1749-4885. doi: 10.1038/nphoton.2007.22. URL <http://link.aps.org/doi/10.1103/PhysRevLett.91.207901> \delimitter"026E30F\$n<GotoISI>://WOS:000246367200015.
- [13] L M Duan, M D Lukin, J I Cirac, and P Zoller. Long-distance quantum communication with atomic ensembles and linear optics. *Nature*, 414(6862):413–418, 2001. ISSN 0028-0836. doi: 10.1038/35106500. URL <http://www.ncbi.nlm.nih.gov/pubmed/11719796>.
- [14] F Castelli, B Plez, R Lallement, R Ferlet, P G Kalas, H J Walker, and W S Holland. Deterministic Generation of Single Photons from One Atom. *Science (80-.)*, 303(March):1992–1995, 2004. doi: 10.1126/science.1095232.
- [15] H G Barros, A Stute, T E Northup, C Russo, P O Schmidt, and R Blatt. Deterministic single-photon source from a single ion. *New J. Phys.*, 11(10):103004, oct 2009. ISSN 1367-2630. doi: 10.1088/1367-2630/11/10/103004. URL <http://iopscience.iop.org/article/10.1088/1367-2630/11/10/103004>.
- [16] Christian Kurtsiefer, Sonja Mayer, Patrick Zarda, and Harald Weinfurter. Stable solid-state source of single photons. *Phys. Rev. Lett.*, 85(2):290–293, jul 2000.

- ISSN 00319007. doi: 10.1103/PhysRevLett.85.290. URL <http://link.aps.org/doi/10.1103/PhysRevLett.85.290>.
- [17] Alexios Beveratos, Rosa Brouri, Thierry Gacoin, André Villing, Jean-Philippe Poizat, and Philippe Grangier. Single Photon Quantum Cryptography. *Phys. Rev. Lett.*, 89(18):187901, 2002. ISSN 0031-9007. doi: 10.1103/PhysRevLett.89.187901. URL <http://link.aps.org/doi/10.1103/PhysRevLett.89.187901>.
- [18] Thomas Volz, Andreas Reinhard, Martin Winger, Antonio Badolato, Kevin J. Hennessy, Evelyn L. Hu, and Ataç Imamoğlu. Ultrafast all-optical switching by single photons. *Nat. Photonics*, 6(9):607–611, 2012. ISSN 1749-4885. doi: 10.1038/nphoton.2012.181.
- [19] W B Gao, P Fallahi, E Togan, J Miguel-Sanchez, and a Imamoglu. Observation of entanglement between a quantum dot spin and a single photon. *Nature*, 491(7424):426–30, nov 2012. ISSN 1476-4687. doi: 10.1038/nature11573. URL <http://www.ncbi.nlm.nih.gov/pubmed/23151586>.
- [20] W. B. Gao, a. Imamoglu, H. Bernien, and R. Hanson. Coherent manipulation, measurement and entanglement of individual solid-state spins using optical fields. *Nat. Photonics*, 9(6):363–373, 2015. ISSN 1749-4885. doi: 10.1038/nphoton.2015.58. URL <http://www.nature.com/doi/10.1038/nphoton.2015.58>.
- [21] J L O'Brien, G J Pryde, A G White, T C Ralph, and D Branning. Demonstration of an all-optical quantum controlled-NOT gate. *Nature*, 426(6964):264–7, nov 2003. ISSN 1476-4687. doi: 10.1038/nature02054. URL <http://www.ncbi.nlm.nih.gov/pubmed/14628045>.
- [22] M W Mitchell, J S Lundeen, and a M Steinberg. Super-resolving phase measurements with a multiphoton entangled state. *Nature*, 429(6988):161–164, 2004. ISSN 0028-0836. doi: 10.1038/nature02493.
- [23] Philip Walther, Jian-Wei Pan, Markus Aspelmeyer, Rupert Ursin, Sara Gasparoni, and Anton Zeilinger. De Broglie wavelength of a non-local four-photon state. *Nature*, 429(6988):158–161, 2004. ISSN 0028-0836. doi: 10.1038/nature02552.
- [24] Dirk Bouwmeester, JW Pan, Klaus Mattle, and Manfred Eibl. Experimental quantum teleportation. *Nature*, pages 575–579, 1997. URL <http://www.nature.com/nature/journal/v390/n6660/abs/390575a0.html>.
- [25] B. P. Lanyon, M. Barbieri, M. P. Almeida, and A. G. White. Experimental Quantum Computing without Entanglement. *Phys. Rev. Lett.*, 101(20):200501, nov 2008. ISSN 0031-9007. doi: 10.1103/PhysRevLett.101.200501. URL <http://link.aps.org/doi/10.1103/PhysRevLett.101.200501>.

- [26] B. P. Lanyon, J. D. Whitfield, G. G. Gillett, M. E. Goggin, M. P. Almeida, I. Kasal, J. D. Biamonte, M. Mohseni, B. J. Powell, M. Barbieri, A. Aspuru-Guzik, and A. G. White. Towards quantum chemistry on a quantum computer. *Nat. Chem.*, 2(2):106–111, jan 2010. ISSN 1755-4330. doi: 10.1038/nchem.483. URL <http://dx.doi.org/10.1038/nchem.483>.
- [27] Xiao-song Ma, Borivoje Dakic, William Naylor, Anton Zeilinger, and Philip Walther. Quantum simulation of the wavefunction to probe frustrated Heisenberg spin systems. *Nat. Phys.*, 7(5):399–405, feb 2011. ISSN 1745-2473. doi: 10.1038/nphys1919. URL <http://dx.doi.org/10.1038/nphys1919>.
- [28] Alán Aspuru-Guzik and Philip Walther. Photonic quantum simulators. *Nat. Phys.*, 8(4):285–291, apr 2012. ISSN 1745-2473. doi: 10.1038/nphys2253. URL <http://dx.doi.org/10.1038/nphys2253>.
- [29] P Michler, A Kiraz, C Becher, W V Schoenfeld, P M Petroff, L Zhang, E Hu, and A Imamoglu. A quantum dot single-photon turnstile device. *Science*, 290(5500):2282–2285, 2000. ISSN 00368075. doi: 10.1126/science.290.5500.2282. URL <http://www.sciencemag.org/content/290/5500/2282.short>.
- [30] Matthew Pelton, Charles Santori, Jelena Vucković, Bingyang Zhang, Glenn Solomon, Jocelyn Plant, and Yoshihisa Yamamoto. Efficient Source of Single Photons: A Single Quantum Dot in a Micropost Microcavity. *Phys. Rev. Lett.*, 89(23):1–4, nov 2002. ISSN 0031-9007. doi: 10.1103/PhysRevLett.89.233602. URL <http://link.aps.org/doi/10.1103/PhysRevLett.89.233602>.
- [31] O. Gazzano, S. Michaelis de Vasconcellos, C. Arnold, a. Nowak, E. Galopin, I. Sagnes, L. Lanco, a. Lemaître, and P. Senellart. Bright solid-state sources of indistinguishable single photons. *Nat. Commun.*, 4:1425, feb 2013. ISSN 2041-1723. doi: 10.1038/ncomms2434. URL <http://www.nature.com/doifinder/10.1038/ncomms2434>.
- [32] Julien Claudon, Joël Bleuse, Nitin Singh Malik, Maela Bazin, Périne Jaffrennou, Niels Gregersen, Christophe Sauvan, Philippe Lalanne, Jean-Michel Gérard, and Jean-michel Ge. A highly efficient single-photon source based on a quantum dot in a photonic nanowire. *Nat. Photonics*, 4(3):174–177, 2010. ISSN 1749-4885. doi: 10.1038/nphoton.2009.287.
- [33] J. Gérard, B. Sermage, B. Gayral, B. Legrand, E. Costard, and V. Thierry-Mieg. Enhanced Spontaneous Emission by Quantum Boxes in a Monolithic Optical Microcavity. *Phys. Rev. Lett.*, 81(5):1110–1113, aug 1998. ISSN 0031-9007. doi: 10.1103/PhysRevLett.81.1110. URL <http://link.aps.org/doi/10.1103/PhysRevLett.81.1110>.

- [34] G. S. Solomon, M. Pelton, and Y. Yamamoto. Single-mode spontaneous emission from a single quantum dot in a three-dimensional microcavity. *Phys. Rev. Lett.*, 86(17):3903–3906, 2001. ISSN 00319007. doi: 10.1103/PhysRevLett.86.3903.
- [35] J P Reithmaier, G Sek, A Löffler, C Hofmann, S Kuhn, S Reitzenstein, L V Keldysh, V D Kulakovskii, T L Reinecke, and A Forchel. Strong coupling in a single quantum dot-semiconductor microcavity system. *Nature*, 432(7014):197–200, nov 2004. ISSN 1476-4687. doi: 10.1038/nature02969. URL <http://dx.doi.org/10.1038/nature02969>.
- [36] Charles Santori, David Fattal, Jelena Vučković, Glenn S Solomon, Yoshihisa Yamamoto, Jelena Vucković, Glenn S Solomon, and Yoshihisa Yamamoto. Indistinguishable photons from a single-photon device. *Nature*, 419(6907):594–597, oct 2002. ISSN 0028-0836. doi: 10.1038/nature01086. URL <http://www.nature.com/doi/10.1038/nature01086>.
- [37] S. Laurent, S. Varoutsis, L. Le Gratiet, A. Lemaitre, I. Sagnes, F. Raineri, A. Levenson, I. Robert-Philip, and I. Abram. Indistinguishable single photons from a single-quantum dot in a two-dimensional photonic crystal cavity. *Appl. Phys. Lett.*, 87(16):163107, oct 2005. ISSN 00036951. doi: 10.1063/1.2103397. URL <http://scitation.aip.org/content/aip/journal/apl/87/16/10.1063/1.2103397>.
- [38] a. J. Bennett, R. B. Patel, a. J. Shields, K. Cooper, P. Atkinson, C. a. Nicoll, and D. a. Ritchie. Indistinguishable photons from a diode. *Appl. Phys. Lett.*, 92(19):193503, 2008. ISSN 00036951. doi: 10.1063/1.2918841. URL <http://link.aip.org/link/APPLAB/v92/i19/p193503/s1{&}Agg=doi>.
- [39] S. Ates, S. Ulrich, S. Reitzenstein, a. Löffler, a. Forchel, and P. Michler. Post-Selected Indistinguishable Photons from the Resonance Fluorescence of a Single Quantum Dot in a Microcavity. *Phys. Rev. Lett.*, 103(16):1–4, oct 2009. ISSN 0031-9007. doi: 10.1103/PhysRevLett.103.167402. URL <http://link.aps.org/doi/10.1103/PhysRevLett.103.167402>.
- [40] Yu-Ming He, Yu He, Yu-Jia Wei, Dian Wu, Mete Atatüre, Christian Schneider, Sven Höfling, Martin Kamp, Chao-Yang Lu, and Jian-Wei Pan. On-demand semiconductor single-photon source with near-unity indistinguishability. *Nat. Nanotechnol.*, 8(3):213–7, 2013. ISSN 1748-3395. doi: 10.1038/nnano.2012.262. URL <http://www.nature.com/nano/journal/v8/n3/abs/nnano.2012.262.html>.
- [41] Léonard Monniello, Antoine Reigue, Richard Hosten, Aristide Lemaitre, Anthony Martinez, Roger Grousson, and Valia Voliotis. Indistinguishable single photons generated by a quantum dot under resonant excitation observable

- without postselection. *Phys. Rev. B*, 90(4):041303, 2014. ISSN 1098-0121. doi: 10.1103/PhysRevB.90.041303. URL <http://link.aps.org/doi/10.1103/PhysRevB.90.041303>.
- [42] M. Müller, S. Bounouar, K. D. Jöns, M. Glässl, and P. Michler. On-demand generation of indistinguishable polarization-entangled photon pairs. *Nat. Photonics*, 8(February), feb 2014. ISSN 1749-4885. doi: 10.1038/nphoton.2013.377. URL <http://www.nature.com/doifinder/10.1038/nphoton.2013.377>.
- [43] Raphaël Proux, Maria Maragkou, Emmanuel Baudin, Christophe Voisin, Philippe Roussignol, and Carole Diederichs. Measuring the Photon Coalescence Time Window in the Continuous-Wave Regime for Resonantly Driven Semiconductor Quantum Dots. *Phys. Rev. Lett.*, 114(6):067401, 2015. ISSN 0031-9007. doi: 10.1103/PhysRevLett.114.067401. URL <http://link.aps.org/doi/10.1103/PhysRevLett.114.067401>.
- [44] M. Gschrey, a. Thoma, P. Schnauber, M. Seifried, R. Schmidt, B. Wohlfeil, L. Krüger, J. H. Schulze, T. Heindel, S. Burger, F. Schmidt, a. Strittmatter, S. Rodt, and S. Reitzenstein. Highly indistinguishable photons from deterministic quantum-dot microlenses utilizing three-dimensional in situ electron-beam lithography. *Nat. Commun.*, 6(May):7662, 2015. ISSN 2041-1723. doi: 10.1038/ncomms8662. URL <http://www.nature.com/doifinder/10.1038/ncomms8662>.
- [45] A. Dousse, L. Lanco, J. Suffczyński, E. Semenova, A. Miard, A. Lemaître, I. Sagnes, C. Roblin, J. Bloch, and P. Senellart. Controlled light-matter coupling for a single quantum dot embedded in a pillar microcavity using far-field optical lithography. *Phys. Rev. Lett.*, 101(26):30–33, 2008. ISSN 00319007. doi: 10.1103/PhysRevLett.101.267404. URL <http://journals.aps.org/prl/abstract/10.1103/PhysRevLett.101.267404>.
- [46] Adrien Dousse, Jan Suffczyński, Alexios Beveratos, Olivier Krebs, Aristide Lemaître, Isabelle Sagnes, Jacqueline Bloch, Paul Voisin, and Pascale Senellart. Ultrabright source of entangled photon pairs. *Nature*, 466(7303):217–20, jul 2010. ISSN 1476-4687. doi: 10.1038/nature09148. URL <http://www.ncbi.nlm.nih.gov/pubmed/20613838>.
- [47] O. Gazzano, M. P. Almeida, a. K. Nowak, S. L. Portalupi, a. Lemaître, I. Sagnes, a. G. White, and P. Senellart. Entangling Quantum-Logic Gate Operated with an Ultrabright Semiconductor Single-Photon Source. *Phys. Rev. Lett.*, 110(25):250501, jun 2013. ISSN 0031-9007. doi: 10.1103/PhysRevLett.110.250501. URL <http://link.aps.org/doi/10.1103/PhysRevLett.110.250501>.

- [48] M J Collins, C Xiong, I H Rey, T D Vo, J He, S Shahnia, C Reardon, T F Krauss, M J Steel, A S Clark, and B J Eggleton. Integrated spatial multiplexing of heralded single-photon sources. *Nat. Commun.*, 4:2582, jan 2013. ISSN 2041-1723. doi: 10.1038/ncomms3582. URL <http://www.nature.com/ncomms/2013/131010/ncomms3582/full/ncomms3582.html?message-global=remove>.
- [49] Andreas Christ and Christine Silberhorn. Limits on the deterministic creation of pure single-photon states using parametric down-conversion. *Phys. Rev. A - At. Mol. Opt. Phys.*, 85(2):1–6, 2012. ISSN 10502947. doi: 10.1103/PhysRevA.85.023829.
- [50] Matthias Keller, Birgit Lange, Kazuhiro Hayasaka, Wolfgang Lange, and Herbert Walther. Continuous generation of single photons with controlled waveform in an ion-trap cavity system. *Nature*, 431(7012):1075–1078, 2004.
- [51] N Schlosser, G Reymond, I Protsenko, and P Grangier. Sub-poissonian loading of single atoms in a microscopic dipole trap. *Nature*, 411(6841):1024–7, jun 2001. ISSN 0028-0836. doi: 10.1038/35082512. URL <http://dx.doi.org/10.1038/35082512>.
- [52] Benoit Darquié, Matthew P A Jones, Jos Dingjan, Jerome Beugnon, Silvia Bergamini, Yvan Sortais, Gaetan Messin, Antoine Browaeys, and Philippe Grangier. Controlled single-photon emission from a single trapped two-level atom. *Science (80-.)*, 309(5733):454–456, 2005.
- [53] Brahim Lounis and W E Moerner. Single photons on demand from a single molecule at room temperature. *Nature*, 407(6803):491–493, 2000.
- [54] Charles Santori, Matthew Pelton, Glenn Solomon, Yseulte Dale, and Yoshihisa Yamamoto. Triggered Single Photons from a Quantum Dot. *Phys. Rev. Lett.*, 86(8):1502–1505, feb 2001. ISSN 0031-9007. doi: 10.1103/PhysRevLett.86.1502. URL <http://link.aps.org/doi/10.1103/PhysRevLett.86.1502>.
- [55] Ivan Stranski and Lubomir Krastanow. No Title. *Abhandlungen der Math. Klasse IIb. Akad. der Wissenschaften Wien*, 146:797–810, 1938.
- [56] L. Goldstein, F. Glas, J. Y. Marzin, M. N. Charasse, and G. Le Roux. Growth by molecular beam epitaxy and characterization of InAs/GaAs strained-layer superlattices. *Appl. Phys. Lett.*, 47(10):1099–1101, 1985. ISSN 00036951. doi: 10.1063/1.96342.
- [57] P. B. Joyce, T. J. Krzyzewski, G. R. Bell, T. S. Jones, S. Malik, D. Childs, and R. Murray. Effect of growth rate on the size, composition, and optical properties

- of InAs/GaAs quantum dots grown by molecular-beam epitaxy. *Phys. Rev. B*, 62(16):10891–10895, oct 2000. ISSN 0163-1829. doi: 10.1103/PhysRevB.62.10891. URL <http://link.aps.org/doi/10.1103/PhysRevB.62.10891>.
- [58] D. Leonard, M. Krishnamurthy, C. M. Reaves, S. P. Denbaars, and P. M. Petroff. Direct formation of quantum-sized dots from uniform coherent islands of InGaAs on GaAs surfaces. *Appl. Phys. Lett.*, 63(23):3203, dec 1993. ISSN 00036951. doi: 10.1063/1.110199. URL <http://scitation.aip.org/content/aip/journal/apl/63/23/10.1063/1.110199>.
- [59] J Y Marzin, J M Gerard, A Izrael, D Barrier, and G Bastard. Photoluminescence of Single Inas Quantum Dots Obtained by Self- Organized Growth on Gaas. *Phys. Rev. Lett.*, 73(5):716–719, 1994. URL <http://dx.doi.org/10.1103/PhysRevLett.73.716>.
- [60] Lin-Wang Wang, Jeongnim Kim, and Alex Zunger. Electronic structures of [110]-faceted self-assembled pyramidal InAs/GaAs quantum dots. *Phys. Rev. B*, 59(8):5678–5687, feb 1999. ISSN 0163-1829. doi: 10.1103/PhysRevB.59.5678. URL <http://link.aps.org/doi/10.1103/PhysRevB.59.5678>.
- [61] A. J. Williamson, L. W. Wang, and Alex Zunger. Theoretical interpretation of the experimental electronic structure of lens-shaped self-assembled InAs/GaAs quantum dots. *Phys. Rev. B*, 62(19):12963–12977, nov 2000. ISSN 0163-1829. doi: 10.1103/PhysRevB.62.12963. URL <http://link.aps.org/doi/10.1103/PhysRevB.62.12963>.
- [62] G. Bastard. Superlattice band structure in the envelope-function approximation. *Phys. Rev. B*, 24(10):5693–5697, nov 1981. ISSN 01631829. doi: 10.1103/PhysRevB.24.5693. URL <http://link.aps.org/doi/10.1103/PhysRevB.24.5693>.
- [63] C. Cohen-Tahnoudji, B. Diu, and F. Lalo{ë}. Quantum mechanics, 1977. ISSN 0369-3546.
- [64] Alberto Franceschetti and Alex Zunger. Direct Pseudopotential Calculation of Exciton Coulomb and Exchange Energies in Semiconductor Quantum Dots. *Phys. Rev. Lett.*, 78(5):915–918, feb 1997. ISSN 0031-9007. doi: 10.1103/PhysRevLett.78.915. URL <http://link.aps.org/doi/10.1103/PhysRevLett.78.915>.
- [65] Angela Vasanelli. *Transitions optiques interbandes et intrabandes dans les boîtes quantiques simples et couplées verticalement*. PhD thesis, 2002.
- [66] R. Seguin, a. Schliwa, S. Rodt, K. Potschke, U. W. Pohl, and D. Bimberg. Size-dependent fine-structure splitting in self-organized InAs/GaAs quantum dots.

- Phys. Rev. Lett.*, 95(25):10–13, 2005. ISSN 00319007. doi: 10.1103/PhysRevLett.95.257402.
- [67] E. Blackwood, M. J. Snelling, R. T. Harley, S. R. Andrews, and C. T. B. Foxon. Exchange interaction of excitons in GaAs heterostructures. *Phys. Rev. B*, 50(19):14246–14254, nov 1994. ISSN 0163-1829. doi: 10.1103/PhysRevB.50.14246. URL <http://link.aps.org/doi/10.1103/PhysRevB.50.14246>.
- [68] T. Takagahara. Theory of exciton doublet structures and polarization relaxation in single quantum dots. *Phys. Rev. B*, 62(24):16840–16855, dec 2000. ISSN 0163-1829. doi: 10.1103/PhysRevB.62.16840. URL <http://link.aps.org/doi/10.1103/PhysRevB.62.16840>.
- [69] N. Akopian, N. H. Lindner, E. Poem, Y. Berlatzky, J. Avron, D. Gershoni, B. D. Gerardot, and P. M. Petroff. Entangled photon pairs from semiconductor quantum dots. *Phys. Rev. Lett.*, 96(13):7–10, 2006. ISSN 00319007. doi: 10.1103/PhysRevLett.96.130501.
- [70] R. J. Young, R. M. Stevenson, a. J. Shields, P. Atkinson, K. Cooper, D. a. Ritchie, K. M. Groom, a. I. Tartakovskii, and M. S. Skolnick. Inversion of exciton level splitting in quantum dots. *Phys. Rev. B - Condens. Matter Mater. Phys.*, 72(11):1–4, 2005. ISSN 10980121. doi: 10.1103/PhysRevB.72.113305.
- [71] D. J. P. Ellis, R. M. Stevenson, R. J. Young, A. J. Shields, P. Atkinson, and D. A. Ritchie. Control of fine-structure splitting of individual InAs quantum dots by rapid thermal annealing. *Appl. Phys. Lett.*, 90(1):011907, jan 2007. ISSN 00036951. doi: 10.1063/1.2430489. URL <http://scitation.aip.org/content/aip/journal/apl/90/1/10.1063/1.2430489>.
- [72] a. Tartakovskii, M. Makhonin, I. Sellers, J. Cahill, a. Andreev, D. Whittaker, J-P. Wells, a. Fox, D. Mowbray, M. Skolnick, K. Groom, M. Steer, H. Liu, and M. Hopkinson. Effect of thermal annealing and strain engineering on the fine structure of quantum dot excitons. *Phys. Rev. B*, 70(19):1–4, 2004. ISSN 1098-0121. doi: 10.1103/PhysRevB.70.193303.
- [73] Rinaldo Trotta, Johannes S Wildmann, Eugenio Zallo, Oliver G Schmidt, and Armando Rastelli. Highly entangled photons from hybrid piezoelectric-semiconductor quantum dot devices. *Nano Lett.*, 14(6):3439–44, jun 2014. ISSN 1530-6992. doi: 10.1021/nl500968k. URL <http://dx.doi.org/10.1021/nl500968k>.
- [74] B. D. Gerardot, S. Seidl, P. A. Dalgarno, R. J. Warburton, D. Granados, J. M. Garcia, K. Kowalik, O. Krebs, K. Karrai, A. Badolato, and P. M. Petroff. Manipulating exciton fine structure in quantum dots with a lateral electric field. *Appl. Phys.*

- Lett.*, 90(4):041101, jan 2007. ISSN 00036951. doi: 10.1063/1.2431758. URL <http://scitation.aip.org/content/aip/journal/apl/90/4/10.1063/1.2431758>.
- [75] Andreas Muller, Wei Fang, John Lawall, and Glenn S. Solomon. Creating polarization-entangled photon pairs from a semiconductor quantum dot using the optical stark effect. *Phys. Rev. Lett.*, 103(21):217402, nov 2009. ISSN 00319007. doi: 10.1103/PhysRevLett.103.217402. URL <http://link.aps.org/doi/10.1103/PhysRevLett.103.217402>.
- [76] Alexei Gilchrist, Kevin J Resch, and Andrew G White. Quantum information: source of triggered entangled photon pairs? *Nature*, 445(7124):E4–E5; discussion E5–E6, 2007. ISSN 0028-0836. doi: 10.1038/nature05546.
- [77] K. Kowalik, O. Krebs, a. Golnik, J. Suffczynski, P. Wojnar, J. Kossut, J. a. Gaj, and P. Voisin. Manipulating the exciton fine structure of single CdTe/ZnTe quantum dots by an in-plane magnetic field. page 6, 2006. ISSN 1098-0121. doi: 10.1103/PhysRevB.75.195340. URL <http://arxiv.org/abs/cond-mat/0610305>.
- [78] Y. Toda, O. Moriwaki, M. Nishioka, and Y. Arakawa. Efficient Carrier Relaxation Mechanism in InGaAs/GaAs Self-Assembled Quantum Dots Based on the Existence of Continuum States. *Phys. Rev. Lett.*, 82(20):4114–4117, may 1999. ISSN 0031-9007. doi: 10.1103/PhysRevLett.82.4114. URL <http://link.aps.org/doi/10.1103/PhysRevLett.82.4114>.
- [79] J. Suffczyński, T. Kazimierzuk, M. Goryca, B. Piechal, A. Trajnerowicz, K. Kowalik, P. Kossacki, A. Golnik, K. P. Korona, M. Nawrocki, J. A. Gaj, and G. Karzewski. Excitation mechanisms of individual Cd Te Zn Te quantum dots studied by photon correlation spectroscopy. *Phys. Rev. B*, 74(8):085319, aug 2006. ISSN 1098-0121. doi: 10.1103/PhysRevB.74.085319. URL <http://link.aps.org/doi/10.1103/PhysRevB.74.085319>.
- [80] Uri Banin, YunWei Cao, David Katz, and Oded Millo. Identification of atomic-like electronic states in indium arsenide nanocrystal quantum dots. *Nature*, 400(6744):542–544, aug 1999. ISSN 0028-0836. doi: 10.1038/22979. URL <http://dx.doi.org/10.1038/22979>.
- [81] G. Medeiros-Ribeiro, F. G. Pikus, P. M. Petroff, and a. L. Efros. Single-Electron Charging and Coulomb Interaction in InAs Self-Assembled Quantum Dot Arrays. *Phys. Rev. B*, 55(3):7, jan 1996. ISSN 0163-1829. doi: 10.1103/PhysRevB.55.1568. URL <http://arxiv.org/abs/cond-mat/9608040>.
- [82] Jeppe Johansen, Søren Stobbe, Ivan S. Nikolaev, Toke Lund-Hansen, Philip T. Kristensen, Jørn M. Hvam, Willem L. Vos, and Peter Lodahl. Size dependence of

- the wavefunction of self-assembled InAs quantum dots from time-resolved optical measurements. *Phys. Rev. B - Condens. Matter Mater. Phys.*, 77(7):073303, feb 2008. ISSN 10980121. doi: 10.1103/PhysRevB.77.073303. URL <http://link.aps.org/doi/10.1103/PhysRevB.77.073303>.
- [83] A. Vasanelli, R. Ferreira, and G. Bastard. Continuous Absorption Background and Decoherence in Quantum Dots. *Phys. Rev. Lett.*, 89(21):216804, nov 2002. ISSN 0031-9007. doi: 10.1103/PhysRevLett.89.216804. URL <http://link.aps.org/doi/10.1103/PhysRevLett.89.216804>.
- [84] Emmanuel Moreau. *Étude d'une source solide monomode de photons uniques constituée par une boîte quantique semi-conductrice dans une microcavité optique*. PhD thesis, 2002. URL <http://www.theses.fr/2002PA066443>.
- [85] Adrien Dousse. *Deterministic cavity-quantum dot coupling and fabrication of an ultrabright source of entangled photon pairs*. PhD thesis, 2010. URL <http://www.theses.fr/2010PA077134>.
- [86] E. Moreau, I. Robert, J. M. Gerard, I. Abram, L. Manin, and V. Thierry-Mieg. Single-mode solid-state single photon source based on isolated quantum dots in pillar microcavities. *Appl. Phys. Lett.*, 79(18):2865, oct 2001. ISSN 00036951. doi: 10.1063/1.1415346. URL <http://scitation.aip.org/content/aip/journal/apl/79/18/10.1063/1.1415346>.
- [87] L. Besombes, K. Kheng, L. Marsal, and H. Mariette. Acoustic phonon broadening mechanism in single quantum dot emission. *Phys. Rev. B*, 63(15):155307, mar 2001. ISSN 0163-1829. doi: 10.1103/PhysRevB.63.155307. URL <http://link.aps.org/doi/10.1103/PhysRevB.63.155307>.
- [88] I. Favero, G. Cassabois, R. Ferreira, D. Darson, C. Voisin, J. Tignon, C. Delalande, G. Bastard, Ph. Roussignol, and J. Gérard. Acoustic phonon sidebands in the emission line of single InAs/GaAs quantum dots. *Phys. Rev. B*, 68(23):233301, dec 2003. ISSN 0163-1829. doi: 10.1103/PhysRevB.68.233301. URL <http://link.aps.org/doi/10.1103/PhysRevB.68.233301>.
- [89] E. Peter, J. Hours, P. Senellart, A. Vasanelli, A. Cavanna, J. Bloch, and J. Gérard. Phonon sidebands in exciton and biexciton emission from single GaAs quantum dots. *Phys. Rev. B*, 69(4):041307, jan 2004. ISSN 1098-0121. doi: 10.1103/PhysRevB.69.041307. URL <http://link.aps.org/doi/10.1103/PhysRevB.69.041307>.
- [90] D. Gammon, E. S. Snow, B. V. Shanabrook, D. S. Katzer, and D. Park. Homogeneous Linewidths in the Optical Spectrum of a Single Gallium Arsenide

- Quantum Dot. *Science (80-.)*, 273(5271):87–90, 1996. ISSN 0036-8075. doi: 10.1126/science.273.5271.87.
- [91] Roy J. Glauber. The quantum theory of optical coherence. *Phys. Rev.*, 130(6): 2529–2539, jun 1963. ISSN 0031899X. doi: 10.1103/PhysRev.130.2529. URL <http://link.aps.org/doi/10.1103/PhysRev.130.2529>.
- [92] B. L. Morgan and L. Mandel. Measurement of Photon Bunching in a Thermal Light Beam. *Phys. Rev. Lett.*, 16(22):1012–1015, may 1966. ISSN 00319007. doi: 10.1103/PhysRevLett.16.1012. URL <http://link.aps.org/doi/10.1103/PhysRevLett.16.1012>.
- [93] Brahim Lounis and Michel Orrit. Single-photon sources. *Reports Prog. Phys.*, 68 (5):1129–1179, 2005. ISSN 0034-4885. doi: 10.1088/0034-4885/68/5/R04.
- [94] H. J. Kimble, M. Dagenais, and L. Mandel. Photon Antibunching in Resonance Fluorescence. *Phys. Rev. Lett.*, 39(11):691–695, sep 1977. ISSN 0031-9007. doi: 10.1103/PhysRevLett.39.691. URL <http://link.aps.org/doi/10.1103/PhysRevLett.39.691>.
- [95] R. HANBURY BROWN and R. Q. TWISS. A Test of a New Type of Stellar Interferometer on Sirius. *Nature*, 178(4541):1046–1048, nov 1956. ISSN 0028-0836. doi: 10.1038/1781046a0. URL <http://www.nature.com/nature/journal/v178/n4541/pdf/1781046a0.pdf>.
- [96] U. Fano. Quantum Theory of Interference Effects in the Mixing of Light from Phase-Independent Sources. *Am. J. Phys.*, 29(8):539, jul 1961. ISSN 00029505. doi: 10.1119/1.1937827. URL <http://scitation.aip.org/content/aapt/journal/ajp/29/8/10.1119/1.1937827>.
- [97] P Grangier, G Roger, and A Aspect. Experimental Evidence for a Photon Anticorrelation Effect on a Beam Splitter: A New Light on Single-Photon Interferences. *Europhys. Lett.*, 1(4):173–179, feb 1986. ISSN 0295-5075. doi: 10.1209/0295-5075/1/4/004. URL <http://stacks.iop.org/0295-5075/1/i=4/a=004>.
- [98] CK Hong, ZY Ou, and L Mandel. Measurement of Subpicosecond Time Intervals Between Two Photo By Interference.Pdf. *Phys. Rev. Lett.*, 1987. URL <http://link.aps.org/doi/10.1103/PhysRevLett.59.2044>.
- [99] Xin-Qi Li and Yasuhiko Arakawa. Optical linewidths in an individual quantum dot. *Phys. Rev. B*, 60(3):1915–1920, 1999. ISSN 0163-1829. doi: 10.1103/PhysRevB.60.1915.

- [100] M. Bayer and a. Forchel. Temperature dependence of the exciton homogeneous linewidth in In_{0.60}Ga_{0.40}As/GaAs self-assembled quantum dots. *Phys. Rev. B*, 65(4):1–4, 2002. ISSN 0163-1829. doi: 10.1103/PhysRevB.65.041308.
- [101] C. Kammerer, G. Cassabois, C. Voisin, M. Perrin, C. Delalande, Ph Roussignol, and J. M. Gérard. Interferometric correlation spectroscopy in single quantum dots. *Appl. Phys. Lett.*, 81(15):2737–2739, 2002. ISSN 00036951. doi: 10.1063/1.1510158.
- [102] C. Kammerer, C. Voisin, G. Cassabois, C. Delalande, Ph. Roussignol, F. Klopff, J. Reithmaier, a. Forchel, and J. Gérard. Line narrowing in single semiconductor quantum dots: Toward the control of environment effects. *Phys. Rev. B*, 66(4): 1–4, jul 2002. ISSN 0163-1829. doi: 10.1103/PhysRevB.66.041306. URL <http://link.aps.org/doi/10.1103/PhysRevB.66.041306>.
- [103] K. Konthasinghe, J. Walker, M. Peiris, C. K. Shih, Y. Yu, M. F. Li, J. F. He, L. J. Wang, H. Q. Ni, Z. C. Niu, and a. Muller. Coherent versus incoherent light scattering from a quantum dot. *Phys. Rev. B - Condens. Matter Mater. Phys.*, 85 (23):1–7, 2012. ISSN 10980121. doi: 10.1103/PhysRevB.85.235315.
- [104] Andreas V. Kuhlmann, Julien Houel, Arne Ludwig, Lukas Greuter, Dirk Reuter, Andreas D. Wieck, Martino Poggio, and Richard J. Warburton. Charge noise and spin noise in a semiconductor quantum device. *Nat. Phys.*, 9(9):570–575, 2013. ISSN 1745-2473. doi: 10.1038/nphys2688. URL <http://www.nature.com/doi/10.1038/nphys2688>.
- [105] C. Arnold, V. Loo, a. Lemaître, I. Sagnes, O. Krebs, P. Voisin, P. Senellart, and L. Lanco. Cavity-enhanced real-time monitoring of single-charge jumps at the microsecond time scale. *Phys. Rev. X*, 4(2):1–6, 2014. ISSN 21603308. doi: 10.1103/PhysRevX.4.021004.
- [106] S. Varoutsis, S. Laurent, P. Kramper, a. Lemaître, I. Sagnes, I. Robert-Philip, and I. Abram. Restoration of photon indistinguishability in the emission of a semiconductor quantum dot. *Phys. Rev. B - Condens. Matter Mater. Phys.*, 72 (4), 2005. ISSN 10980121. doi: 10.1103/PhysRevB.72.041303.
- [107] Yu-jia Wei, Yu-Ming He, Ming-cheng Chen, Yi-nan Hu, Yu He, Dian Wu, Christian Schneider, Martin Kamp, Sven Höfling, Chao-Yang Lu, and Jian-Wei Pan. Deterministic and Robust Generation of Single Photons On a Chip with 99.5% Indistinguishability Using Rapid Adiabatic Passage. *Nano Lett.*, page 5, 2014. ISSN 15306992. doi: 10.1021/nl503081n.

- [108] EM Purcell. Spontaneous emission probabilities at radio frequencies. *Phys. Rev.*, 69, 1946.
- [109] K.H. Drexhage. Influence of a dielectric interface on fluorescence decay time. *J. Lumin.*, 1-2:693–701, jan 1970. ISSN 00222313. doi: 10.1016/0022-2313(70)90082-7. URL <http://www.sciencedirect.com/science/article/pii/0022231370900827>.
- [110] P. Goy, J. M. Raimond, M. Gross, and S. Haroche. Observation of Cavity-Enhanced Single-Atom Spontaneous Emission. *Phys. Rev. Lett.*, 50(24):1903–1906, jun 1983. ISSN 0031-9007. doi: 10.1103/PhysRevLett.50.1903. URL <http://link.aps.org/doi/10.1103/PhysRevLett.50.1903>.
- [111] Jean Michel Gérard and Bruno Gayral. Strong Purcell effect for InAs quantum boxes in three-dimensional solid-state microcavities. *J. Light. Technol.*, 17(11):2089–2095, 1999. ISSN 07338724. doi: 10.1109/50.802999. URL <http://ieeexplore.ieee.org/articleDetails.jsp?arnumber=802999>.
- [112] Dirk Englund, David Fattal, Edo Waks, Glenn Solomon, Bingyang Zhang, Toshihiro Nakaoka, Yasuhiko Arakawa, Yoshihisa Yamamoto, and Jelena Vučković. Controlling the Spontaneous Emission Rate of Single Quantum Dots in a Two-Dimensional Photonic Crystal. *Phys. Rev. Lett.*, 95(1):013904, jul 2005. ISSN 0031-9007. doi: 10.1103/PhysRevLett.95.013904. URL <http://link.aps.org/doi/10.1103/PhysRevLett.95.013904>.
- [113] G Grynberg, A Aspect, and C Fabre. *Introduction to quantum optics: from the semi-classical approach to quantized light*. 2010. ISBN 9780521551120. URL [http://books.google.com/books?hl=en{&}lr={&}id=l-10L8YInA0C{&}oi=fnd{&}pg=PR5{&}dq=Introduction+to+Quantum+Optics+From+the+Semi-classical+Approach+to+Quantized+Light{&}ots=DCrppZeACp{&}sig=RZKmHd{ }UDdj7L6Gpa2MNZQhAXcg](http://books.google.com/books?hl=en&lr={&}id=l-10L8YInA0C{&}oi=fnd{&}pg=PR5{&}dq=Introduction+to+Quantum+Optics+From+the+Semi-classical+Approach+to+Quantized+Light{&}ots=DCrppZeACp{&}sig=RZKmHd{ }UDdj7L6Gpa2MNZQhAXcg).
- [114] S. Haroche and J. M. Raimond. *Exploring the quantum : atoms, cavities, photons*, volume 5. 2012.
- [115] E.T. Jaynes and F.W. Cummings. Comparison of quantum and semiclassical radiation theories with application to the beam maser. *Proc. IEEE*, 51(1):89–109, jan 1963. ISSN 0018-9219. doi: 10.1109/PROC.1963.1664. URL <http://ieeexplore.ieee.org/articleDetails.jsp?arnumber=1443594>.
- [116] B. Gayral, J. M. Gerard, A. Lemaitre, C. Dupuis, L. Manin, and J. L. Pelouard. High-Q wet-etched GaAs microdisks containing InAs quantum boxes. *Appl. Phys.*

- Lett.*, 75(13):1908, sep 1999. ISSN 00036951. doi: 10.1063/1.124894. URL <http://scitation.aip.org/content/aip/journal/apl/75/13/10.1063/1.124894>.
- [117] B. Gayral, J.-M. Gerard, B. Sermage, A. Lemaitre, and C. Dupuis. Time-resolved probing of the Purcell effect for InAs quantum boxes in GaAs microdisks. *Appl. Phys. Lett.*, 78(19):2828, may 2001. ISSN 00036951. doi: 10.1063/1.1370123. URL <http://scitation.aip.org/content/aip/journal/apl/78/19/10.1063/1.1370123>.
- [118] E. Peter, P. Senellart, D. Martrou, A. Lemaître, J. Hours, J. Gérard, and J. Bloch. Exciton-Photon Strong-Coupling Regime for a Single Quantum Dot Embedded in a Microcavity. *Phys. Rev. Lett.*, 95(6):067401, aug 2005. ISSN 0031-9007. doi: 10.1103/PhysRevLett.95.067401. URL <http://link.aps.org/doi/10.1103/PhysRevLett.95.067401>.
- [119] Kartik Srinivasan, Andreas Stintz, Sanjay Krishna, and Oskar Painter. Photoluminescence measurements of quantum-dot-containing semiconductor microdisk resonators using optical fiber taper waveguides. *Phys. Rev. B*, 72(20):205318, nov 2005. ISSN 1098-0121. doi: 10.1103/PhysRevB.72.205318. URL <http://link.aps.org/doi/10.1103/PhysRevB.72.205318>.
- [120] Peter Lodahl, a Floris Van Driel, Ivan S Nikolaev, Arie Irman, Karin Overgaag, Daniël Vanmaekelbergh, and Willem L Vos. Controlling the dynamics of spontaneous emission from quantum dots by photonic crystals. *Nature*, 430(7000):654–657, 2004. ISSN 0028-0836. doi: 10.1038/nature02772.
- [121] Susumu Noda, Masayuki Fujita, and Takashi Asano. Spontaneous-emission control by photonic crystals and nanocavities. *Nat. Photonics*, 1(8):449–458, 2007. ISSN 1749-4885. doi: 10.1038/nphoton.2007.141.
- [122] T. Lund-Hansen, S. Stobbe, B. Julsgaard, H. Thyrrestrup, T. Sünner, M. Kamp, A. Forchel, and P. Lodahl. Experimental Realization of Highly Efficient Broadband Coupling of Single Quantum Dots to a Photonic Crystal Waveguide. *Phys. Rev. Lett.*, 101(11):113903, sep 2008. ISSN 0031-9007. doi: 10.1103/PhysRevLett.101.113903. URL <http://link.aps.org/doi/10.1103/PhysRevLett.101.113903>.
- [123] Antonio Badolato, Kevin Hennessy, Mete Atatüre, Jan Dreiser, Evelyn Hu, Pierre M Petroff, and Atac Imamoglu. Deterministic coupling of single quantum dots to single nanocavity modes. *Science*, 308(5725):1158–61, may 2005. ISSN 1095-9203. doi: 10.1126/science.1109815. URL <http://www.sciencemag.org/content/308/5725/1158.short>.

- [124] K Hennesy, A Badolato, M Winger, D Gerace, M Atatüre, S Gulde, S Fält, E L Hu, and A Imamoglu. Quantum nature of a strongly coupled single quantum dot-cavity system. *Nature*, 445(7130):896–9, mar 2007. ISSN 1476-4687. doi: 10.1038/nature05586. URL <http://dx.doi.org/10.1038/nature05586>.
- [125] P. Gallo, M. Felici, B. Dwir, K. A. Atlasov, K. F. Karlsson, A. Rudra, A. Mohan, G. Biasiol, L. Sorba, and E. Kapon. Integration of site-controlled pyramidal quantum dots and photonic crystal membrane cavities. *Appl. Phys. Lett.*, 92(26):263101, jun 2008. ISSN 00036951. doi: 10.1063/1.2952278. URL <http://scitation.aip.org/content/aip/journal/apl/92/26/10.1063/1.2952278>.
- [126] F. Albert, S. Stobbe, C. Schneider, T. Heindel, S. Reitzenstein, S. Hofling, P. Lodahl, L. Worschech, and A. Forchel. Quantum efficiency and oscillator strength of site-controlled InAs quantum dots. *Appl. Phys. Lett.*, 96(15):151102, apr 2010. ISSN 00036951. doi: 10.1063/1.3393988. URL <http://scitation.aip.org/content/aip/journal/apl/96/15/10.1063/1.3393988>.
- [127] Andreas Muller, Edward B. Flagg, Michael Metcalfe, John Lawall, and Glenn S. Solomon. Coupling an epitaxial quantum dot to a fiber-based external-mirror microcavity. *Appl. Phys. Lett.*, 95(17):33–36, 2009. ISSN 00036951. doi: 10.1063/1.3245311.
- [128] Lukas Greuter, Daniel Najer, Andreas V. Kuhlmann, Sascha Valentin, Arne Ludwig, Andreas D. Wieck, Sebastian Starosielec, and Richard J. Warburton. Epitaxial lift-off for solid-state cavity quantum electrodynamics. page 6, may 2015. URL <http://arxiv.org/abs/1505.00658>.
- [129] J. M. Gerard, D. Barrier, J. Y. Marzin, R. Kuszelewicz, L. Manin, E. Costard, V. Thierry-Mieg, and T. Rivera. Quantum boxes as active probes for photonic microstructures: The pillar microcavity case. *Appl. Phys. Lett.*, 69(4):449, jul 1996. ISSN 00036951. doi: 10.1063/1.118135. URL <http://scitation.aip.org/content/aip/journal/apl/69/4/10.1063/1.118135>.
- [130] T. Heindel, C. Schneider, M. Lerner, S. H. Kwon, T. Braun, S. Reitzenstein, S. Hofling, M. Kamp, and A. Forchel. Electrically driven quantum dot-micropillar single photon source with 34% overall efficiency. *Appl. Phys. Lett.*, 96(1):011107, jan 2010. ISSN 00036951. doi: 10.1063/1.3284514. URL <http://scitation.aip.org/content/aip/journal/apl/96/1/10.1063/1.3284514>.
- [131] Edward B. Flagg, Andreas Muller, Sergey V. Polyakov, Alex Ling, Alan Migdall, and Glenn S. Solomon. Interference of single photons from two separate semiconductor quantum dots. *Phys. Rev. Lett.*, 104(13):1–4, apr 2010. ISSN 00319007. doi:

- 10.1103/PhysRevLett.104.137401. URL <http://link.aps.org/doi/10.1103/PhysRevLett.104.137401>.
- [132] R. B. Patel, a. J. Bennett, I. Farrer, C. a. Nicoll, D. a. Ritchie, and a. J. Shields. Two-photon interference of the emission from electrically tunable remote quantum dots. *Nat. Photonics*, 4(July):632–635, 2010. ISSN 1749-4885. doi: 10.1038/nphoton.2010.161. URL <http://www.nature.com/nphoton/journal/v4/n9/full/nphoton.2010.161.html>.
- [133] M. Lermer, N. Gregersen, F. Dunzer, S. Reitzenstein, S. Höfling, J. Mørk, L. Worschech, M. Kamp, and A. Forchel. Bloch-wave engineering of quantum dot micropillars for cavity quantum electrodynamics experiments. *Phys. Rev. Lett.*, 108(5), 2012. ISSN 00319007. doi: 10.1103/PhysRevLett.108.057402. URL <http://journals.aps.org/prl/abstract/10.1103/PhysRevLett.108.057402>.
- [134] Bruno GAYRAL. *Modification de l'émission spontanée de boîtes quantiques semi-conductrices dans des microcavités optiques*. PhD thesis, 2000. URL <http://www.theses.fr/2000PA066183>.
- [135] Daniel Valente, Jan Suffczyński, Tomasz Jakubczyk, Adrien Dousse, Aristide Lemaître, Isabelle Sagnes, Loïc Lanco, Paul Voisin, Alexia Auffèves, and Pascale Senellart. Frequency cavity pulling induced by a single semiconductor quantum dot. *Phys. Rev. B*, 89(4):041302, jan 2014. ISSN 1098-0121. doi: 10.1103/PhysRevB.89.041302. URL <http://link.aps.org/doi/10.1103/PhysRevB.89.041302>.
- [136] Simone Luca Portalupi, Gaston Hornecker, Valérian Giesz, Thomas Grange, Aristide Lemaître, Justin Demory, Isabelle Sagnes, Norberto D. Lanzillotti-Kimura, Loïc Lanco, Alexia Auffèves, and Pascale Senellart. Bright Phonon-Tuned Single-Photon Source. *Nano Lett.*, page 150904102049004, 2015. ISSN 1530-6984. doi: 10.1021/acs.nanolett.5b00876. URL <http://pubs.acs.org/doi/10.1021/acs.nanolett.5b00876>.
- [137] C. Schneider, T. Heindel, A. Huggenberger, T. A. Niederstrasser, S. Reitzenstein, A. Forchel, S. Hoffing, and M. Kamp. Microcavity enhanced single photon emission from an electrically driven site-controlled quantum dot. *Appl. Phys. Lett.*, 100(9):091108, feb 2012. ISSN 00036951. doi: 10.1063/1.3689782. URL <http://scitation.aip.org/content/aip/journal/apl/100/9/10.1063/1.3689782>.
- [138] S. Strauf, K. Hennessy, M. T. Rakher, Y.-S. Choi, A. Badolato, L. C. Andreani, E. L. Hu, P. M. Petroff, and D. Bouwmeester. Self-Tuned Quantum Dot Gain in

- Photonic Crystal Lasers. *Phys. Rev. Lett.*, 96(12):127404, mar 2006. ISSN 0031-9007. doi: 10.1103/PhysRevLett.96.127404. URL <http://link.aps.org/doi/10.1103/PhysRevLett.96.127404>.
- [139] Edward Flagg, Sergey Polyakov, Tim Thomay, and Glenn Solomon. Dynamics of Nonclassical Light from a Single Solid-State Quantum Emitter. *Phys. Rev. Lett.*, 109(16):163601, oct 2012. ISSN 0031-9007. doi: 10.1103/PhysRevLett.109.163601. URL <http://link.aps.org/doi/10.1103/PhysRevLett.109.163601>.
- [140] J. Suffczyński, A. Dousse, K. Gauthron, A. Lemaître, I. Sagnes, L. Lanco, J. Bloch, P. Voisin, and P. Senellart. Origin of the Optical Emission within the Cavity Mode of Coupled Quantum Dot-Cavity Systems. *Phys. Rev. Lett.*, 103(2):027401–, jul 2009. ISSN 0031-9007. doi: 10.1103/PhysRevLett.103.027401. URL <http://link.aps.org/doi/10.1103/PhysRevLett.103.027401>.
- [141] E. Peter, S. Laurent, J. Bloch, J. Hours, S. Varoutsis, I. Robert-Philip, A. Beveratos, A. Lemaitre, A. Cavanna, G. Patriarche, P. Senellart, and D. Martrou. Fast radiative quantum dots: From single to multiple photon emission. *Appl. Phys. Lett.*, 90(22):223118, 2007. ISSN 00036951. doi: 10.1063/1.2744475. URL <http://link.aip.org/link/APPLAB/v90/i22/p223118/s1{&}Agg=doi>.
- [142] Olivier Gazzano. *Sources brillantes de photons uniques indiscernables et démonstration d’une porte logique quantique*. Theses, Université Paris-Diderot - Paris VII, 2013. URL <https://tel.archives-ouvertes.fr/tel-01006555>.
- [143] Paul G Kwiat and Aephraim M Steinberg. Observation of a quantum eraser : a revival of coherence in a two-photon interference experiment. 45(11), 1992.
- [144] M. Metcalfe, S. M. Carr, a. Muller, G. S. Solomon, and J. Lawall. Resolved sideband emission of InAs/GaAs quantum dots strained by surface acoustic waves. *Phys. Rev. Lett.*, 105(3), 2010. ISSN 00319007. doi: 10.1103/PhysRevLett.105.037401.
- [145] Hai Son Nguyen, Gregory Sallen, Marco Abbarchi, Robson Ferreira, Christophe Voisin, Philippe Roussignol, Guillaume Cassabois, and Carole Diederichs. Photon neutralization and slow capture of carriers in quantum dots probed by resonant excitation spectroscopy. *Phys. Rev. B - Condens. Matter Mater. Phys.*, 87(11):115305, mar 2013. ISSN 10980121. doi: 10.1103/PhysRevB.87.115305. URL <http://link.aps.org/doi/10.1103/PhysRevB.87.115305>.
- [146] J. Houel, a. V. Kuhlmann, L. Greuter, F. Xue, M. Poggio, B. D. Gerardot, P. a. Dalgarno, a. Badolato, P. M. Petroff, a. Ludwig, D. Reuter, a. D. Wieck, and R. J. Warburton. Probing Single-Charge Fluctuations at a GaAs/AlAs Interface Using

- Laser Spectroscopy on a Nearby InGaAs Quantum Dot. *Phys. Rev. Lett.*, 108(10):107401, mar 2012. ISSN 0031-9007. doi: 10.1103/PhysRevLett.108.107401. URL <http://link.aps.org/doi/10.1103/PhysRevLett.108.107401>.
- [147] Al. L. Efros and M. Rosen. Random Telegraph Signal in the Photoluminescence Intensity of a Single Quantum Dot. *Phys. Rev. Lett.*, 78(6):1110–1113, feb 1997. ISSN 0031-9007. doi: 10.1103/PhysRevLett.78.1110. URL <http://link.aps.org/doi/10.1103/PhysRevLett.78.1110>.
- [148] M-E. Pistol, P. Castrillo, D. Hessman, J. A. Prieto, and L. Samuelson. Random telegraph noise in photoluminescence from individual self-assembled quantum dots. *Phys. Rev. B*, 59(16):10725–10729, apr 1999. ISSN 0163-1829. doi: 10.1103/PhysRevB.59.10725. URL <http://link.aps.org/doi/10.1103/PhysRevB.59.10725>.
- [149] R. G. Neuhauser, K. T. Shimizu, W. K. Woo, S. A. Emepedocles, and M. G. Bawendi. Correlation between Fluorescence Intermittency and Spectral Diffusion in Single Semiconductor Quantum Dots. *Phys. Rev. Lett.*, 85(15):3301–3304, oct 2000. ISSN 0031-9007. doi: 10.1103/PhysRevLett.85.3301. URL <http://link.aps.org/doi/10.1103/PhysRevLett.85.3301>.
- [150] V. TÜRCK, S. Rodt, O. Stier, R. Heitz, R. Engelhardt, U. W. Pohl, D. Bimberg, and R. Steingrüber. Effect of random field fluctuations on excitonic transitions of individual CdSe quantum dots. *Phys. Rev. B*, 61(15):9944–9947, apr 2000. ISSN 0163-1829. doi: 10.1103/PhysRevB.61.9944. URL <http://link.aps.org/doi/10.1103/PhysRevB.61.9944>.
- [151] Charles Santori. *Generation of nonclassical light using semiconductor quantum dots*. PhD thesis.
- [152] F. Findeis, M. Baier, E. Beham, A. Zrenner, and G. Abstreiter. Photocurrent and photoluminescence of a single self-assembled quantum dot in electric fields. *Appl. Phys. Lett.*, 78(19):2958, may 2001. ISSN 00036951. doi: 10.1063/1.1369148. URL <http://scitation.aip.org/content/aip/journal/apl/78/19/10.1063/1.1369148>.
- [153] R. Oulton, J. Finley, a. Ashmore, I. Gregory, D. Mowbray, M. Skolnick, M. Steer, San-Lin Liew, M. Migliorato, and a. Cullis. Manipulation of the homogeneous linewidth of an individual In(Ga)As quantum dot. *Phys. Rev. B*, 66(4):045313, jul 2002. ISSN 0163-1829. doi: 10.1103/PhysRevB.66.045313. URL <http://link.aps.org/doi/10.1103/PhysRevB.66.045313>.

- [154] J. J. Finley, M. Sabathil, P. Vogl, G. Abstreiter, R. Oulton, a. I. Tartakovskii, D. J. Mowbray, M. S. Skolnick, S. L. Liew, a. G. Cullis, and M. Hopkinson. Quantum-confined Stark shifts of charged exciton complexes in quantum dots. *Phys. Rev. B - Condens. Matter Mater. Phys.*, 70(20):201308, nov 2004. ISSN 01631829. doi: 10.1103/PhysRevB.70.201308. URL <http://link.aps.org/doi/10.1103/PhysRevB.70.201308>.
- [155] S Laurent, B Eble, O Krebs, A Lemaître, B Urbaszek, X Marie, T Amand, and P Voisin. Electrical Control of Hole Spin Relaxation in Charge Tunable InAs/GaAs Quantum Dots. *Phys. Rev. Lett.*, 94(14):147401, 2005. ISSN 0031-9007. doi: 10.1103/PhysRevLett.94.147401. URL <http://journals.aps.org/prl/abstract/10.1103/PhysRevLett.94.147401>.
- [156] K. Kowalik, O. Krebs, a. Lemaître, S. Laurent, P. Senellart, P. Voisin, and J. a. Gaj. Influence of an in-plane electric field on exciton fine structure in InAs-GaAs self-assembled quantum dots. *Appl. Phys. Lett.*, 86(4):10–13, 2005. ISSN 00036951. doi: 10.1063/1.1855409.
- [157] A J Bennett, M A Pooley, R M Stevenson, M B Ward, R B Patel, A Boyer De Giroday, N Sköld, I Farrer, C A Nicoll, D A Ritchie, and A J Shields. Electric-field-induced coherent coupling of the exciton states in a single quantum dot. *Nat. Phys.*, 6(12):947–950, 2010. ISSN 1745-2473. doi: 10.1038/nphys1780. URL <http://dx.doi.org/10.1038/nphys1780>.
- [158] Alexander Högele, Stefan Seidl, Martin Kroner, Khaled Karrai, Richard J. Warburton, Brian D. Gerardot, and Pierre M. Petroff. Voltage-controlled optics of a quantum dot. *Phys. Rev. Lett.*, 93(21):19–22, 2004. ISSN 00319007. doi: 10.1103/PhysRevLett.93.217401.
- [159] M. M. Vogel, S. M. Ulrich, R. Hafenbrak, P. Michler, L. Wang, a. Rastelli, and O. G. Schmidt. Influence of lateral electric fields on multiexcitonic transitions and fine structure of single quantum dots. *Appl. Phys. Lett.*, 91(5):2005–2008, 2007. ISSN 00036951. doi: 10.1063/1.2761522.
- [160] Stefan Strauf, Nick G. Stoltz, Matthew T. Rakher, Larry a. Coldren, Pierre M. Petroff, and Dirk Bouwmeester. High-frequency single-photon source with polarization control. *Nat. Photonics*, 1(12):704–708, 2007. ISSN 1749-4885. doi: 10.1038/nphoton.2007.227. URL <http://dx.doi.org/10.1038/nphoton.2007.227>.
- [161] C. Böckler, S. Reitzenstein, C. Kistner, R. Debusmann, a. Löffler, T. Kida, S. Höfling, a. Forchel, L. Grenouillet, J. Claudon, and J. M. rard. Electrically driven high- Q quantum dot-micropillar cavities. *Appl. Phys. Lett.*, 92(9):2006–2009, 2008. ISSN 00036951. doi: 10.1063/1.2890166.

- [162] a. Kiraz, M. Atatüre, and a. Imamoglu. Quantum-dot single-photon sources: Prospects for applications in linear optics quantum-information processing. *Phys. Rev. A*, 69(3):1–10, mar 2004. ISSN 1050-2947. doi: 10.1103/PhysRevA.69.032305. URL <http://link.aps.org/doi/10.1103/PhysRevA.69.032305>.
- [163] A K Nowak, S L Portalupi, V Giesz, O Gazzano, C Dal Savio, P-F Braun, K Karrai, C Arnold, L Lanco, I Sagnes, A Lemaître, and P Senellart. Deterministic and electrically tunable bright single-photon source. *Nat. Commun.*, 5:3240, 2014. ISSN 2041-1723. doi: 10.1038/ncomms4240. URL <http://www.nature.com/ncomms/2014/140205/ncomms4240/full/ncomms4240.html>.
- [164] A. Muller, E. B. Flagg, P. Bianucci, X. Y. Wang, D. G. Deppe, W. Ma, J. Zhang, G. J. Salamo, M. Xiao, and C. K. Shih. Resonance fluorescence from a coherently driven semiconductor quantum dot in a cavity. *Phys. Rev. Lett.*, 99(18):2–5, 2007. ISSN 00319007. doi: 10.1103/PhysRevLett.99.187402.
- [165] K. Kuroda, T. Kuroda, K. Watanabe, T. Mano, K. Sakoda, G. Kido, and N. Koguchi. Final-state readout of exciton qubits by observing resonantly excited photoluminescence in quantum dots. *Appl. Phys. Lett.*, 90(5):051909, 2007. ISSN 00036951. doi: 10.1063/1.2435600. URL <http://scitation.aip.org/content/aip/journal/apl/90/5/10.1063/1.2435600>.
- [166] R. Melet, V. Voliotis, a. Enderlin, D. Roditchev, X. L. Wang, T. Guillet, and R. Grousson. Resonant excitonic emission of a single quantum dot in the Rabi regime. *Phys. Rev. B - Condens. Matter Mater. Phys.*, 78(7):3–6, 2008. ISSN 10980121. doi: 10.1103/PhysRevB.78.073301.
- [167] E. B. Flagg, a. Muller, J. W. Robertson, S. Founta, D. G. Deppe, M. Xiao, W. Ma, G. J. Salamo, and C. K. Shih. Resonantly driven coherent oscillations in a solid-state quantum emitter. *Nat. Phys.*, 5(3):203–207, 2009. ISSN 1745-2473. doi: 10.1038/nphys1184.
- [168] A. Ulhaq, S. Weiler, S. M. Ulrich, R. Roßbach, M. Jetter, and P. Michler. Cascaded single-photon emission from the Mollow triplet sidebands of a quantum dot. *Nat. Photonics*, 6(4):238–242, feb 2012. ISSN 1749-4885. doi: 10.1038/nphoton.2012.23. URL <http://dx.doi.org/10.1038/nphoton.2012.23>.
- [169] Léonard Monniello, Catherine Tonin, Richard Hostein, Aristide Lemaitre, Anthony Martinez, Valia Voliotis, and Roger Grousson. Excitation-induced dephasing in a resonantly driven InAs/GaAs quantum dot. *Phys. Rev. Lett.*, 111(2):1–5, 2013. ISSN 00319007. doi: 10.1103/PhysRevLett.111.026403.

- [170] V Loo, C Arnold, and O Gazzano. Optical nonlinearity for few-photon pulses on a quantum dot-pillar cavity device. *arXiv Prepr. arXiv ...*, 1:1–5, 2012. URL <http://arxiv.org/abs/1208.0850>.
- [171] V. Loo, C. Arnold, O. Gazzano, A. Lemaître, I. Sagnes, O. Krebs, P. Voisin, P. Senellart, and L. Lanco. Optical Nonlinearity for Few-Photon Pulses on a Quantum Dot-Pillar Cavity Device. *Phys. Rev. Lett.*, 109(16):166806, oct 2012. ISSN 0031-9007. doi: 10.1103/PhysRevLett.109.166806. URL <http://link.aps.org/doi/10.1103/PhysRevLett.109.166806>.
- [172] Christophe Arnold, Justin Demory, Vivien Loo, Aristide Lemaître, Isabelle Sagnes, Mikhail Glazov, Olivier Krebs, Paul Voisin, Pascale Senellart, and Loïc Lanco. Macroscopic rotation of photon polarization induced by a single spin. *Nat. Commun.*, 6:6236, 2015. ISSN 2041-1723. doi: 10.1038/ncomms7236. URL <http://www.nature.com/doi/10.1038/ncomms7236>.
- [173] T. Stievater, Xiaoqin Li, D. Steel, D. Gammon, D. Katzer, D. Park, C. Piermarocchi, and L. Sham. Rabi Oscillations of Excitons in Single Quantum Dots. *Phys. Rev. Lett.*, 87(13):5–8, 2001. ISSN 0031-9007. doi: 10.1103/PhysRevLett.87.133603.
- [174] H Kamada, H Gotoh, J Temmyo, T Takagahara, and H Ando. Exciton Rabi oscillation in a single quantum dot. *Phys. Rev. Lett.*, 87(24):246401, nov 2001. ISSN 0031-9007. doi: 10.1103/PhysRevLett.87.246401. URL <http://link.aps.org/doi/10.1103/PhysRevLett.87.246401>.
- [175] H Htoon, T Takagahara, D Kulik, O Baklenov, a L Holmes, and C K Shih. Interplay of Rabi oscillations and quantum interference in semiconductor quantum dots. *Phys. Rev. Lett.*, 88(8):087401, feb 2002. ISSN 0031-9007. doi: 10.1103/PhysRevLett.88.087401. URL <http://link.aps.org/doi/10.1103/PhysRevLett.88.087401>.
- [176] a Zrenner, E Beham, S Stuffer, F Findeis, M Bichler, and G Abstreiter. Coherent properties of a two-level system based on a quantum-dot photodiode. *Nature*, 418(6898):612–614, 2002. ISSN 0028-0836. doi: 10.1038/nature00912.
- [177] H J Kimble. The quantum internet. *Nature*, 453(7198):1023–1030, 2008. ISSN 0028-0836. doi: 10.1038/nature07127.
- [178] Ranojoy Bose, Deepak Sridharan, Hyochul Kim, Glenn S. Solomon, and Edo Waks. Low-photon-number optical switching with a single quantum dot coupled to a photonic crystal cavity. *Phys. Rev. Lett.*, 108(22):1–5, 2012. ISSN 00319007. doi: 10.1103/PhysRevLett.108.227402.

- [179] J D Thompson, T G Tiecke, N P de Leon, J Feist, A V Akimov, M Gullans, A S Zibrov, V Vuletić, and M D Lukin. Coupling a single trapped atom to a nanoscale optical cavity. *Science*, 340(6137):1202–5, jun 2013. ISSN 1095-9203. doi: 10.1126/science.1237125. URL <http://www.sciencemag.org/content/340/6137/1202.abstract>.
- [180] K M Birnbaum, A Boca, R Miller, A D Boozer, T E Northup, and H J Kimble. Photon blockade in an optical cavity with one trapped atom. *Nature*, 436(7047):87–90, jul 2005. ISSN 1476-4687. doi: 10.1038/nature03804. URL <http://dx.doi.org/10.1038/nature03804>.
- [181] Stephan Ritter, Christian Nölleke, Carolin Hahn, Andreas Reiserer, Andreas Neuzner, Manuel Uphoff, Martin Mücke, Eden Figueroa, Joerg Bochmann, and Gerhard Rempe. An elementary quantum network of single atoms in optical cavities. *Nature*, 484(7393):195–200, apr 2012. ISSN 0028-0836. doi: 10.1038/nature11023. URL <http://www.nature.com/doifinder/10.1038/nature11023>.
- [182] Andreas Reiserer, Norbert Kalb, Gerhard Rempe, and Stephan Ritter. A quantum gate between a flying optical photon and a single trapped atom. *Nature*, 508(7495):237–40, 2014. ISSN 1476-4687. doi: 10.1038/nature13177. URL <http://www.ncbi.nlm.nih.gov/pubmed/24717512>.
- [183] J Beugnon, M P A Jones, J Dingjan, B Darquié, G Messin, A Browaeys, and P Grangier. Quantum interference between two single photons emitted by independently trapped atoms. *Nature*, 440(7085):779–82, apr 2006. ISSN 1476-4687. doi: 10.1038/nature04628. URL <http://dx.doi.org/10.1038/nature04628>.
- [184] H. de Riedmatten, I. Marcikic, W. Tittel, H. Zbinden, and N. Gisin. Quantum interference with photon pairs created in spatially separated sources. *Phys. Rev. A*, 67(2):5, feb 2002. ISSN 1050-2947. doi: 10.1103/PhysRevA.67.022301. URL <http://arxiv.org/abs/quant-ph/0208174>.
- [185] Rainer Kaltenbaek, Bibiane Blauensteiner, Marek Zukowski, Markus Aspelmeyer, and Anton Zeilinger. Experimental interference of independent photons. *Phys. Rev. Lett.*, 96(24):240502, jun 2006. ISSN 00319007. doi: 10.1103/PhysRevLett.96.240502. URL <http://link.aps.org/doi/10.1103/PhysRevLett.96.240502>.
- [186] P. Maunz, D. L. Moehring, S. Olmschenk, K. C. Younge, D. N. Matsukevich, and C. Monroe. Quantum interference of photon pairs from two remote trapped atomic ions. *Nat. Phys.*, 3(8):538–541, jun 2007. ISSN 1745-2473. doi: 10.1038/nphys644. URL <http://dx.doi.org/10.1038/nphys644>.

- [187] R. Lettow, Y. L. a Rezus, a. Renn, G. Zumofen, E. Ikonen, S. Götzinger, and V. Sandoghdar. Quantum interference of tunably indistinguishable photons from remote organic molecules. *Phys. Rev. Lett.*, 104(12):123605, mar 2010. ISSN 00319007. doi: 10.1103/PhysRevLett.104.123605. URL <http://link.aps.org/doi/10.1103/PhysRevLett.104.123605>.
- [188] Hannes Bernien, Lilian Childress, Lucio Robledo, Matthew Markham, Daniel Twitchen, and Ronald Hanson. Two-Photon Quantum Interference from Separate Nitrogen Vacancy Centers in Diamond. *Phys. Rev. Lett.*, 108(4):043604, jan 2012. ISSN 0031-9007. doi: 10.1103/PhysRevLett.108.043604. URL <http://link.aps.org/doi/10.1103/PhysRevLett.108.043604>.
- [189] W B Gao, P Fallahi, E Togan, A Delteil, Y S Chin, J Miguel-Sanchez, and A Imamoglu. Quantum teleportation from a propagating photon to a solid-state spin qubit. *Nat. Commun.*, 4:2744, nov 2013. ISSN 2041-1723. doi: 10.1038/ncomms3744. URL <http://www.nature.com/ncomms/2013/131101/ncomms3744/full/ncomms3744.html>.
- [190] P. Gold, a. Thoma, S. Maier, S. Reitzenstein, C. Schneider, S. Höfling, and M. Kamp. Two-photon interference from remote quantum dots with inhomogeneously broadened linewidths. *Phys. Rev. B*, 89(3):035313, jan 2014. ISSN 1098-0121. doi: 10.1103/PhysRevB.89.035313. URL <http://link.aps.org/doi/10.1103/PhysRevB.89.035313>.
- [191] V. Giesz, S. L. Portalupi, T. Grange, C. Antón, L. De Santis, J. Demory, N. Somaschi, I. Sagnes, A. Lemaitre, L. Lanco, A. Auffeves, and P. Senellart. Cavity-Enhanced Two-Photon Interference using Remote Quantum Dot Sources. *Phys. Rev. B*, 92, 2015. doi: <http://dx.doi.org/10.1103/PhysRevB.92.161302>. URL <http://journals.aps.org/prb/abstract/10.1103/PhysRevB.92.161302>.
- [192] S. Stuffer, P. Machnikowski, P. Ester, M. Bichler, V. M. Axt, T. Kuhn, and A. Zrenner. Two-photon Rabi oscillations in a single In x Ga 1 - x As Ga As quantum dot. *Phys. Rev. B*, 73(12):125304, mar 2006. ISSN 1098-0121. doi: 10.1103/PhysRevB.73.125304. URL <http://link.aps.org/doi/10.1103/PhysRevB.73.125304>.
- [193] Tobias Huber, Thomas Kauten, Glenn S. Solomon, Gregor Weihs, Harishankar Jayakumar, Ana Predojević, Tobias Huber, Thomas Kauten, Glenn S. Solomon, and Gregor Weihs. Deterministic Photon Pairs via Coherent Optical Control of a Single Quantum Dot. *Phys. Rev. Lett.*, 110(13):135505, mar 2013. ISSN 0031-9007. doi: 10.1103/PhysRevLett.110.135505. URL <http://link.aps.org/doi/10.1103/PhysRevLett.110.135505>.

- [194] Yonatan Israel, Shamir Rosen, and Yaron Silberberg. Supersensitive Polarization Microscopy Using NOON States of Light. *Phys. Rev. Lett.*, 112(10):103604, 2014. ISSN 0031-9007. doi: 10.1103/PhysRevLett.112.103604. URL <http://link.aps.org/doi/10.1103/PhysRevLett.112.103604>.
- [195] Jaewoo Joo, William J. Munro, and Timothy P. Spiller. Quantum Metrology with Entangled Coherent States. *Phys. Rev. Lett.*, 107(8):083601, aug 2011. ISSN 0031-9007. doi: 10.1103/PhysRevLett.107.083601. URL <http://link.aps.org/doi/10.1103/PhysRevLett.107.083601>.
- [196] Itai Afek, Oron Ambar, and Yaron Silberberg. High-NOON states by mixing quantum and classical light. *Science*, 328(5980):879–881, 2010. ISSN 0036-8075. doi: 10.1126/science.1188172.
- [197] Z. Y. Ou, X. Y. Zou, L. J. Wang, and L. Mandel. Experiment on nonclassical fourth-order interference. *Phys. Rev. A*, 42(5):2957–2965, 1990. ISSN 10502947. doi: 10.1103/PhysRevA.42.2957.
- [198] Tomohisa Nagata, Ryo Okamoto, Jeremy L O’Brien, Keiji Sasaki, and Shigeki Takeuchi. Beating the standard quantum limit with four-entangled photons. *Science*, 316(5825):726–729, 2007. ISSN 0036-8075. doi: 10.1126/science.1138007.
- [199] Yonatan Israel, Itai Afek, Shamir Rosen, Oron Ambar, and Yaron Silberberg. Experimental tomography of NOON states with large photon numbers. *Phys. Rev. A*, 85(2):022115, feb 2012. ISSN 1050-2947. doi: 10.1103/PhysRevA.85.022115. URL <http://link.aps.org/doi/10.1103/PhysRevA.85.022115>.
- [200] Max Tillmann, Borivoje Dakić, René Heilmann, Stefan Nolte, Alexander Szameit, and Philip Walther. Experimental boson sampling. *Nat. Photonics*, 7(7):540–544, 2013. ISSN 1749-4885. doi: 10.1038/nphoton.2013.102. URL <http://arxiv.org/abs/1212.2240>~~http://www.nature.com/doi/10.1038/nphoton.2013.102~~.
- [201] Andrea Crespi, Roberto Osellame, Roberta Ramponi, Daniel J Brod, Ernesto F. Galvão, Nicolò Spagnolo, Chiara Vitelli, Enrico Maiorino, Paolo Mataloni, and Fabio Sciarrino. Integrated multimode interferometers with arbitrary designs for photonic boson sampling. *Nat. Photonics*, 7(7):545–549, 2013. ISSN 1749-4885. doi: 10.1038/nphoton.2013.112. URL <http://www.nature.com/doi/10.1038/nphoton.2013.112>.
- [202] Matthew a. Broome, Alessandro Fedrizzi, Saleh Rahimi-Keshari, Justin Dove, Scott Aaronson, Timothy C. Ralph, and Andrew G. White. Photonic boson sampling in a tunable circuit. *Science (80-.)*, 339:794, 2013. ISSN 1095-9203.

- doi: 10.1126/science.1231440. URL <http://www.sciencemag.org/content/339/6121/794.full.html>.
- [203] Nicolò Spagnolo, Chiara Vitelli, Marco Bentivegna, Daniel J. Brod, Andrea Crespi, Fulvio Flamini, Sandro Giacomini, Giorgio Milani, Roberta Ramponi, Paolo Mataloni, Roberto Osellame, Ernesto F. Galvão, and Fabio Sciarrino. Experimental validation of photonic boson sampling. *Nat. Photonics*, 8(June):3–9, 2014. ISSN 1749-4885. doi: 10.1038/nphoton.2014.135. URL <http://arxiv.org/abs/1311.1622> <http://www.nature.com/doi/10.1038/nphoton.2014.135>.
- [204] A. Thoma, P. Schnauber, M. Gschrey, M. Seifried, J. Wolters, J. H. Schulze, A. Strittmatter, S. Rodt, A. Carmele, A. Knorr, T. Heindel, and S. Reitzenstein. Exploring Dephasing of a Solid-State Quantum Emitter via Time- and Temperature- Dependent Hong-Ou-Mandel Experiments. (CI):1–10, jul 2015. URL <http://arxiv.org/abs/1507.05900>.
- [205] Brian D Gerardot, Daniel Brunner, Paul a Dalgarno, Patrik Ohberg, Stefan Seidl, Martin Kroner, Khaled Karrai, Nick G Stoltz, Pierre M Petroff, and Richard J Warburton. Optical pumping of a single hole spin in a quantum dot. *Nature*, 451(7177):441–444, 2008. ISSN 0028-0836. doi: 10.1038/nature06472.
- [206] Ulrich Hohenester, Arne Laucht, Michael Kaniber, Norman Hauke, Andre Neumann, Abbas Mohtashami, Marek Seliger, Max Bichler, and Jonathan J. Finley. Phonon-assisted transitions from quantum dot excitons to cavity photons. *Phys. Rev. B - Condens. Matter Mater. Phys.*, 80(20):201311, nov 2009. ISSN 10980121. doi: 10.1103/PhysRevB.80.201311. URL <http://link.aps.org/doi/10.1103/PhysRevB.80.201311>.
- [207] K. H. Madsen, P. Kaer, A. Kreiner-Møller, S. Stobbe, A. Nysteen, J. Mørk, and P. Lodahl. Measuring the effective phonon density of states of a quantum dot. *Phys. Rev. B*, 88(4):5, jul 2013. ISSN 10980121. doi: 10.1103/PhysRevB.88.045316. URL <http://journals.aps.org/prb/abstract/10.1103/PhysRevB.88.045316>.
- [208] Yumin Shen, Timothy M. Sweeney, and Hailin Wang. Zero-phonon linewidth of single nitrogen vacancy centers in diamond nanocrystals. *Phys. Rev. B - Condens. Matter Mater. Phys.*, 77(3):033201, jan 2008. ISSN 10980121. doi: 10.1103/PhysRevB.77.033201. URL <http://link.aps.org/doi/10.1103/PhysRevB.77.033201>.

Cavity-Enhanced Photon-Photon Interactions Using Bright Quantum Dot Sources

Summary

In the pursuit of developing a quantum information network, photons appear to be the most convenient carriers to interconnect distant ports. The need to get on-demand single photons that is one and only one photon is the main driving force for the development of bright solid-state sources. One important parameter is the brightness defined as the probability that one collected pulse contains a single photon. For some applications, the emitted single photons must be also indistinguishable, so that the photons can interfere. By coupling a semiconductor quantum dot to an optical cavity, the spontaneous emission of the emitter can be modified to obtain bright single-photon sources. An innovative technique was developed by Pr. Pascale Senellart and her team at the Laboratory of Photonics and Nanostructures (LPN) from CNRS that allows making such sources in a very reproducible way.

This work explores the performance of single quantum dot coupled to micropillars. First, the cavity was modified using an adiabatic architecture such that the spontaneous emission was accelerated further. Then, a technique to apply an electric bias on the micropillars has been developed. The combination of the electric bias with a resonant optical excitation of the quantum dot allows to collect purely indistinguishable photons with a brightness greater by one order of magnitude compared to other sources.

The results developed in this thesis open a vast field of novel applications in quantum technologies, from quantum cryptography, metrology to quantum imaging.

Keywords: Quantum dots (QDs), CQED, Semiconductor, Quantum Optics

Résumé

Dans le domaine de l'information quantique, les photons apparaissent comme de parfaits bits quantiques (qubits) pour le transport de l'information. Le besoin de photons uniques sur demande, où un et un seul photon est émis conduit à une recherche considérable dans le développement de sources de photons. Un paramètre clé est la brillance, défini comme la probabilité qu'un photon émis par l'émetteur soit collecté. Pour certaines applications, il est important que les photons émis soient indiscernables. Dans ce cas les photons peuvent interférer. En couplant une boîte quantique avec une cavité optique, l'émission spontanée est de la boîte quantique est modifiée pour obtenir des sources brillantes de photons uniques. Une technique innovante développée dans l'équipe du Pr. Pascale Senellart au Laboratoire de Photonique et Nanostructures (LPN) du CNRS permet de fabriquer des sources brillantes de manière reproductible avec une excellente fiabilité.

Ce travail explore les performances de boîtes quantiques uniques couplées dans des micropiliers. Dans un premier temps, une structure de cavité adiabatique a été utilisée pour obtenir une plus grande accélération de l'émission spontanée des BQs par effet Purcell. Ces sources sont utilisées pour réaliser un réseau embryonnaire avec plusieurs sources. Ensuite, une technique a été développée pour appliquer une tension électrique sur les micropiliers. Grâce à cette technique et à une excitation optique résonante, des photons parfaitement indiscernables sont collectés avec une brillance plus élevée d'un ordre de grandeur par rapport à d'autres sources.

Les résultats présentés ouvrent de nombreuses perspectives pour diverses applications telles que la fabrication d'un réseau quantique, pour la cryptographie quantique, pour la métrologie ou pour la microscopie.

Mot-Clés: Boîtes Quantiques (BQs), CQED, Semiconducteur, Optique Quantique